

Direct Air Capture of CO₂ using Amine-Functionalised Nanofibrous Silica



Jake Edwards

A thesis submitted to UEA for the degree of

Doctor of Philosophy (PhD)

School of Engineering, Mathematics and Physics

University of East Anglia (UEA)

August 2024

© This copy of the thesis has been supplied on condition that anyone who consults it is understood to recognise that its copyright rests with the author and that use of any information derived therefrom must be in accordance with current UK Copyright Law. In addition, any quotation or extract must include full attribution.

Abstract

Limiting global warming to 1.5°C by 2100 necessitates both decarbonisation of the global economy and also the deployment of carbon dioxide removal technologies like direct air capture (DAC) at scale. Amine-functionalised solid adsorbents are one of the most widely studied family of materials for DAC, however, most are powders, which are impractical for industrial scale application. This thesis focuses on developing scalable amine-functionalised nanofibrous silicas for DAC.

Porous silica nanofibrous supports were prepared *via* electrospinning of colloidal silica and poly(vinyl alcohol), followed by heat treatment to remove the organic template. The optimal silica-to-polymer weight ratio was 2:1, with a calcination temperature of 700°C, yielding mesoporous nanofibres with a specific surface area of 130 m²/g.

The nanofibres were functionalised with amine groups *via* hydrous silane grafting. The grafting conditions, such as the amount of silane added and choice of grafting agent, significantly affected the resulting silane loading and grafting efficiency. The nanofibres were characterised at various stages of synthesis using TGA, FTIR, and ¹³C and ²⁹Si solid-state NMR techniques.

Testing of amine-functionalised nanofibres under simulated DAC conditions revealed that amine loading, temperature, flow rate and humidity impacted the pseudo-equilibrium capacity and uptake kinetics of the amine-modified nanofibres. ¹³C NMR experiments indicated that the dominant product of adsorption was ammonium carbamate. The Avrami kinetic model best described the CO₂ uptake behaviour of functionalised nanofibres. This study introduces a new interpretation of the Avrami exponent to understand mechanistic changes to the uptake process when the adsorption conditions were altered.

When factoring in both adsorption capacity and half-time, triamine-grafted nanofibrous silica (4.7 mmol_N/g_{sample}) had comparable performance to other similarly-loaded amine adsorbents from the literature, with an average uptake rate of 0.42 and 0.34 mmol·g⁻¹·h⁻¹ under dry and humid conditions, respectively. The presented findings indicate that amine-functionalised nanofibrous silicas have promising application for DAC.

Access Condition and Agreement

Each deposit in UEA Digital Repository is protected by copyright and other intellectual property rights, and duplication or sale of all or part of any of the Data Collections is not permitted, except that material may be duplicated by you for your research use or for educational purposes in electronic or print form. You must obtain permission from the copyright holder, usually the author, for any other use. Exceptions only apply where a deposit may be explicitly provided under a stated licence, such as a Creative Commons licence or Open Government licence.

Electronic or print copies may not be offered, whether for sale or otherwise to anyone, unless explicitly stated under a Creative Commons or Open Government license. Unauthorised reproduction, editing or reformatting for resale purposes is explicitly prohibited (except where approved by the copyright holder themselves) and UEA reserves the right to take immediate 'take down' action on behalf of the copyright and/or rights holder if this Access condition of the UEA Digital Repository is breached. Any material in this database has been supplied on the understanding that it is copyright material and that no quotation from the material may be published without proper acknowledgement.

Table of Contents

List of Tables.....	1
List of Figures.....	2
Acknowledgements.....	10
1 Introduction.....	11
1.1 Background.....	11
1.1.1 Brief History of Climate Science and Policy	11
1.1.2 The Need for Direct Air Capture of CO ₂	12
1.1.3 Financial Cost of DAC using Adsorbents	14
1.2 Literature Review on Porous Adsorbents for DAC	17
1.2.1 Amine Impregnated Inorganic Oxides	17
1.2.2 Amine-Grafted Inorganic Oxides.....	22
1.2.3 Polyamine-Tethered Inorganic Oxides.....	26
1.2.4 Metal Organic Frameworks.....	27
1.2.5 Zeolites.....	28
1.2.6 Amine-Supported Organic Sorbents	29
1.2.7 Alkali and Alkaline-earth Metal Compounds.....	29
1.2.8 Ion Exchange Resins	31
1.3 Discussion and Conclusions	32
1.4 Aims and Objectives.....	34
2 Experimental Part.....	35
2.1 Material Synthesis	35
2.1.1 Electrospinning	35
2.1.2 Factors Affecting the Electrospinning Process.....	38
2.1.3 Synthesis of SBA-15 Mesoporous Silica	41
2.1.4 Amine-Functionalisation of Silica	42
2.2 Material Characterisation	45
2.2.1 Scanning Electron Microscopy	45
2.2.2 Thermogravimetric Analysis	46
2.2.3 Fourier Transform Infrared Spectroscopy	47
2.2.4 Nitrogen Physisorption Analysis.....	50

2.2.5	Nuclear Magnetic Resonance Spectroscopy	57
2.2.6	Fixed-Bed Flow-Through System.....	69
2.2.7	Kinetic Modelling of Adsorption	71
2.3	Experimental Protocols.....	73
2.3.1	Reagents	73
2.3.2	Preparation of Nanofibres	73
2.3.3	Preparation of SBA-15	76
2.3.4	Surface Functionalisation of Silica	77
2.3.5	Scanning Electron Microscopy	78
2.3.6	Fibre Diameter Distribution	78
2.3.7	Characterisation of the Electrospinning Solutions	79
2.3.8	Thermogravimetric Analysis	79
2.3.9	Fourier Transform Infrared Spectroscopy (FTIR).....	80
2.3.10	Solid-state Nuclear Magnetic Resonance Spectroscopy	80
2.3.11	N ₂ Physisorption	81
2.3.12	Small Angle X-ray Scattering	81
2.3.13	CO ₂ Gravimetric Experiments	81
2.3.14	Fixed-Bed Column Experiments.....	82
2.3.15	Kinetic Modelling.....	84
2.3.16	Solid-State NMR Studies of CO ₂ Adsorption	84
2.3.17	Equations Used for Comparing Amine-Functionalised Nanofibrous Silica with other Grafted Silicas from the Literature	85
3	Synthesis and Characterisation of Functionalised Nanofibres.....	86
3.1	Overview of Electrospun Materials for CO ₂ Capture.....	86
3.2	Optimisation of the Synthesis of Silica Nanofibres.....	90
3.2.1	Effect of Flow Rate	91
3.2.2	Effect of Spinneret-to-Collector Distance	93
3.2.3	Effect of Formulation Composition	96
3.2.4	Effect of Calcination Temperature	98
3.2.5	Synthesis of Nanofibrous Silica using the Rotating Collector.....	99
3.2.6	Summary	100

3.3	Characterisation of Nanofibrous Silica Prepared Using the Optimised Synthesis Protocol	101
3.3.1	FTIR Analysis	101
3.3.2	Studying the Textural Properties of Electrospun Materials using Nitrogen Physisorption.....	103
3.3.3	Assessing the Thermal Stability of Electrospun Materials using Thermogravimetric Analysis.....	105
3.3.4	Assessing Chemical and Conformational Changes in the Polymeric Template using Solid-State NMR.....	106
3.3.5	Probing the Local Structure of Nanofibrous Silica using ^1H - ^{29}Si CP/MAS NMR....	109
3.4	Surface Functionalisation of Nanofibrous Silica	110
3.5	Effect of Silane Concentration on the Grafting Process	118
3.6	Effect of Silane Type on the Grafting Process.....	123
3.7	Effect of Water on the Grafting Process	134
3.8	Comparison with Silane Grafting of SBA-15 Mesoporous Silica.....	139
3.9	Conclusions	148
4	Direct Air Capture Studies of Amine-Functionalised Nanofibrous Silica	149
4.1	Techniques for Studying CO_2 Capture on Solid Adsorbents	149
4.2	TGA Studies	152
4.2.1	Bare <i>versus</i> Functionalised Nanofibrous Silica.....	152
4.2.2	Effect of Amine Loading	153
4.2.3	Effect of Amine Type	156
4.2.4	Effect of Adsorption Temperature	162
4.2.5	Regenerability Testing.....	164
4.3	Fixed-Bed Tests	169
4.3.1	Dynamic CO_2 Adsorption Behaviour of an APS-modified Nanofibrous Silica	169
4.3.2	Effect of Amine Type	172
4.3.3	Effect of Amine Loading.....	173
4.3.4	Effect of Flow Rate	175
4.3.5	Effect of Temperature.....	179
4.3.6	Effect of Humidity	187
4.3.7	Kinetic Modelling	194

4.4	Conclusions	203
5	Discussion and Future Work	204
5.1	Comparison of Nanofibrous Silica with Other Silicas from the Literature	204
5.2	Comparison of Functionalised Materials.....	206
5.3	Comparison of CO ₂ Capture Performance of Functionalised Nanofibrous Silicas with Other Adsorbents from the Literature	209
5.3.1	Dry Adsorption Comparison	209
5.3.2	Humid Adsorption Comparison	211
5.3.3	Comparison with Other Nanofibrous Adsorbents	213
5.3.4	Dynamic Performance Comparison at Various Flow Rates	214
5.3.5	Summary	215
5.4	Future Work.....	216
6	Overall Conclusions.....	219
	Appendix.....	221
	List of References	245

List of Tables

Table 1.1. Information on selected novel CDR technologies. ^[17] Technology Readiness Level (TLR) is on a 1-9 scale, with 1 denoting ‘basic principles observed’ and 9 ‘operationally proven systems’.	13
Table 2.1. List of amine-functionalised silicas prepared for Chapter 3. NFS = Nanofibrous silica.	78
Table 2.2. List of amine-functionalised nanofibrous silicas prepared for Chapter 4. All materials were grafted under hydrous conditions (0.6 ml _{water} /g _{silica}).	78
Table 3.1. Physical properties of the electrospinning formulations at 20°C.	97
Table 3.2. Relative areas of the deconvoluted C2 peaks from the ¹ H- ¹³ C CP-MAS spectra.	108

List of Figures

Figure 1.1. Breakdown of the estimated annualised cost of a generic solid sorbent direct air capture plant with a removal capacity of 1 MtCO ₂ /y. ^[22] CAPEX – capital expenditure, OPEX – operational expenditure. Costs are in 2019 USD.	15
Figure 2.1. Diagram of the electrospinning apparatus. Figure created by the author.	36
Figure 2.2. Diagram of a polymer jet's trajectory during the electrospinning process. Reproduced with permission from: [149]. Copyright 2006 American Chemical Society.	38
Figure 2.3. Cooperative self-assembly mechanism of SBA-15 silica. 1) Rod-like micelles form from the polymeric template, onto which the silica precursor condenses. 2) The micellar rods stack together into an ordered, hexagonal structure. 3) During hydrothermal treatment, TEOS continues to condense onto the micelles, resulting in a dense network of silica surrounding the rods. 4) The removal of the micelle rods <i>via</i> calcination results in a hexagonal array of cylindrical mesopores. Adapted with permission from: [163]. Copyright 1992 American Chemical Society.	42
Figure 2.4. Simplified schematic diagram of a scanning electron microscope. Reproduced with permission from: [173]. Copyright 2007 Springer Nature.	46
Figure 2.5. Schematic diagram of a thermogravimetric analysis instrument. Adapted with permission from: [176]. Copyright 2011 Springer Nature.	47
Figure 2.6. Pictorial representation of the different molecular stretching and bending modes detectable in FTIR spectroscopy. Reproduced from: [179]. Published by MDPI under a Creative Commons Attribution licence.	48
Figure 2.7. Simplified schematic diagram of an FTIR spectrometer. Adapted with permission from: [181]. Copyright 2014 John Wiley and Sons.	49
Figure 2.8. Simplified schematic diagram of an ATR sample cell. Figure created by author.	50
Figure 2.9. Types of IUPAC sorption isotherms. The up and down arrows indicate the adsorption and desorption branches, respectively. Reproduced from: [183]. Copyright 2015 IUPAC & De Gruyter.	52
Figure 2.10. Types of hysteresis loops. The up and down arrows indicate the adsorption and desorption branches, respectively. Copyright 2015 IUPAC & De Gruyter.	53
Figure 2.11. Schematic diagram of an NMR spectrometer with its main components. Reproduced with permission from: [191]. Copyright 2024 Technology Networks.	59
Figure 2.12.a) Vector (classical) model with a static (laboratory) frame of reference showing the precession of the bulk magnetic moment M about the applied static field B ₀ at equilibrium. b) Quantum model of NMR showing the two quantum levels that result from B ₀ . The dotted arrow indicates the energy gap between the two spin states. Reproduced with permission from Springer Nature [190].	60
Figure 2.13. Vector model with a rotating frame of reference showing the manipulation of the bulk magnetisation vector M during a direct polarisation experiment. a) Initially, M is parallel to B ₀ . b) A radiofrequency pulse is applied along the <i>x</i> -axis, causing M to precess about the axis of the alternating magnetic field B ₁ associated with the pulse. c) After the application of a $(\pi/2)_x/90^\circ_x$ pulse,	

M is situation along the y -axis. d) Spin-lattice relaxation results in the recovery of M along the z -axis, during which the NMR probe picks up a decaying signal (the free induction decay, FID). Adapted with permission from Springer Nature [190].	62
Figure 2.14. The NMR signal is converted from the time domain to the frequency domain using Fourier transformation. The resulting graph is an NMR spectrum which shows peaks at specific frequencies that reveal chemical information about the sample. Figure created by the author.	62
Figure 2.15. Geometrical representation of the shielding tensor. Θ relates the orientation of the interaction tensor with respect to \mathbf{B}_0 and ϕ with respect to the x - y plane (perpendicular to \mathbf{B}_0). Adapted from [193]. Published by LibreTexts under a Creative Commons Attribution licence.	66
Figure 2.16. Orientation of the shielding tensor of a nuclear spin in a rotor spinning at angle θ_r to the applied field. Adapted with permission from [192]. Copyright 2005 John Wiley and Sons.	68
Figure 2.17. Schematic diagram of the fixed-bed flow-through system. Figure created by the author.	70
Figure 2.18. Diagram of the electrospinning set-up used in this work. Figure created by the author.	74
Figure 3.1. Operating voltage at various syringe pump flow rates for the electrospinning of silica-PVA hybrid nanofibres at a fixed spinneret-to-collector distance of 15 cm.	91
Figure 3.2. SEM images and fibre diameter distributions for silica-PVA hybrid nanofibres electrospun at various flow rates: 0.5 ml/h (a), 0.75 ml/h (b) and 1.0 ml/h (c).	92
Figure 3.3. SEM images at 1k magnification for silica-PVA nanofibres electrospun at: 0.5 ml/h (a), 0.75 ml/h (b), 1.0 ml/h (c).	93
Figure 3.4. Operating voltage <i>versus</i> spinneret-to-collector distance for the electrospinning of silica-PVA hybrid nanofibres at a fixed flow rate of 0.75 ml/h.	94
Figure 3.5. Diameter of the collected mat <i>versus</i> spinneret-to-collector distance for the electrospinning of silica-PVA nanofibres at a fixed flow rate of 0.75 ml/h.	95
Figure 3.6. SEM images and fibre diameter distributions for silica-PVA hybrid nanofibres electrospun at various spinneret-to-collector distances: (a) 10 cm, (b) 15 cm and (c) 20 cm.	96
Figure 3.7. SEM images and fibre diameter distributions for 1:1 (a), 2:1 (b) and 3:1 (c) silica-to-polymer formulations.	98
Figure 3.8. SEM images of silica nanofibres synthesised from the three formulations after calcination in air at different temperatures. The samples were heated from room temperature to the calcination temperature at a ramp rate of 10°C/min. After 2 h of calcination, the samples were left to naturally cool down to room temperature inside the furnace.	99
Figure 3.9. Silica mats electrospun from 1:1 (a) and 2:1 (b) silica-polymer formulations after calcination at 700°C.	100
Figure 3.10. FTIR spectra of as-spun silica-PVA nanofibres (red) and heat-treated nanofibres (blue).	102

Figure 3.11. Ball-and-stick models of (a) four-fold and (b) six-fold siloxane ring structures commonly found in siliceous materials. Silicon and oxygen atoms are represented by the purple and red balls, respectively. Figure created by the author.....	102
Figure 3.12. Nitrogen adsorption/desorption isotherms at 77 K. The solid and open datapoints correspond to the adsorption and desorption branches of the isotherms, respectively.....	104
Figure 3.13. BJH pore size distribution of silica nanofibres.....	104
Figure 3.14. TGA and DTG curves (solid and dashed lines respectively) for silica-PVA (red) and silica (blue) nanofibres. Test conditions: 10°C/min ramp rate, Ar purge.....	105
Figure 3.15. TGA and DTG curves (solid and dashed lines respectively) for 2:1 PVA-silica nanofibres, along with the pure polymer in nanofibrous and granular form. Test conditions: 10°C/min ramp rate, Ar purge.	106
Figure 3.16. ¹ H- ¹³ C CP-MAS NMR spectra of raw PVA granules (top), PVA nanofibres (middle) and silica-PVA nanofibres (bottom). The spectra were collected using the same experimental parameters (4 k scans, 1.1 ms contact pulse, 5 s recycle delay) and have been normalised with respect to the C3 peak.....	107
Figure 3.17. ¹ H- ²⁹ Si CP-MAS NMR spectra for as-spun silica-PVA nanofibres (top) and silica nanofibres (bottom). The spectra were acquired using identical experimental conditions (4 k scans, 2 ms contact pulse, 10 s recycle delay).....	109
Figure 3.18. A nanofibrous silica mat before (a) and after (b) amine functionalisation.	110
Figure 3.19. FTIR spectra of silica nanofibres before (black) and after (red) APS functionalisation.	111
Figure 3.20. TGA thermograms of nanofibrous silica before (black) and after (red) APS functionalisation. Test conditions: 10°C/min ramp rate, Ar purge.....	113
Figure 3.21. SEM images of nanofibrous silica before (a) and after (b) APS-functionalisation. ...	113
Figure 3.22. ¹ H- ¹³ C CP-MAS NMR spectrum of APS-functionalised nanofibrous silica.	114
Figure 3.23. ¹ H- ²⁹ Si CP-MAS NMR spectra of nanofibrous silica before (black) and after (red) APS-functionalisation.	115
Figure 3.24. ²⁹ Si DP NMR spectra of nanofibrous silica before (blue) and after (pink) APS-functionalisation.	116
Figure 3.25. Three idealised aminosilane binding motifs that may contribute to the T ³ signal observed in ²⁹ Si NMR analysis of the surface-modified silica. The grey rectangles represent the silica surface and the bold silicon atoms are the T ³ sites.	117
Figure 3.26. Silane loading and grafting efficiency <i>versus</i> silane added for APS-modified nanofibres.	118
Figure 3.27. TGA thermograms of APS-modified nanofibrous silica of differing silane loadings. Test conditions: 10°C/min ramp rate, Ar purge.....	119
Figure 3.28. FTIR spectra of APS-modified silica nanofibres at various silane loadings.	120
Figure 3.29. ¹ H- ¹³ C CP-MAS NMR spectra for APS-functionalised nanofibrous silica at various silane loadings.....	121

Figure 3.30. ^1H - ^{29}Si CP-MAS NMR spectra of APS-grafted nanofibrous silica at different silane loadings.....	122
Figure 3.31. Silane loading (a) and grafting efficiency (b) <i>versus</i> silane added for silica nanofibres modified with three different silanes.	125
Figure 3.32. TGA thermograms of DAS-modified silica nanofibres prepared using different silane concentrations. Test conditions: 10°C/min ramp rate, Ar purge.	126
Figure 3.33. TGA thermograms of TAS-modified silica nanofibres prepared using different silane concentrations. Test conditions: 10°C/min ramp rate, Ar purge.	127
Figure 3.34. FTIR spectra of DAS-functionalised silica nanofibres.....	128
Figure 3.35. FTIR spectra of TAS-functionalised silica nanofibres.....	129
Figure 3.36. ^1H - ^{13}C CP-MAS NMR spectra for DAS-functionalised nanofibres at different silane loadings.....	130
Figure 3.37. ^1H - ^{13}C CP-MAS NMR spectra for TAS-functionalised nanofibres at different silane loadings.....	131
Figure 3.38. ^1H - ^{29}Si CP-MAS NMR spectra of DAS-grafted silica nanofibres at different loadings.	132
Figure 3.39. ^1H - ^{29}Si CP-MAS NMR spectra of TAS-grafted silica nanofibres at different loadings.	133
Figure 3.40. Silane loadings (a) and corresponding grafting efficiencies (b) of nanofibrous silica functionalised in anhydrous and hydrous conditions.	134
Figure 3.41. TGA traces of APS-modified silica grafted under anhydrous (green) and hydrous conditions (pink). Test conditions: 10°C/min ramp rate, Ar purge.	135
Figure 3.42. FTIR spectra of silica nanofibres grafted under anhydrous (pink) and hydrous (green) conditions with comparable silane loadings.	136
Figure 3.43. ^1H - ^{13}C CP-MAS NMR spectra of APS-functionalised silica nanofibres grafted under anhydrous and hydrous conditions with comparable silane loadings.	137
Figure 3.44. ^1H - ^{29}Si CP-MAS NMR spectra of silica nanofibres grafted under anhydrous (green) and hydrous (pink) conditions.	138
Figure 3.45. SAXS diffraction pattern of SBA-15 showing three interferences peaks indexed as (100), (110) and (200) Bragg reflections, characteristic of hexagonal mesoporous silica. ^[164]	139
Figure 3.46. TGA/DTG thermograms of SBA-15 (green) and silica nanofibres (red). Test conditions: 10°C/min ramp rate, Ar purge.	140
Figure 3.47. TGA/DTG thermograms of APS-modified silicas; SBA-15 (blue) and nanofibres (pink). Test conditions: 10°C/min ramp rate, Ar purge.	141
Figure 3.48. Aminosilane loading and efficiency for silica nanofibres and SBA-15 silica grafted under the same conditions (APS, 5 ml _{AS} /g _{silica} , 0.6 ml _{water} /g _{silica}).....	142
Figure 3.49. FTIR spectra of SBA-15 (green) and silica nanofibres (red).....	143
Figure 3.50. FTIR spectra of APS-functionalised SBA-15 (blue) and silica nanofibres (pink).....	144

Figure 3.51. ^1H - ^{13}C CP-MAS NMR spectra of APS-functionalised SBA-15 (blue) and silica nanofibres (pink).....	145
Figure 3.52. ^1H - ^{29}Si CP-MAS NMR spectra of SBA-15 (green) and silica nanofibres (red).The spectra were collected using the same experimental parameters (2 ms contact time, 10 s recycle delay, 4 k scans).	146
Figure 3.53. ^1H - ^{29}Si CP-MAS NMR spectra of APS-modified SBA-15 (blue) and functionalised silica nanofibres (pink). The spectra were collected using the same experimental parameters (2 ms contact time, 10 s recycle delay, 4 k scans).....	147
Figure 4.1. Movement of a mass transfer zone across a fixed bed reactor during a breakthrough test. Adapted with permission from: [279].	151
Figure 4.2. TGA CO_2 adsorption isotherms of bare and APS-functionalised nanofibrous silica during exposure to 400 ppm CO_2 at 25°C	152
Figure 4.3. TGA CO_2 adsorption isotherms recorded at 25°C for APS-modified silica nanofibres of differing amine loadings.	154
Figure 4.4. Final CO_2 adsorption capacities and amine efficiencies of the three APS-loaded nanofibrous silicas. Error: $\leq \pm 0.003 \text{ mmol/g}$ (adsorption capacity), $\leq \pm 0.015 \text{ mmolCO}_2/\text{mmolN}$.(amine efficiency).	155
Figure 4.5. Initial adsorption rates of the three APS-loaded nanofibrous silicas.	156
Figure 4.6. TGA CO_2 adsorption isotherms at 25°C of DAS-modified silica nanofibres with different amine loadings.	157
Figure 4.7. TGA CO_2 adsorption isotherms at 25°C of TAS-modified silica nanofibres with different amine loadings.	157
Figure 4.8. Final CO_2 adsorption capacities and amine efficiencies of the three DAS-loaded nanofibrous silicas. Error: $\leq \pm 0.003 \text{ mmol/g}$ (adsorption capacity), $\leq \pm 0.015 \text{ mmolCO}_2/\text{mmolN}$.(amine efficiency).	158
Figure 4.9. Final CO_2 adsorption capacities and amine efficiencies of the three TAS-loaded nanofibrous silicas. Error: $\leq \pm 0.003 \text{ mmol/g}$ (adsorption capacity), $\leq \pm 0.015 \text{ mmolCO}_2/\text{mmolN}$.(amine efficiency).	159
Figure 4.10. Initial adsorption rates of the three DAS-loaded nanofibrous silicas.	160
Figure 4.11. Initial adsorption rates of the three TAS-loaded nanofibrous silicas.	160
Figure 4.12. Final CO_2 adsorption capacities and amine efficiencies of APS, DAS and TAS functionalised nanofibrous silicas with similar amine loadings (2.6, 2.6 and 2.1 mmolN/g , respectively). Error: $\leq \pm 0.003 \text{ mmol/g}$ (adsorption capacity), $\leq \pm 0.015 \text{ mmolCO}_2/\text{mmolN}$.(amine efficiency).	161
Figure 4.13. Initial adsorption rates of APS, DAS and TAS functionalised nanofibrous silicas with similar amine loadings.	162
Figure 4.14. Final adsorption capacities of silica nanofibres functionalised with APS (2.6 mmolN/g), DAS (2.2 mmolN/g) and TAS (2.6 mmolN/g) aminosilanes after three hours of CO_2 exposure at different temperatures. Error: $\leq \pm 0.003 \text{ mmol/g}$	163

Figure 4.15. Initial adsorption rates of three amine-grafted nanofibrous silicas of similar amine loadings after three hours of CO ₂ exposure at different temperatures.	164
Figure 4.16. Temperature and weight variation during five adsorption-desorption cycles for an APS-grafted material (amine loading = 2.4 mmol _N /g).....	165
Figure 4.17. Final adsorption capacity of APS-grafted silica (2.4 mmol _N /g) after each cycle. Error: ≤ ± 0.003 mmol/g.	166
Figure 4.18. Overlaid adsorption isotherms of APS-grafted silica (2.4 mmol _N /g) obtained from each cycle during regeneration testing.	167
Figure 4.19. SEM images of APS-grafted nanofibres (2.4 mmol _N /g) before (a) and after (b) five adsorption-desorption cycles.	167
Figure 4.20. Final adsorption capacity (a) and overlaid CO ₂ uptake profiles (b) of TAS-grafted nanofibrous silica (2.6 mmol _N /g) during regeneration testing. Error: ≤ ± 0.003 mmol/g.	168
Figure 4.21. Relative CO ₂ concentration in the column effluent during dynamic DAC testing of APS-2.6 (red) and a blank run with no adsorbent (black) at 25°C (100 SCCM flow rate).	170
Figure 4.22. ¹ H- ¹³ C CP/MAS NMR spectra of outgassed APS-2.6 and the same material after exposure to 400 ppm CO ₂ (25°C). The dashed line corresponds to the chemical shift at which the chemisorbed CO ₂ resonance is located.	171
Figure 4.23. Breakthrough profiles of APS-2.6 and TAS-2.6 (100 SCCM, 25°C).	173
Figure 4.24. Breakthrough profiles of TAS-grafted nanofibrous silicas with different amine loadings (100 SCCM, 25°C).	174
Figure 4.25. Pseudo-equilibrium capacity and amine efficiency of the three TAS-grafted materials (25°C, 100 SCCM).	174
Figure 4.26. CO ₂ extraction rate and capture fraction of the three TAS-grafted adsorbents at C/C ₀ = 0.95.....	175
Figure 4.27. Breakthrough curves for APS-2.6 under various flow rates at 25°C.	176
Figure 4.28. Breakthrough times of the four adsorbents under various flow rates at 25°C.	177
Figure 4.29. CO ₂ extraction rates of the four adsorbents at various flow rates.....	178
Figure 4.30. Capture fraction of the four amine-modified nanofibrous silicas at various flow rates.	179
Figure 4.31. Breakthrough curves for APS-2.6 at various temperatures (100 SCCM flow rate)....	180
Figure 4.32. Pseudo-equilibrium adsorption capacity of APS-2.6 at various temperatures (100 SCCM).....	181
Figure 4.33. ¹ H- ¹³ C CP-MAS NMR spectra of APS-2.6 after 400 ppm CO ₂ exposure at various temperatures.....	182
Figure 4.34. CO ₂ extraction rate for APS-2.6 at different temperatures.	183
Figure 4.35. Capture fraction for APS-2.6 at different temperatures.	183
Figure 4.36. Variation in breakthrough time with temperature of four amine-functionalised nanofibrous silicas (100 SCCM flow rate).	184

Figure 4.37. Variation in pseudo-equilibrium adsorption capacity with temperature of the four adsorbents.	185
Figure 4.38. ^1H - ^{13}C CP-MAS NMR spectra of TAS-4.9 after exposure to dry 400 ppm CO_2 at four adsorption temperatures.	186
Figure 4.39. CO_2 extraction rates at different temperatures for the four amine-functionalised nanofibrous silicas.	187
Figure 4.40. CO_2 capture fraction at different temperatures for the four amine-functionalised nanofibrous silicas.	187
Figure 4.41. Breakthrough curves for TAS-2.6 under dry and humid conditions (25°C, 100 SCCM).	188
Figure 4.42. Breakthrough curve for TAS-4.9 under dry and humid conditions (25°C, 100 SCCM).	189
Figure 4.43. Breakthrough curves for TAS-6.4 under dry and humid conditions (25°C, 100 SCCM).	189
Figure 4.44. Breakthrough times of the three triamine-grafted materials under dry and humid conditions.	190
Figure 4.45. Pseudo-equilibrium capacities of the three triamine-grafted nanofibrous silicas after exposure to dry and humid CO_2	191
Figure 4.46. ^1H - ^{13}C CP-MAS NMR spectra of TAS-functionalised silica nanofibre after 3 h of exposure to dry and humid CO_2 gas feeds. The spectra are normalised with respect to the tallest methylene peak.	193
Figure 4.47. Extraction rate of the triamine-grafted materials under dry and humid conditions. ...	194
Figure 4.48. Capture fraction of the triamine-grafted materials under dry and humid conditions. ...	194
Figure 4.49. Percentage of fittings that yielded an R^2 greater than 0.99 for the different kinetic models.	195
Figure 4.50. Avrami exponents (n_a) from fixed-bed tests at different flow rates (25°C).	197
Figure 4.51. Avrami exponents (n_a) from fixed-bed tests at different temperatures (100 SCCM). ...	198
Figure 4.52. Avrami exponents (n_a) from fixed-bed tests under dry and humid conditions (25°C, 100 SCCM).	199
Figure 4.53. Avrami constants (k_a) from fixed-bed tests at different flow rates (25°C).	200
Figure 4.54. Avrami constants (k_a) from fixed-bed tests at different temperatures (100 SCCM). ...	201
Figure 4.55. Avrami constants (k_a) from fixed-bed tests under dry and humid conditions (25°C, 100 SCCM).	202
Figure 5.1. Surface area and total pore volume of nanofibrous silica (NFS) synthesised in this work compared to other mesoporous silicas from the literature: SBA-15 ^[298] , pore-expanded SBA-15 (PE-SBA-15) ^[298] , KIT-6 ^[299] , MCM-48 ^[299] and pore-expanded MCM-41 (PE-MCM-41). ^[281] The average pore diameter of each support is shown in brackets.	204

Figure 5.2. Surface area and total pore volume against average particle size of nanofibres synthesised from colloidal silica. NFS (this work), K15, K50 and K100 from the study by Kanehata <i>et al.</i> ^[231]	205
Figure 5.3. Grafting efficiency <i>versus</i> silane added to the reaction mixture of various triamine-modified silicas: TAS-2.1, TAS-2.6, TAS-4.9 and TAS-7.4 (own work), AG-SBA-15-PE-0.6 ^[298] , MCM-41-30-TP-9-75-0.5 ^[281] , and SBA-15/D-1, D-1.5 and D-4. ^[300]	206
Figure 5.4. Pore fill fraction <i>versus</i> amine loading of various triamine-modified silicas.	207
Figure 5.5. Amine coverage <i>versus</i> amine loading of various triamine-modified silicas.	208
Figure 5.6. Maximum CO ₂ uptake and adsorption half-times of amine-functionalised materials with similar amine loadings to TAS-4.9 under dry DAC conditions. *No kinetic data was available for S-T-4.6.....	210
Figure 5.7. Average uptake rates of various amine-functionalised adsorbents tested under dry DAC conditions.....	211
Figure 5.8. CO ₂ uptake and adsorption half-times of amine-functionalised materials with similar amine loadings to TAS-4.9 tested under humid DAC conditions.	212
Figure 5.9. Average uptake rates of amine-functionalised adsorbents tested under humid DAC conditions.....	213
Figure 5.10. Average uptake rates of nanofibrous adsorbents tested under humid DAC conditions	214
Figure 5.11. Rate of CO ₂ extraction <i>versus</i> flow rate for TAS-6.4 and an amine-appended MOF at C/C ₀ = 0.95 from fixed-bed experiments.	215
Figure 5.12. Capture fraction <i>versus</i> flow rate for TAS-6.4 and an amine-appended MOF at C/C ₀ = 0.95 from fixed-bed experiments.	215
Figure 5.13. Proposed laminate DAC contactor for testing of functionalised nanofibrous silica under more realistic processing conditions. As-synthesised nanofibrous mats (blue) are stacked inside the contactor and the CO ₂ feed is passed through it parallel to the adsorbent sheets. Adapted with permission from: [207]. Copyright 2022 American Chemical Society.....	218

Acknowledgements

First and foremost, I would like to extend my gratitude to Professor Yaroslav Khimyak, my primary supervisor, for his invaluable and unwavering support throughout my PhD journey.

I would also like to pay tribute to the following individuals:

Dr Matthew Alexander, for encouraging me to embark on this project and guiding me through the first few years of my research.

Dr Sonia Melendi-Espina, my secondary supervisor, for her guidance during my final year.

Dr Alexander Morritt for the invaluable and extensive laboratory training when I was starting out.

Dr Trey Koev for his all-round support and for being a listening ear whenever I encountered challenges, whether personal or research-related.

Sincere thanks are also due to the following:

Professor Chris Atkin, Head of Engineering.

The School's administrative staff.

The Faculty technical support staff.

Finally, this research would not have been possible without the love, patience and encouragement of my family and friends. They know who they are!

1 Introduction

1.1 Background

1.1.1 Brief History of Climate Science and Policy

Anthropogenic climate change is one of the greatest threats to human civilisation this century, with the potential to irreversibly destroy ecosystems across the globe and lead to the displacement of millions of people from regions rendered uninhabitable by the phenomenon.

Due to variations in Earth's orbital pattern, the average surface temperature has naturally cycled between periods of cooling (ice ages) and warming (interglacial periods) on the timescale of hundreds of thousands of years. The presence of greenhouse gases such as carbon dioxide ensured that even during the coolest spells, Earth's temperature was sufficient to sustain life.^[1] This changed, however, with the invention of the steam engine, which heralded the Industrial Revolution. It is now indisputable that increasing emissions of greenhouse gases from human activity since then are responsible for the observed mean global surface temperature rise of *ca.* 1.1°C relative to the preindustrial average. This is wreaking havoc with Earth's climate system, impacting humans and ecosystems across the planet.^[2, 3]

The concept of the 'greenhouse effect' was first developed in the late 18th and 19th centuries, when scientists proposed that solar energy absorbed and re-emitted by the Earth's surface could be trapped in the planet's atmosphere in a similar fashion to how a greenhouse retains heat.^[4] In 1861, John Tyndall attributed the heating phenomenon to water vapour and CO₂.^[5] Then, in 1938, G.S. Callendar published a groundbreaking paper linking the increase in global temperature over the previous 50 years to greenhouse gas emissions produced by combustion.^[6] Accurate, continuous readings of atmospheric CO₂ levels, first started in 1958 in Mauna Loa, Hawaii by Charles Keeling, enabled scientists to decouple natural variations in CO₂ levels from the increasing contribution from anthropogenic sources.^[7] In the 1970s, methane, dinitrogen oxide and chlorofluorocarbons from anthropogenic sources were also identified as greenhouse gases that contribute to human-induced global warming.^[8, 9]

In the 1980s, the dangers of climate change became apparent. A notable milestone came in 1980 when an interdisciplinary meeting of distinguished Earth scientists in Villach, Austria provoked the realisation that the potential consequences of anthropogenic warming were of grave concern. Consequently, a more comprehensive analysis of the physical science was commissioned by the US Academy of Sciences, the results of which were discussed in Villach in 1985. During this pivotal conference, a global panel of scientists agreed that there would be an unprecedented rise in Earth's average temperature in the first half of the 21st century. As result, it was seen of vital importance that policy-makers were brought into the fold at future climate conferences to ensure that governmental strategy took into consideration the latest knowledge on climate change.^[10] This ultimately lead to

the establishment of the Inter-Governmental Panel on Climate Change (IPCC) by the United Nations in 1988.^[11]

Since its founding, the IPCC has published a series of comprehensive reports on climate change, detailing: the latest physical science, natural and socioeconomic consequences, and possible courses of action to adapt to the impacts and limit warming. The IPCC reports have informed monumental international agreements to address climate change. For example, the 2nd Assessment Report helped shape the Kyoto Protocol, an international treaty adopted in 1997 by countries party to the United Nations Framework Convention on Climate Change (UNFCCC).^[12] This was an international treaty that, for the first time, committed industrialised nations to reducing their greenhouse gas emissions.^[13] Publishing of the fifth assessment informed the Paris Agreement, a UNFCCC treaty which superseded the Kyoto Protocol.^[12]

The Paris Agreement was conceived at the 21st annual gathering of members of the UNFCCC in 2015. Ratified by 195 parties (194 countries plus the European Union), the Agreement aims to limit global warming by the end of the century to “well below 2°C above pre-industrial levels”, and endeavours to cap warming at 1.5°C. Signatories are required to submit their own “nationally determined contribution” (NDC) - a comprehensive plan which details how a particular country is going to contribute to curbing dangerous climate change pursuant to the Agreement. NDCs must be revised every five years, with each successive action plan a “ratcheting up” of ambitions.^[14]

1.1.2 The Need for Direct Air Capture of CO₂

In addition to decarbonisation of the world’s economies, carbon dioxide removal (CDR) deployment appears in all future emission scenarios congruent with 1.5°C of global warming.^[15] CDR involves the removal and sequestration of carbon dioxide from the atmosphere on land, in oceans and geological formations. Its purpose is three-fold: to accelerate the global reduction in CO₂ emissions, compensate for residual emissions from hard-to-abate sources, and facilitate net negative carbon emissions required in the latter half of this century.^[15, 16] So-called ‘conventional’ techniques such as afforestation and reforestation have a high degree of technological maturity and are already being deployed at scale, achieving 2 GtCO₂ negative emissions per year. Additionally, most 1.5°C emission scenarios involve ‘novel’ CDR technologies such as direct air capture (DAC), bioenergy carbon capture and storage (BECCS), enhanced weathering, ocean fertilisation and biochar.^[17] CDR technologies are at various stages of technological readiness level and have their own unique advantages and drawbacks (Table 1.1).

Table 1.1. Information on selected novel CDR technologies.^[17] Technology Readiness Level (TRL) is on a 1-9 scale, with 1 denoting ‘basic principles observed’ and 9 ‘operationally proven systems’.

Technology	Description	TRL	Capture Potential (GtCO ₂ /yr)	Advantages	Drawbacks
Direct Air Capture	Synthetic removal and geological sequestration of CO ₂ from ambient air.	6	5-40	High capture potential. Reliable methods for monitoring, reporting and verification (MRV) of removal rates.	High capital investment. High energy requirement.
Bioenergy with Carbon Capture and Storage	Capture and geological sequestration of CO ₂ from combustion of biomass.	5-6	0.5-11	Positive energy balance. Reliable MRV methods.	High land demand. High water demand.
Enhanced Weathering	Deposition of milled silicate minerals on fields and in the ocean.	3-4	2-4	Low land footprint. Low water requirement.	Lack of methodology for MRV.
Ocean Fertilisation	Scattering of nutrients in the ocean to stimulate plankton growth.	1-2	1-3	Increased biological productivity, potentially leading to higher catch of fish.	Lack of methodology for MRV. Impact on marine ecosystems not fully understood.
Biochar	Pyrolysis of biomass. Storage of resulting biochar in soil.	6-7	0.3-6.6	Enhanced crop yields. Improved soil water retention.	Air pollution from biochar production.

To date, the total contribution to negative emissions from novel CDR is 0.002 GtCO₂/yr. When averaged across all 1.5°C pathways, novel CDR needs to scale to 0.06 GtCO₂/yr by 2030 and 2.6 GtCO₂/yr by 2050.^[17] This is equivalent to 0.5% and 7% of global CO₂ emissions in 2022, respectively.^[18]

Projected global CDR removal rates based on countries’ NDCs fall short of what is required to limit warming.^[17] Thus, achieving net zero emissions by 2050 necessitates the urgent development and deployment of novel CDR at scale. Direct air capture (DAC) holds particular promise, the main advantages over the other mooted CDR technologies being: a very high storage potential, small spatial footprint, and the ability to site plants close to a low-carbon energy source and/or a storage

reservoir, thereby lowering the cost of transmission of electricity to the plant and transport of CO₂ to the sequestration site, respectively.^[19]

There is a plethora of gas separation technologies being developed for DAC such as sorption, membranes, electrochemical separation and cryogenic systems. However, the overwhelming focus in the research and development community has been on the development of sorption-based DAC systems.^[20]

The most common DAC system comprises three stages:

1. Ambient air is passed through a contactor containing the sorbent which captures carbon dioxide from the gas feed. The sorption medium is typically either a porous adsorbent or a liquid solvent.
2. Once the sorbent is saturated, the captured gas is reformed via a regeneration process.
3. The CO₂ is transported to an external facility for storage or utilisation.

1.1.3 Financial Cost of DAC using Adsorbents

Regarding the cost of DAC, the industry target is \$100 per tonne of CO₂ captured, transported and stored.^[21] The National Academy of Sciences simulated the capture cost of a generic solid sorbent capture system in five scenarios. The total cost varied greatly from \$18/tCO₂ to \$1000/tCO₂, although the best case scenario was considered unachievable due to the interrelatedness of the cost parameters, meaning they could not all be simultaneously optimised in the real world. Apart from the most optimistic scenario, the expenditure on the adsorbent was overwhelmingly the biggest contributor to the estimated cost of DAC (Figure 1.1).^[22]

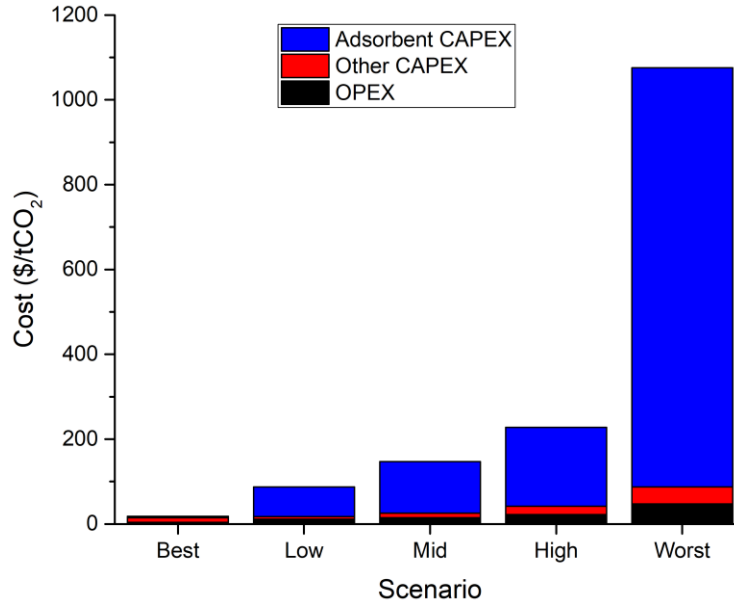


Figure 1.1. Breakdown of the estimated annualised cost of a generic solid sorbent direct air capture plant with a removal capacity of 1 MtCO₂/y.^[22] CAPEX – capital expenditure, OPEX – operational expenditure. Costs are in 2019 USD.

The maximum allowable budget (B) provides a useful metric for determining the acceptable expenditure on the adsorbent (Equation (1.1)).^[23,24] If the material cost exceeds B, then the adsorbent is financially unviable for DAC.

$$B = \frac{PC}{rt_{\text{cycle}}} (1 - e^{-rt_{\text{life}}}) \quad (1.1)$$

Where P = fraction of the price of a unit mass of CO₂ allocated to the sorbent, C = dimensionless adsorption capacity, r = discount rate, t_{cycle} = cycle length, t_{life} = sorbent lifetime

Equation (1.1) demonstrates there are three key performance metrics underlying the allowable budget of a particular adsorbent.

- CO₂ loading or adsorption capacity (C) – a measure of the amount of CO₂ bound to the sorbent relative to the sorbent mass. Higher capacities imply better value for money, since the same unit mass of adsorbent can soak up more CO₂. Aside from the physiochemical properties of the adsorbent (e.g. active site density and accessibility, heat of adsorption), humidity and temperature significantly influence the CO₂ uptake of materials for DAC.^[25] Equilibrium adsorption capacity denotes the maximum CO₂ loading for the material under fixed conditions. In practical applications of the material, the working capacity, which is the

amount of CO₂ removed per gram of sorbent after one complete cycle, is more relevant in evaluating the economic viability of a material for DAC. It may take hours for the equilibrium capacity to be attained which may correspond to a sub-optimal removal rate. Therefore, the working capacity, which is found by balancing kinetics with loading to maximise productivity, is of more relevance to the practical application of adsorbents for DAC.

- Cycle time (t_{cycle}) – this depends on the time allocated to the removal of CO₂ (adsorption) and regeneration of the material (desorption), along with the intermediate preparatory steps such as evacuation of air from the spent adsorbent prior to regeneration. Gas transfer *via* dispersion and diffusive driving forces effect the choice of cycle time, which are themselves dependent on the micro- and macroscopic structural characteristics of the adsorbent. For example, porosity, permeability and adsorbent form (powder, pellets, monoliths, fibres). As with adsorption capacity, reactor conditions (temperature, humidity, superficial gas velocity) also influence sorption kinetics.^[25, 26]
- Sorbent lifetime – this is determined by regenerability, hydrothermal stability, oxidative stability and the material's mechanical properties. It is worth noting that Equation (1.1) assumes that the adsorption capacity is constant throughout the sorbent's operation. Physical and chemical deterioration of the sorbent is inevitable. Therefore, the equation should be viewed as the most optimistic allowable budget.

A further property of the adsorbents that is of importance to the economics of direct air capture is the heat of adsorption. Adsorption is an exothermic process whilst desorption is endothermic, meaning that thermal energy is required to strip off the captured CO₂ during material regeneration. Desorption heat is the biggest contributor to the total energy requirement of a solid sorbent DAC system^[22] and therefore strategies to lower the energy requirement of the regeneration step like using a lower temperature would make DAC more commercially viable.^[27]

Significant work has been invested into the development of porous adsorbents for DAC based on the performance metrics discussed above. The next sub-section will review the literature on the main families of materials explored to date.

1.2 Literature Review on Porous Adsorbents for DAC

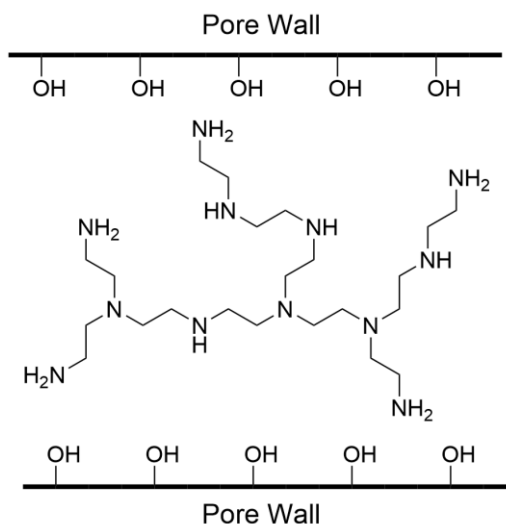
Throughout this literature review, where possible, the test conditions used for measuring the performance of a particular solid adsorbent are stated in parentheses. These include: the method of measurement, gas stream composition, adsorption/desorption temperature and experimental time.

There are three principal methods of measurement outlined below.

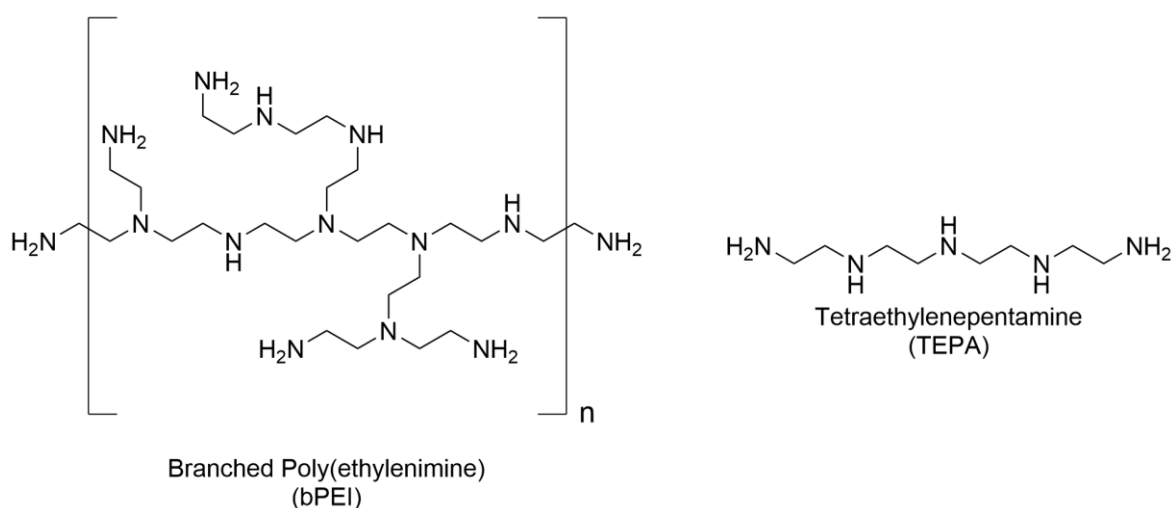
- The thermogravimetric analysis (TGA) method. A TGA instrument is used to measure the increase in sample weight during CO₂ exposure which is then converted into the adsorption capacity (mmolCO₂/g_{adsorbent}).
- The volumetric method. This makes use of a surface area and pore analyser to measure the CO₂ adsorption capacity at equilibrium across a range of pressures. The DAC adsorption capacity is typically the value recorded at a pressure of *ca* 0.04 kPa, roughly the CO₂ partial pressure of ambient air.
- Reactor method. The adsorbent is tested in a lab-scale reactor with a fixed-bed or fluidised-bed. The adsorption capacity is deduced from the change in CO₂ concentration from the gas flowing out of the reactor during the experiment.

1.2.1 Amine Impregnated Inorganic Oxides

Amine-impregnated inorganic oxides are a class of material comprising amine-bearing reagent physically loaded into the pores of an inorganic oxide support (Scheme 1.1). The two most commonly used amines are branched poly(ethylenimine) (bPEI) and tetraethylenepentamine (TEPA), shown in Scheme 1.2.



Scheme 1.1. Skeletal diagram of an amine impregnated inorganic oxide.



Scheme 1.2. Skeletal diagrams of branched poly(ethylenimine) and tetraethylenepentamine.

Amine-impregnated adsorbents were pioneered for CO₂ capture in 2002 by Xu *et al.*^[28] They proposed “molecular baskets” comprising mesoporous MCM-41 silica physically loaded with bPEI in the pore channels of the support as a means of scrubbing CO₂ from flue gas. Physisorbents such as zeolites and activated carbons perform poorly at elevated temperatures and this motivated the group to explore amine adsorbents, which have a higher CO₂ binding affinity due to the chemical mechanism underpinning the uptake of adsorbate. The group found that the presence of branched PEI on the pore walls significantly enhanced the CO₂ uptake of MCM-41 by a factor of 24 when subjected to 100% CO₂ flow at 75°C in a thermogravimetric analysis (TGA) instrument. Testing of the molecular baskets in gas mixtures similar to that in flue gases revealed that bPEI-impregnated MCM-41 had a superior selectivity for CO₂ over other gaseous components of the feed gas (N₂, O₂ and CO).^[29] Several years later, a suite of other mesoporous supports were functionalised with bPEI

(KIT-6, SBA-15, SBA-16, MCM-48). Like MCM-41, the other silica supports reversibly adsorbed CO₂ whilst retaining their porous, ordered morphology. This demonstrated the universality of the functionalisation route for CO₂ removal.^[30] Comparable gravimetric CO₂ capacities were also achieved for commercially available supports such as fumed silica.^[31] Notably, support morphology and pore size played a more important role than surface area in determining adsorption capacity and uptake kinetics of the sorbent.^[30, 31]

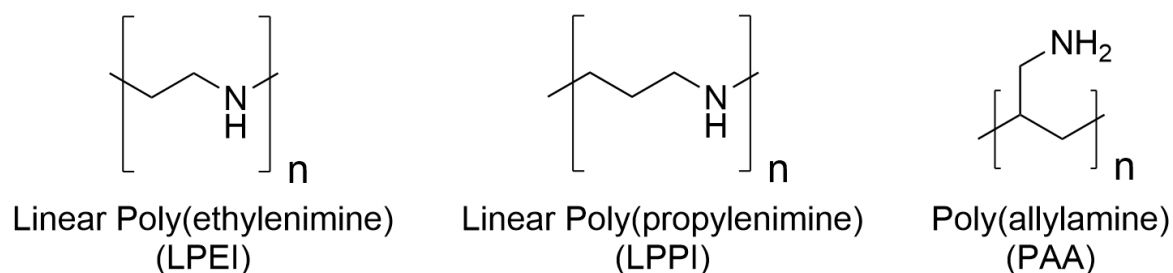
Application of amine-impregnated silicas for CO₂ removal from ambient air was first proposed by Goeppert *et al* in 2011. They found that bPEI-impregnated fumed silica could effectively adsorb CO₂ from dry laboratory air in a fixed-bed flow through reactor. After 25 hours of adsorption, the highest achieved capacity was 1.7 mmol/g under humid conditions, which was the highest reported CO₂ loading for a DAC solid sorbent at the time of publishing (fixed-bed, 420 ppm CO₂, air, 67% RH, 25°C).^[32]

Thereafter, efforts have been pursued to improve the performance of amine-impregnated inorganic oxides adsorbents subjected to DAC-like conditions. One way of achieving this is to increase the loading of polyamine. In the case of bPEI/TEPA-silica sorbents, at low loadings, an even coating of polyamine forms on the pore walls. Amine accessibility is impeded by interactions at the amine-silica interface resulting in low amine mobility and low CO₂ uptake. Increasing loading increases the amine efficiency (molar ratio of CO₂ captured to the amount of nitrogen in the material) as well as adsorption rate, since a greater proportion of reactive amines are not interacting with pore walls and are thus more mobile. Beyond a certain point, additional polymer forms aggregates in the pores which grow in size with loading. Eventually, pore occlusion occurs which impedes mass transfer of CO₂ through the pore channels.^[33-35]

TEPA-loaded silicas have a better uptake capacity compared to bPEI at equivalent loadings due to the former's higher mobility endowed by its lower molecular weight.^[35] However, because of its lower molecular weight, TEPA has the tendency to leach out of the support over repeat adsorption-desorption cycles, resulting in a reduction in its working capacity (adsorption capacity after each cycle) during regeneration testing. This is not an issue for bPEI due its higher viscosity and boiling point.^[36] Notwithstanding, both compounds are susceptible to chemical degradation in the presence of oxygen under conditions pertinent to DAC. It has been reported that bPEI and TEPA deactivate *via* the formation of nitrogenous compounds such as amides, imides and imines.^[37, 38]

Numerous polymeric alternatives have been investigated to improve the antioxidation properties of amine-impregnated oxides (Scheme 1.3). Poly(allylamine) (PAA), a polymer containing exclusively primary amines, was impregnated in porous gamma alumina and its adsorption behaviour was studied under simulated flue gas conditions (TGA, 10% CO₂ in He, 50°C, 6 h). Its adsorption capacity after exposure to a harsh oxygen-rich environment (TGA, 21% O₂ in N₂ at 110°C for 20 h) decreased by 11%. In contrast, for bPEI-impregnated alumina, the capacity decrease was 70%.^[39]

Linear poly(propylenimine)(LPPI)-impregnated SBA-15 has also been studied. PPI is structurally similar to linear PEI (LPEI), except there are propyl rather than ethyl spacers between the amine groups. LPPI-impregnated SBA-15 was found to be chemically more resilient after exposure to accelerated oxidative conditions (ultrazero grade air, 100°C, 24 h) compared to LPEI-impregnated SBA-15. Furthermore, LPPI-based adsorbents were found to adsorb CO₂ more efficiently under DAC-like conditions (TGA, 400 ppm CO₂/N₂, 35°C, 18 h).^[40]



Scheme 1.3. Skeletal diagrams of alternative polyamines used in the preparation of amine-impregnate inorganic oxides.

Other viable polyamines loaded into oxide supports have been proposed for ambient air removal of CO₂.^[41-43] Nevertheless, bPEI and TEPA remain the most studied amines for this class of adsorbent, most likely owing to their commercial availability. To this effect, other groups have attempted to improve the CO₂ capture properties of bPEI/TEPA-impregnated oxides under ultradilute conditions *via* chemical and physical modifications of the active phase. For instance, polyethylene oxide-modified TEPA impregnated silica was found to retain 86% of its original adsorption capacity (TGA, 90% CO₂/N₂, 25°C, 3 h) after harsh oxidative treatment (21% O₂/N₂, 100°C, 20 h). In contrast, its unmodified counterpart had a retained capacity of only 10% post-oxidative treatment. Under simulated DAC conditions (TGA, 400 ppm CO₂/N₂, 25°C, 3 h), the epoxide-modified TEPA silica was found to have a comparable adsorption capacity to other linear polyamine impregnated adsorbents.^[36] The co-impregnation of additives with polyamines onto oxide supports has also been investigated as a way of improving mass transfer of CO₂ into the active phase. When tested under DAC-like conditions (TGA 400 ppm CO₂/He, 30°C, 12 h), poly(ethylene glycol) was reported to enhance amine efficiency of bPEI-impregnated SBA-15 by up to 60%. This improvement was hypothesised to be due to the clustering of PEG with bPEI *via* hydrogen bonding in the silica pores, reducing bPEI-bPEI and bPEI-silica intermolecular bonding.^[44] These interactions are considered to create diffusional and chemical barriers for adsorption, respectively.^[33]

Recently, silicas impregnated with a mixture of amines have been proposed for overcoming the limitations of using a single amine in the active phase.^[45-47] For example, blending of diethanolamine and bPEI was reported to improve the adsorption capacity of amine-impregnated SBA-15 by 46%

compared to silica containing only bPEI of a similar amine loading (TGA, 400 ppm CO₂/N₂, 25°C, 2 h).^[47]

The support plays an (equally) important role in the CO₂ chemisorption behaviour of amine-impregnated inorganic oxides. For instance, use of templated alumina in place of mesoporous silica as a support for bPEI-functionalisation has been demonstrated to enhance adsorption capacity and amine efficiency under DAC conditions. Chaikittsilp *et al.* found that the adsorption capacity of bPEI-impregnated mesoporous alumina was 1.33 mmol/g compared to 1.05 mmol/g for bPEI-silica with a similar nitrogen loading (TGA, 400 ppm CO₂/Ar, 25°C, 12 h). This was attributed to the abundance of basic sites in the synthesised alumina, which are averse to interacting with the amine groups in the active phase. This results in a more strongly-basic active phase. On the other hand, silanols (Si-OH) on the surface of silicas are mildly acidic and as such they interact strongly with the aminopolymer through the formation of acid-base interactions, resulting in a much weaker affinity between bPEI and CO₂.^[48] Zirconosilicate-based sorbents have also been touted, achieving enhanced uptake capacities, desorption kinetics and regenerability under DAC conditions. As with alumina, it was postulated that differences in the acid-base properties of the support were responsible for their improved performance over conventional amine-impregnated silica.^[49] Incorporation of other heteroatoms into the silica support such as titanium and cerium has also been shown to have a promotive effect on the sorption performance of bPEI-impregnated silica.^[50]

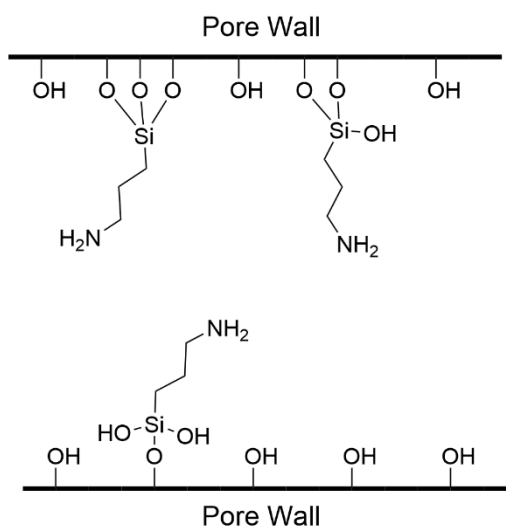
Using silicas with a surface layer of surfactant cations has also been shown to improve CO₂ removal of amine-impregnated inorganic oxide adsorbents. Sayari *et al.* prepared PEI-impregnated, pore-expanded MCM-41 silica with a retained coating of cetyltrimethylammonium cations (CTAB⁺) from the structure-directing surfactant. They found that the adsorbent had a higher amine efficiency across a range of bPEI loadings, with one material having three times the amine efficiency of an equivalent porous silica without the surfactant layer (TGA, 400 ppm CO₂/N₂, 25°C). They attributed this enhancement to improved dispersion of the polyamine, along with the physical barrier created by the surfactant that prevented interactions between bPEI and the silica support.^[51] Qi *et al.* also demonstrated the promotive effect of CTAB⁺ cations on CO₂ adsorption using TEPA as the active phase and a micro-mesoporous silica as the support. However, based on *in-situ* FTIR analysis of adsorbents with and without the cation layer, they postulated that it was a change in speciation that was responsible for the observed improvement in amine efficiency; namely the preferable formation of carbamic acid over carbamate in the adsorbent containing CTAB⁺ cations. Carbamic acid has a reaction stoichiometry of 1:1 amine:CO₂ as opposed to 2:1 in the case of carbamate.^[52]

Pore geometry also affects the adsorption behaviour in amine-impregnated inorganic oxides. A meso/macro-porous silica material impregnated with bPEI had very similar adsorption capacities under 400 ppm and 10% CO₂ feed streams at 30°C. This was contrary to the typical trend seen with bPEI-impregnated mesoporous silica wherein CO₂ uptake and kinetics are better during exposure to more concentrated gas feeds.^[53] The observation was attributed to differences in aminopolymer

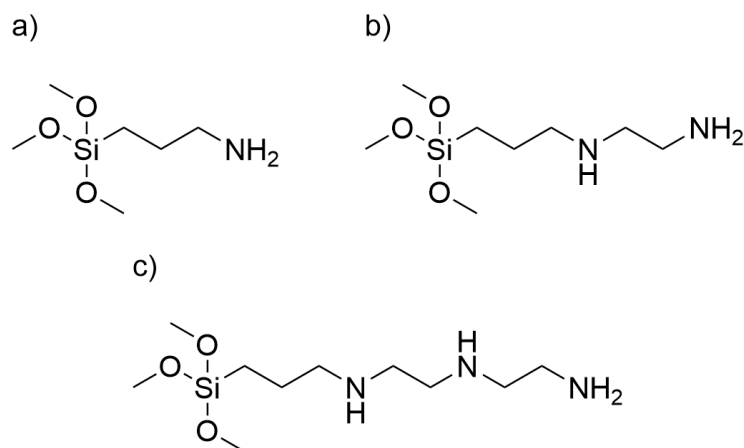
distribution on the pore walls of the support^[54] The impregnation of hierarchical meso/macro-porous silica with TEPA has been shown to result in one of the highest reported dry adsorption capacities of an amine-impregnated inorganic oxide (5.2 mmol/g, TGA, 400 ppm CO₂/He, 30°C, 12 h). The large pore volume of the support meant the silica could be loaded with higher amounts of amine compared to conventional mesoporous silicas. Furthermore, the adsorbent had relatively fast adsorption kinetics for a material with such a high amine loading due to the interconnected system of meso- and macropores which facilitated better mass transfer and diffusion of CO₂.^[55]

1.2.2 Amine-Grafted Inorganic Oxides

Amine-grafted inorganic oxides comprise amines covalently tethered to the pore walls of the support *via* a silane coupling agent (Scheme 1.4). There are several commonly used aminosilanes used in the functionalisation of porous inorganic oxides, each bearing a different number of amine functionalities (Scheme 1.5).



Scheme 1.4. Skeletal diagram of an amine-grafted adsorbent.



Scheme 1.5. Skeletal diagrams of monoamine (a), diamine (b) and triamine (c) reagents commonly used in the preparation of amine-grafted adsorbents.

Removal of CO₂ using amine-grafted silicas was first reported in 1995 by Leal *et al.* They found that pure CO₂ could be adsorbed reversibly on to the surface of silica gel grafted with 3-aminopropyl groups. Simultaneous desorption and reforming of the sorbent was achieved through the application of a temperature swing (adsorption at 27°C, regeneration at 100°C).^[56] Over ten years later, triamine grafted MCM-41 and pore-expanded MCM-41 silicas were studied for CO₂ removal from a dilute gas feed. At comparable amine loadings, the pore-expanded silica achieved a higher CO₂ capacity compared to standard MCM-41 (1.41 mmol/g *versus* 0.97 mmol/g, TGA, 5% CO₂/N₂, 25 °C). This was attributed to the larger pore volume and size of the pore-expanded silica.^[57] In a later study, it was found that grafting under hydrous conditions increased the degree of amine functionalisation, which translated into a higher CO₂ loading capacity for triamine functionalised PE-MCM-41 (2.65 mmol/g, TGA, 5% CO₂/N₂, 25°C).^[58] Later, it was found that this material performed well under DAC conditions, achieving an equilibrium adsorption capacity of *ca.* 0.98 mmol/g (volumetric method, 0.004 bar CO₂, 25°C). This was almost double that of zeolite 13X, a physisorbent commonly used for the purification of dry air. Furthermore, the material demonstrated a very high selectivity for CO₂ over nitrogen and oxygen, regardless of the presence/absence of water vapour in the gas stream.^[59, 60] Amine-grafted inorganic oxides have also been shown to be highly regenerable. Wurzbacher *et al.* demonstrated the utility of a diamine functionalised silica gel for DAC in a practical system using a fixed-bed column. Over forty cycles of adsorption-desorption using a temperature-vacuum swing for the regeneration step, the sorbent's working capacity was fairly constant at 0.17 – 0.19 mmol/g (adsorption conditions: dry air, 25°C, 3 h, desorption conditions: 74 - 90 °C, 50 - 150 mbar, 1.25 h).^[61]

The CO₂ uptake efficiency of amine-grafted oxides is strongly influenced by the structure of the tethered amines (primary, secondary, tertiary). Didas *et al.* studied how the amine type affects CO₂ sorption on functionalised mesocellular foam silica across a range of CO₂ pressures relevant to DAC and flue gas capture. At ultralow pressures pertinent to ambient air capture and at similar amine

loadings, the amine efficiency of MCF endowed with primary amines was double that of the secondary amine-modified sorbent (volumetric method, 0.4 mbar CO₂, 25°C). Meanwhile, as expected, the silica bearing tertiary amines adsorbed negligible amounts of CO₂, regardless of the adsorbate pressure, since this type of amine only reacts with CO₂ in the presence of water.^[62] Based on the recorded CO₂ volumetric isotherms, the isosteric heats of adsorption were calculated for the primary and secondary amine-modified materials. The primary amine adsorbent had a higher isosteric heat of adsorption, implying it was a stronger chemisorbent compared to the secondary amine-appended MCF.^[63] However, this finding was questioned by Alkhabbaz *et al.*, who found that samples of SBA-15 grafted with primary and secondary amines had similar heats of adsorption at comparable amine loadings. They measured adsorption enthalpies directly using calorimetry rather than indirectly using volumetric CO₂ isotherms similarly to Didas *et al.* Based on this finding, Alkhabbaz *et al.* postulated that entropic rather than enthalpic factors account for the higher amine efficiency of primary amines compared to the secondary type.^[64]

Amine efficiency is also affected by the structure of the covalently-tethered aminosilane. Yoo *et al.* prepared four functionalised SBA-15 adsorbents using grafting agents of differing structure (linear and branched). It was found that branched aminosilanes had higher pseudo-equilibrium capacities compared to their linear counterparts at similar active amine loadings (TGA, 400 ppm CO₂, 25°C, 10 h). This was attributed to the fact that the branched aminosilanes contained two primary amines compared to one primary and one secondary in the linear compounds. As already established, primary amines are more reactive towards CO₂ than the secondary type. It was also found that the spacer type affected the oxidative stability of the adsorbent; SBA-15 grafted with aminosilane bearing propyl spacers between amine groups retained more of their capacity after exposure to harsh oxidative conditions (21% O₂ in N₂, 110°C, 3 h) compared to their ethyl analogues. FTIR experiments revealed that the formation of amides and imines was responsible for amine deactivation.^[65]

Pore size, pore architecture and amine loading play a more important role in determining the adsorption behaviour of amine-grafted adsorbents than the specific surface area of the support. Anyanwu *et al.* prepared triamine-grafting materials using commercially-available silica gels of varying textural properties (surface area, pore size and pore volume). Despite having the lowest specific surface area, it was found that the siliceous material with the largest pore size (AG-150A) exhibited the highest adsorption capacity (volumetric method, 1.35 mmol/g, 1 bar CO₂, 25°C). In contrast, AG-22A silica gel, with a specific surface area five times higher than AG-150A, had the lowest capacity (0.66 mmol/g). Furthermore, they demonstrated that grafting AG-150A under wet conditions enhanced adsorption further to 1.97 mmol/g, as more amine could be tethered to the support compared to using the conventional dry grafting technique.^[66] In a later study, the group found that the optimal amine loading (controlled by varying the water added) was dependent on the type of silica. Maximal adsorption capacity was achieved at a much higher amine loading for bimodal mesoporous silica with two mesopore sizes (BMS) compared to SBA-15 silica (volumetric method,

1 bar CO₂, 25°C). Furthermore, they found that the optimally-loaded BMS exhibited a dynamic CO₂ capacity of 1.04 mmol/g (fixed-bed, 415 ppm CO₂, dry ambient air, 25°C) which at the time was one of the highest for an amine-grafted silica tested under DAC conditions. This was attributed to the bimodal network of pores which facilitated quicker CO₂ diffusion compared to what is observed with conventional mesoporous silica.^[67]

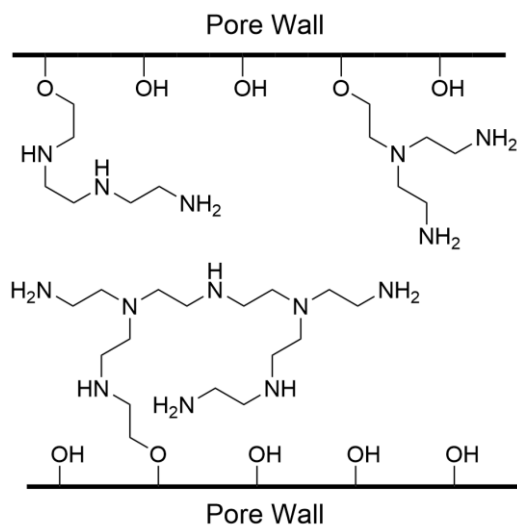
Kulkarni *et al.* studied CO₂ uptake under DAC conditions on mono and triamine-grafted hierarchical silica. They found that the pseudo-equilibrium capacity increased with amine loading up to 70 wt%. The highest CO₂ uptake was achieved using the triamine-grafted silica (1.5 mmol/g, TGA, 400 ppm CO₂/He, 30°C, 12 h). They also tested the material under humid conditions (50% RH) after a pre-hydration step and found the material's CO₂ uptake increased to 2.1 mmol/g. To date, these are the highest capacities reported for amine-grafted inorganic oxide adsorbents. They attributed the high capacities to the hierarchical nature of the silica support which facilitated enhanced amine dispersion during functionalisation compared to conventional supports like SBA-15, which are liable to pore blockage at high amine loadings which impedes CO₂ mass transfer.^[68]

Another strategy of achieving higher amine loadings is to modify the density of tethering sites on the support for the aminosilane grafting agent. Typically, during the synthesis of porous silica, the organic template is removed *via* calcination which causes a decrease in the density of tethering sites (silanol groups) on the pore walls. To this effect, Wang *et al.* proposed the use of an ionic liquid treatment to remove the organic template in SBA-15, thereby preserving the silanol groups on the support. As expected, a higher amine loading was achieved on this material compared to calcined SBA-15. More than a two-fold increase of the adsorption capacity was reported for the ionic-liquid treated silica compared to amine-modified conventional SBA-15 (0.15 and 0.38 mmol/g respectively, fixed-bed, 415 ppm CO₂, dry ambient air, 25°C).^[69] In a later study, the group prepared a boron-doped SBA-15 which they then subjected to acid treatment to remove the heteroatom. Again, as with the ionic liquid treatment method, they were able to graft significantly more aminosilane onto this substrate compared to conventional SBA-15 under the same functionalisation conditions. This was due to the formation of silanol clusters during the boron removal step, which endowed the material with a greater silanol density. This translated into an adsorption capacity of 0.46 mmol/g (pelletised form, fixed-bed, dry ambient air, 25 °C), higher than both conventional SBA-15 and the ionic liquid treated SBA-15 from their previous study.^[70]

The surface chemistry of the support also plays an important role in the CO₂ sorption behaviour of amine-grafted inorganic oxides under DAC conditions. For instance, it has been shown that, at low amine loadings, the support of amine-grafted alumina can participate in the CO₂ uptake process. This is due to the presence of basic sites on the surface of alumina. However, at high loadings, the support did not play a role in the adsorption process as clustering of the amine minimised CO₂-support interactions.^[71]

1.2.3 Polyamine-Tethered Inorganic Oxides

Polyamine-tethered adsorbents were first proposed by Hicks *et al* for post-combustion CO₂ capture. They prepared a hyperbranched aminosilica (HAS) *via in situ* open-ring polymerisation of aziridine off the surface of SBA-15.^[72] The amino dendrimer is structurally similar to branched poly(ethylenimine) commonly used in the preparation of amine-impregnated adsorbents, with tertiary amines at the junctions between branches, and secondary and primary amines along the length and at the ends of the branches, respectively (Scheme 1.6). However, unlike amine-impregnated adsorbents, the aminopolymer is anchored to the support. The same HAS material prepared by Hicks *et al* was also studied for DAC. Adsorbents with various amine loadings were prepared by adding different amounts of aziridine monomer to the chemical solution in which the silicas were functionalised. The adsorption capacity increased with amine loading, achieving 1.5 mmol/g at the highest loading (fixed-bed, 400 ppm CO₂, humid, ambient temperature). However, adsorption kinetics was compromised, reflected by the increase in adsorption half-time (time taken to attain half of the final adsorption capacity) with amine content.^[73] Using a similar methodology, poly(L-lysine) and linear poly(ethylenimine) have also been synthesised from the surface of porous silicas, with maximum respective CO₂ uptakes of 0.6 mmol/g (TGA, 400 ppm CO₂/Ar, 25°C, 12 h) and 1.5 mmol/g (fixed-bed, 400 ppm CO₂/N₂, 25°C, 65% RH, 2 h).^[74, 75] Polyamine-tethered adsorbents exhibit excellent regenerability, with a negligible change in uptake capacity after multiple temperature-swing cycles.^[53, 73]



Scheme 1.6. Skeletal diagram of a polyamine-tethered inorganic oxide adsorbent.

1.2.4 Metal Organic Frameworks

Metal organic frameworks (MOFs) are microporous, crystalline materials comprising a network of metal centres linked by organic ligands. MOFs with unsaturated metal centres are capable of capturing CO₂ *via* physisorption,^[76] however, they commonly have poor adsorption capacities in DAC conditions owing to their low heat of adsorption. Such materials also perform poorly in humid environments due to competition for active sites between CO₂ and water.^[77] Water sorption causes considerable destruction to the crystallinity and textural properties of such MOFs, resulting in poor regenerability.^[78] Thus their applicability for DAC is particularly challenging, given that ambient air almost always contains a certain amount of water vapour.

MOFs incorporating fluorine anions have been shown to exhibit much higher CO₂ binding energies from ultradilute feeds compared to standard open metal site (OMS) MOFs, owing to their narrower pore size and the high electronegativity of the fluoride constituent. One reported fluorine-incorporated MOF had a CO₂ adsorption capacity of 1.3 mmol/g (volumetric method, 0.4 mbar CO₂, 25°C), over an order of magnitude higher than OMS-MOFs at the same CO₂ pressure.^[79, 80] The CO₂ uptake capacity of the fluoride-incorporated MOF increased further to 1.44 mmol/g (volumetric method, 0.4 mbar CO₂, 25°C) after incorporation into an amine-grafted poly(acrylamide) support. Crucially, the hydrophobic nature of the support improved the CO₂/H₂O selectivity, resulting in a reasonable working adsorption capacity in humid DAC conditions during multiple cycling experiments (0.84 mmol/g, 2000 cycles, fluidised bed, adsorption conditions: air, 50% RH, 25°C, 6 min, desorption conditions: pure water vapour flow, 125°C, 15 min). The grafted amine did not participate in the adsorption process but rather anchored the MOF to the support.^[81]

Amine functionalisation is another method of enhancing CO₂ uptake on MOFs, whilst also improving their hydrolytic stability. As with amine-supported inorganic oxides, both amine impregnation and amine grafting has been studied. Amine impregnation of MOFs involves physically loading an amine bearing reagent like branched PEI^[82, 83] or TEPA^[84, 85] into the pores of the support. Darunte *et al.* studied the physical impregnation of the MIL-101(Cr) with tris(2-amino ethyl) (TREN) and bPEI for the application of DAC. The TREN-loaded MOF exhibited high capacities at high amine loadings however suffered from poor regenerability during multiple cycling tests due to leaching of the active phase. The bPEI-loaded MOF was more stable, with an adsorption capacity of 1.35 mmol/g at the highest amine loading of 1.76 mmol_{PEI}/g (TGA, 400 ppm CO₂/He, 25°C, 6 h). However, this material had the poorest uptake kinetics, taking 341 min to reach pseudo-equilibrium. In contrast, the material with a lower loading of 0.97 mmol_{PEI}/g attained a final capacity of 1.15 mmol/g after 237 min of CO₂ exposure.^[82]

Synthesising amine-grafted MOFs involves the appending of small molecular weight amines to coordinatively unsaturated metal sites. Studied amines include ethylene diamine^[78, 86-89] dimethylethylenediamine.^[26, 90, 91] and hydrazine^[92] Liao *et al.* prepared a hydrazine-appended MOF,

with an adsorption capacity of 3.7 mmol/g (TGA, dry air, 25°C, 15.8 h), which is one of the highest values reported for a MOF-based DAC adsorbent.^[92]

1.2.5 Zeolites

Zeolites are a family of porous aluminosilicate materials typically containing micropores between 0.3 and 0.8 nm in size. The presence of aluminium in the lattice results in the framework being negatively charged, and this is counterbalanced by the presence of extra-framework cations like H⁺ and Na⁺. In general, CO₂ capture in zeolites is mediated predominantly by electrostatic interactions between the adsorbate and the cations, with diffusion and size exclusion playing a supplementary role in CO₂ separation in small-pore zeolites (0.3-0.45 nm). The Si/Al ratio plays an important role in dictating the adsorption capacity of zeolites, the lower the ratio the higher the amount of extra-framework cations and hence the greater the adsorption potential of the zeolite. At the same time, the adsorbent hydrophilicity increases, resulting in zeolites with low Si/Al ratios performing poorly in humid conditions.^[93] For example, in one study, the molecular sieve 13X was reported to adsorb 8.1 mmol/g of water compared to 0.03 mmol/g of CO₂ after exposure to humid air (fixed bed, laboratory air, 49% RH, 12 h).^[77] As discussed in the previous sub-section, air is rarely moisture-free, thus a pre-drying step would be necessary for the application of zeolites for DAC, which adds to the energy and financial cost of the capture system.^[94-96] Improving capacity and CO₂/H₂O selectivity can be achieved by modifying the zeolite with different extra-framework cations.^[97-100] Incorporation of cations with high charge densities results in greater CO₂ loading, although an excessively high charge-to-size ratio impedes CO₂ uptake due to strong interactions between pre-adsorbed species and the active sites. Ca²⁺ ions were found to have the optimal charge-to-size ratio when incorporated into LTA zeolite, achieving a DAC adsorption capacity of 1.2 mmol/g (fixed-bed, dry air, 350 ppm CO₂, room temperature).^[101]

Zeolites show promising application for DAC in cold climates where water vapour content in air is generally low.^[96, 102] For example, Song *et al.* found that the zeolite 5A exhibited over a 10-fold enhancement in its equilibrium capacity when the adsorption temperature was reduced from 25°C to -20°C (0.16 to 1.92 mmol/g respectively, fixed-bed, 395 ppm CO₂, 720 ppm humidity, 2 h). Notwithstanding, the material adsorbed a significant amount of water during testing and as such the estimated energy consumption for thermal regeneration of the zeolite was prohibitive. Yet adding a pre-drying step rendered the capture process energetically feasible at -20°C, with the estimated energy requirement comparable to other DAC technologies.^[96]

Enhancement in adsorption capacity of zeolites is also achievable *via* amine functionalisation. Functionalised zeolites with a large volume of mesopores were found to have superior adsorption capacities compared to purely microporous zeolites due to pore filling and blockage in the latter which impedes CO₂ diffusion through the pore network.^[103] Recently, a bPEI-impregnated

hierarchical zeolite comprising mesoporous zeolitic nanotubes with pore channels interconnected *via* micropores was studied under simulated DAC conditions. It was found to have an adsorption capacity up to 25% higher than a benchmark amine-functionalised mesoporous silica, and uptake kinetics that were four times quicker (TGA, 400 ppm CO₂/He, 30°C, 3 h).^[104]

1.2.6 Amine-Supported Organic Sorbents

Amine-functionalised porous organic substrates have also been explored for CO₂ removal from ambient air. For example, an amine-modified nanofibrillated cellulose matrix (AS-NFC) was prepared by adding an aminosilane to a cellulosic hydrogel, followed by centrifugation and freeze-drying to remove the water. The dynamic adsorption capacity of the material was 1.39 mmol/g (fixed-bed, ambient air, 40% RH, 25°C, 12 h).^[105] A further study demonstrated this material was highly regenerable, retaining 95% of its initial working capacity after 100 temperature-vacuum swing cycles in a dynamic set-up (fixed-bed, 0.9 mmol/g, adsorption conditions: air, 60% RH, 30°C, 150 min, desorption conditions: 90°C, 30 mbar, 45 min).^[106] Impregnating nanofibrillated cellulose with bPEI (bPEI-NFC) yielded an adsorbent with a higher CO₂ uptake of 2.22 mmol/g (fixed-bed, air, 80% RH, 25°C), higher than AS-NFC. The bPEI-NFC material also exhibited faster uptake kinetics compared to AS-NFC, with an adsorption half-time of 10.6 min *versus* 92 min for the latter adsorbent.^[105, 107] Other amine-modified porous substrates have also been studied for removal of CO₂ from ambient air such as epoxy resins^[108-110], mesoporous carbon^[111], porous polymer networks^[112] and polymeric hollow fibres.^[113, 114]

1.2.7 Alkali and Alkaline-earth Metal Compounds

There are three main categories of alkali and alkaline-earth adsorbents: metal carbonates, oxides and hydroxides.

Carbonate-bicarbonate looping involves the reaction of a metal carbonate with CO₂ and water vapour, forming a bicarbonate. Heating the spent material to 150 – 300°C results in desorption of the captured CO₂ and the simultaneous reforming of the original adsorbent. Potassium carbonate has been extensively studied for CO₂ removal from ambient air using a variety of porous supports such as alumina^[115, 116], yttrium oxide^[117], zirconia^[117] and carbon.^[118-120] Chemical interactions between the carbonate and the support can increase the necessary regeneration temperature. For instance, one of the products of CO₂ adsorption on K₂CO₃-impregnated alumina is KAlCO₃(OH)₂ which forms as a result of chemical interactions between K₂CO₃ and alumina in the presence of CO₂ and water. This compound is stable to a much higher temperature compared to KHCO₃, another adsorption product (300°C and 200°C, respectively).^[115, 116] On the other hand, K₂CO₃-loaded zirconia can be fully regenerated at 200°C, since only KHCO₃ forms on this adsorbent during CO₂ exposure.^[121] Recently,

an adsorbent comprising potassium carbonate incorporated in carbon nanotubes has been demonstrated to attain an adsorption capacity of *ca.* 2 mmol/g from humidified air during multiple cycling (adsorption: humid air, 380 – 420 ppm CO₂, 30°C, 6 h, desorption: Ar flow, 150°C, 1 h). This is the highest reported adsorption capacity for potassium carbonate sorbents tested under DAC conditions. Notably, the material could be regenerated at 150°C, 50°C lower than the typical desorption temperature for K₂CO₃-based adsorbents.^[120] Nevertheless, the regeneration temperature of this adsorbent is still higher than that of amine-based adsorbents (60 – 100°C).^[27] Sodium carbonate has also been studied for DAC, although its reported capacity and energy requirement is inferior to K₂CO₃-based technologies.^[122]

Metal oxides in the form of particles,^[123] pellets^[124] and loaded on to a porous support have also been studied for direct air capture.^[125] Goldman *et al.* studied CO₂ uptake from air on various metal oxides impregnated on gamma alumina (Na₂O, K₂O, Cs₂O, MgO, CaO and BaO). The sodium oxide adsorbent had the highest CO₂ uptake of 0.13 mmol/g (TGA dry air, 400 ppm CO₂, 20°C). During dynamic testing of Na₂O/Alumina suspended on a ceramic honeycomb monolith, it was found that humidity greatly enhanced the working capacity, from 0.15 mmol/g under dry conditions to 0.4 mmol/g at 90% RH (fixed-bed, adsorption: 400 ppm CO₂, 20°C, desorption: N₂, 200°C).^[125] As with carbonate-bicarbonate looping systems, the need for a high temperature during the regeneration step (relative to amine adsorbents) could make the application of metal oxides for DAC challenging.

Porous masses of slaked lime (Ca(OH)₂) shaped into various forms (pellets, bricks) have also been investigated for the application of DAC. One study reported that the molar conversion of Ca(OH)₂ into CaCO₃ was strongly dependent on the humidity of the feed gas. During TGA testing of a 6 mm pellet, the conversion when exposed to dry air (RH < 5%) plateaued out at *ca.* 0.1 after *ca.* 140 h of exposure. When the gas feed was then switched to humid air (95% RH), molar conversion rose to *ca.* 0.35 after a further *ca.* 30 h of adsorption (air, 450 ppm CO₂, 20°C). The form of the adsorbent strongly influenced the evolution of the depth of the carbonated layer on Ca(OH)₂ during CO₂ capture; forms with high porosities and specific surface areas exhibited faster carbonation rates and a thicker carbonated layer by the end of the DAC experiments. Using a higher grade of Ca(OH)₂ also increased the maximum molar conversion in the carbonated layer from 0.6 to 0.8 (passive testing, laboratory air, 500 ppm CO₂, 52% RH, 19°C, 500 h).^[126] Using oxy-calcination to recycle spent bricks of CaCO₃ from DAC back into lime yields a system that is potentially cost-competitive.^[127] An eco-friendly adsorbent comprising KOH supported on activated carbon derived from bamboo was studied for CO₂ capture, although it had a poor adsorption capacity when exposed to ambient air (0.05 mmol/g, fixed-bed, ambient air, room temperature).^[128]

1.2.8 Ion Exchange Resins

Unlike the other adsorbent categories discussed, which require a thermal swing for sorbent regeneration, ion exchange resins (IERS) use a moisture swing to switch between adsorption (dry) and desorption (humid) modalities, making IERS a less energy-intensive technology for DAC with respect to reactivation of the adsorbent.^[129, 130] The most widely studied category of IER comprises positively-charged quaternary ammonium groups and carbonate counterions. Gas diffusion properties such as porosity significantly contribute to the adsorption rate and the percentage utility of the resin and, as such, the IER particles are commonly incorporated into a porous support made of carbon or a polymer to enhance sorption kinetics^[131-134] At site occupancies greater than 0.5, diffusion through the product layer on the resin is the dominating impediment to CO₂ mass transfer.^[132] The chemical properties of the IER, namely the functional groups, play an important role in determining the adsorption capacity.^[135, 136] Recently, alternative anions have been explored to the traditional carbonate/bicarbonate system.^[137, 138] For example, Song *et al.* studied a commercially-available IER and found that using phosphate anions in lieu of carbonate ions in the preparation of the material resulted in an 80% enhancement in CO₂ uptake at equilibrium from 0.3 to 0.55 mmol/g (closed-circuit, 400 ppm CO₂/N₂, 3% RH). The material retained its adsorption capacity after six moisture swing cycles (desorption at 95% RH).^[137]

One of the main challenges to implementing moisture-swing sorbents for DAC is the material's hydrophilicity. Surface-bound water on the resin is responsible for the activation of the sorbent for CO₂ chemisorption, however, oversaturation of the material results in kinetic and chemical limits to the CO₂ uptake process. To this end, several groups have studied optimising the hydrophilicity of IER-based sorbents.^[134, 139] By synthesising porous supports with a certain amount of hydrophobic fluorinated components, the variation in CO₂ capacity with relative humidity can be controlled in such a way that materials are usable over a greater range of humidities. For example, Dong *et al.* doped an IER supported on a cellulose acetate binder with poly(vinylidene difluoride). The non-doped adsorbent's DAC capacity decreased with relative humidity from *ca.* 0.85 to 0.57 mmol/g between 21 and 85% RH (fixed-bed closed circuit, 400 ppm CO₂/N₂, 20°C). In contrast, the material containing 25 wt% PVDF had a constant capacity across this humidity range of 0.9 mmol/g. The material was found to retain over 90% of its initial CO₂ capacity during 10 adsorption-desorption cycles at both low and high humidities (desorption involved immersion of the adsorbent in deionised water).^[139]

1.3 Discussion and Conclusions

Direct air capture of CO₂ offers an invaluable strategy to accelerating the decarbonisation of the world's economies, along with achieving the necessary net negative emissions in the latter half of the century needed to limit warming to 1.5°C by 2100. Due to the high share of the total capture cost, developing and optimising novel adsorbents is vital for the widespread deployment of DAC for climate change mitigation. As discussed in Section 1.1.3, the main material performance metrics which affect the capture cost are the adsorption capacity, sorption kinetics and regenerability.

The literature review covered the main categories of adsorbents studied for DAC. To date, amine-functionalised inorganic oxides are the most extensively studied category of adsorbents. Oxide supports physically loaded with amines like bPEI and TEPA have achieved the highest adsorption capacities over their amine-grafted counterparts, although leaching of the active phase compromises the regenerability of amine-impregnated oxides when using small molecular weight amines like TEPA. Furthermore, conventional bPEI and TEPA-based adsorbents are susceptible to oxidative degradation. Alternative amines have been explored which are more resilient to degradation, yet such reagents are not commercially available, and their in-house synthesis is complex. Physical and chemical modification of the active phase and blending of different amines has also been studied for improving the chemical stability of physically impregnated amine adsorbents. The surface chemistry of the support plays an equally significant role in the CO₂ capture process on amine-functionalised inorganic oxides. Supports with basic surface sites like alumina can achieve higher adsorption capacities compared to silica owing to weaker support-amine interactions, which increase the number of accessible adsorption sites for CO₂ capture. Concerning amine-grafted inorganic oxides, maximising the surface density of hydroxyl groups provides more anchorage sites for the grafting agent, which translates into higher amine loadings and CO₂ uptake. The structure of the grafted amine impacts the adsorption efficiency in the order of primary > secondary > tertiary.

The application of conventional MOFs and zeolites as physisorbents for direct air capture is challenging owing to their hydrophilicity and poor adsorption capacities during ambient air exposure. Incorporation of fluorine and high charge density cations into the frameworks of MOFs and zeolites respectively improves their adsorption performance, as does amine-functionalisation. Potassium carbonate-based adsorbents are a promising category of material for DAC, although, as with other alkali and alkaline earth metal adsorbents, they require a higher regeneration temperature compared to amine-based materials. IER-based adsorbents overcome the need for a temperature-swing altogether by employing changes in humidity to switch between adsorption and desorption. However, upscaling of such adsorbents could be challenging in dry climates with scarce water resources. Furthermore, a pre-drying step might be necessary for their application in humid environments.

Amine-functionalised adsorbents appear to hold the most promise for direct air capture of CO₂ due to their high heat of adsorption compared to physisorbents, their ability to adsorb reasonable amounts

of CO₂ regardless of the relative humidity and comparatively low regeneration temperature. Regardless of the choice of support and amine, pore architecture is of immense importance to the performance of amine adsorbents. Pore size, volume and connectivity of the substrate dictate amine dispersion on the pore walls and influence the uptake kinetics, the latter of which is equally as important as adsorption capacity when evaluating the CO₂ capture performance of porous materials. Whilst mesoporous silicas are the most widely used supports, bimodal silicas with either two sizes of mesopores or meso-macroporosity offer quicker CO₂ mass transfer to the adsorption sites. Microporous materials, like zeolites and MOFs, despite their large specific surface areas, are liable to pore blockage after amine functionalisation and as such have slow uptake kinetics compared to other porous supports. In general, there is a trade-off between adsorption capacity and kinetics, with the optimal amine loading dependent on the textural properties of the support. Both performance metrics must be balanced to achieve maximum adsorbent productivity.

Making like-for-like comparisons between the performance of adsorbents is challenging since there is not a standard protocol for DAC testing, with research groups using different set-ups (volumetric method, TGA, fixed-bed, fluidised bed), gas feeds of varying CO₂ concentration (binary mixtures, bottled dry air, laboratory air) and adsorption conditions (temperature, humidity, gas feed flow rate).

A significant issue with the existing body of literature on amine adsorbents is that there are few studies that test amine adsorbents under DAC-like conditions in scalable forms. Several studies have looked at monoliths^[140], pellets^[55, 70, 141] and macroscopic fibres.^[142] Nevertheless, most DAC amine adsorbents presented to date are powders and would be impractical for industrial-scale DAC due to the high system pressure drops and mass transfer limitations associated with fixed-bed reactors containing powders.

1.4 Aims and Objectives

Considering the pressing need for the development of capture systems for DAC and their deployment at scale, the number of studies investigating adsorbents in scalable forms is inadequate in meeting the challenge. To this effect, the aim of this thesis was to develop amine-functionalised scalable adsorbents for DAC using electrospinning. Optimisation of the synthesis procedure was carried out, along with the testing of these novel materials under CO₂ capture conditions relevant to direct air capture.

The objectives of the thesis were as follows:

1. Investigate the impact of electrospinning parameters on the morphological characteristics of nanofibres suitable for amine functionalisation.
2. Select synthesis conditions for producing a nanofibrous scaffold with optimal properties.
3. Examine the physiochemical properties of the optimised nanofibrous supports.
4. Functionalise the optimised support with amine functional groups.
5. Compare the physiochemical characteristics of electrospun scaffolds functionalised under different grafting conditions.
6. Design and build a lab-scale fixed-bed flow-through system for dynamic CO₂ capture testing of materials under more realistic processing conditions.
7. Investigate the effect of adsorbent properties (amine loading and amine type) and testing conditions (flow rate, temperature and humidity) on the CO₂ adsorption behaviour of amine-functionalised nanofibres.

2 Experimental Part

2.1 Material Synthesis

2.1.1 Electrospinning

Electrospinning is a fabrication technique that produces micro-/nanoscale polymer fibres with highly tuneable morphologies. Rather than relying on a mechanical tensile force, as seen in the case of more established fibre manufacturing methods (dry spinning, wet spinning, melt spinning), electrospinning harnesses electrostatic interactions as the driving force for fibre formation. Polymers can be electrospun in solution or as melts. However, sub-micron fibres are only achievable *via* the former technique.

2.1.1.1 Description of the Electrospinning Process

The basic setup for electrospinning is shown in Figure 2.1. A syringe filled with polymer solution is attached to a blunt-ended syringe needle (the spinneret). Next, a conductive collector, such as a static plate or a rotating drum, is positioned a fixed distance from the needle tip, normal to the spinneret axis. The spinneret is connected to a high-voltage supply, and the collector is grounded or connected to the same power source. When a high voltage is applied to the system, an electrical field forms between the spinneret and collector. A syringe pump is then used to deliver the solution to the spinneret at a fixed flow rate.^[143-145]

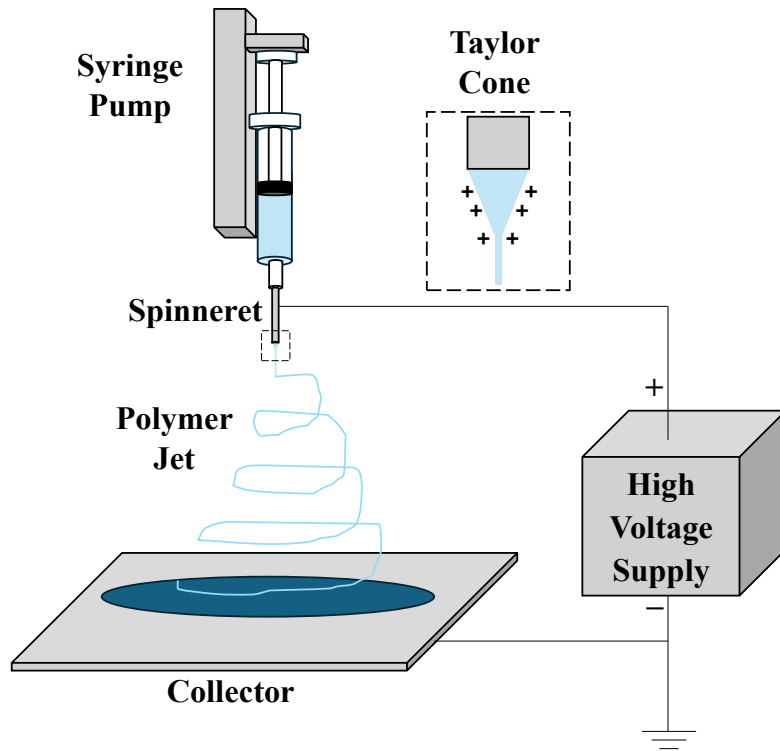


Figure 2.1. Diagram of the electrospinning apparatus. Figure created by the author.

With the syringe pump activated, a droplet of solution emerges from the spinneret and assumes a pendant shape owing to its surface tension. Over time, droplets fall onto the collector under the influence of gravity. Switching on the high-voltage power supply produces an electric field gradient between the spinneret and collector while simultaneously charging the pendant drop at the needle tip. Increasing the voltage leads to an augmentation in charge density at the droplet surface. The charged liquid will continue to drip until a critical voltage is reached.

At the critical voltage, Coulomb repulsion in the pendant drop suspended on the needle tip causes it to assume a conical shape, termed the Taylor cone.^[146] Interactions between charges and the system's electrical potential overcome the surface tension of the drop, resulting in the ejection of solution from the cone's apex. Depending on the solution properties, the liquid is emitted as either charged droplets or a continuous, accelerating jet. The former phenomenon is termed electrospray atomisation, while the latter is electrospinning.^[144, 147]

The critical voltage for Taylor cone formation can be estimated using Equation (2.1).^[148]

$$V_k^2 = \frac{4H^2}{L^2} \cdot \left(\ln\left(\frac{2L}{R}\right) - 1.5 \right) \cdot ((2\cos(\alpha)\pi R\gamma) \cdot 0.09) \quad (2.1)$$

Where: V_k is the critical voltage (kV), H is the spinneret-to-collector distance (cm), L is the spinneret length (cm), R is the internal radius of the capillary at the spinneret tip (cm), α is the semi-vertical angle of the Taylor cone (49.3°) and γ is the solution surface tension (dyn/cm). The factor of 0.09 is necessary to convert the computed value into kilovolts.

In the case of electrospinning, the expelled jet initially follows a straight trajectory parallel to the spinneret axis, accelerating towards the grounded collector due to a combination of gravity, Coulomb repulsion amongst like charges in the jet, and tensile stress due to the external electric field. Meanwhile, the jet diameter decreases, which increases the liquid charge density. This results in more electrical repulsion and an increase in jet acceleration.

Jet breakup is prevented by the viscoelasticity of the liquid, which suppresses the Rayleigh instability responsible for drop formation. At the same time, the charged solution's viscoelasticity and surface tension oppose the jet's acceleration. After a few centimetres of travel, the jet becomes susceptible to bending/whipping instabilities (Figure 2.2). The first bending instability is initiated by a kink in the jet, which arises from aerodynamic and radial Coulomb repulsive forces perturbing the fluid flow. Once formed, the kink extends axisymmetrically, causing the jet to assume a spiralling trajectory, with each successive loop having a greater diameter due to jet elongation as result of Coulomb repulsion. The jet diameter continues to decrease, and the loop eventually assumes a spiralling pattern (the second-order bending stability). Evaporation of the solvent leads to a further thinning of the jet, and it eventually solidifies, by which time several higher-order bending instabilities may have occurred. The jet stops stretching and falls onto the collector, forming a non-woven mat of nanofibres.

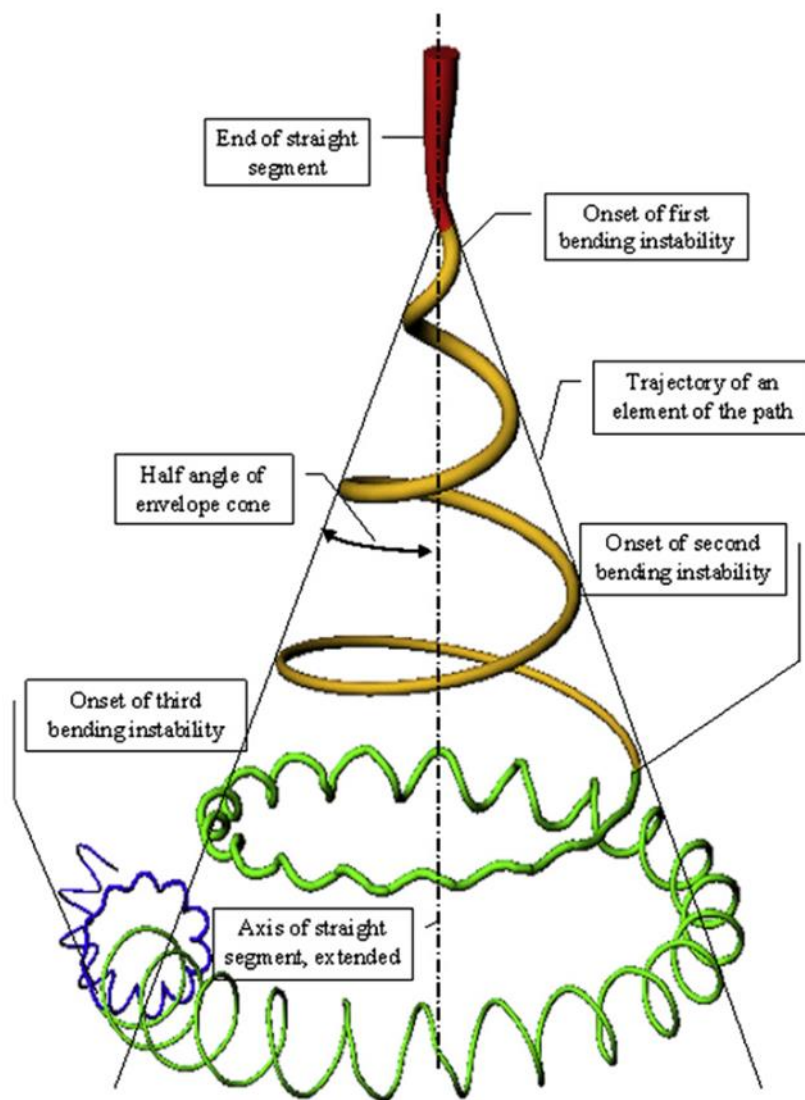


Figure 2.2. Diagram of a polymer jet's trajectory during the electrospinning process. Reproduced with permission from: [149]. Copyright 2006 American Chemical Society.

The so-called instability region, where the jet's trajectory becomes coiled, is pivotal in the formation of sub-micron diameter nanofibres. In this region, the jet's path length increases to the order of kilometres, resulting in a reduction in the jet diameter by several orders of magnitude.^[143, 150]

2.1.2 Factors Affecting the Electrospinning Process

Multiple variables affect the electrospinning process, which can be optimised to achieve the desired morphology. These conditions can be grouped into solution properties, processing parameters and environmental conditions.

2.1.2.1 Solution Properties

Solution properties include viscosity, molecular weight, molecular entanglement, polymer concentration, surface tension, conductivity, choice of solvent, dielectric constant, and volatility.

The solution's viscosity is critical in determining a formulation's ability to be electrospun. If it is too low, then a charged solution will be electrosprayed rather than electrospun because the Rayleigh instability, which is responsible for drop formation, dominates over the solution's viscoelasticity, which facilitates jet formation. At a fixed polymer concentration, higher molecular weight polymers result in greater molecular entanglement, which augments the solution's viscosity. Owing to this interrelationship, increasing the polymer concentration acts to increase viscosity and molecular entanglement. Moderate viscosities yield beaded fibres. Increasing the viscosity by augmenting the polymer concentration causes the formed beads to stretch longitudinally into spheroid structures and eventually, bead-free fibres are produced. As described in the previous section, viscoelastic forces oppose the electrical force responsible for jet elongation and hence, solutions with a high viscosity yield thicker electrospun fibres. Formulations excessively high in viscosity are susceptible to clogging the capillary inside the spinneret and therefore cannot be electrospun.^[144, 147, 151, 152]

In accordance with Equation (2.1) in the previous sub-section, the higher the surface tension, the greater the critical voltage necessary for electrospinning. Furthermore, the surface tension influences the terminal diameter of the electrospinning jet, as demonstrated by Equation (2.2).^[153]

$$d_t = \left(\gamma \epsilon \cdot \frac{Q^2}{I^2} \cdot \frac{2}{\pi(2 \ln \chi - 3)} \right)^{\frac{1}{3}} \quad (2.2)$$

Where: d_t is the terminal diameter of the electrospinning jet, γ is the solution surface tension, ϵ is the dielectric constant of the air surrounding the jet, Q is the jet's flow rate, I is the electric current flowing through the jet and χ is the dimensionless wavelength of the bending instability.

For solutions with very high surface tensions, the Rayleigh instability dominates over the jet thinning forces, causing jet breakup and the deposition of beaded fibres and particles on the collector.^[144]

There is an optimal range for electrical conductivity within which stable electrospinning is feasible. If it is zero, then the solution cannot be electrospun since electrical charge cannot accumulate on the surface of the pendant drop attached to the spinneret, impeding Taylor cone formation. Solutions with very high electrical conductivities are also challenging to electrospin since they tend to discharge into the surrounding air, causing a significant reduction in Coulomb repulsion and thereby inhibiting stable jet formation.^[144, 154]

Sub-micron diameter fibres have been reported when the dielectric constant of the electrospinning solution exceeds 20. As the dielectric constant increases above this threshold, the mean fibre diameter, along with the prevalence of beading, decreases. Below the threshold, thicker fibres in the micron to millimetre range and electrospaying of the solution have been observed.^[155, 156]

Solvent volatility is also an important parameter, as it determines the rate of solvent removal from the jet. If it is too low, the jet has insufficient time to dry during its journey between the spinneret and collector, leading to the deposition of wet fibres which can fuse together on the collector. For solutions with a high vapour pressure, there is little time for the polymer jet to thin before it solidifies, resulting in thicker fibres.^[145, 147] Additionally, using a binary system consisting of solvents of differing volatility can facilitate the production of porous fibres via phase separation.^[157]

2.1.2.2 Operational Parameters

As discussed in Section 2.1.1.1, there is a critical applied voltage above which electrospinning will commence; increasing the voltage beyond this threshold results in two competing effects on the jet diameter. Firstly, since the voltage is correlated with the solution's charge density, increasing the voltage will result in more electrostatic repulsion and the instability region in which the jet spirals will draw closer to the spinneret. The larger instability region enables the emitted jet to thin more, resulting in theoretically smaller fibres. Secondly, more solution is drawn out of the Taylor cone per unit time to compensate for the increased velocity of the jet. The increase in mass transfer acts to augment the jet diameter.^[144, 147]

These competing effects (larger instability region and increased mass flow rate) have resulted in different reported trends between voltage and fibre diameter.^[152, 158, 159] At very high applied voltages, the enlarged instability region also diminishes the size of the Taylor cone, causing beading on the collected fibres.^[144, 154]

Spinneret-to-collector distance is also an important consideration when optimising the electrospinning process. Together with the applied voltage, it determines the average field strength the charged jet is subjected to (commonly expressed as kV/cm). The gap is commonly in the range of 10 to 20 cm. At low distances, although the field strength is higher, the jet's path length is reduced, leading to the fusing of fibres on the substrate due to incomplete evaporation of the solvent. Extending the distance increases the jet's path length, facilitating the formation of thinner fibres and complete evaporation of the solvent. When the spinneret-to-collector distance is too high, the field strength is inadequate for maintaining stable jetting from the Taylor cone. This may lead to the formation of thicker and beaded fibres.^[144, 147]

As with the other parameters discussed, there is an optimal range of flow rates within which stable, defect-free nanofibres are fabricated. Below this range, the rate of fluid ejection from the Taylor cone

exceeds the rate of fluid replacement by the syringe pump, resulting in intermittent jetting from the spinneret and a fibre mat with a wide diameter distribution.^[160] Increasing the flow rate increases the thickness of the deposited nanofibres. Above the optimal range, there is insufficient flight time for the solvent to completely evaporate from the jet, leading to beaded and wrinkled fibre morphologies.^[144]

2.1.2.3 Environmental Conditions

Temperature and humidity are the dominant environmental factors that affect the electrospinning process. Increasing the temperature changes the solution properties. The viscosity and surface tension are reduced whilst conductivity is enhanced, favouring the production of thinner fibres. However, the rate of solvent evaporation also increases, which favours the formation of thicker fibres as there is less time for the jet to elongate before it dries during its journey between the spinneret and collector. The net effect on average fibre diameter appears to depend on the polymer of interest.^[161]

For polymers dissolved in hydrous solvent systems or ethanol, as the relative humidity is increased, a reduction in the mean fibre diameter is observed. This can be attributed to the slower evaporation rate of the solvent, which provides more time for the jet to elongate before solidification. However, the opposite effect has been reported for polymers dissolved in anhydrous solvent systems. This has been attributed to the propensity of the polymer to precipitate when the jet absorbs water from the air. At higher relative humidities, more water is absorbed and the jet precipitates quicker, allowing less time for jet elongation.^[161] Significant changes to mat morphology are also observed at relative humidities above 60% such as film formation, cross-linked fibres and intra-fibre pores.^[162]

2.1.3 Synthesis of SBA-15 Mesoporous Silica

Preparation of mesoporous silicas like SBA-15 and MCM-41 are carried out using the sol-gel technique. The widely-used physicochemical description of the synthesis of mesoporous silicas produced *via* sol-gel is the cooperative self-assembly mechanism (Figure 2.3). In the synthesis of SBA-15, the first step involves adding the surfactant P123 to an aqueous solution of hydrochloric acid. The surfactant forms rod-like micelles in the solution. Next, the silica precursor tetraethyl orthosilicate (TEOS) is added dropwise to the reaction mixture. The silica precursor starts hydrolysing and condensing around the micellar rods. Over time, the rods stack together into an ordered, hexagonal structure. Meanwhile, TEOS continues to hydrolyse and condense, eventually forming a dense network of silica surrounding the rods. After that, the mixture is subjected to hydrothermal treatment at an elevated temperature, during which the rods expand in diameter and the silica network densifies. The solution is filtered and washed, and the collected precipitate is calcined at 550°C to remove the micellar rods, producing silica particles containing

hexagonally-arranged, cylindrical mesopores.^[163-165] Other mesoporous silicas are obtained by changing the surfactant template, adjusting the sol-gel conditions in terms of pH and temperature, and additions of salts or other reagents.^[163, 166]

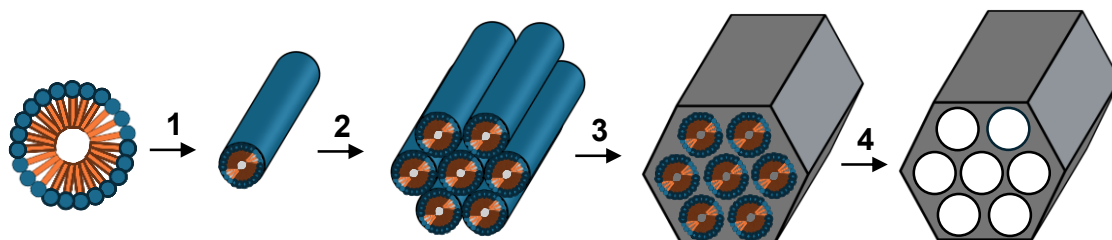


Figure 2.3. Cooperative self-assembly mechanism of SBA-15 silica. 1) Rod-like micelles form from the polymeric template, onto which the silica precursor condenses. 2) The micellar rods stack together into an ordered, hexagonal structure. 3) During hydrothermal treatment, TEOS continues to condense onto the micelles, resulting in a dense network of silica surrounding the rods. 4) The removal of the micelle rods *via* calcination results in a hexagonal array of cylindrical mesopores.

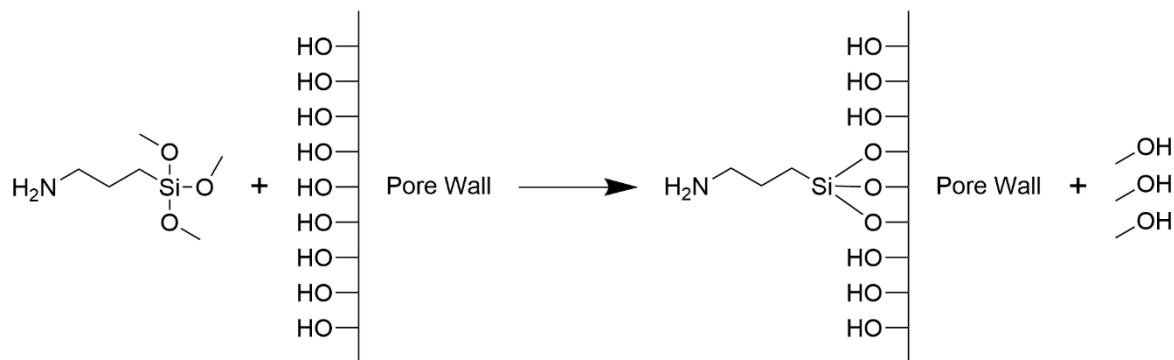
Adapted with permission from: [163]. Copyright 1992 American Chemical Society.

In this work, structural verification of SBA-15 was carried out using small angle x-ray scattering (SAXS). The analytical technique involves passing a monochromatic X-ray beam through the sample and measuring the scattered intensity across a range of small angles (typically $0.1 - 10^\circ$).^[167] The ordered, two-dimensional hexagonal lattice of pores (corresponding to $p6mm$ symmetry) results in SBA-15 having a distinctive pattern of interference peaks, which correspond to interactions between the X-ray beam and specific sets of planes in the periodic structure.^[164]

2.1.4 Amine-Functionalisation of Silica

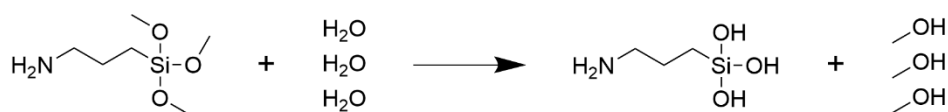
In this work, amine functionalisation of silica is achieved *via* grafting of a trialkoxyaminosilane on to the pore walls of the support.

There are two mechanisms for grafting of silicas. The first is direct solvolysis, which only takes place under extremely anhydrous conditions (Scheme 2.1). Up to three siloxane bonds may form between the aminosilane and the pore wall. The second mechanism is a two-step process which occurs when water is present in the reaction mixture (Scheme 2.2). The grafting agent is hydrolysed (partially or completely) and the intermediate aminosilanols react with surface hydroxyl groups on the silica.

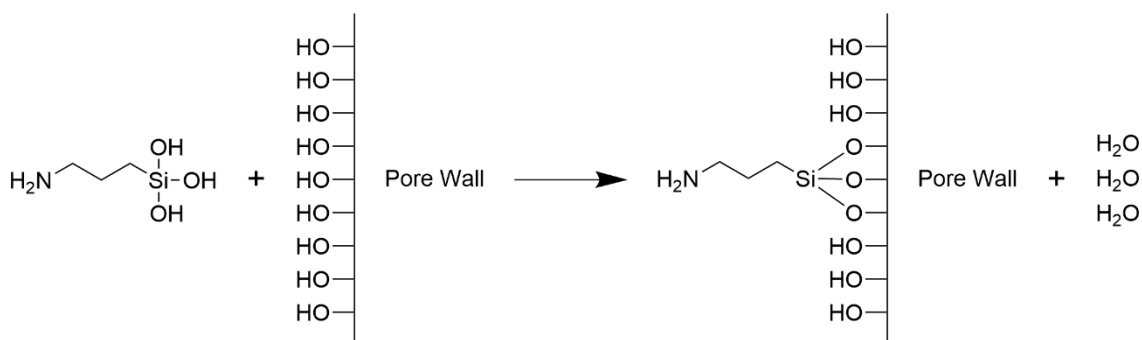


Scheme 2.1. Anhydrous grafting of an aminosilane on to a pore wall *via* direct solvolysis.

1)

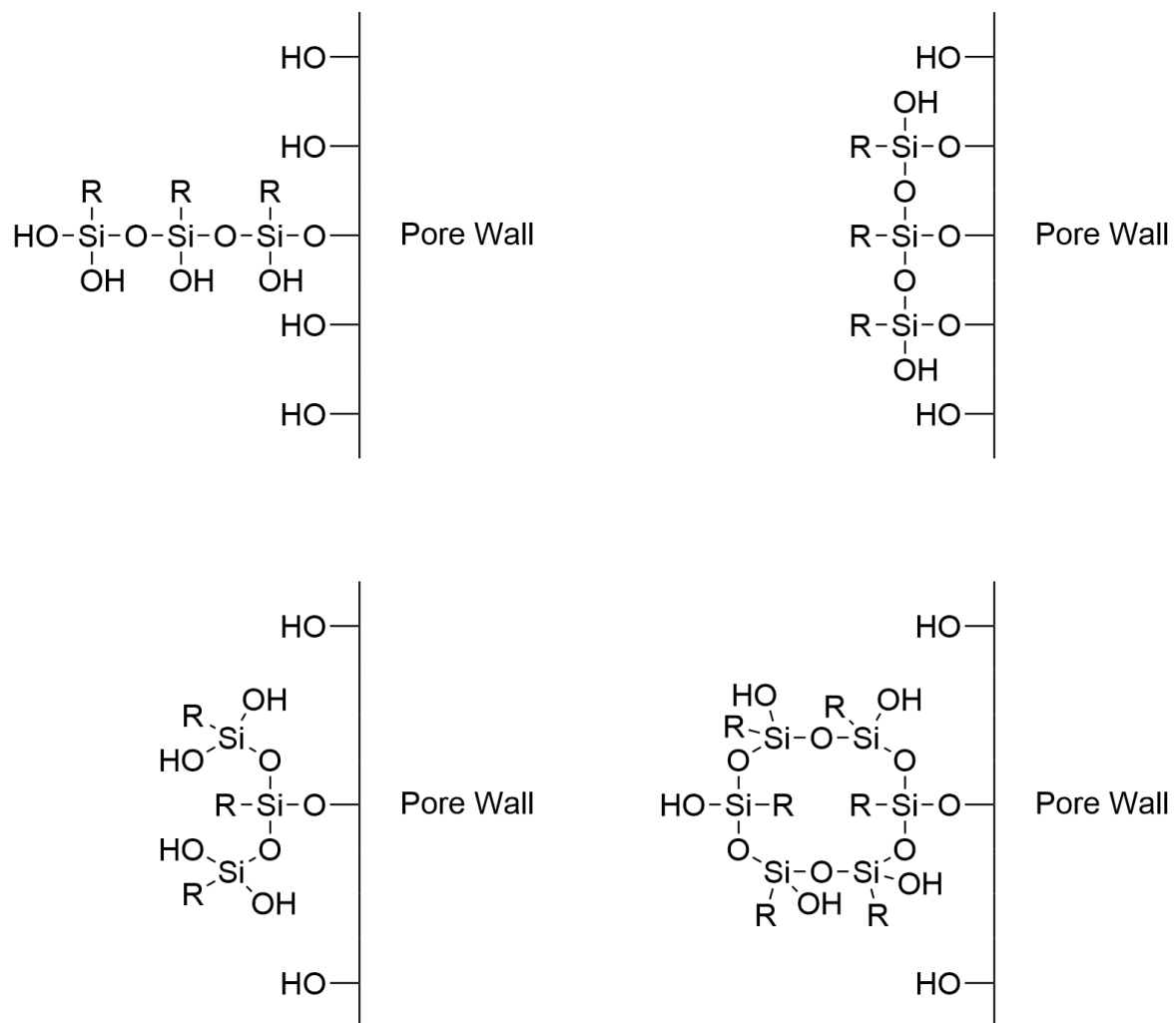


2)



Scheme 2.2. Hydrous grafting of an aminosilane on to a pore wall. 1) Pre-hydrolysis of the aminosilane. 2) Condensation of the aminosilanol intermediate on to the pore wall.

Hydrous grafting can give rise to various oligomeric/polymeric structures formed *via* cross-linking of the aminosilanol intermediates. These may be linear, branched or cyclical in nature (Scheme 2.3).



Scheme 2.3. Several siloxane structures that may form during hydrous silane grafting.

2.2 Material Characterisation

2.2.1 Scanning Electron Microscopy

Scanning electron microscopes offer the ability to generate images of specimens with a magnification up to 500,000 times.^[168] The theoretical basis of the scanning electron microscope was first proposed by von Ardenne in the 1930s to overcome optical distortions encountered with transmission electron microscopes.^[169] Between 1948 and 1965, Oatley and co-workers developed the first commercial SEM.^[170] Below is a brief description of the operating principles.

A simplified diagram of a scanning electron microscope is shown in Figure 2.4. At the top of the instrument, an electron gun generates an electron beam which accelerates towards an anode at a potential of 200 V – 30 kV. It then passes through a series of condenser lenses which focus the beam down to 1000 times its original size. On its journey down the column, it also passes through one or more apertures that remove stray electrons from the beam. The final objective lens, situated below the scan coils, controls the spot size of the beam when it contacts the specimen. The spot size dictates the resolution and depth of field of the generated image. As the spot size is reduced, the resolution and depth of field improves at the expense of image brightness. The scan coils are used to raster the electron beam across the sample and the detection system picks up the signal from the sample and converts it into an image. The entire column is kept under vacuum to ensure optimal functioning of the microscope.^[168, 171, 172]

Several types of signals are generated as a consequence of interactions between the beam and the specimen, each sort carrying specific information about the sample. SEM images in this work were generated from the detection of secondary electrons, which are produced when a primary electron from the beam displaces an electron from the surface of the specimen. Secondary electrons provide topographical information about the specimen at a high resolution. Scanning electron microscopes can contain multiple detectors, each capable of picking up a particular signal.^[168, 171, 172]

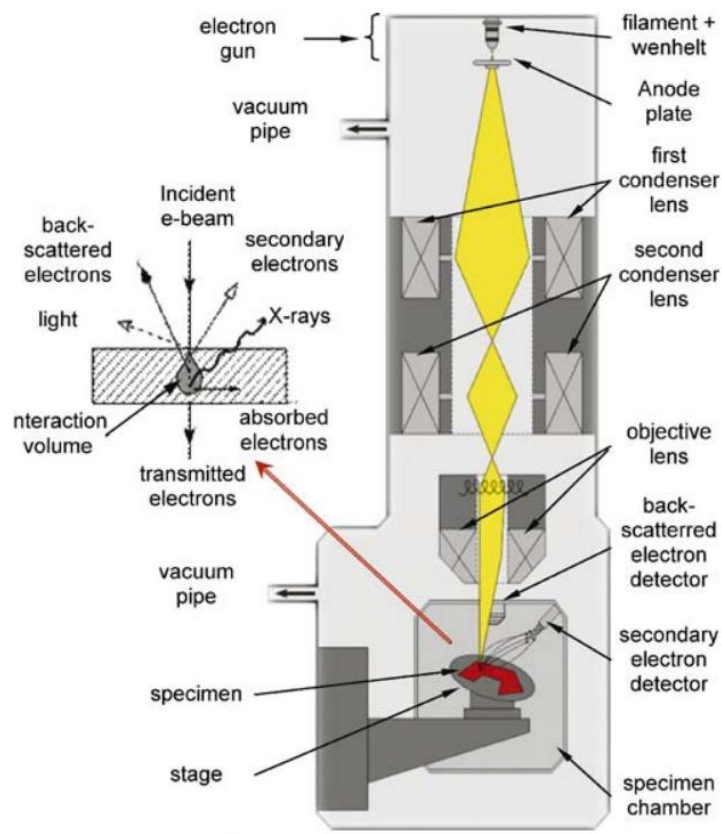


Figure 2.4. Simplified schematic diagram of a scanning electron microscope. Reproduced with permission from: [173]. Copyright 2007 Springer Nature.

2.2.2 Thermogravimetric Analysis

Thermogravimetric analysis (TGA) is a thermal technique which provides information about the physiochemical properties of a material based off changes in its mass. A small amount of sample, typically 1 – 20 mg, is placed on a sample pan which is then loaded on to a precision balance (Figure 2.5). The balance is encased in an electrical furnace and a purge gas is swept through the sample chamber to maintain a controlled atmosphere. The main data collected during a TGA experiment are the change in sample weight with temperature. Different purge gases can be passed through the chamber depending on the experiment. For instance, an inert purge like nitrogen or argon is used for thermal stability experiments whilst an oxygen-rich gas feed is used for determining the oxidative stability of a material. Evolved gases from the sample are swept out of the chamber by the purge gas and may be passed through a mass spectrometer or infrared spectrometer to identify the chemical species present in the exhaust.^[174, 175]

One of the most basic experiments is a ramp procedure, during which the temperature in the furnace is steadily increased at a programmed rate (typically between 5 and 50°C/min) to a target temperature. Weight changes can provide quantitative information like the amount of moisture or volatile content in the sample and qualitative information such as the way in which components of

the sample are bonded. The differential of the weight with respect to time or temperature (differential thermogravimetry; DTG) enables the discernment of overlapping weight changes and also the temperature/time at which maximum change in sample mass occurs during a thermal event.^[174, 175]

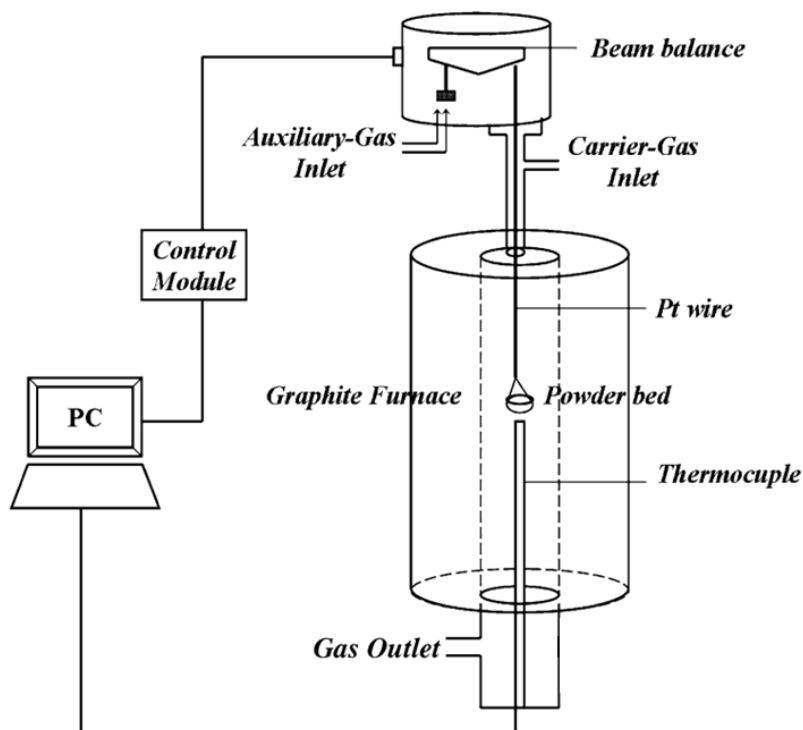


Figure 2.5. Schematic diagram of a thermogravimetric analysis instrument. Adapted with permission from: [176]. Copyright 2011 Springer Nature.

2.2.3 Fourier Transform Infrared Spectroscopy

Fourier-transform infrared spectroscopy (FTIR) is an analytical technique which looks at how much light a sample absorbs across a range of frequencies in the infrared region of the electromagnetic spectrum. For IR wavenumbers of $10,000 - 100 \text{ cm}^{-1}$, light absorption by a material gives rise to molecular vibration. On an FTIR spectrum, bands appear that are centred at specific wavenumbers corresponding to different molecular bonds within the specimen. The frequency of absorption of a given vibration depends on the relative masses of the atoms involved, bond strength and molecule geometry.^[177]

There are two types of molecular vibration that contribute to the absorption bands in an FTIR spectrum: stretching and bending. Stretching of bonds is a result of the oscillatory movement of atoms along the bond axis, resulting in a change in bond length. These can be symmetrical or asymmetrical in nature. Hooke's law can be used to approximate the uncoupled frequencies of such interatomic motion.^[177, 178]

$$\bar{\nu} = \frac{1}{2\pi c} \left[\frac{k}{\frac{m_x m_y}{m_x + m_y}} \right]^{\frac{1}{2}} \quad (2.3)$$

Where: $\bar{\nu}$ is the vibrational frequency, c is the velocity of light, k is the bond force constant, and m_x and m_y are the molar masses of atoms x and y , respectively.

A bending vibration is an interatomic movement that results in a change in bond angle. These can be categorised as scissoring, wagging, twisting and rocking modes. The stretching and bending modes in FTIR spectroscopy are shown in Figure 2.6.^[177, 178]

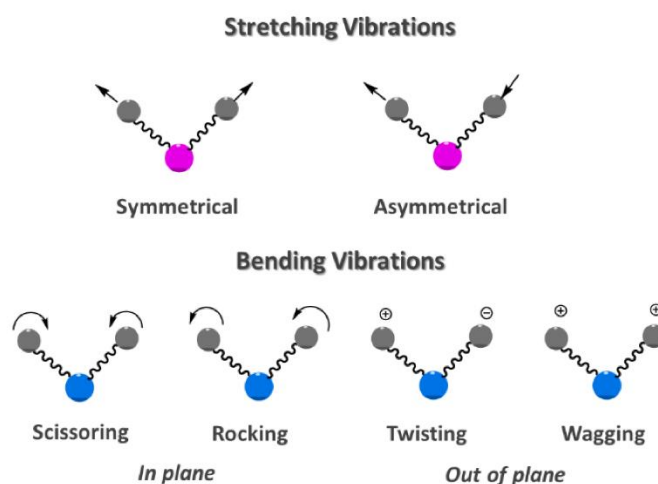


Figure 2.6. Pictorial representation of the different molecular stretching and bending modes detectable in FTIR spectroscopy. Reproduced from: [179]. Published by MDPI under a Creative Commons Attribution licence.

The number of fundamental frequencies of a molecule is equal to the number of vibrational degrees of freedom. Linear and non-linear molecules with N atoms have $3N - 5$ and $3N - 6$ degrees of freedom, respectively. However, for bonds/groups in the middle of a molecule *e.g.* methylene (CH_2), said rules are inapplicable since their vibrations do not involve the entire molecule. Typically, not all fundamental vibrational modes of a bond/group appear in an IR spectrum due to factors such as the signal being too weak, spectral convolution and no change in the dipole moment of the molecule, which is necessary for the vibration to be IR active. For example, the symmetrical stretching mode of CO_2 is IR inactive because it is a linear molecule and therefore the dipolar moments of the individual bonds cancel each other out when they vibrate in a symmetrical manner. Furthermore, bands that are visible on the spectrum may not necessarily appear where they are expected to due to

such phenomena as coupling between vibrations in close proximity and hydrogen bonding, which affects the force constants of the associated groups.^[177, 178]

The main component of an FTIR spectrometer is an interferometer, comprising a broadband infrared source, beam splitter, two mirrors (one fixed and one moveable) a sample cell and a detector (Figure 2.7). During data acquisition, the IR radiation hits the beam splitter. Roughly half of the beam (Beam A) is redirected towards the fixed mirror (Mirror A) whilst the other half (Beam B) travels to the moveable mirror (Mirror B). The two daughter beams reflect off the mirrors and recombine at the beam splitter. Due to the difference in path lengths of Beams A and B, an interference pattern is produced after their recombination. The recombined IR beam then passes through the sample cell and the sample absorbs infrared energy of certain wavelengths corresponding to vibrational frequencies of the bonds in the material. After passing through the sample cell, the beam hits the detector.

During one scan, the path length of Beam B is varied by changing the distance between the beam splitter and the moveable mirror. This results in an interference pattern that varies with the position of Mirror B. The detector records this variation as a function of the position of the moveable mirror, producing an interferogram. The interferogram is then Fourier-transformed to obtain the FTIR spectrum of the sample. Multiple scans are carried out and added together to improve the signal-to-noise ratio of the spectrum.^[177, 178, 180]

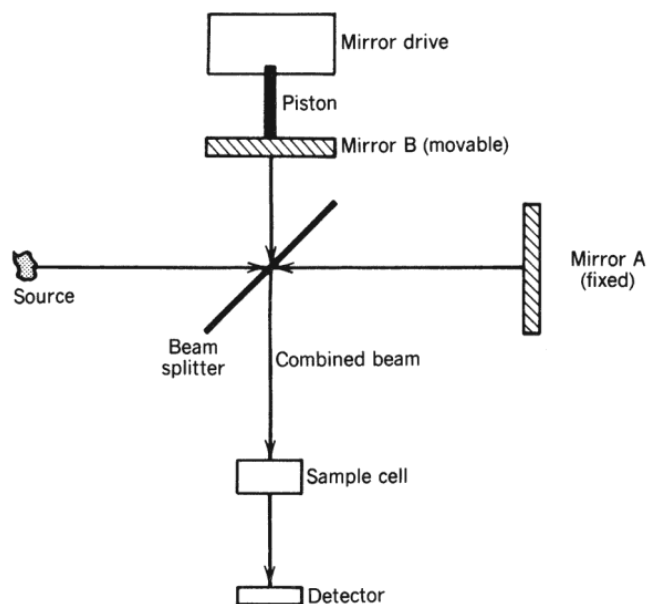


Figure 2.7. Simplified schematic diagram of an FTIR spectrometer. Adapted with permission from: [181]. Copyright 2014 John Wiley and Sons.

There are several main sampling techniques used in FTIR spectroscopy: attenuated total reflectance (ATR), diffuse reflectance and transmission.^[180] The FTIR spectrometer used in this work relies on ATR. An ATR sample cell (Figure 2.8) contains a crystal of high refractive index. The sample is clamped on top of it to ensure good sample-crystal contact. During data acquisition, the IR beam, having travelled through the interferometer, passes through the crystal at such an angle that it is internally reflected off the crystal surface. Provided the sample has a much lower refractive index than the crystal, some of the IR energy travels a short distance beyond the crystal, penetrating between 0.5 – 5 microns into the sample. The energy that interacts with the sample takes the form of an evanescent wave which rapidly decays with distance from the crystal-surface interface. The sample absorbs some of this radiation, thereby attenuating the reflected wave. After one or more reflections, the IR beam is picked up by the detector.^[177, 178, 180]

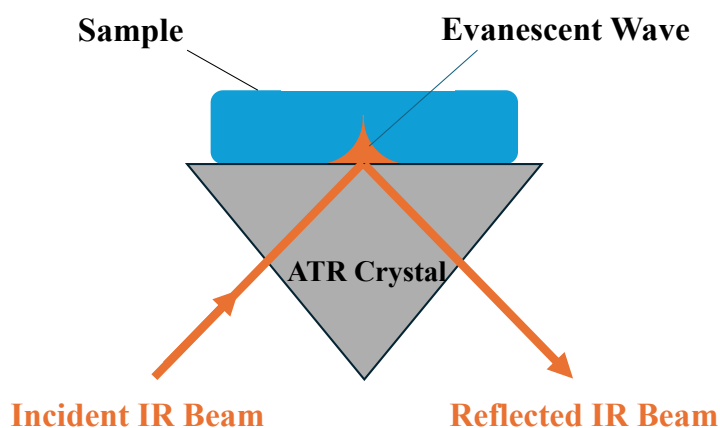


Figure 2.8. Simplified schematic diagram of an ATR sample cell. Figure created by author.

2.2.4 Nitrogen Physisorption Analysis

2.2.4.1 IUPAC Isotherms

The IUPAC definition of adsorption is “an increase in the concentration of a dissolved substance at the interface of a condensed and a liquid phase due to the operation of surface forces. Adsorption can also occur at the interface of a condensed and gaseous phase.”^[182] There are two types of adsorption: physisorption and chemisorption. In the case of physisorption, weak intermolecular interactions such as van der Waal forces are responsible for the adherence of the adsorptive to the interface. In contrast, chemisorption is mediated *via* chemical bonds.^[183]

Measuring the amount of adsorbed gas on a solid sample across a range of pressures (P) using an appropriate adsorptive and temperature, yields a sorption isotherm from which information can be

derived about the textural properties of the sample. Namely, specific surface area, total pore volume, and pore size distribution.

Nitrogen physisorption isotherms are measured up to the saturation vapour pressure (P_0) of the gas at 77 K and consist of two branches, one representing adsorption, wherein each datapoint is recorded after an increment in the relative pressure (P/P_0) and the other desorption, in which each volume measurement is recorded after a decrease in P/P_0 .

In accordance with IUPAC recommendations, there are six types of sorption isotherms (Figure 2.9). The Type I isotherm is concave to the P/P_0 axis and is characteristic of microporous materials such as activated carbon. The steep uptake of gas at low relative pressures is due to the filling of the micropores in the material. Uptake is limited to the accessible pore volume rather than the internal surface area. Type Ia corresponds to narrow micropores less than 1 nm in width whilst Type Ib is representative of materials with a broad range of micropore sizes, up to 2 nm in width. Type II isotherms are common for non-porous and macroporous materials. There is an inflection point B which indicates the completion of monolayer surface coverage. Beyond the inflection point, multilayer adsorption on the sample occurs. Type III is like Type II in that there is unlimited monolayer-multilayer adsorption, however, such an isotherm lacks an inflection point demarking the transition between monolayer and multilayer adsorption and is a result of weak adsorbent-adsorbate interactions.^[183]

Type IV isotherms are indicative of mesoporosity, with pore sizes in the range of 2 – 50 nm. Initially, they exhibit similar monolayer/multilayer adsorption to Type II, but at higher partial pressures, capillary condensation occurs wherein at pressures less than the saturation pressure P_0 , the adsorptive condenses into a liquid-like phase in the mesopores. For Type IVa, pore condensation results in a hysteresis loop in which the corresponding relative pressure at a given adsorbed amount is lower for the desorption branch compared to the adsorption branch. Meanwhile, Type IVb exhibits reversible sorption. Type V initially shows similar sorption behaviour to Type III due to weak adsorbate-adsorbent interaction, however, pore filling causes the adsorbed amount to plateau out at high relative pressures. Finally, Type VI shows step changes in the adsorbed amount with pressure due to sequential layer formation on a non-porous solid.^[183]

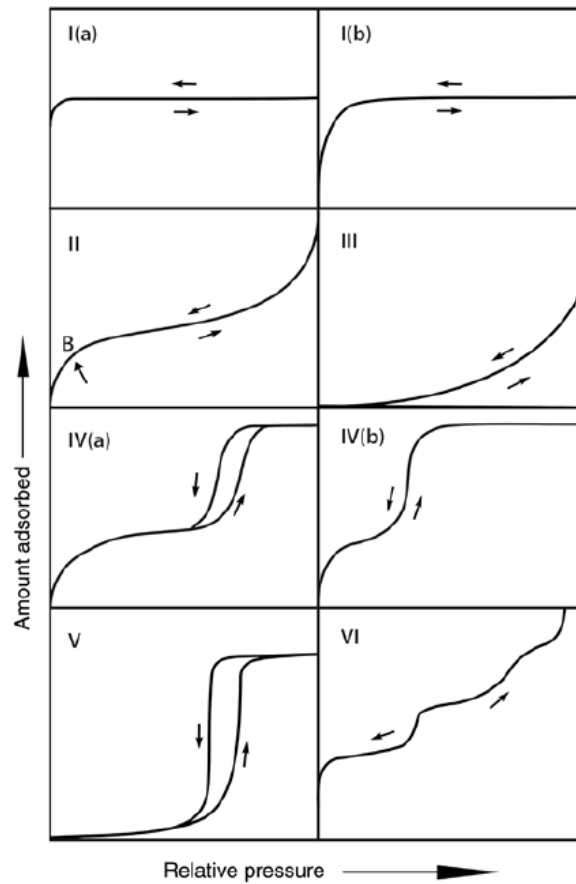


Figure 2.9. Types of IUPAC sorption isotherms. The up and down arrows indicate the adsorption and desorption branches, respectively. Reproduced from: [183]. Copyright 2015 IUPAC & De Gruyter.

There are five principal types of hysteresis for Type IV (mesoporous) materials (Figure 2.10). H1 is common for mesoporous materials with a narrow range of pore sizes like templated silicas (SBA-15, MCM-41). Type H2 corresponds to more complex pore structures; the steep desorption branch in H2a and H2b is a result of pore-blocking in a narrow and wide range of pore neck sizes, respectively. The Type H3 loop shows no limit to adsorption at high P/P_0 . H4 is similar to H3 except there is considerable adsorption in the low P/P_0 range due to microporosity. The desorption branch of H5 is indicative of materials with both open and partially blocked pores.^[183]

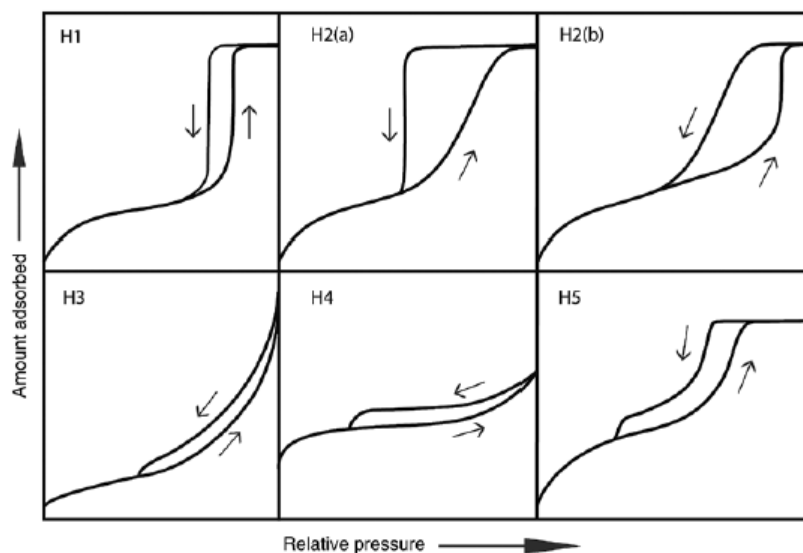


Figure 2.10. Types of hysteresis loops. The up and down arrows indicate the adsorption and desorption branches, respectively. Copyright 2015 IUPAC & De Gruyter.

2.2.4.2 Specific Surface Area Determination using the Brunauer-Emmett-Teller Method

The specific surface area of a material can be obtained using the Brunauer-Emmett-Teller (BET) method.^[184] This involves the use of Equation (2.4), the BET equation.

$$\frac{1}{V \left(\left(\frac{P_0}{P} \right) - 1 \right)} = \frac{1}{V_m C} + \frac{C - 1}{V_m C} \cdot \left(\frac{P}{P_0} \right) \quad (2.4)$$

Where V is the volume of adsorbed gas at a relative pressure P/P_0 and V_m is the volume of adsorbate corresponding to monolayer surface coverage. The value of the BET constant C is related to the strength of the adsorbent/adsorbate interactions.

Datapoints from the sorption isotherm, typically in the relative pressure range of 0.05 to 0.35, are used to produce a linear plot of $1/[V(P_0/P)-1]$ against P/P_0 .

The weight of the monolayer is then found using the slope (s) and intercept (i) of the BET plot.

$$V_m = \frac{1}{s + i} \quad (2.5)$$

Where: $s = \frac{c-1}{V_m c}$ and $i = \frac{1}{V_m c}$.

Using V_m , the total surface area of the sample (S_t) can be found.

$$S_t = \frac{V_m N A_{CS}}{V} \quad (2.6)$$

Where: N is Avogadro's number (6.02×10^{23} /mol), A_{CS} is the cross-sectional area of a single molecule of the adsorbate, V is the molar volume of gas at standard room temperature and pressure (22.4 L/mol for an ideal gas).

Dividing by the sample mass (m) yields the specific surface area of the sample (S).

$$S = \frac{S_t}{m} \quad (2.7)$$

2.2.4.3 Determination of the Pore Size Distribution using the Barrett-Joyner-Halenda Method

The pore size distribution of a mesoporous material is commonly found using the Barrett-Joyner-Halenda (BJH) method.^[185] The following discussion applies for the use of nitrogen as the adsorbate and assumes cylindrical pore geometry. Henceforth in this sub-section, 'mesopore' and 'pore' are used interchangeably.

Adsorption data from the desorption branch of the isotherm is typically used for the determination of pore size distribution using the BJH method. At an initial relative pressure close to unity, $(P/P_0)_0$, all mesopores are filled with condensate.

The relationship between the pore volume of the largest mesopore (V_{p1}) and the inner capillary volume (V_{K1}) is:

$$V_{p1} = V_{K1} \times \frac{r_{p1}^2}{r_{K1}^2} \quad (2.8)$$

Where r_{p1} is the radius of the largest pore and r_{K1} is the radius of the inner capillary.

During the first decrement in relative pressure, from $(P/P_0)_0$ to $(P/P_0)_1$, a volume of adsorbate (ΔV_1) is desorbed from the sample due to a combination of capillary evaporation in the largest mesopore and a reduction in the layer of physisorbed nitrogen on the pore wall (Δt_1).

V_{p1} is obtained from Equation (2.9).

$$V_{p1} = \Delta V_1 \cdot \left(\frac{r_{p1}}{r_{K1} + \Delta t_1} \right)^2 \quad (2.9)$$

When the relative pressure is lowered again to $(P/P_0)_2$, the second-largest mesopore is emptied of its condensate and there is a reduction in thickness of the physisorbed layer (Δt_2) on the wall of this pore and the largest pore. The volume desorbed (ΔV_2) is the sum of the volume of nitrogen from capillary evaporation and the volume of nitrogen from the reduction in the physisorbed layer.

The pore volume of the second-largest pore (V_{p2}) is obtained from Equation (2.10).

$$V_{p2} = (\Delta V_2 - V_{\Delta t_2}) \cdot \left(\frac{r_{p2}}{r_{K2} + \Delta t_2} \right)^2 \quad (2.10)$$

Where $V_{\Delta t_2}$ is the volume of nitrogen desorbed due to the reduction in thickness of the physisorbed layer in the largest pore.

When the relative pressure is lowered a third time to $(P/P_0)_3$, capillary evaporation occurs in the third-largest pore, along with a reduction in the physisorbed layer thickness on the wall of this pore and the two larger pores (Δt_3)

The pore volume of the third-largest pore (V_{p3}) is obtained from (2.11).

$$V_{p3} = (\Delta V_3 - V_{\Delta t_3}) \cdot \left(\frac{r_{p3}}{r_{K3} + \Delta t_3} \right)^2 \quad (2.11)$$

The term $V_{\Delta t_3}$ represents the total volume of nitrogen desorbed due to the reduction in physisorbed layer thickness on the walls of the largest and second-largest pores.

In general, the volume of the pore with average radius r_{pn} that is emptied of its condensate during the n^{th} pressure decrement is found from Equation (2.12).

$$V_{pn} = (\Delta V_n - V_{\Delta t_n}) \cdot \left(\frac{r_{pn}}{r_{Kn} + \Delta t_n} \right)^2 \quad (2.12)$$

The term $V_{\Delta t_n}$, corresponds to the sum of the total volume of nitrogen desorbed from the reduction in thickness of physisorbed nitrogen on unfilled pores down to but not including the pore that was emptied of its condensate during the n^{th} pressure decrement.

$V_{\Delta t_n}$ can be expressed as:

$$V_{\Delta t_n} = \sum_{j=1}^{n-1} \Delta t_n A_{pj} c_j \quad (2.13)$$

Where A_{pj} is the surface area of the pore of radius r_{pj} which was emptied of its condensate during pressure decrement j .

The term c_j is the ratio of the capillary radius after condensate removal (r_{cj}) to r_{pj} .

$$c_j = \frac{r_{cj}}{r_{pj}} = \frac{r_{pj} - t_j}{r_{pj}} \quad (2.14)$$

Where t_j is the thickness of the physisorbed layer on the pore.

Thus, the term $A_{pj} c_j$ in Equation (2.13) is the surface area of the capillary in the pore of size r_{pj} straight after pressure decrement j and $\Delta t_n A_{pj} c_j$ is the volume of nitrogen desorbed from the pore of size r_{pj} during the n^{th} pressure decrement.

Substituting (2.14) into (2.13) yields:

$$V_{\Delta t_n} = \Delta t_n \cdot \sum_{j=1}^{n-1} A_{pj} \frac{r_{pj} - t_j}{r_{pj}} \quad (2.15)$$

The BJH equation is obtained by substituting (2.15) into (2.12).^[185]

$$V_{pn} = \left(\Delta V_n - \Delta t_n \cdot \sum_{j=1}^{n-1} A_{pj} \frac{(r_{pj} - t_j)}{r_{pj}} \right) \cdot \left(\frac{r_{pn}}{r_{Kn} + \Delta t_n} \right)^2 \quad (2.16)$$

The average pore radius r_{pn} with volume V_{pn} derived from the BJH equation is found using Equation (2.17).

$$r_{pn} = r_{Kn} + t_n \quad (2.17)$$

Where the inner capillary radius r_{Kn} is obtained from Equation (2.18), known as the Kelvin equation,^[186] and t_n is the physisorbed layer thickness, which can be estimated using Equation (2.19).^[187]

$$r_{Kn} = \frac{4.5}{\log \left(\left(\frac{P_0}{P} \right)_n \right)} \quad (2.18)$$

$$t_n = \left[\frac{13.99}{\log \left(\left(\frac{P_0}{P} \right)_n \right) + 0.034} \right]^{\frac{1}{2}} \quad (2.19)$$

Plotting V_{pn} against r_{pn} using datapoints from the desorption isotherm produces the BJH pore size distribution, from which the average pore size can be obtained.

2.2.5 Nuclear Magnetic Resonance Spectroscopy

Atomic nuclei possess an intrinsic form of angular momentum termed spin. For a given nucleus, its net spin is the sum of the individual spins of its constituent nucleons (1/2 and -1/2 for protons and neutrons respectively). Nuclei, by virtue of their charge, generate a magnetic field. Their spin

quantum number (I) gives rise to a magnetic moment (μ) related by the nuclear gyromagnetic ratio (γ).

$$\mu = \gamma I \quad (2.20)$$

To be detectable using NMR, nuclei must be magnetically active which, according to the above equation, implies they have a non-zero spin quantum number ($1/2, 1, 3/2$ etc.). Nuclei with an I value of zero cannot be studied using NMR and are known as ‘NMR-silent’. Henceforth, ‘nucleus’ refers to an NMR-active nucleus.^[188-190]

Considering this work utilises only spin $1/2$ nuclei (*i.e.* ^1H , ^{13}C and ^{29}Si), the subsequent discussion applies only to the physics of such species. Nuclei with higher spin quantum numbers possess also a quadrupole moment by virtue of their asymmetric charge distribution. This results in additional complexity to the physical basis of NMR which, for the sake of brevity, is omitted in this discussion.

2.2.5.1 Experimental Set-Up

The basic NMR set-up (Figure 2.11) comprises a superconducting magnet with a bore in the middle in which the sample to be analysed is placed. The sample is contained in a sealed glass tube or a capped zirconia rotor for solution-state and solid-state NMR, respectively. The spectrometer transmits radiofrequency pulses into the sample *via* a probe surrounding the sample. During the experiment, the sample is subjected to the external static field from the superconducting magnet (\mathbf{B}_0) and an alternating magnetic field (\mathbf{B}_1) from one or more pulses of radiofrequency energy from the probe.

During data acquisition, the probe picks up the NMR signal from the sample and transmits it to the spectrometer. A computer connected to the spectrometer processes the signal into a frequency-domain spectrum *via* Fourier transformation, from which chemical information about the sample can be obtained.

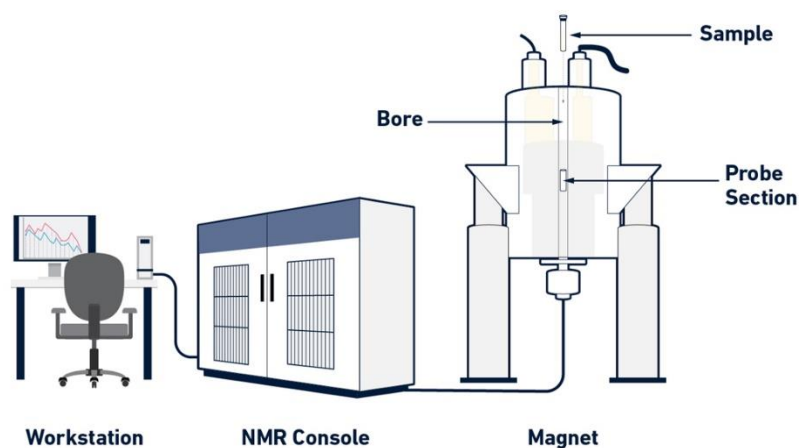


Figure 2.11. Schematic diagram of an NMR spectrometer with its main components. Reproduced with permission from: [191]. Copyright 2024 Technology Networks.

2.2.5.2 Physical Description of a Simple NMR Experiment

To understand the principles of NMR, a physical description is provided of a direct polarisation experiment in which the sample is subjected to a single radiofrequency pulse, followed by the recording of the NMR signal emitted by the sample.

When placed in a static, homogeneous magnetic field, \mathbf{B}_0 , the magnetic moments of the spin $\frac{1}{2}$ nuclei in the sample possess a component parallel or anti-parallel to the direction of the external field. The magnetic dipoles aligned parallel to the external field are in a lower (α) energy state whilst those anti-parallel are in a higher (β) energy state. The proportion of the total population of spins quantised in each energy state is temperature dependent and is described by the Boltzmann distribution, as given in Equation (2.21).

$$\frac{N_{\beta}}{N_{\alpha}} = e^{\frac{-\Delta E}{kT}} \quad (2.21)$$

Where N_{β} is the spin population in the higher energy state, N_{α} is the spin population in the lower energy state, ΔE is the energy gap between the two spin states, k is the Boltzmann constant, and T is temperature.

From a quantum mechanical perspective, the two energy populations are separated by an energy gap, which is proportional to the magnitude of \mathbf{B}_0 .^[188-190]

The sample possesses a bulk magnetic moment, represented by the vector \mathbf{M} , which is the sum of the magnetic moments of the individual spins (μ).

$$\mathbf{M} = \sum \mu \quad (2.22)$$

In a three-dimensional vector model, where the positive z direction represents the direction of the static magnetic field \mathbf{B}_0 , the components of the individual magnetic moments in the x - y plane are randomly distributed. The direction of \mathbf{M} is therefore dependent on the proportion of spins in each energy state (*i.e.* the z components of the magnetic moments). The Boltzmann distribution dictates that slightly more spins are in the lower (α) energy state at equilibrium, resulting in \mathbf{M} being parallel to the static magnetic field (*i.e.* in the positive z direction). The external field exerts a torque on \mathbf{M} , causing the bulk magnetisation vector to precess about \mathbf{B}_0 (Figure 2.12).

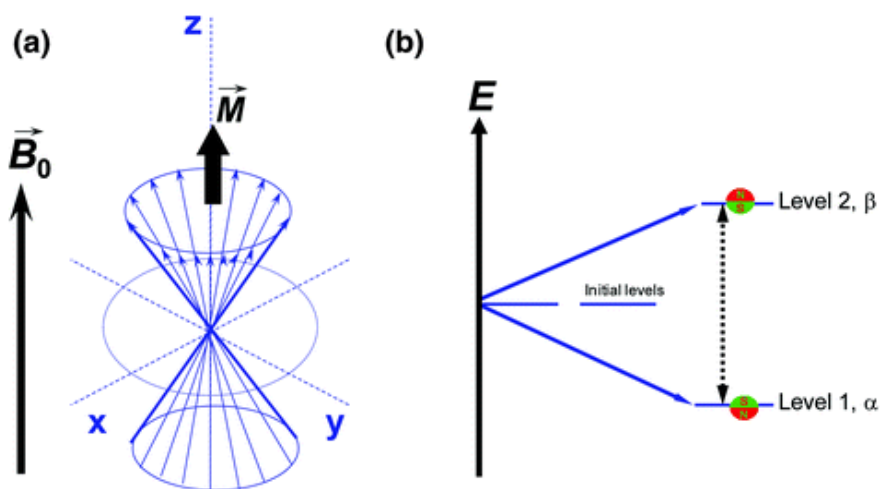


Figure 2.12.a) Vector (classical) model with a static (laboratory) frame of reference showing the precession of the bulk magnetic moment \mathbf{M} about the applied static field \mathbf{B}_0 at equilibrium. b) Quantum model of NMR showing the two quantum levels that result from \mathbf{B}_0 . The dotted arrow indicates the energy gap between the two spin states. Reproduced with permission from Springer Nature [190].

The rate of precession of \mathbf{M} is called the Larmor frequency (ν_0) and is obtained from Equation (2.23).^[188-190]

$$\nu_0 = -\gamma B_0 \quad (2.23)$$

To describe a simple direct polarisation NMR experiment involving spin $\frac{1}{2}$ nuclei, a vector model is used in which the frame of reference rotates at ν_0 of the nucleus of interest (the rotating frame). From this perspective, the vector \mathbf{M} is static when subjected to \mathbf{B}_0 , as the frame rotates at the rate of precession of \mathbf{M} about \mathbf{B}_0 (Figure 2.13a). Use of vector models for describing NMR experiments assumes that each nucleus interacts only with \mathbf{B}_0 , and the oscillating magnetic field \mathbf{B}_1 (associated with radiofrequency pulses generated by the probe). In reality, there are additional magnetic interactions that also influence the resonant frequencies of the spins such as chemical shielding and dipolar coupling.

When a single, on-resonance radiofrequency pulse is applied along the x -axis of the vector model, the associated alternating magnetic field \mathbf{B}_1 exerts a torque on \mathbf{M} , and the bulk magnetisation vector proceeds to precess about the \mathbf{B}_1 axis (Figure 2.13b). The pulse duration determines the final position of \mathbf{M} , expressed as the angle between \mathbf{M} and the positive z -direction (the flip angle). We now consider a scenario in which the pulse is applied long enough that \mathbf{M} ends up on the y -axis (a $(\pi/2)_x$ pulse), as shown schematically in Figure 2.13c. From a quantum mechanical perspective, this has the effect of equalising the energy populations, placing the spin system in a non-equilibrium state. After the pulse is applied, \mathbf{M} continues to precess about \mathbf{B}_0 at a frequency of ν_0 . Interactions between the spins and their environment (termed the lattice) result in energy losses, during which the spin system returns to its equilibrium state. This is termed ‘spin lattice relaxation’. During the process, \mathbf{M} reappears along the z -axis at a rate determined by the time constant T_1 .

Spin-lattice relaxation results in the sample emitting a decaying signal (the free induction decay, FID), which is a sum of the resonant frequencies of all the spin environments in that sample (Figure 2.13d). In this simplified case, there is only one resonant frequency, determined by Equation (2.23) above. The FID is picked up by the probe and recorded by the spectrometer. Fourier transformation of the FID produces an NMR spectrum showing a single peak at the resonant frequency of the nuclei (Figure 2.14). Repeat scans are recorded and the spectra added together to improve the signal-to-noise ratio (spectral sensitivity is proportional to the square-root of the number of scans). A recycle delay is necessary between scans to allow the spin system to return to equilibrium and this is normally several multiples of T_1 .^[188, 190]

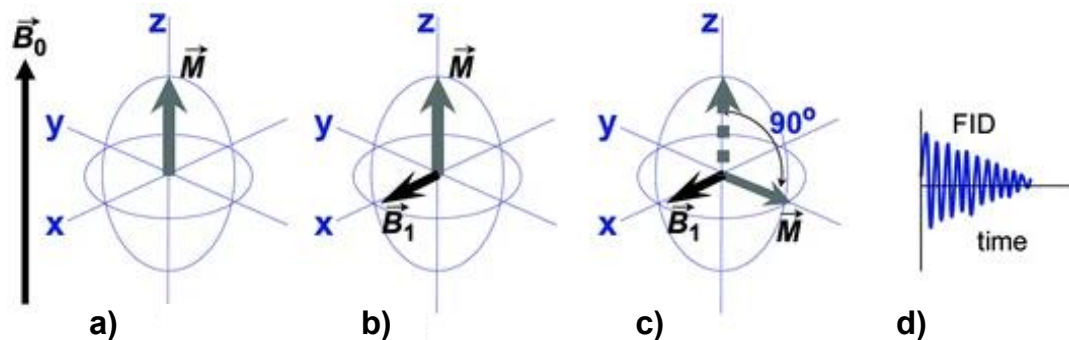


Figure 2.13. Vector model with a rotating frame of reference showing the manipulation of the bulk magnetisation vector \mathbf{M} during a direct polarisation experiment. a) Initially, \mathbf{M} is parallel to \mathbf{B}_0 . b) A radiofrequency pulse is applied along the x -axis, causing \mathbf{M} to precess about the axis of the alternating magnetic field \mathbf{B}_1 associated with the pulse. c) After the application of a $(\pi/2)_x/90_x$ pulse, \mathbf{M} is situated along the y -axis. d) Spin-lattice relaxation results in the recovery of \mathbf{M} along the z -axis, during which the NMR probe picks up a decaying signal (the free induction decay, FID). Adapted with permission from Springer Nature [190].

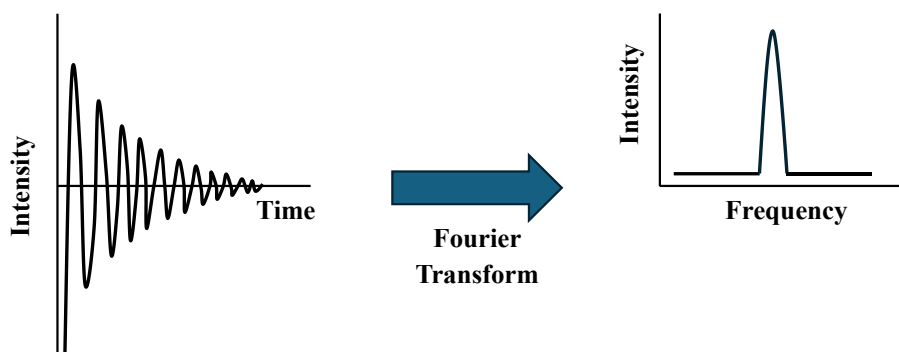


Figure 2.14. The NMR signal is converted from the time domain to the frequency domain using Fourier transformation. The resulting graph is an NMR spectrum which shows peaks at specific frequencies that reveal chemical information about the sample. Figure created by the author.

2.2.5.3 Chemical Shifts

In the above discussion, only the effects of the external magnetic field \mathbf{B}_0 and an oscillating field \mathbf{B}_1 on the energy states of the magnetic moments are considered. In reality, other interactions exist which act to alter the size of the NMR energy transitions of a nucleus.

The circulation of electrons around a nucleus generates a magnetic field in opposition to \mathbf{B}_0 . This reduces the overall magnetic field experienced by the nucleus and is termed chemical shielding.

$$B_{loc} = (1 - \sigma)B_0 \quad (2.24)$$

Where B_{loc} is the local magnetic field and σ is the shielding constant.

The isotropic resonant frequency of the nucleus (ν) is therefore:

$$\nu = -\gamma B_0(1 - \sigma) \quad (2.25)$$

The extent of shielding is impacted by chemical bonding. For example, connection to a neighbouring nucleus with a much higher electronegativity causes significant deshielding of a nucleus. In other words, an electron-withdrawing group reduces the electron density surrounding the nucleus meaning when it is placed in a static magnetic field, its local magnetic field (and associated resonant frequency) is higher. Hydrogen bonding also impacts shielding. Thus, different nuclear environments experience different degrees of shielding meaning that each environment has a distinctive isotropic resonant frequency, or peak on the NMR spectrum. Assuming there are no anisotropic magnetic interactions, the number and position of peaks on an NMR spectrum provides information about the different types of chemical environments in the sample.^[188-190]

Conventionally, the resonant frequencies of nuclei are expressed as a chemical shift, δ .

$$\delta = \frac{\nu - \nu_{ref}}{\nu_{ref}} \quad (2.26)$$

Where ν_{ref} is the resonant frequency of a reference compound. ^1H , ^{13}C and ^{29}Si chemical shifts are commonly reported relative to tetramethylsilane (TMS).^[188, 189]

2.2.5.4 Chemical Shielding Anisotropy and Dipolar Coupling

Since the electron density surrounding a nucleus is often non-uniform, chemical shielding has an anisotropic component. Consequently, the orientation of chemical bonds relative to the external field impacts the extent of shielding experienced by the nucleus (termed chemical shielding anisotropy,

CSA). Each orientation has its own resonant frequency. In solution-state NMR, molecular tumbling averages chemical shielding to its single isotropic value. However, in solid-state NMR, CSA results in line broadening and ‘powder patterns’ in which multiple chemical shifts corresponding to all possible orientations are present in the spectrum of a given nuclear environment. Furthermore, magnetic interactions between neighbouring nuclear dipoles (dipolar coupling) also impact the strength of the local magnetic field that a nucleus experiences. Similar to CSA, these interactions are averaged out to zero in solution-state NMR but are present in solid-state NMR, causing further line broadening and ‘dipolar splitting’ of peaks. Both CSA and dipolar coupling make interpreting NMR spectra of solids challenging when using solution-state experimental techniques.^[189, 190, 192]

2.2.5.5 Overcoming Anisotropic Interactions in Solid-State NMR using Magic Angle Spinning

In general, the effect of a magnetic interaction on the local magnetic field of a nucleus can be expressed as:

$$\mathbf{B}_{loc} = \mathbf{A}_{loc} \cdot \mathbf{J} \quad (2.27)$$

\mathbf{J} is the vector representing the source of the interaction. In the case of chemical shielding, $\mathbf{J} = \mathbf{B}_0$ because the applied field induces the electron current which generates the shielding magnetic field. For dipolar coupling, \mathbf{J} is the spin vector of another nucleus.

\mathbf{A}_{loc} is the coupling tensor, which is a 3 x 3 matrix with 9 components that relate vector \mathbf{B}_{loc} with \mathbf{J} .

$$\mathbf{A}_{loc} = \begin{bmatrix} A_{xx} & A_{xy} & A_{xz} \\ A_{yx} & A_{yy} & A_{yz} \\ A_{zx} & A_{zy} & A_{zz} \end{bmatrix} \quad (2.28)$$

Where (x, y, z) refer to an unspecified axis system. It is possible to simplify the coupling tensor by choosing axes such that the interaction tensor is diagonalized (termed the principal axis frame, PAF).^[192]

$$\mathbf{A}_{loc} = \begin{bmatrix} A_{xx}^{PAF} & 0 & 0 \\ 0 & A_{yy}^{PAF} & 0 \\ 0 & 0 & A_{zz}^{PAF} \end{bmatrix} \quad (2.29)$$

For chemical shielding, Equation (2.27) becomes:

$$\mathbf{B}_{loc} = \boldsymbol{\sigma} \cdot \mathbf{B}_0 \quad (2.30)$$

Where $\boldsymbol{\sigma}$ is the shielding tensor.

In the PAF, the shielding tensor can be expressed as:

$$\boldsymbol{\sigma} = \begin{bmatrix} \sigma_{xx}^{PAF} & 0 & 0 \\ 0 & \sigma_{yy}^{PAF} & 0 \\ 0 & 0 & \sigma_{zz}^{PAF} \end{bmatrix} \quad (2.31)$$

Where σ_{xx}^{PAF} , σ_{yy}^{PAF} and σ_{zz}^{PAF} are the strengths of the shielding interaction along the x , y and z axes, respectively. Collectively, they are known as the principal values of the shielding tensor.^[192]

In this form, the shielding tensor can be represented geometrically by an ellipsoid (Figure 2.15). The principal axes of the ellipsoid coincide with the principal axis frame of the interaction tensor. The size of the principal values of the interaction tensor in each direction determine the geometry of the ellipsoid.

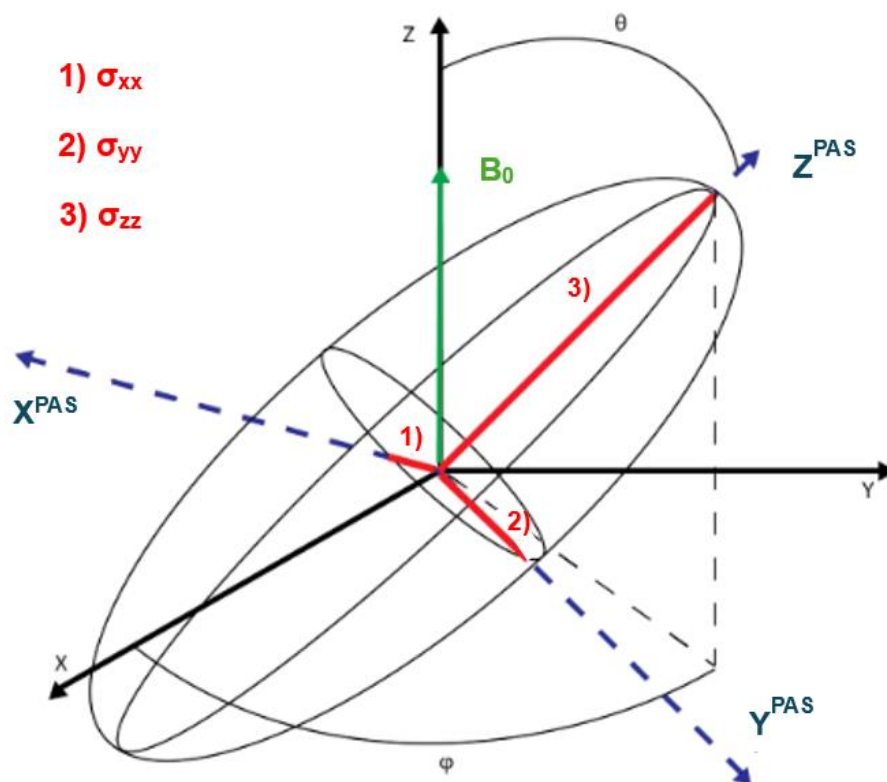


Figure 2.15. Geometrical representation of the shielding tensor. θ relates the orientation of the interaction tensor with respect to \mathbf{B}_0 and ϕ with respect to the x - y plane (perpendicular to \mathbf{B}_0). Adapted from [193]. Published by LibreTexts under a Creative Commons Attribution licence.

The principal values of the shielding tensor are commonly expressed in the form of the isotropic value (σ_{iso}), the anisotropy (Δ) and the asymmetry (η), shown in Equations (2.32), (2.33) and (2.34), respectively. For a given nuclear environment, if the principal values are equal, then the ellipsoid representing the interaction tensor is spherical and the magnitude of chemical shielding takes the same value in all directions ($\sigma_{iso} = 1, \Delta = 0, \eta = 0$). The resulting solid-state NMR spectrum would display a single (isotropic) chemical shift for that nuclear environment.^[192]

$$\sigma_{iso} = \frac{1}{3}(\sigma_{xx}^{PAF} + \sigma_{yy}^{PAF} + \sigma_{zz}^{PAF}) \quad (2.32)$$

$$\Delta = \sigma_{zz}^{PAF} - \sigma_{iso} \quad (2.33)$$

$$\eta = \frac{\sigma_{xx}^{PAF} - \sigma_{iso}}{\Delta} \quad (2.34)$$

These terms, along with angles Θ and φ defined in Figure 2.15 above, appear in the chemical shielding Hamiltonian, which shows how chemical shielding affects the energy levels of the nuclear spins.^[194]

$$H_{CS} = \left\{ \omega_0 \sigma_{iso} + \left[\frac{\omega_0 \Delta}{2} [(3 \cos^2(\theta) - 1) - \eta \sin^2 \theta \cos(2\phi)] \right] \right\} \cdot \hat{I}_z \quad (2.35)$$

Where \hat{I}_z is an operator representing the z -component of the spin angular momentum of the nucleus.

The first-order average Hamiltonian of the dipolar interaction takes two forms depending on whether the interaction is between like-spins (homonuclear) or unlike spins (heteronuclear).^[192, 194]

$$H_{dd}^{hetero} = -d(3 \cos^2 \theta - 1) \hat{I}_z \hat{S}_z \quad (2.36)$$

$$H_{dd}^{homo} = -d(3 \cos^2 \theta - 1) [\hat{I}_z \hat{S}_z - \hat{\mathbf{I}} \cdot \hat{\mathbf{S}}] \quad (2.37)$$

Where:

- d is the dipolar coupling constant, which determines the magnitude of the interaction.
- \hat{I}_z and \hat{S}_z are the z -components of the spin operators for the two interacting nuclei. Multiplied together, they represent the z -component of the dipolar interaction.
- $\hat{\mathbf{I}} \cdot \hat{\mathbf{S}}$ is the scalar product of the spin operators of the two nuclei and represents the total interaction between the two nuclei.

Common to both chemical shielding and dipolar coupling Hamiltonians is the term ‘ $3\cos^2\theta-1$ ’, which represents the orientation dependence of the interaction. Packing the sample in a rotor and spinning it at an angle Θ_R to the applied field results in θ varying with time (Figure 2.16).

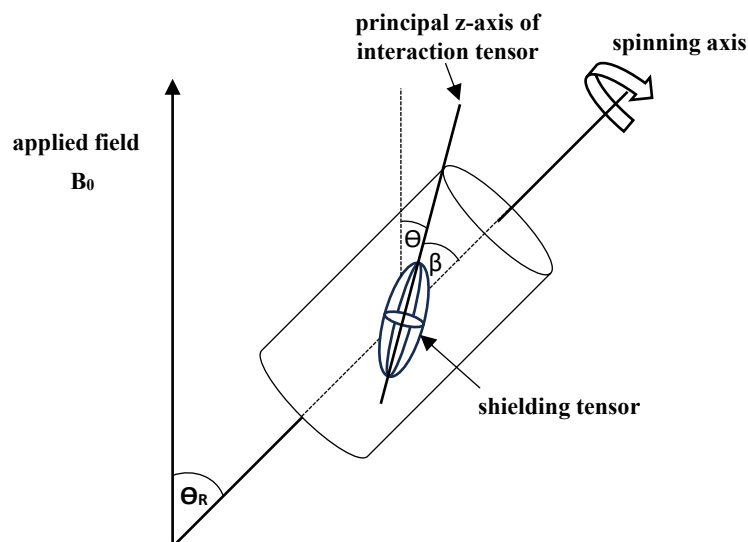


Figure 2.16. Orientation of the shielding tensor of a nuclear spin in a rotor spinning at angle θ_r to the applied field. Adapted with permission from [192]. Copyright 2005 John Wiley and Sons.

In this scenario, the average of the orientation dependence of a given magnetic interaction can be expressed as Equation (2.38).^[192]

$$\langle 3 \cos^2 \theta - 1 \rangle = \frac{1}{2} (3 \cos^2 \theta_R - 1)(3 \cos^2 \beta - 1) \quad (2.38)$$

Where β is the angle between the principal z -axis of the interaction tensor and the spinning axis.

Setting θ_R to 54.74° , the so-called magic angle, reduces Equation (2.38) to zero, removing all anisotropic interactions.^a Only the isotropic chemical shifts of the nuclear environments in the sample will appear on the NMR spectrum, making it easier to interpret. This technique is termed magic angle spinning (MAS) and is widely used in solid-state NMR to remove anisotropic interactions (chiefly CSA and dipolar coupling in the case of spin $\frac{1}{2}$ nuclei).^[192, 194]

2.2.5.6 Cross-Polarisation

Obtaining spectra of ^{13}C and ^{29}Si nuclei in the solid-state using the simple direct polarisation experiment described in Section 2.2.5.2 is challenging because their low natural abundance and relatively low gyromagnetic ratios result in spectra with a poor signal-to-noise ratio. Fortunately, a

^aThis assumes that the spin rate is sufficient so that θ averages quickly compared to the magnitude of the interaction anisotropy when expressed in frequency units.

technique called cross-polarisation (CP) is employed alongside MAS to overcome the sensitivity issues associated with dilute spins.

During the CP experiment, magnetisation is transferred from an abundant, high γ nuclei (commonly ^1H) to the dilute X spins *via* heteronuclear coupling by simultaneously irradiating both spin populations with separate radiofrequency pulses.^[192]

Maximum CP efficiency occurs when the Hartmann-Hahn condition is satisfied,^[195] as described by Equation (2.39).

$$\gamma_H B_1(^1\text{H}) = \gamma_X B_1(\text{X}) \quad (2.39)$$

Where γ_H and γ_X are the respective gyromagnetic ratios of ^1H and the X nucleus, and $B_1(^1\text{H})$ and $B_1(\text{X})$ are the strengths of the alternating magnetic fields used to irradiate the ^1H and X nuclei, respectively. In CP, the highest attainable sensitivity enhancement is γ_H/γ_X .^[192]

2.2.6 Fixed-Bed Flow-Through System

In this work, we developed a fixed-bed flow-through system for dynamic CO_2 capture testing of materials (Figure 2.17). The set-up comprises a $\frac{1}{2}$ inch diameter column packed with adsorbent material connected to two gas cylinders, one containing nitrogen and the other 400 ppm CO_2/N_2 . Prior to testing, the adsorbent is activated by heating the column using heat tape connected to a temperature controller whilst continuously purging the system with nitrogen. Meanwhile, the CO_2 concentration at the column outlet is monitored using a mass spectrometer with a sampling capillary line. Once the activation step is finished, the column's temperature is reduced to the desired adsorption temperature. Switching the gas supply from nitrogen to 400 ppm CO_2 initiates the adsorption step. water bath. To test materials under humid conditions, the CO_2 supply is directed through a bubbler placed inside a recirculating bath prior to the gas entering the column. The temperature of the column during sub-ambient DAC experiments is regulated by placing the column in the recirculating bath.

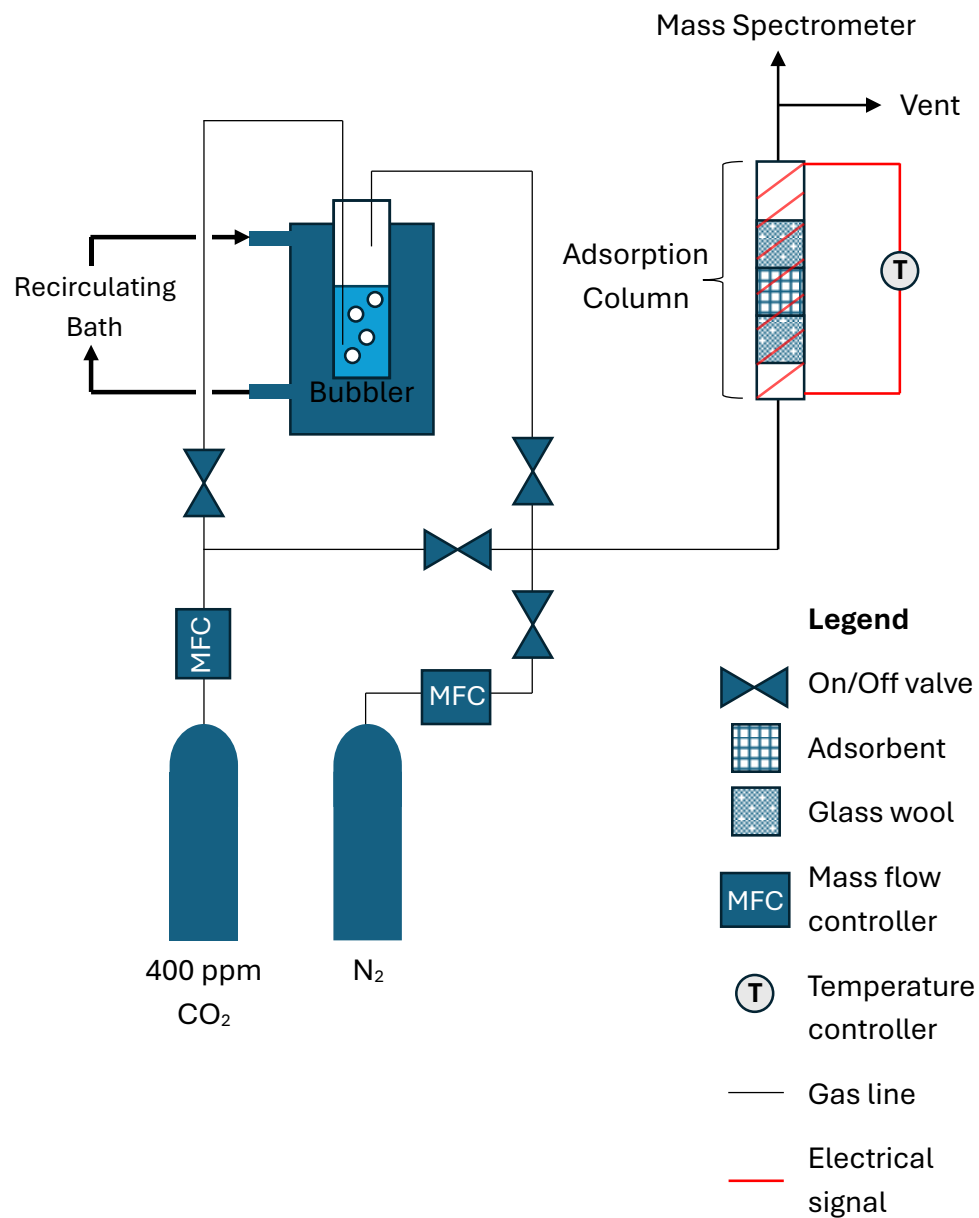


Figure 2.17. Schematic diagram of the fixed-bed flow-through system. Figure created by the author.

2.2.7 Kinetic Modelling of Adsorption

Three kinetic models from the literature are used for simulating CO₂ adsorption in this work.

The first is Lagergren's pseudo first-order model (PFO).^[196] This model assumes that the adsorption rate is proportional to the number of available active sites and is expressed mathematically by Equation (2.40).

$$\frac{\partial q_t}{\partial t} = k_f(q_e - q_t) \quad (2.40)$$

Where: q_t is the adsorption capacity at time t , q_e is the equilibrium adsorption capacity and k_f is the PFO kinetic rate constant. Integrating Equation (2.40) using the boundary conditions: $q_t = 0$ at $t = 0$ and $q_t = q_e$ as t tends towards infinity yields Equation (2.41).

$$q_t = q_e(1 - e^{-k_f t}) \quad (2.41)$$

The pseudo second-order (PSO) model assumes that the adsorption rate is proportional to the square of the number of available adsorption sites. This was first proposed by Ho *et al.* to describe the removal of heavy metal ions and dyes by adsorbents.^[197] It is expressed mathematically by Equation (2.42).

$$\frac{\partial q_t}{\partial t} = k_s(q_e - q_t)^2 \quad (2.42)$$

Where k_s is the PSO rate constant.

Integrating Equation (2.42) using the same boundary conditions as with the PFO model leads to Equation (2.43).

$$q_t = \frac{q_e^2 k_s t}{(1 + q_e k_s t)} \quad (2.43)$$

The last model considered in this work is the Avrami model. This model was originally developed for simulating the kinetics of nucleation and growth during phase changes,^[198-200] however, for some

amine sorbents, it has been found to simulate CO₂ adsorption better than the PFO and PSO models.^[201, 202] The model is described by Equation (2.44).

$$\frac{\partial q_t}{\partial t} = k_a^{n_a} \times t^{n_a-1} (q_e - q_t) \quad (2.44)$$

Where: k_a is the Avrami rate constant and n_a is the Avrami exponent.

Integration of (2.44) with the same boundary conditions as with the other models results in Equation (2.45).

$$q_t = q_e (1 - e^{-(k_a t)^{n_a}}) \quad (2.45)$$

2.3 Experimental Protocols

2.3.1 Reagents

Poly(vinyl alcohol) (PVA; $M_w = 85\text{-}124$ kDa, 87-89% hydrolysed), Ludox TMA colloidal silica (34 wt% suspension in H_2O), (3-Aminopropyl)trimethoxysilane (APS, 98.8%), N-[3-(Trimethoxysilyl)propyl]ethylenediamine (DAS, 99.1%), N1-(3-Trimethoxysilylpropyl)diethylenetriamine (TAS, 89.9%), tetraethyl orthosilicate (TEOS, 98%), Pluronic P-123, sodium chloride (NaCl), hydrochloric acid (HCl, 37%), ethanol (>99%) and toluene (99.8%) were purchased from Merck (Sigma-Aldrich) and used as received.

2.3.2 Preparation of Nanofibres

2.3.2.1 Preparation of Electrospinning Solutions

PVA was dissolved in Milli Q quality water at 80°C for 6 h under vigorous stirring. Next, the solution was left to cool down to room temperature, after which the desired amount of colloidal silica was added to form a precursor solution with a certain silica to polymer weight ratio (1:1, 2:1 or 3:1, corresponding to approximate molar ratios of 1740:1, 3480:1 and 5220:1, respectively). The total dissolved solids were kept constant at 15 wt% for all three solutions. A fourth electrospinning solution was also prepared with a 5 wt% PVA concentration using the same polymer dissolution conditions.

2.3.2.2 Description of the Electrospinning Apparatus

The electrospinning apparatus comprised an electrospinning unit (TL Pro BM, Tong Li Tech) housing a grounded collector, and a height-adjustable platform connected to a motorised gantry crane (Figure 2.18). Two collectors were used: a static aluminium plate (15 cm x 15 cm) and a rotating aluminium drum (10 cm diameter, 30 cm length). A 20 gauge blunt-ended stainless steel syringe needle (the spinneret) was inserted through a hole in the platform and connected to the electrospinning system's high voltage supply via a coaxial cable. During each run, a syringe containing the electrospinning solution of interest was connected to the spinneret via plastic tubing and clamped onto a syringe pump. During preparation of the nanofibres, the average temperature and relative humidity inside the electrospinning unit were 20°C and 50%, respectively.

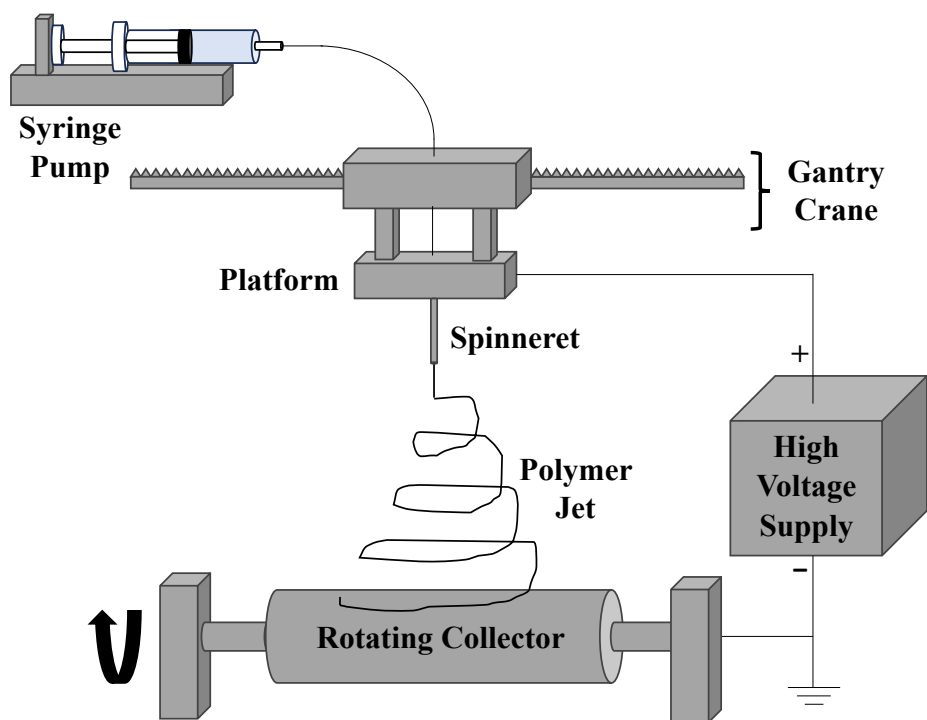


Figure 2.18. Diagram of the electrospinning set-up used in this work. Figure created by the author.

2.3.2.3 Optimisation of the Synthesis of Polymer-Silica and Silica Nanofibres

Effect of Flow Rate

The effect of the solution flow rate on the electrospinning of silica-PVA hybrid mats was investigated using the electrospinning apparatus and the 2:1 silica-to-polymer solution. Mats were synthesised using three different flow rates: 0.5, 0.75 and 1.0 ml/h. The spinneret-to-collector distance was fixed at 15 cm. Prior to each run, a dummy run was carried out, during which the applied voltage was increased until stable jetting from the spinneret was achieved. Next, 0.5 ml of solution was electrospun onto aluminium foil on top of the flat plate collector (15 cm x 15 cm) using the applied voltage from the dummy run.

Effect of Spinneret-to-Collector Distance

The effect of the spinneret-to-collector distance on the electrospinning of silica-PVA hybrid mats was investigated using the electrospinning apparatus and the 2:1 silica-to-polymer solution. Mats were synthesised using three different spinneret-to-collector distances: 10, 15 and 20 cm. The solution flow rate was fixed at 0.75 ml/min. Prior to each run, a dummy run was carried out, during which the applied voltage was increased until stable jetting from the spinneret was achieved. Next, 0.5 ml

of solution was electrospun onto aluminium foil on top of the flat plate collector (15 cm x 15 cm) using the applied voltage from the dummy run and a solution flow rate of 0.75 ml/h.

Effect of Formulation Composition

The effect of the formulation/solution composition on the electrospinning of silica-PVA hybrid mats was investigated using the electrospinning apparatus and the three silica-PVA formulations (1:1, 2:1 and 3:1 silica-to-polymer weight ratio). Mats were prepared using each formulation. During each run, the spinneret-to-collector distance, solution flow rate and applied voltage were fixed at 15 cm, 0.75 ml/h, and 23 kV respectively. Next, 2 ml of solution was electrospun onto aluminium foil on top of the grounded flat plate collector.

Effect of Calcination Temperature

The effect of calcination temperature on the preparation of silica nanofibres was investigated using precursor mats of electrospun silica-PVA mats synthesised using the 1:1, 2:1 and 3:1 silica-to-polymer formulations. Each precursor mat was prepared from 2 ml of solution electrospun on to aluminium foil on top of the flat plate collector using the electrospinning apparatus. The operating parameters were as follows: 15 cm spinneret-to-collector distance, 0.75 ml/h solution flow rate and 23 kV applied voltage.

Each precursor mat was carefully peeled off the foil and placed in a ceramic crucible inside an electrical furnace (Carbolite CWF 11/5). The furnace temperature was then ramped at 10°C/min from room temperature (*ca.* 20°C) to the desired calcination temperature (500, 700 or 900°C, air atmosphere). The furnace temperature was maintained at the calcination temperature for 2 h before automatically shutting off. The mats were removed from the furnace after it had cooled down to room temperature.

Preparation of Silica Nanofibres using the Rotating Collector

Larger mats of silica nanofibres were prepared from the electrospinning of silica-polymer solutions onto the rotating metal drum collector in lieu of the flat plate collector. During a typical run, 6 ml of formulation (1:1 or 2:1) was electrospun onto foil wrapped around the rotating collector (60 RPM angular velocity) using the electrospinning apparatus. The operating conditions were as follows: 15 cm spinneret-to-collector distance, 0.75 ml/h solution flow rate and 23 kV applied voltage. The motorised gantry moved the spinneret axially back and forth across the drum (1 cm/s scan speed) to ensure an even coating of nanofibres on the foil.

The precursor mats were cut in half, and each half folded several times to improve handleability. Next, the mats were placed inside the electrical furnace and calcined in air at 700°C for 2 h (10°C/min ramp rate). The mats were then removed from the furnace after it had cooled down to room temperature.

2.3.2.4 Preparation of Nanofibrous Silica for Characterisation and Amine Functionalisation

Multiple mats of nanofibrous silica were prepared for characterisation and subsequent amine functionalisation as follows. Using the electrospinning apparatus, 6 ml of 2:1 silica-PVA formulation was electrospun onto aluminium foil wrapped around the rotating collector (60 RPM, 1 cm/s scan speed). The operating conditions were: 15 cm spinneret-to-collector distance, 0.75 ml/h solution flow rate and 23 kV applied voltage.

Each precursor mat was cut in half, and each half folded several times to improve handleability. Next, the mats were placed inside the electrical furnace and calcined in air at 700°C for 2 h (10°C/min ramp rate). The mats were then removed from the furnace after it had cooled down to room temperature.

2.3.2.5 Preparation of PVA Nanofibres

A mat of PVA nanofibres was prepared as follows. Using the electrospinning apparatus, 6 ml of 5 wt% PVA solution was electrospun on to aluminium foil wrapped around the rotating collector (60 RPM, 1 cm/s scan speed). The operating conditions were: 15 cm spinneret-to-collector distance, 0.75 ml/h solution flow rate and 19 kV applied voltage. The mat was cut in half, and each half folded several times to improve handleability.

2.3.3 Preparation of SBA-15

SBA-15 mesoporous silica was synthesised following the established procedure from the literature^[164] with the addition of sodium chloride to obtain a highly ordered, hydrothermally stable material.^[203] Pluronic P-123 triblock polymer (2.0 g) and NaCl (5.0 g) were dissolved in 2M aqueous HCl (62.5 ml) at room temperature in a 250 ml polypropylene bottle. Next, TEOS (4.23 ml) was added dropwise, and the mixture was left to stir at 40°C for 20 h. After that, the mixture was aged in a hydrothermal vessel at 90°C for 24 h and then filtered. The obtained precipitate was washed with copious amounts of Milli-Q quality water, dried in an oven at 40°C overnight, and calcined at 550°C for 6 h.

2.3.4 Surface Functionalisation of Silica

Samples of silica were grafted with three different silane coupling agents (APS, DAS and TAS) using a procedure adapted from the literature.^[57, 204-206] Each grafting run used either one folded mat of nanofibrous silica (*ca.* 300 mg) or 100 mg of SBA-15.

Before modification, the silica was dried in an electric oven for 3 h at 110°C. The desired volumes of toluene ($100 \text{ ml}_{\text{toluene}}/\text{g}_{\text{silica}}$), aminosilane ($0.6\text{-}5.0 \text{ ml}_{\text{silane}}/\text{g}_{\text{silica}}$) and Milli-Q quality water (0 or $0.6 \text{ ml}_{\text{water}}/\text{g}_{\text{silica}}$) were combined in a 50 ml round-bottomed flask and stirred for 10 minutes. After that, the dried silica was immersed in the reaction mixture and grafted at 85°C for 2 h under reflux (atmospheric pressure). The functionalised material was washed with 250 ml of ethanol in a Büchner funnel and left to air-dry in a fume hood for 48 h.

To investigate the effect of the silane concentration on the resulting silane loading, silica mats were grafted under hydrous conditions using four different volumes of silane added; 0.6, 1.2, 2.5 and 5.0 $\text{ml}_{\text{silane}}/\text{g}_{\text{silica}}$. Additionally, two mats were grafted under anhydrous conditions using two different volumes of silane added (2.5 and 5.0 $\text{ml}_{\text{silane}}/\text{g}_{\text{silica}}$). A sample of SBA-15 was also grafted under hydrous conditions using 5.0 $\text{ml}_{\text{silane}}/\text{g}_{\text{silica}}$.

The corresponding amount of silane added was obtained using Equation (2.46).

$$\text{Amount of Silane Added} = \frac{V_{\text{silane}} \cdot \rho_{\text{silane}} \cdot P_{\text{silane}}}{M_{\text{silane}}} \cdot 100 \quad (2.46)$$

Where V_{silane} is the volume of silane added ($\text{ml}/\text{g}_{\text{silica}}$), and ρ_{silane} , P_{silane} and M_{silane} are the density, purity and molar mass of the silane, respectively.

Lists of the materials prepared for Chapter 3 and Chapter 4 are in shown in Table 2.1 and Table 2.2, respectively.

Table 2.1. List of amine-functionalised silicas prepared for Chapter 3. NFS = Nanofibrous silica.

Material	Silane Type	Silica Type	Volume of Water Added (ml _{water} /g _{silica})	Amount of Water Added (mmol _{water} /g _{silica})	Volume of Silane Added (ml _{silane} /g _{silica})	Amount of Silane Added (mmol _{silane} /g _{silica})		
1	APS	NFS	0.6	33	0.6	3.4		
2					1.2	6.8		
3					2.5	14.2		
4					5.0	28.4		
5					0	0	2.5	14.2
6							5.0	28.4
7		SBA-15	0.6	33	5.0	14.2		
8	DAS	NFS	0.6	33	0.6	2.8		
9					1.2	5.5		
10					2.5	11.5		
11					5.0	23.0		
12	TAS	NFS	0.6	33	0.6	2.1		
13					1.2	4.2		
14					2.5	8.7		
15					5.0	17.4		

Table 2.2. List of amine-functionalised nanofibrous silicas prepared for Chapter 4. All materials were grafted under hydrous conditions (0.6 ml_{water}/g_{silica}).

Material	Silane Type	Amine Loading (mmol _N /g _{sample})	Volume of Silane Added (ml _{silane} /g _{silica})	Amount of Silane Added (mmol _{silane} /g _{silica})
1	APS	1.2	0.6	3.4
2		2.6	2.5	14.2
3		3.2	5.0	28.4
4	DAS	1.4	0.6	2.8
5		2.2	1.2	5.5
6		2.6	2.5	11.5
7		3.7	5.0	23.0
8	TAS	2.1	0.6	2.1
9		2.6	1.2	4.2
10		4.9	2.5	8.7
11		6.4	5.0	17.4
12		7.4	5.0	17.4

2.3.5 Scanning Electron Microscopy

Scanning electron microscopy (SEM) images were recorded on a Zeiss Gemini 300 scanning electron microscope using an accelerating voltage of 2 kV.

2.3.6 Fibre Diameter Distribution

The fibre diameter distributions were obtained using the GIFT plug-in on ImageJ. Three SEM images per sample were inputted into the macro, and the resulting histogram files were combined. Recorded widths below 100 nm and above 500 nm were assumed to be erroneous and were removed from the

dataset. The average fibre diameter and standard deviation were found by fitting a Gaussian function to each distribution on Origin Pro.

2.3.7 Characterisation of the Electrospinning Solutions

The dynamic viscosity of the electrospinning solutions was measured using a Discovery HR-2 hybrid rheometer (TA instruments) with a 40 mm parallel plate geometry. Stress measurements were recorded between shear rates of 0.1 and 100 s⁻¹ at 20°C. The viscosity was obtained from the linear best fit of the resulting graph.

Surface tension measurements were taken at 20°C using an OCA 50 fully automatic contact angle and contour analysis instrument (DataPhysics Instruments). A droplet of solution was vertically suspended on a syringe needle tip. An image of the droplet was then recorded, and the ‘Pedant Drop’ method was used to calculate the surface tension based off the drop geometry and solution density (measured using an Anton Paar DMA 4100 M Density Meter).

Solution conductivities were measured at 20°C using a Jenway 4510 Conductivity Meter. Prior to measurement, the conductivity meter was calibrated using a 0.1 M aqueous solution of potassium chloride. Next, 50 ml of solution was dispensed into a 100 ml glass beaker and placed in a thermostatically-controlled water bath with a preset temperature of 20°C. A mercury thermometer was used to monitor the temperature of the solution. Once the temperature had stabilised at 20°C, the probe was immersed in the solution and the reading on the conductivity meter was recorded. Between measurements, the probe was washed with copious amounts of Milli-Q quality water.

2.3.8 Thermogravimetric Analysis

The thermal stability of the synthesised materials was studied using an SDT 650 thermal analysis instrument (TA instruments). During each run, 5 mg of material was placed inside a 90 µL alumina cup and heated from 25 to 900°C at a ramp rate of 10°C/min under Argon purge flow. Thermograms were recorded using TRIOS software (TA instruments). The onset temperature of a weight change was obtained using the analysis tools in the application.

The silane loading per gram of silica (mmol_{silane}/g_{silica}) was calculated using Equation (2.47).

$$\text{Silane Loading} = \frac{m(200^\circ\text{C}) - m(900^\circ\text{C})}{m(900^\circ\text{C})} \cdot \left(\frac{1000}{M_R}\right) \quad (2.47)$$

Where: $m(200^\circ\text{C})$ and $m(900^\circ\text{C})$ are the respective sample weights at 200 and 900°C, and M_R is the molar mass of the silane’s R-group.

Three TGA runs per sample were recorded and the triplicate average of the silane loading was computed.

The grafting efficiency (%) was obtained from Equation (2.48). For the derivation of ‘amount of silane added, see Equation (2.46).

$$\text{Grafting Efficiency} = \frac{\text{Silane Loading}}{\text{Amount of Silane Added}} \cdot 100 \quad (2.48)$$

The triplicate average amine loading per gram of sample ($\text{mmol}_N/\text{g}_{\text{sample}}$) was found from Equation (2.49) using the same TGA data as that used for calculating silane loading.

$$\text{Amine Loading} = \frac{m(200^\circ\text{C}) - m(900^\circ\text{C})}{m(200^\circ\text{C})} \cdot \frac{n_{\text{amine}}}{n_{\text{silane}}} \quad (2.49)$$

Where $n_{\text{amine}}/n_{\text{silane}}$ is the molar ratio of amine groups to silane (1, 2 and 3 for APS, DAS and TAS, respectively).

2.3.9 Fourier Transform Infrared Spectroscopy (FTIR)

FTIR spectra were recorded on a Bruker Vertex 70 spectrometer equipped with a Specac Golden Gate diamond attenuated reflectance (ATR) accessory. During each run, enough sample was placed on the ATR stage to cover the diamond. A clamp was used to press the sample against the diamond to ensure good physical contact between the two and thereby maximise the intensity of the recorded signal. A total of 64 scans were recorded per spectrum, with a wavenumber range of 650 to 4000 cm^{-1} and a resolution of 2 cm^{-1} . A background spectrum was also recorded using the same parameters and subtracted from the sample spectrum. After data acquisition, a baseline correction was applied to the spectrum using Bruker OPUS 7.8 software.

2.3.10 Solid-state Nuclear Magnetic Resonance Spectroscopy

In Chapter 3, ^{13}C and ^{29}Si solid-state spectra were acquired using a Bruker 300 MHz Avance III spectrometer with a 4 mm double-resonance probe at frequencies of 300.13 MHz for ^1H , 75.46 MHz for ^{13}C and 59.63 MHz for ^{29}Si . Samples were packed in 4 mm zirconia rotors and sealed with Kel-F caps.

^{13}C solid-state spectra were recorded using the cross-polarisation with magic angle spinning (CP/MAS) pulse program at 25°C and a MAS rate of 10 kHz. The ^1H 90° pulse and Hartmann-Hahn condition were optimised using hexamethylbenzene. A total of 4096 scans were recorded, with a recycle delay of 5 s. Chemical shifts were recorded relative to tetramethylsilane (TMS).

^{29}Si CP/MAS solid-state spectra were recorded at 25°C using a MAS rate of 4 kHz. The ^1H 90° pulse and Hartmann-Hahn condition were optimised using kaolinite. A contact time of 2 ms was used and a total of 4096 scans were recorded, with a recycle delay of 10 s. Chemical shifts were recorded relative to TMS.

^{29}Si direct polarisation experiments were conducted at 25°C using a MAS rate of 4 kHz, a $4.2\ \mu\text{s}$ 90° pulse length and a 180 s recycle delay. A total of 512 scans were recorded.

Baseline and phase corrections were applied for all recorded spectra using Bruker Top Spin 4.1.4.

2.3.11 N_2 Physisorption

N_2 adsorption-desorption isotherms were recorded at 77 K using a Quantachrome Autosorb iQ instrument (Anton Paar). Specific surface areas were calculated using the Brunauer-Emmet-Teller (BET) method for datapoints recorded between 0.05 and 0.2 relative pressure (P/P_0). Total pore volume was derived from the adsorption datapoint closest to unity ($P/P_0 = 0.99$), whilst the mesopore size distribution and mean pore size were obtained using the Barrett-Joyner-Halenda (BJH) method for desorption datapoints at relative pressures greater than 0.35.

2.3.12 Small Angle X-ray Scattering

Small angle X-ray scattering (SAXS) measurements were obtained using a Rigaku Smartlab diffractometer equipped with a Cu-K α 1 radiation source (1.54059 Å wavelength). X-rays were generated using an accelerating voltage of 40 kV and a current of 50 mA. SAXS data were recorded between 2θ scattering angles of 0.5° and 8° , with a step width of 0.02° and scanning speed of $0.75^\circ/\text{min}$.

2.3.13 CO_2 Gravimetric Experiments

Gravimetric CO_2 adsorption isotherms were collected using a thermogravimetric analyser (TGA 550, TA Instruments). During a typical run, *ca.* 5 mg of material was placed on a platinum basket and loaded into the furnace. To activate the sample, the furnace was heated to 110°C ($10^\circ\text{C}/\text{min}$ ramp rate) and held at that temperature for 3 h under continuous N_2 flow (60 ml/min). Next, the sample was cooled down to the desired adsorption temperature. To ensure the sample weight had stabilised

prior to the experiment, the sample was kept at the adsorption temperature for 30 minutes under nitrogen flow. After that, the feed gas was switched from N₂ to 400 ppm CO₂/N₂ (60 ml/min) and left for the desired adsorption time. For single adsorption runs, the experimental time was three hours.

To assess the regenerability of amine-grafted silica nanofibers, several samples were subjected to five consecutive adsorption-desorption cycles, using a combination of a temperature-swing and nitrogen sweep for the regeneration step. Prior to testing, the sample was degassed at 110°C for 3 h in nitrogen. During the first cycle, the sample was cooled down and held at 25°C for 10 minutes under N₂ flow. Next, the material was exposed to 400 ppm CO₂/N₂ for 1 h. The feed gas was subsequently switched back to nitrogen and the sample was regenerated at 110°C for 1 h. The same adsorption-desorption sequence was repeated four times.

The CO₂ adsorption capacity at time t was calculated using Equation (2.50).

$$q_t = \frac{m_t - m_0}{m_0} \times \frac{1000}{44} \quad (2.50)$$

Where q_t = CO₂ adsorption capacity (mmolCO₂/g_{sample}), m_t = sample mass at time t and m_0 = initial sample mass after degasification.

The amine efficiency was obtained from Equation (2.51).

$$AE = \frac{q_f}{L_N} \quad (2.51)$$

Where: AE = amine efficiency (mmolCO₂/mmol_N), q_f = final adsorption capacity (mmolCO₂/g_{sample}) and L_N = amine loading of the material (mmol_N/g). For the derivation of the amine loading, see Equation (2.49) in Section 2.3.8.

The initial adsorption rate (IAR) was found using the ‘Tangent’ app on Origin Pro 2016. A tangent was drawn at the beginning of the linear segment of the isotherms and the IAR was obtained from the gradient of the tangent.

2.3.14 Fixed-Bed Column Experiments

A purpose-built fixed bed flow-through system was assembled for studying adsorption dynamics under simulated DAC conditions (see Section 2.2.6 for description of the set-up). Approximately 100 mg of amine-functionalised silica nanofibres was packed into the reactor. Two plugs of fibre glass were inserted into either end of the column and used to compress the adsorbent until there was

no change in its volume. The reactor was then wrapped in heat tape and connected to the flow-through system. Nitrogen (200 SCCM^b) was passed through the reactor for 10 minutes to flush out laboratory air. Next, the reactor was heated to 110°C. Meanwhile, the CO₂ concentration of the column effluent was monitored using a mass spectrometer (Pfeifer Vacuum Thermostar). The adsorbent was held at 110°C until the concentration stabilised at its minimum level under nitrogen flow or 30 minutes had elapsed, whichever came last. After that, the column was left to cool down to the desired adsorption temperature. For adsorption temperatures at or above 25 °C, the temperature controller was used to adjust the power of the heat tape to achieve the target temperature. For adsorption temperatures below 25°C, the heat tape was removed, and the reactor placed vertically in a jacketed beaker filled with ethylene glycol/water mixture (1:1 vol). Ethylene glycol/water was pumped through the cavity of the beaker from a refrigerated recirculating bath at the desired temperature. The reactor was allowed to equilibrate at the target temperature for 45 minutes. After that, the feed gas was switched from nitrogen to the 400 ppm CO₂ (N₂ balance). The concentration of CO₂ in the effluent was then recorded until it had plateaued out at the partial pressure of adsorbate in the feed gas (400 ppm).

Equation (2.52) was used to calculate the adsorption capacity of the sample at time t into the adsorption experiment.^[105]

$$q_t = \frac{\dot{n}}{m_{\text{sorbent}}} \left[\int_{t=0}^t C_0 - C_t \cdot dt - \int_{t=0}^t C_0 - C_{t,\text{blank}} \cdot dt \right] \quad (2.52)$$

Where: q_t = CO₂ adsorption capacity at time t (mmolCO₂/g_{sample}), \dot{n} = molar flow rate of the gas stream (mmol/min), m = sample mass (g), C_0 = CO₂ concentration in the feed gas (400 ppm), C_t = CO₂ concentration in the column outlet at time t, $C_{t,\text{blank}}$ = CO₂ concentration at time t during a blank run conducted at the same flow rate as that used for the experiment (ppm).

For the fixed-bed tests, the pseudo-equilibrium capacity, corresponding to CO₂ uptake when the column outlet CO₂ concentration is 95% of the inlet ($C/C_0 = 0.95$), was used as the final adsorption capacity during each run, as it would be impractical to allow the adsorbent to reach true equilibrium during each cycle in a real-world DAC system.^[142, 207]

The process performance of the adsorbents was evaluated by calculating the CO₂ extraction rate (\dot{q}) and capture fraction (f) at pseudo-equilibrium, using Equations(2.53) and (2.54), respectively.

$$\dot{q} = \frac{q_{0.95}}{t_{0.95}} \cdot 60 \quad (2.53)$$

^b SCCM – standard cubic centimeters per minute (1 SCCM = 1 cm³STP/min)

$$f = \frac{q_{0.95} m_{\text{sorbent}}}{t_{0.95} \dot{n}} \quad (2.54)$$

Where: $q_{0.95}$ is the pseudo-equilibrium capacity (mmolCO₂/g_{sample}) and $t_{0.95}$ is the pseudo-equilibrium time (min).

2.3.15 Kinetic Modelling

Using Origin Pro software, three kinetics models were fitted to the adsorption data from the fixed-bed experiment: pseudo-first order (PFO), pseudo-second order (PSO) and Avrami, corresponding to Equations (2.55), (2.56) and (2.57), respectively.

$$q_t = q_e(1 - e^{-k_f t}) \quad (2.55)$$

$$q_t = \frac{q_e^2 k_s t}{(1 + q_e k_s t)} \quad (2.56)$$

$$q_t = q_e(1 - e^{-(k_a t)^{n_a}}) \quad (2.57)$$

Where: q_e is the amount of adsorbed CO₂ at equilibrium, k_f , k_s and k_a are rate constants for the PFO, PSO and Avrami models respectively, and n_a is Avrami exponent. The goodness of fit of each model was assessed using the computed coefficient of determination (R^2). Further information about the kinetic models can be found in Section 2.2.7.

2.3.16 Solid-State NMR Studies of CO₂ Adsorption

The procedure for sample preparation was as follows. Approximately 100 mg of sample was packed inside the adsorption column used in the fixed-bed tests and then connected to the flow-through system (see Section 2.2.6 for details). Next, the sample was degassed for 30 min at 100°C under N₂ flow (200 SCCM). The column was then cooled down to the desired adsorption temperature and the feed gas switched from nitrogen to 400 ppm CO₂/N₂. Once the column outlet CO₂ concentration reached that of the inlet, the adsorbent was removed from the column, packed immediately inside a 4 mm zirconia rotor and inserted into the spectrometer. One sample was removed from the adsorption column straight after the outgassing step.

^{13}C solid-state NMR spectra were collected using a Bruker 400 MHz Avance III spectrometer with a 4 mm triple-resonance probe at frequencies of 400.23 MHz for ^1H and 100.64 MHz for ^{13}C .

The ^1H - ^{13}C CP/MAS pulse program was used at a MAS rate of 10 kHz. The ^1H 90° pulse and Hartmann-Hahn condition were optimised using hexamethylbenzene. A total of 8192 scans were recorded, with a contact time of 2 ms and recycle delay of 5 s. Chemical shifts were recorded relative to TMS.

2.3.17 Equations Used for Comparing Amine-Functionalised Nanofibrous Silica with other Grafted Silicas from the Literature

The pore fill fraction of each grafted material (%) was found using Equation (2.58).

$$\text{Pore Fill Fraction} = \frac{TPV_{\text{support}} - TPV_{\text{grafted}}}{TPV_{\text{grafted}}} \quad (2.58)$$

Where: TPV_{support} and TPV_{grafted} are the total pore volumes of the bare support and the grafted material, respectively.

The amine coverage of each grafted material ($\mu\text{mol}_\text{N}/\text{m}^2_{\text{support}}$) was obtained from Equation (2.59).

$$\text{Amine Coveage} = \frac{L_N}{S_{\text{support}}} \cdot 1000 \quad (2.59)$$

Where L_N is the amine loading and S_{support} is the specific surface area of the bare support.

3 Synthesis and Characterisation of Functionalised Nanofibres

3.1 Overview of Electrospun Materials for CO₂ Capture

To date, an array of electrospun materials have been studied for CO₂ capture. The fabrication of porous polymer adsorbents typically involves the electrospinning of a polymer or polymer linkers with a pore-forming auxiliary polymer such as poly(vinylpyrrolidone) (PVP).^[208, 209] Curing of the mat, along with selective removal of the secondary polymer *via* dissolution or pyrolysis, results in the formation of rough-textured porous polymer nanofibres. For examples, Zhang *et al.* prepared porous poly(acrylonitrile) (PAN) via the electrospinning of a mixture of PAN and PVP. Selective removal of the latter polymer via hot immersion in water resulted in an enhancement in total pore volume and specific surface area by an order of magnitude (0.01 to 0.2 cm³/g and 5 to 50 m²/g respectively).^[208] Such materials are commonly functionalised with amine-bearing chemicals to improve their CO₂ selectivity and uptake capacity.^[208, 210, 211] Zainab and co-workers found that the impregnation of low molecular weight branched poly(ethylenimine) (bPEI) on to porous poly(styrene)/poly(urethane) nanofibrous mats enhanced the TGA CO₂ adsorption capacity of the nanofibres by up to a factor of five. However, the total pore volume and specific surface area decreased as a function of amine loading. Thus, there existed an optimal loading at which maximal uptake was achieved before pore blockage impeded CO₂ mass transfer into the nanofibres.^[211]

Porous carbon nanofibres are another widely studied group of electrospun materials for carbon capture. In general, these materials are synthesised *via* several steps. Firstly, electrospinning of a precursor polymer. Secondly, stabilisation of the nanofibres between 200 and 300 °C in zero grade air. This causes a change in configuration of the polymer from linear chains to cross-linked structures. Lastly, carbonisation in an inert atmosphere, which causes the thermal decomposition of functional groups whilst simultaneously increasing the carbon content. Often, the carbonised material is then subjected to physical or chemical activation, which enhances the specific area and microporosity of the material.^[212] In place of activation, an auxiliary polymer may also be incorporated into the precursor nanofibres which is then selectively removed prior to carbonisation to create porosity.^[213] Physisorption chiefly underpins the interaction of CO₂ with carbon nanofibrous adsorbents.^[214, 215]

The properties that determine the CO₂ adsorption potential of carbon nanofibres is a subject of debate. On the one hand, the nitrogen content is considered more important, since residual nitrogen functionalities on carbonised fibres like imines, pyrroles, pyridines, amides and quaternary amines are mildly basic, which may enhance the affinity of the sorbent towards CO₂ which is a Lewis acid^[214, 215]. Increasing the nitrogen content of porous carbon nanofibres can be achieved by using nitrogen-rich polymers like PAN^[214], a higher stabilisation temperature^[214], lower carbonisation and activation temperatures^[215] or doping the nanofibres with nitrogenous compounds prior to carbonisation.^[212] It has been shown that the nitrogen content *per se* does not correlate with CO₂ uptake, rather the proportions of different nitrogen groups. Maruccia *et al.* prepared two PAN-derived

carbon nanofibrous materials that had differing nitrogen contents and found that the lower nitrogen-loaded material had a higher CO₂ TGA capacity. This was attributed to the higher proportion of quaternary ammonium groups (NQ) in the material.^[214] Other studies contend that the textural properties of the materials, namely their microporosity and pore size, has a greater influence on the adsorption behaviour of carbon nanofibres. Greater micropore volume and smaller mean pore size have been correlated with greater CO₂ uptake.^[212, 216, 217] Indeed, in one study, carbon nanofibres were prepared from a resin with negligible nitrogen functionalities and were found to have over double the volumetric CO₂ capacity of benchmark PAN-derived nanofibres (2.9 and 1.2 mmol/g respectively, volumetric method, 1 bar CO₂, 25°C).^[216] Meanwhile, Jeong *et al.* found that which property influences sorption more was pressure dependent, with surface basicity playing a greater role at CO₂ pressures below 0.4 bar whilst textural properties were more influential between 0.4 and 1 bar.^[218] Notwithstanding, as with porous polymers, introducing strongly nucleophilic amines on to carbon nanofibres greatly increases the capacity, since amines chemically react with CO₂, endowing carbon nanofibres with a higher heat of adsorption.^[219] Doping electrospun polymers with inorganic compounds and carbon nanotubes has been demonstrated to also enhance CO₂ uptake whilst concomitantly improving the mechanical stability of the resulting mat.^[220, 221]

Inorganic nanofibrous materials have also been studied for CO₂ capture.^[222-224] Typically, the inorganic material of interest, or a soluble precursor, is electrospun with a structure-directing polymer. The resultant mat is then calcinated to remove the template and yield purely inorganic nanofibers. Unlike carbon nanofibers, the reported inorganic mats are mesoporous rather than microporous and possess surface areas on the order of 10 m²/g as opposed to 100 m²/g. As result, the reported capacities of these materials at ambient temperatures are much lower. For example, a nanofibrous material comprised of MgO-Mg(OH)₂ exhibited a pseudo-equilibrium capacity of 0.9 mmol/g (TGA, 100 % CO₂, 30°C) compared to 2.9 mmol/g for resin-derived carbon nanofibers under similar conditions.^[216, 224] Inorganic nanofibers have been demonstrated as a viable material for integrated CO₂ capture. Meng *et al.* prepared TiO₂ nanofibres on which they deposited Ni(OH)₂. It was demonstrated that the material could simultaneously capture and reduce CO₂ *via* photocatalysis into value-added products such as methane and methanol.^[222]

The strategy of using organic nanofibers as supports for CO₂-philic substances has also been explored in the production of self-standing metal organic framework (MOF) materials for CO₂ capture.^[225-227] MOF particles are either electrospun with a structure-directing polymer or crystals are grown on an electrospun support. Electrostatic attraction between open metal sites and the adsorbate together with van der Waals forces are the mechanisms responsible for CO₂ binding for this class of material. As with carbon nanofibers, MOF-based nanofibers have high specific surface areas on the order of 100 - 1000 m²/g and a large volume of micropores, which, together with their favourable surface chemistry, provides them with some of the highest adsorption capacities of electrospun sorbents.^[225-227] Chiang *et al.* studied the zinc-based MOF ZIF-8 deposited on PAN nanofibers and found the

volumetric CO₂ loading at 1 bar and 25°C was over a third higher than benchmark PAN-derived carbon nanofibers (4.2 and 2.9 mmol/g, respectively). Remarkably, the ZIF-8 nanofibers outperformed pristine ZIF-8 (0.88 mmol/g, 1 bar, 25°C), despite the latter having a higher specific surface area, suggesting nanofibers endow better accessibility to active sites for CO₂ adsorption compared to MOFs in their powdered form.^[227]

Despite the plethora of electrospun materials investigated to date, most publications evaluate the sorption behaviour using a pure feed of CO₂.^[208, 211, 214, 220, 221, 224] There are only a few papers that study the sorption behaviour of electrospun sorbents under dilute gas mixtures relevant to CO₂ capture applications such as post-combustion capture (10 – 15% CO₂) and direct air capture (*ca.* 400 ppm). Concerning flue gas capture, some of the papers that discuss this application quote the equilibrium CO₂ capacity from volumetric isotherm data at a pressure corresponding to that from a flue gas feed (0.15 bar).^[215, 216, 227] For evaluating the suitability of a material for CO₂ capture, understanding CO₂ selectivity is essential since competition between CO₂ and other gases for active sites will compromise the working capacity of the adsorbent in real-world applications, and also effect the purity of the captured CO₂.^[228] Some papers have attempted to address this by quantifying CO₂/N₂ selectivity from volumetric adsorption isotherms whilst others have studied adsorption behaviour in dry, binary mixtures of CO₂/N₂.^[214, 217] However, there is a lack of understanding of the interactions of other gaseous components in flue gases with electrospun sorbents, such as water vapour and oxygen, and how they impact sorbent regenerability.

There are no reports on the application of any of the main categories of porous electrospun materials for DAC (*e.g.*, porous polymers, carbon nanofibres, inorganic, MOFs). Many of the electrospun materials discussed so far are physisorbents which generally perform poorly under ultra-dilute conditions owing to their low isosteric heat of adsorption and poor selectivity over water.^[77] Indeed Jeong *et al.* simulated the CO₂ capture performance of melamine-doped carbon nanofibres and showed that the uptake capacity was only 0.01 – 0.02 mmol/g for a 1% CO₂ gas feed, regardless of the nitrogen loading of the material.^[218] This suggests that the nitrogen functional groups in porous carbon nanofibres are insufficiently basic to remove CO₂ from ultra-dilute gas streams.

The reported nanofibrous materials that have been studied for DAC typically incorporate reactive compounds into an inert polymeric support. Armstrong *et al.* prepared mats comprising poly(styrene) and poly(ethylene oxide) (PEO) nanofibres embedded with a CO₂-reactive ion exchange resin (IER). To endow the matrix with porosity, the PEO polymer was selectively removed *via* immersion of the material in aqueous sodium hydroxide, which also activated the IER particles. The porous material exhibited rapid uptake of CO₂ from dry air, with an adsorption half-time of 10 minutes. Introduction of porosity greatly enhanced sorbent utility from 50% for the as-spun dense mat to 90% for its porous equivalent. It is worth noting that a closed loop system was used in this work, which is unrepresentative of a direct air capture system.^[133] Korah *et al.* investigated the incorporation of the amino acid arginine into electrospun poly(vinyl alcohol) nanofibres for DAC. After steam activation,

the material successfully removed CO₂ from air *via* chemisorption onto the basic functional groups in the amino acid (amines and guanidines). Increasing the gas feed humidity enhanced adsorption, however, the structural integrity of the material was compromised due to PVA's solubility in water. As a result, there was a deterioration in the uptake behaviour when the material was cycled^c.^[229] The regenerability of a sorbent is a crucial metric for DAC since the sorbent capital cost comprises the biggest expense for industrial air capture using a solid sorbent, as discussed in Section 1.1.3 of Chapter 1.

In general, there is limited data on the influence of temperature on adsorption capacity and uptake kinetics of electrospun adsorbents. This information is particularly crucial in assessing the viability of sorbents for DAC, since air temperature varies temporally and spatially across the planet.^[25]

As mentioned in the main literature review in Chapter 1, the most widely studied adsorbents for ambient air removal of CO₂ are amine-functionalised materials. Viable supports for synthesising amine-supported sorbents for DAC have high surface areas and porosities to maximise the available area for functionalisation, facilitate good dispersion of the amine-bearing compound and facilitate high active site accessibility during CO₂ adsorption. Porous silicas are a popular support, owing to their high surface areas, wide array of pore architectures and favourable surface chemistry for amine functionalisation. However, as revealed in the literature review in Chapter 1, most amine-functionalised adsorbents from the literature are powders, which are impractical for industrial scale-up.

The preparation of electrospun-derived silica nanofibres has been reported in the literature.^[230-232] However, their chemical modification and potential application as substrates for DAC has not been explored. To this end, this chapter will study the synthesis and amine functionalisation of silica nanofibres in preparation for DAC testing. Electrospinning conditions will be optimised to produce mats with the best physiochemical properties for amine grafting. Then, samples of optimised silica mats will be functionalised with amine functional groups, and the impact of changing various grafting parameters on the properties of the resulting material will be studied.

^c There is no quantitative data in the publication on the regenerability of the sorbent.

3.2 Optimisation of the Synthesis of Silica Nanofibres

In this work, the protocol for the synthesis of silica nanofibres is based on a study by Kanehata *et al.*^[231] They synthesised templated silica *via* the electrospinning of aqueous blends of poly(vinyl alcohol) and colloidal silica, followed by calcination to remove the polymer template. The resulting nanofibres were composed of aggregated silica nanoparticles. Varying the silica particle size altered the textural properties of the nanofibres, with specific surface area and total pore volume decreasing and pore diameter increasing with particle diameter. The highest surface area and pore volume was achieved using colloidal silica with a particle diameter of 15 nm (270 m²/g, 0.66 cm³/g). These nanofibres had a pore diameter of 8.8 nm, meaning the material was mesoporous. The mesoporosity of the nanofibres, together with their facile synthesis, inspired this study to investigate the production of silica nanofibres using polymer-colloidal silica blends. For the silica source, we selected Ludox TMA colloidal silica (22 nm average particle diameter). This particular colloidal silica is stabilised without the use of counterions and contains low levels of sodium, meaning that silica nanofibres produced from this reagent should contain negligible amounts of impurities.^[233] For the template, we used poly(vinyl alcohol) with a molecular weight close to that used by Kanehata *et al.*

Since the reagents and the electrospinning equipment differ from the study by Kanehata *et al.*, we sought to optimise the synthesis procedure to produce the highest quality nanofibres (defect-free, narrow fibre diameter). Regarding the electrospinning process parameters, flow rate and spinneret-to-collector distance and applied voltage were the key variables that needed optimising. Due to the interrelationship between applied voltage and the latter two parameters,^[144] the voltage had to be constantly adjusted to achieve stable jetting during optimisation of the flow rate and spinneret-to-collector distance. Therefore, the optimal voltage was that which produced stable electrospinning at the optimal flow rate and spinneret-to-collector distance. Parameter optimisation was conducted using an electrospinning solution containing a silica-PVA weight ratio of 2:1, which is a similar blend composition to that used by Kanehata *et al.* and another study on electrospun silica-PVA composites.^[234]

Blend composition and calcination temperature have been shown to influence the morphology and mechanical properties of silica nanofibres.^[234] To this effect, two other silica-PVA blends (1:1 and 3:1) were electrospun to understand the influence of the formulation composition on the resulting nanofibres. Samples of silica-PVA nanofibres from all three blends were then calcinated at three different temperatures (500, 700 and 900°C) to remove the polymer template. A blend and temperature that produced the best mat with respect to nanofibre quality and handleability were then selected.

3.2.1 Effect of Flow Rate

Using the flat plate collector and a spinneret-to-collector distance fixed at 15 cm, there is a positive correlation between the syringe pump flow rate and the voltage required for stable electrospinning (Figure 3.1). To achieve stable jetting from the spinneret, the rate at which solution is ejected from the Taylor cone must match the flow rate of solution entering the spinneret. Increasing the operating voltage augments the surface charge density of the solution emerging from the spinneret and the system's electrical field strength, resulting in more Coulomb repulsion and greater affinity between the charged jet and the grounded collector, respectively. The two effects combine to cause the jet to accelerate more, which draws more fluid from the spinneret. Therefore, a higher voltage is necessary to ensure the fluid emission rate from the spinneret matches the flow rate of the syringe pump when the latter is increased.^[144]

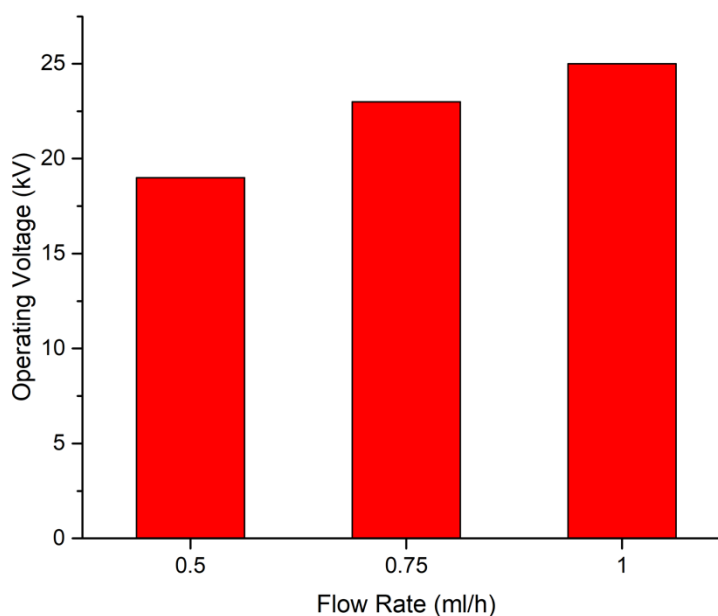


Figure 3.1. Operating voltage at various syringe pump flow rates for the electrospinning of silica-PVA hybrid nanofibres at a fixed spinneret-to-collector distance of 15 cm.

Increasing the flow rate decreases the fibre thickness slightly – the average diameters obtained from the Gaussian fit of the diameter distributions are 211, 206 and 181 nm in order of flow rate (Figure 3.2).

The slight decrease in average fibre diameter with flow rate contradicts the typical trend from the literature, which reports thicker fibres at higher flow rates.^[144, 147] However, it is worth noting that these studies kept the voltage fixed when varying the flow rate. This investigation found that no single voltage could achieve stable jetting across the range of tested flow rates.

Nevertheless, two competing factors may explain the observed trend. Firstly, as the flow rate increases, the emitted jet takes longer to dry during its journey to the collector, providing more time for jet elongation. Secondly, the increase in voltage necessary to maintain stable electrospinning at higher flow rates may also influence the jet's behaviour. A higher applied voltage results in a larger instability region between the spinneret and collector. Since the instability region is where the majority of jet shrinkage occurs, its augmented size results in the formation of thinner fibres.

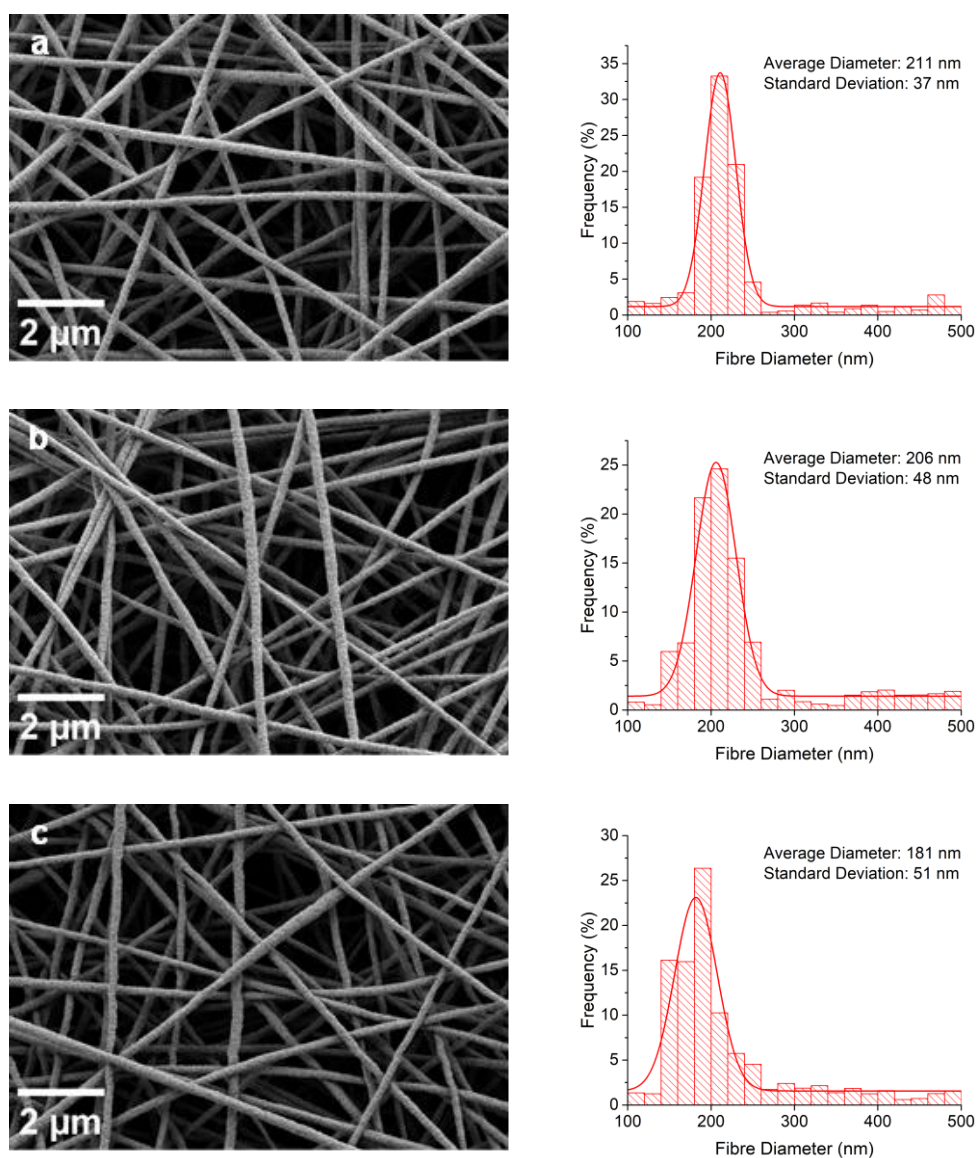


Figure 3.2. SEM images and fibre diameter distributions for silica-PVA hybrid nanofibres electrospun at various flow rates: 0.5 ml/h (a), 0.75 ml/h (b) and 1.0 ml/h (c).

SEM images at a lower magnification (Figure 3.3) indicated that the two lower flow rates produced homogeneous mats with few defects. However, the mat produced using a flow rate of 1 ml/h caused

some of the nanofibres to exhibit beading. Considering flow rate affects the productivity of the electrospinning process (the higher the flow rate, the greater the production rate of nanofibres), we chose 0.75 ml/h as the optimal value, since it is the highest flow rate that yielded defect-free fibres.

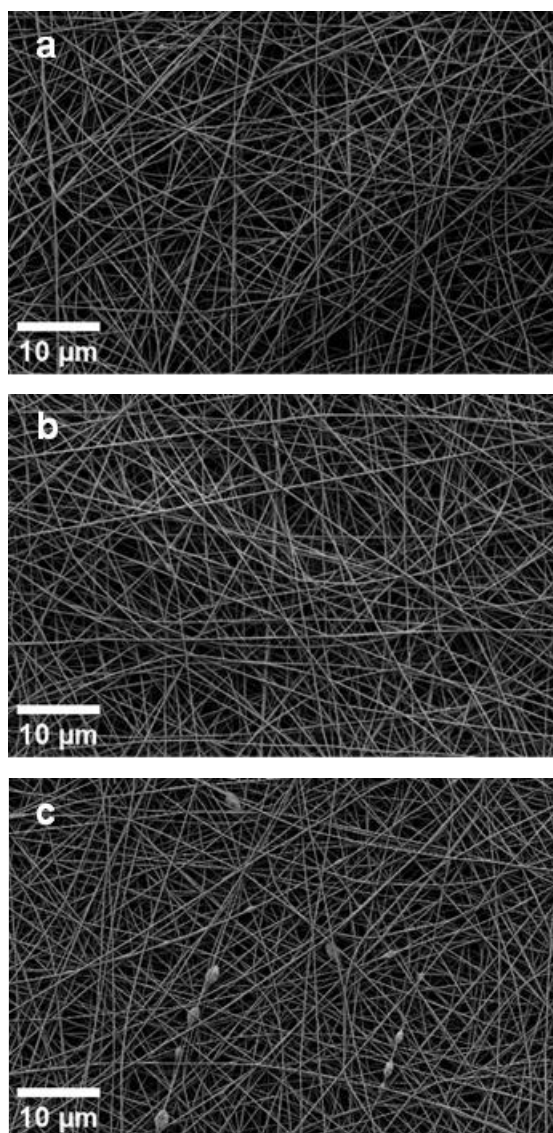


Figure 3.3. SEM images at 1k magnification for silica-PVA nanofibres electrospun at: 0.5 ml/h (a), 0.75 ml/h (b), 1.0 ml/h (c).

3.2.2 Effect of Spinneret-to-Collector Distance

With the flow rate fixed at 0.75 ml/h, the effect of the distance between the spinneret and collector was investigated using the flat plate collector. A positive correlation is observed between the distance and operating voltage (Figure 3.4). As discussed in Section 3.2.1, for stable electrospinning, the fluid removal rate from the spinneret must match the flow rate at which the solution is delivered to the spinneret. At a given voltage, increasing the tip-to-collector distance reduces the electrical field

strength of the system, meaning acceleration of the jet towards the collector decreases. Thus, to ensure stable mass flow between the fluid reservoir and the collector, the voltage must be increased to maintain a constant electrical field strength.

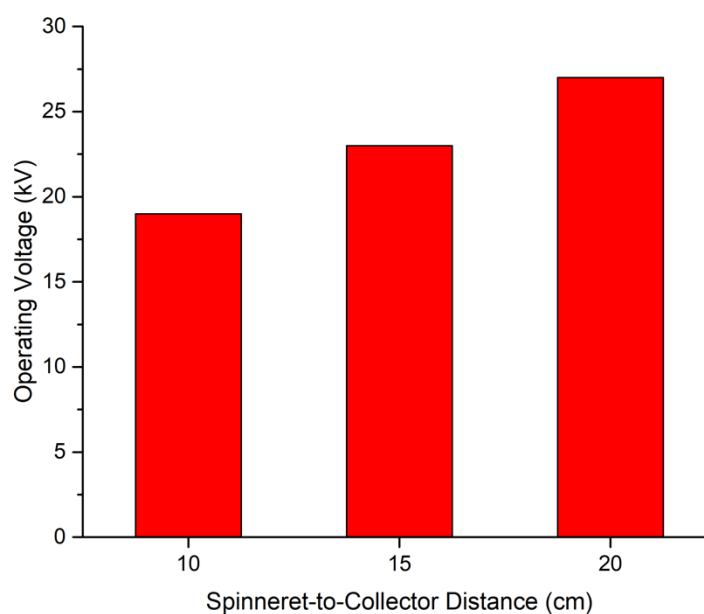


Figure 3.4. Operating voltage *versus* spinneret-to-collector distance for the electrospinning of silica-PVA hybrid nanofibres at a fixed flow rate of 0.75 ml/h.

The diameter of the collected mat increases with tip-to-collector distance (Figure 3.5). It is known that, after a short distance of travel parallel to the spinneret axis, the jet generated during the electrospinning process assumes a spiralling trajectory, with each successive coil having a greater radius than the last.^[143] Thus, a larger gap between the spinneret and collector enables the jet to spiral more. Consequently, fibres are collected over a larger area of the collector.

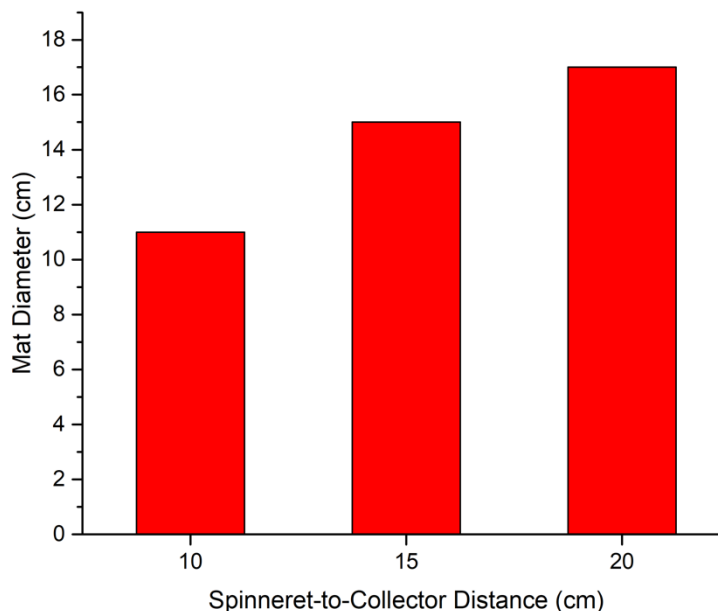


Figure 3.5. Diameter of the collected mat *versus* spinneret-to-collector distance for the electrospinning of silica-PVA nanofibres at a fixed flow rate of 0.75 ml/h.

The average fibre diameter of electrospun silica-PVA nanofibres varied slightly with spinneret-to-collector distance (Figure 3.6). The thinnest fibres are formed at the intermediate distance (206 nm), whilst fibres synthesised using the highest and lowest spinneret-to-collector distance yield fibres slightly larger in diameter (216 and 221 nm, respectively). This finding agrees with the literature which found that there is an optimal distance at which the thinnest fibres are formed. At shorter distances, incomplete evaporation of the solvent occurs, leading to thicker fibres, while at longer distances, unstable jetting from the spinneret results in the same outcome.^[144, 147] The SEM micrographs show that all three distances yield bead-free and continuous nanofibres. Therefore, aside from a slight change in fibre diameter, the tip-to-collector distance does not cause a notable change in fibre morphology.

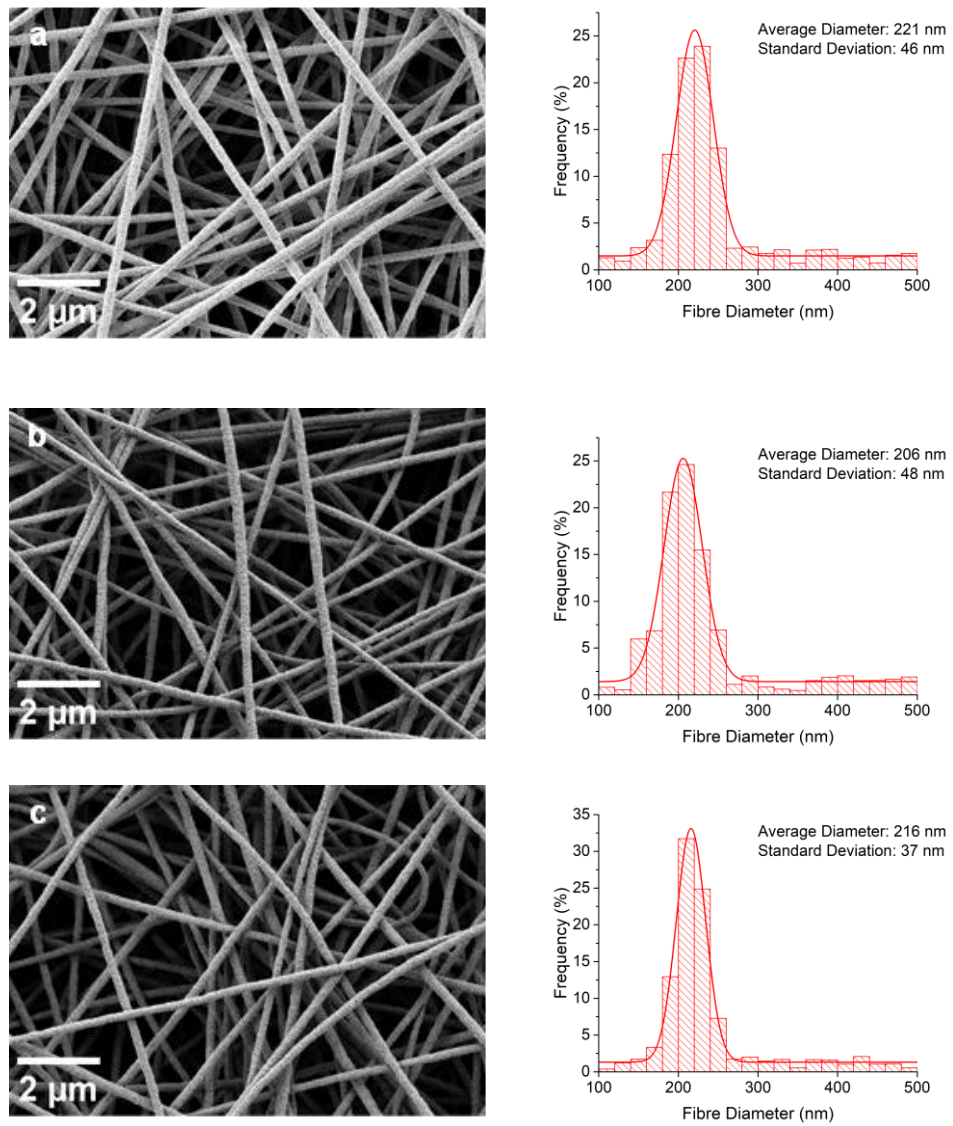


Figure 3.6. SEM images and fibre diameter distributions for silica-PVA hybrid nanofibres electrospun at various spinneret-to-collector distances: (a) 10 cm, (b) 15 cm and (c) 20 cm.

3.2.3 Effect of Formulation Composition

Three electrospinning formulations were prepared using different silica-polymer weight ratios (1:1, 2:1 and 3:1). The surface tension, viscosity, and conductivity of the three blends are shown in Table 3.1.

Table 3.1. Physical properties of the electrospinning formulations at 20°C.

Silica-to-Polymer Mass Ratio	Surface Tension (mN/m)	Dynamic Viscosity (Pa·s)	Conductivity (μS/cm)
1:1	49.5	0.52	1030
2:1	50.1	0.23	870
3:1	49.5	0.07	730

The surface tension remains approximately constant regardless of the silica-to-polymer ratio. On the other hand, the blend viscosity decreases dramatically as the silica content increases. The decreasing polymer concentration results in less molecular entanglement, and therefore, the resistance of the formulation to shear flow is diminished. Meanwhile, the solution conductivity decreases with an increase in the amount of colloidal silica in the formulation.

Nanofibres were electrospun from the three formulations onto the flat plate collector using the optimised flow rate and spinneret-to-collector distance from Sections 3.2.1 and 3.2.2 (0.75 ml/h and 15 cm, respectively). The applied voltage was fixed at 23 kV.

At a low silica-to-polymer ratio, it is expected that the resulting mat morphology will comprise continuous, defect-free nanofibres. Increasing the silica-to-polymer ratio is predicted to result in the occurrence of defective and discontinuous nanofibres owing to the lower amount of structure-directing polymer.

Figure 3.7 shows SEM micrographs of the resulting materials, along with their respective fibre diameter distributions. The mat prepared from the formulation with the lowest silica-to-polymer ratio comprises randomly-orientated nanofibres with few defects. Likewise, fibres electrospun from the 2:1 blend also yielded defect-free nanofibres.

Interestingly, fibres prepared from the 2:1 solution are slightly thicker than the 1:1 nanofibres, with mean fibre diameters of 176 and 152 nm, respectively. The fibres with the highest proportion of silica (3:1) exhibit the lowest average fibre diameter of 135 nm. However, beading is prevalent on these nanofibres.

One possible explanation for the observed fibre diameter and morphology changes is the competing effects of solution viscosity and conductivity on electrospinning. The initial increase in fibre diameter from a silica-polymer ratio of 1:1 to 2:1 could be attributed to the reduction in solution conductivity, since a lower charge density results in less electrostatic repulsion in the charged solution during electrospinning and, in turn, a weaker tensile force exerted on the jet during its journey between the spinneret and collector. Although conductivity decreases again from 2:1 to 3:1, there is a dramatic decrease in solution viscosity. Solutions with low viscoelasticity enable the Rayleigh instability to contract jet segments into spherical globules during electrospinning, which could be the cause of the beading seen in Figure 3.7c. To conserve mass, the jet connecting connecting the globules becomes

narrower as the beads grow in size, hence the dramatic decrease in mean fibre diameter for the nanofibres prepared from the 3:1 solution.

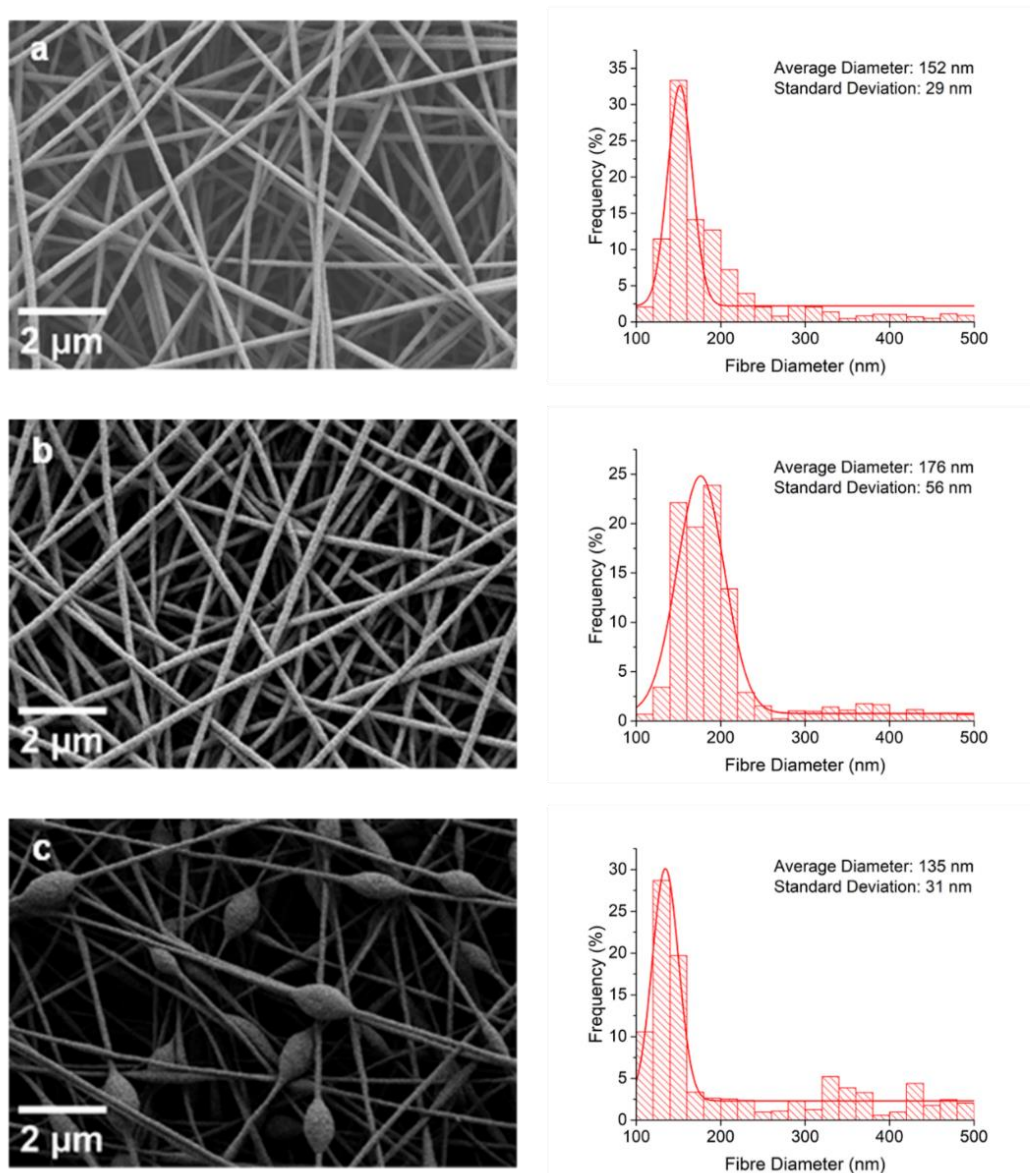


Figure 3.7. SEM images and fibre diameter distributions for 1:1 (a), 2:1 (b) and 3:1 (c) silica-to-polymer formulations.

3.2.4 Effect of Calcination Temperature

Hybrid silica-PVA samples prepared from all three formulations were calcined at 500, 700 and 900°C for 2 h to yield purely siliceous materials (Figure 3.8). Regardless of the amount of organic template in the precursor nanofibres, fibre fragmentation is prevalent after heat treatment at 500°C. In contrast, the fibres produced after heat treatment at 700°C and 900°C are continuous for the 1:1 and 2:1 samples. Meanwhile, the 3:1 nanofibres are still moderately fragmented after calcination at 700°C

but become fully continuous after heat treatment at 900°C. The nanofibres produced from the 3:1 formulation were not investigated any further due to their poor morphology.

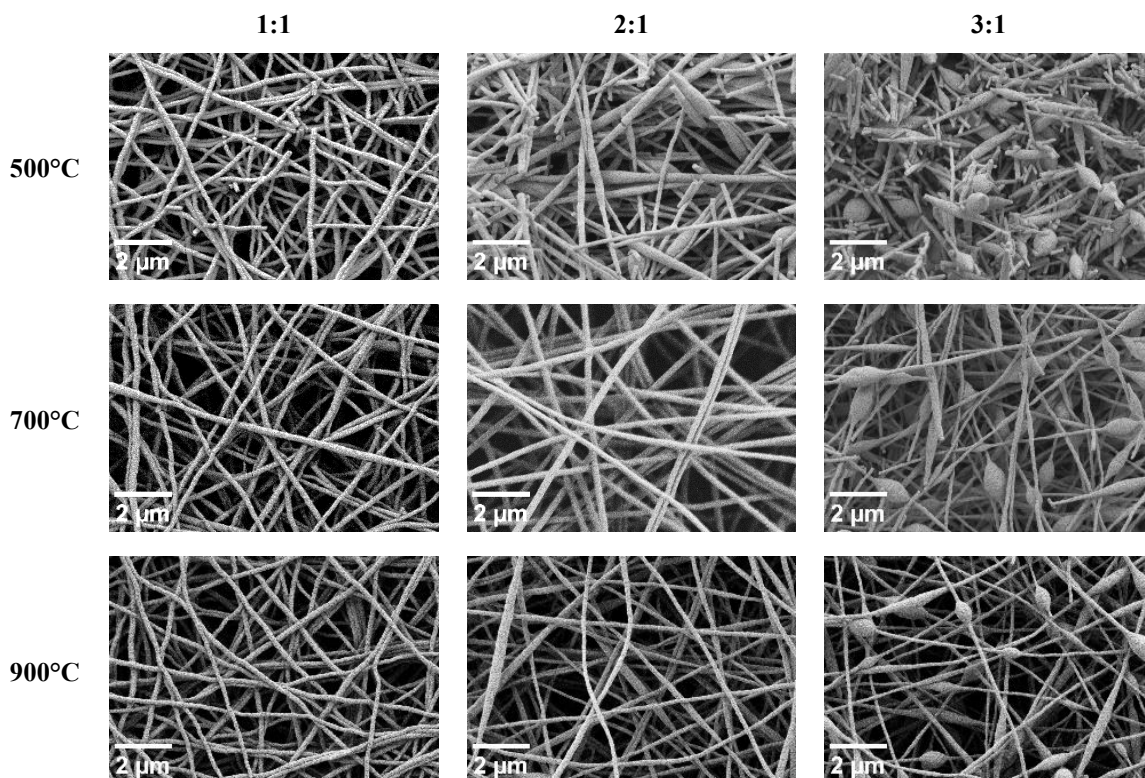


Figure 3.8. SEM images of silica nanofibres synthesised from the three formulations after calcination in air at different temperatures. The samples were heated from room temperature to the calcination temperature at a ramp rate of 10°C/min. After 2 h of calcination, the samples were left to naturally cool down to room temperature inside the furnace.

The principal aim of this chapter is to synthesise amine-functionalised materials using an electrospun silica mat as a substrate. Grafting of amines on to the surface of silica involves the reaction of aminosilane with surface silanol groups ($\equiv\text{Si-OH}$) thus achieving a siliceous mat with a high silanol density is desirable to maximise the number of grafting sites. However, during heat treatment of silica, silanol density decreases as a function of temperature due to thermally-induced dehydroxylation.^[235, 236] Thus, we selected 700°C as the calcination temperature for the optimised protocol as this was the lowest temperature that yielded good quality nanofibres using the 1:1 and 2:1 formulations.

3.2.5 Synthesis of Nanofibrous Silica using the Rotating Collector

The main limitation of using a flat plate collector for electrospinning is that the plate area restricts the maximum amount of sample that can be collected. Two larger mats of 1:1 and 2:1 silica-PVA

nanofibres were electrospun by replacing the flat plat collector with a rotating metal drum. The electrospinning system was run for 8 h, and the collected mats were calcined at 700°C.

The calcined mat produced using the 1:1 precursor blend was fragile and could not be picked up with tweezers without disintegrating (Figure 3.9a). In contrast, the mat synthesised from the 2:1 blend had superior flexibility and could be unfolded without tearing (Figure 3.9b). Therefore, the 2:1 precursor blend was selected for the synthesis of silica mats for amine functionalisation and subsequent direct air capture studies.

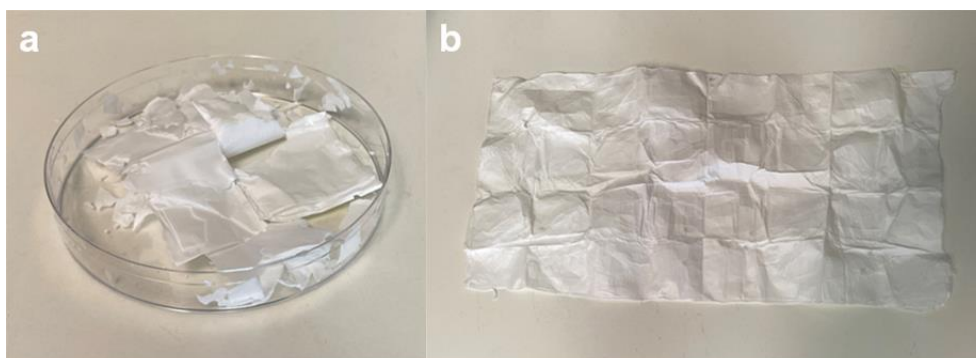


Figure 3.9. Silica mats electrospun from 1:1 (a) and 2:1 (b) silica-polymer formulations after calcination at 700°C.

3.2.6 Summary

In summary, electrospinning of the 2:1 silica-polymer solution at a flow rate of 0.75 ml/h, with a tip-to-collector distance of 15 cm and an applied voltage of 23 kV, followed by calcination at 700°C, produced the best siliceous material with respect to morphology and handleability. Henceforth, ‘silica-PVA nanofibres’ refers to electrospun materials prepared from the 2:1 silica-polymer blend using the optimised electrospinning conditions and silica nanofibres/nanofibrous silica refers to the same nanofibres after calcination at 700°C.

3.3 Characterisation of Nanofibrous Silica Prepared Using the Optimised Synthesis Protocol

3.3.1 FTIR Analysis

FTIR spectra were recorded for samples of silica-PVA and silica nanofibres (Figure 3.10).

For the as-spun material, a broad band between 3000 and 3700 cm^{-1} is associated with a stretching mode of hydroxyl groups (O-H) from the polymer and surface silanol groups on the silica nanoparticles. Other absorption peaks from the polymer are present at 2943 cm^{-1} (CH_n stretching), 1717 cm^{-1} (C=O stretching), 1429 cm^{-1} (C-O bending) and 1375 cm^{-1} (CH_2 wagging).^[231, 237-239]

Multiple peaks can be ascribed to the siliceous component of the hybrid fibres. Infrared absorption in the 1250 to 1000 cm^{-1} range corresponds to asymmetric stretching of the siloxane bond (Si-O-Si). The literature reports that up to four vibrational modes can contribute to absorption in this region: transversal optical (TO) and longitudinal optical (LO) vibrations of Si-O-Si in a four-ring siloxane structural unit, $(\text{SiO})_4$, and a second TO-LO pair for a six-ring unit, $(\text{SiO})_6$ (Figure 3.11).^[240] TO and LO modes correspond to bond vibrations parallel and perpendicular to the silica surface, respectively. In the case of the silica-PVA spectrum, a tall band centred at 1082 cm^{-1} can be attributed to the TO mode of the four-fold siloxane structure (TO_4).^[240-242] Additionally, an absorption peak at 795 cm^{-1} is ascribed to a symmetrical stretching vibration of Si-O-Si. Lastly, a small band at 970 cm^{-1} is due to the symmetrical stretching of silanol groups (Si-OH).^[243]

Several spectral changes occur after calcination of the nanofibres. As expected, all peaks associated with PVA disappear, verifying the removal of the organic template from the material. The Si-OH peak is invisible, which can be attributed to a decrease in silanol density on the nanofibres as a result of thermally-induced dehydroxylation.^[235, 236] Furthermore, the siloxane peak at 1082 cm^{-1} in the as-spun fibres shifts to 1060 cm^{-1} in the thermally treated sample. The appearance of a shoulder in the Si-O-Si asymmetric region at 1125 cm^{-1} might correspond to the LO mode of the four-ring siloxane structural unit (LO_4).^[240]

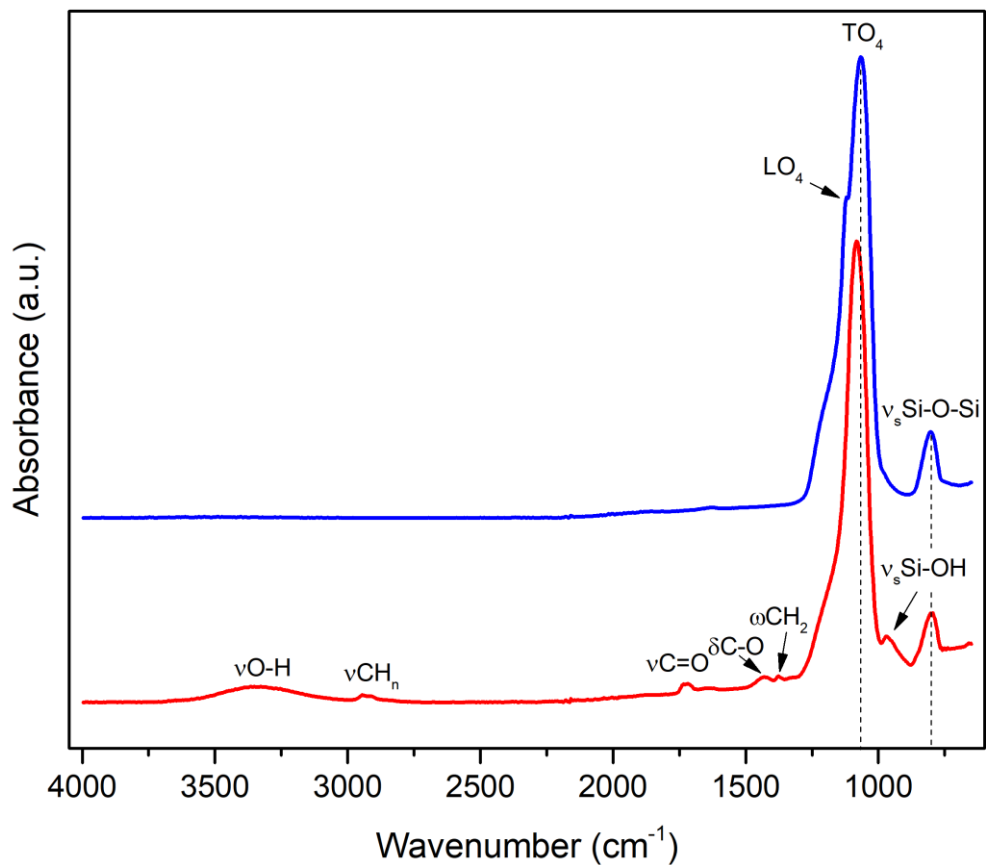


Figure 3.10. FTIR spectra of as-spun silica-PVA nanofibres (red) and heat-treated nanofibres (blue).

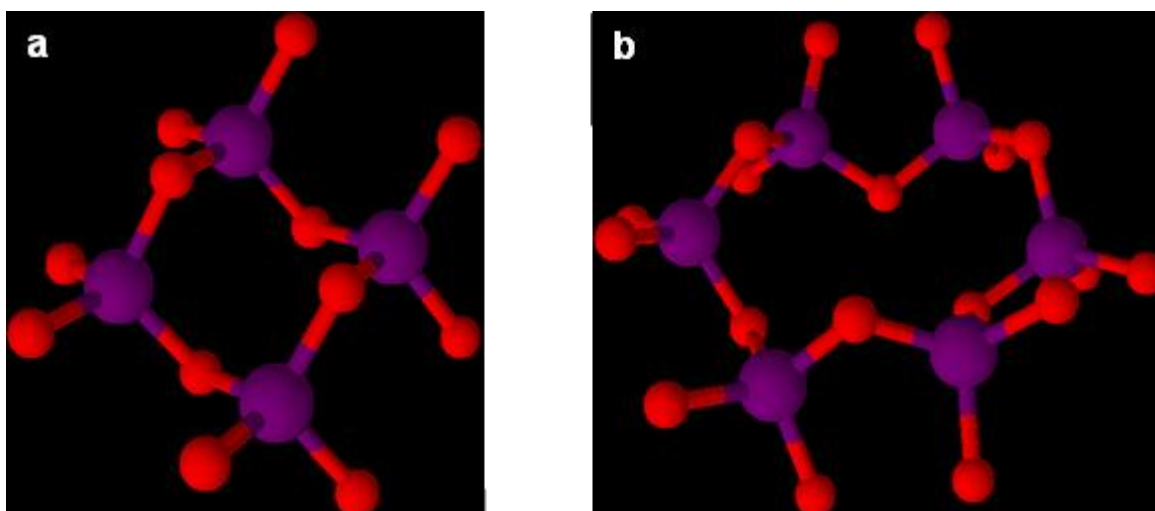


Figure 3.11. Ball-and-stick models of (a) four-fold and (b) six-fold siloxane ring structures commonly found in siliceous materials. Silicon and oxygen atoms are represented by the purple and red balls, respectively. Figure created by the author.

3.3.2 Studying the Textural Properties of Electrospun Materials using Nitrogen Physisorption

Nitrogen physisorption isotherms for the optimised material were recorded before and after calcination (Figure 3.12). The isotherm for the as-spun silica-PVA nanofibres resembles Type III under the IUPAC classification system. Such an isotherm indicates weak adsorbent-adsorbate interactions, characteristic of non-porous and macroporous materials. Since there is no evidence of macroporosity from SEM images of the as-spun nanofibres in Section 3.2, it can be inferred that the as-spun silica-PVA material is non-porous. In contrast, the silica nanofibres exhibit greater nitrogen uptake across the entire range of relative pressures. The shape of the isotherm is categorised as Type IV, corresponding to a mesoporous material. The hysteresis loop most closely resembles Type H3, which is typical for non-rigid aggregates of particles.^[183] Thermal removal of the polymer template also significantly enhanced the surface area and total pore volume (TPV) of the nanofibres; the calculated BET surface area increases twenty-six-fold from 5 m²/g to 131 m²/g whilst the TPV is augmented from 0.01 to 0.39 cm³/g.

The BJH pore size distribution (Figure 3.13) shows that the silica nanofibres have pores predominantly in the range of 10 and 14 nm, with a mean pore diameter of 10.7 nm. Small fluctuations in dV(logd) below 5 nm indicate the presence of small mesopores, although their contribution to the total pore volume is marginal in comparison to the larger mesopores.

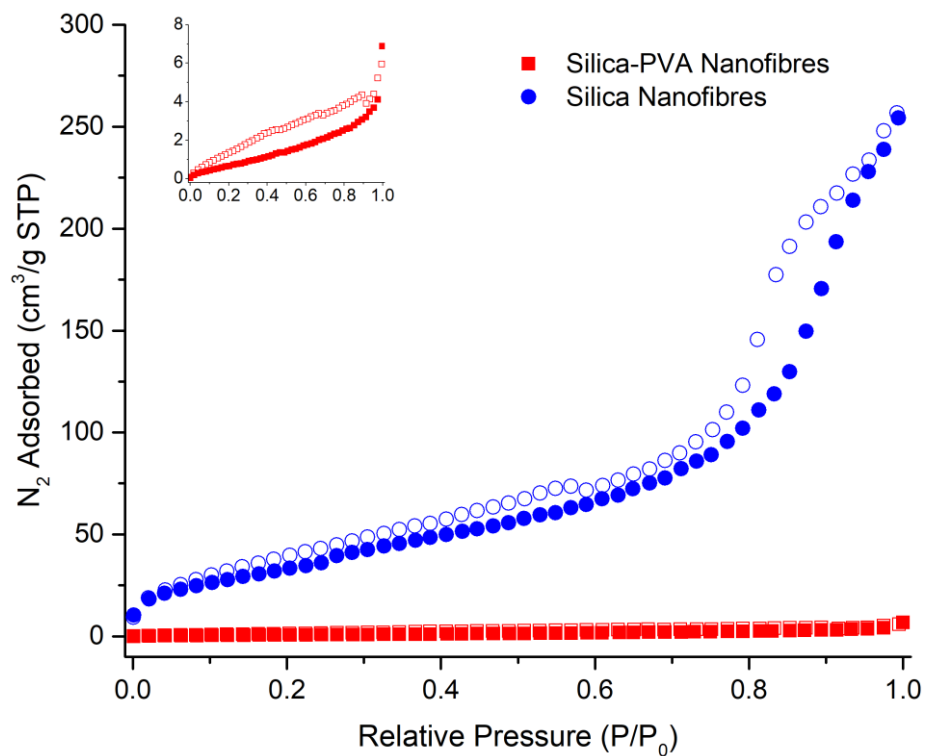


Figure 3.12. Nitrogen adsorption/desorption isotherms at 77 K. The solid and open datapoints correspond to the adsorption and desorption branches of the isotherms, respectively.

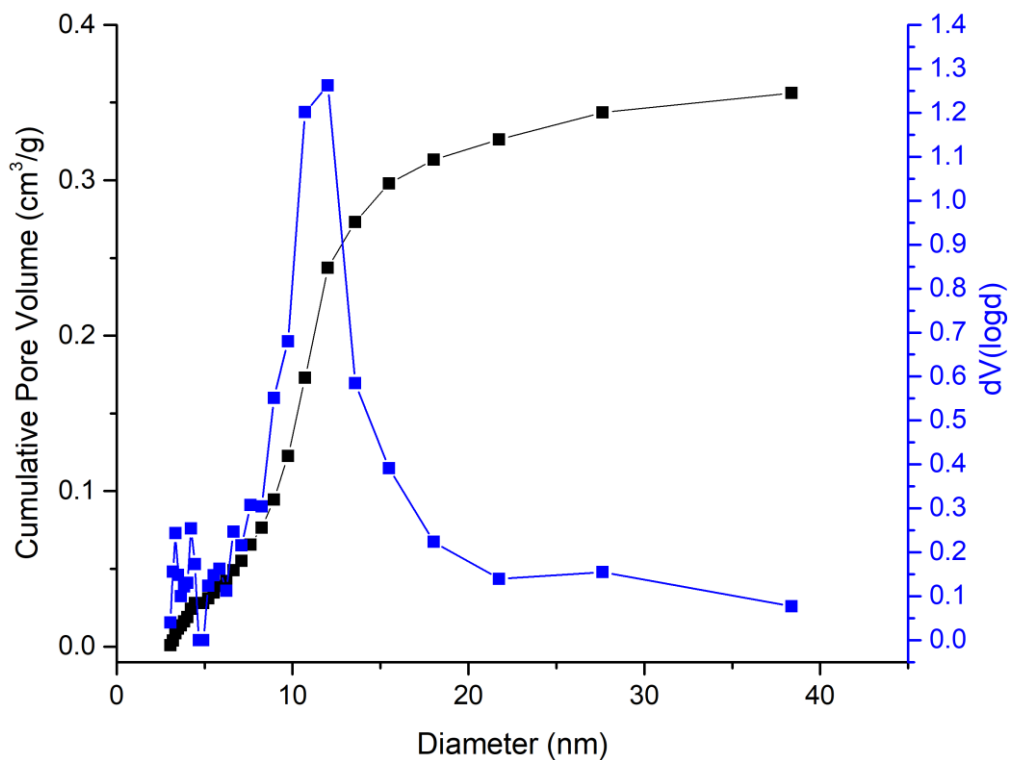


Figure 3.13. BJH pore size distribution of silica nanofibres.

3.3.3 Assessing the Thermal Stability of Electrospun Materials using Thermogravimetric Analysis

TGA traces were recorded for as-spun silica-PVA nanofibres and silica nanofibres (Figure 3.14). Regarding the silica-PVA samples, there is an initial weight drop of 0.7 wt% between room temperature and 110°C, mainly due to the removal of absorbed moisture from the sample. The onset of decomposition of the polymer occurs at *ca.* 225°C, finishing at *ca.* 600°C. Degradation of the polymer chains follows a two-step mechanism.^[244] The first step corresponds to a weight drop of 23.5 wt% between 225 and 400°C. The second step occurs immediately after the first, corresponding to a weight decrease of 9.2 wt% between 400 and 600°C.

The total organic content, found by discounting the moisture weight drop from the total weight change, is 33 wt%, verifying that the silica-PVA weight ratio of the nanofibres is indeed 2:1. Two further TGA tests were carried out on samples from other parts of the electrospun mat (Figure A1 in the Appendix). The triplicate average organic loading is 33.5%, suggesting the organic and inorganic components from the electrospinning solution are homogeneously distributed across the nanofibrous mat.

The weight of silica fibres shows a marginal decrease of 1.5 wt% between 180 and 900°C. This can be attributed to the evolution of water from the condensation of surface silanol groups (Si-OH).

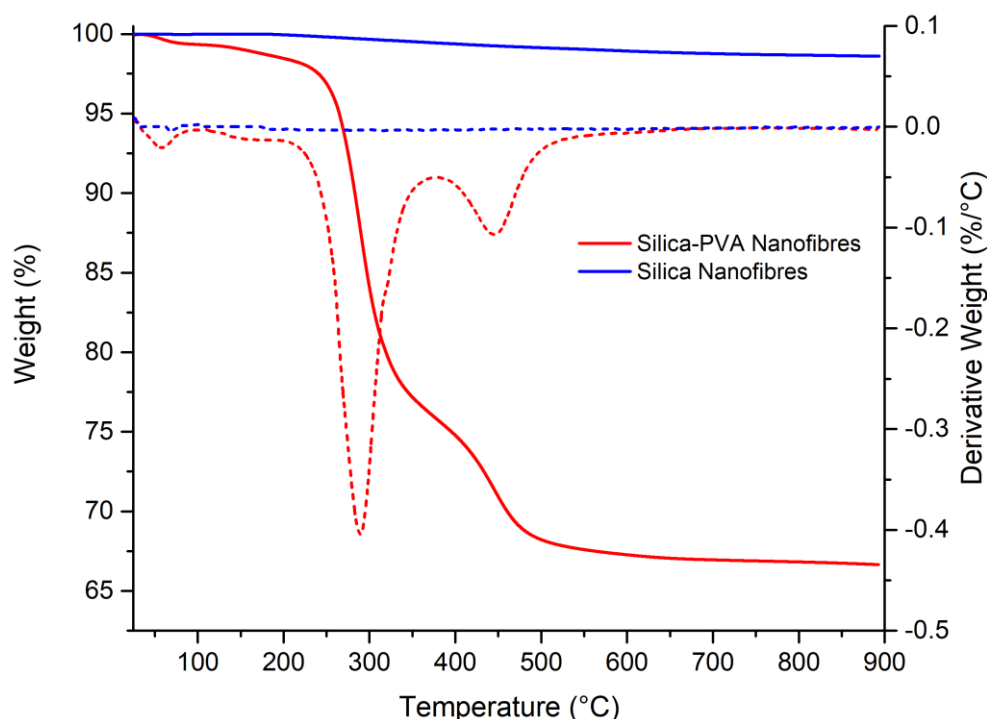


Figure 3.14. TGA and DTG curves (solid and dashed lines respectively) for silica-PVA (red) and silica (blue) nanofibres. Test conditions: 10°C/min ramp rate, Ar purge.

TGA tests were also performed on raw PVA granules and pure PVA nanofibres electrospun from a 5 wt% PVA solution using the same electrospinning conditions as for the hybrid nanofibres (Figure 3.15). The decomposition of the polymer in the pure PVA nanofibres exhibits a similar TGA profile to that for the silica-PVA material, showing that the presence of silica nanoparticles in the nanofibres does not impact the thermal stability of the polymer. The raw PVA trace shows a similar two-step decomposition mechanism as the hybrid and PVA nanofibres. However, the onset temperature of decomposition is slightly higher for the PVA granules than for both nanofibrous samples (225 and 210°C respectively).

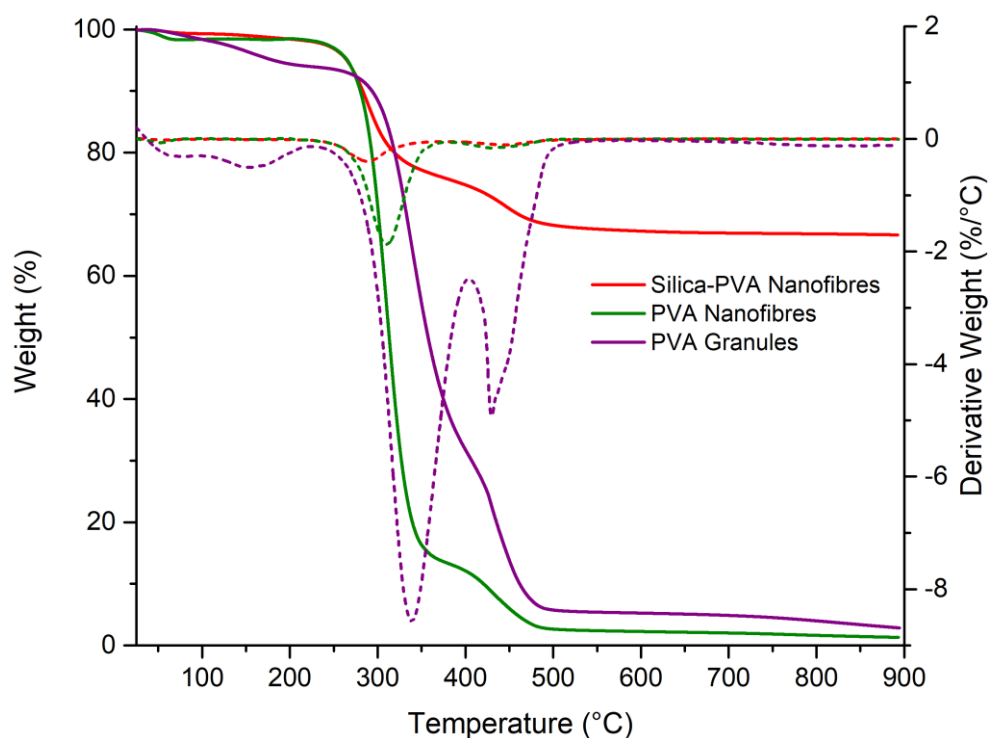


Figure 3.15. TGA and DTG curves (solid and dashed lines respectively) for 2:1 PVA-silica nanofibres, along with the pure polymer in nanofibrous and granular form. Test conditions: 10°C/min ramp rate, Ar purge.

3.3.4 Assessing Chemical and Conformational Changes in the Polymeric Template using Solid-State NMR.

^1H - ^{13}C CP/MAS NMR spectra were recorded for the raw PVA reagent, PVA nanofibres and 2:1 silica-PVA nanofibres to ascertain whether the polymer undergoes any chemical or conformational changes during the electrospinning process (Figure 3.16).

In the specific type of PVA reagent used, 88% of the chemical units are vinyl alcohol monomers whilst the remaining 12% are vinyl acetate, meaning that, for all three spectra, there are peaks associated with both types of monomers. The resonances at 172 ppm (C=O, carbonyl) and 22 ppm

(CH₃, methyl) originate from the carbons of the acetate functional groups. The peak at 45 ppm is assigned to the methylene linkers in the polymer backbone.^[245] Three overlapping peaks at 77, 71 and 65 ppm are attributed to the methine (CH) carbons. Respectively, these peaks can be assigned to methine environments connected to OH groups that are associated with two, one and no intramolecular hydrogen bonds (Scheme 3.1).^[246, 247] The methine carbon in the vinyl acetate monomer also contributes to the resonance at 65 ppm, since the acetate functional group cannot hydrogen bond.

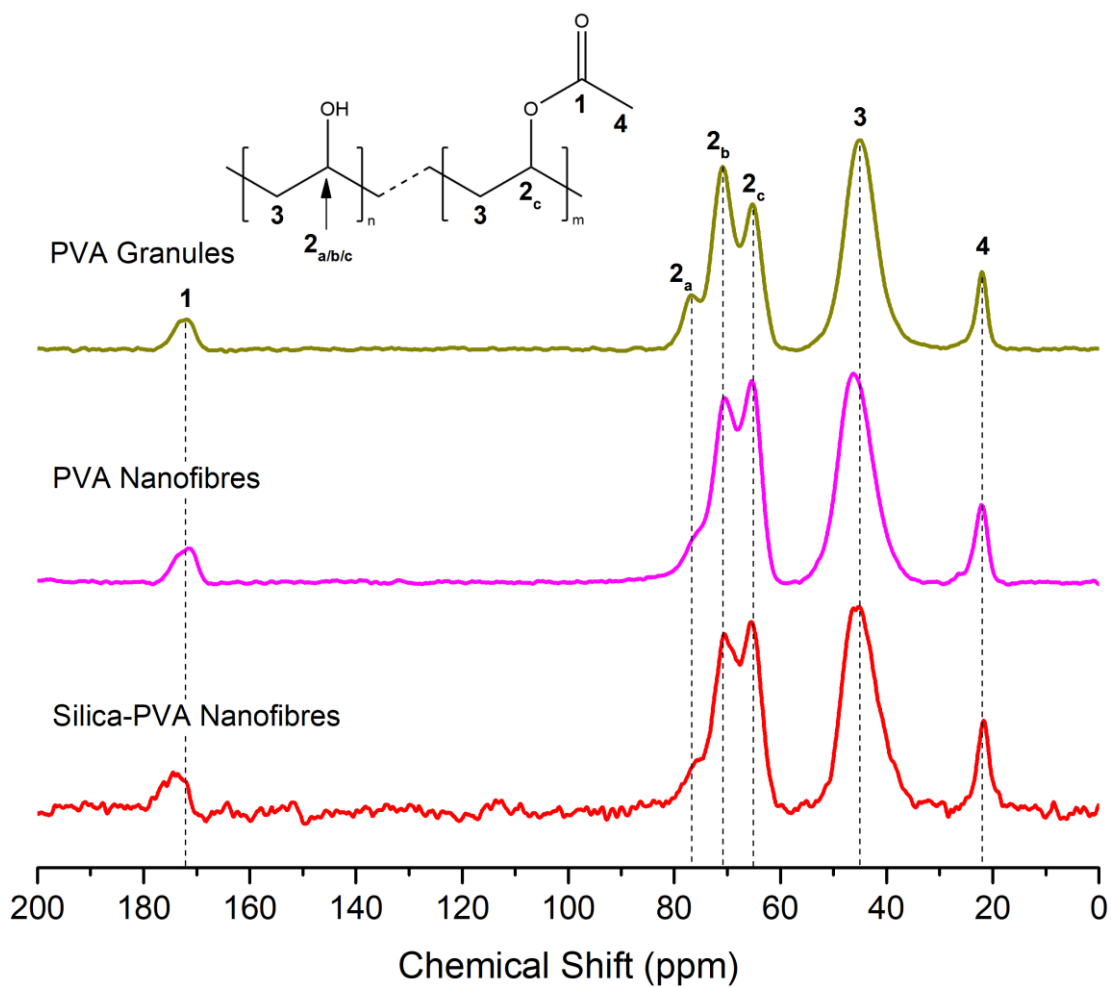
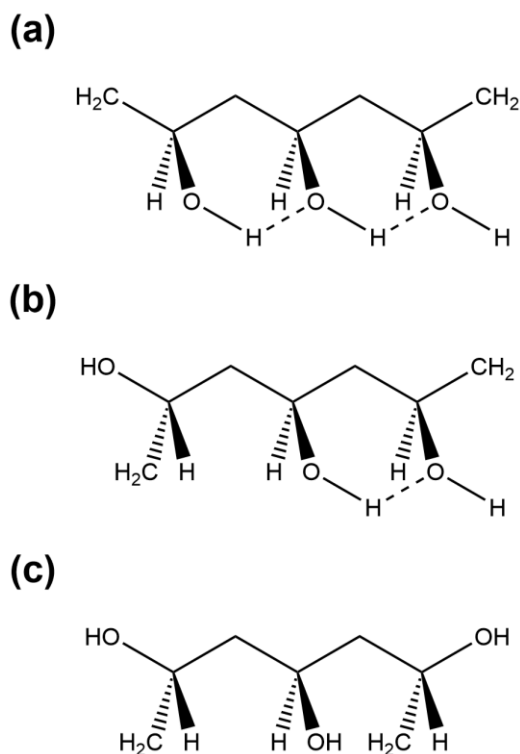


Figure 3.16. ¹H-¹³C CP-MAS NMR spectra of raw PVA granules (top), PVA nanofibres (middle) and silica-PVA nanofibres (bottom). The spectra were collected using the same experimental parameters (4 k scans, 1.1 ms contact pulse, 5 s recycle delay) and have been normalised with respect to the C3 peak.



Scheme 3.1. Skeletal diagrams of an oligomer comprising three vinyl alcohol monomers, with the middle hydroxyl group exhibiting two (a), one (b) and zero (c) intramolecular bonds.

Calculating the areas of the methine peaks after deconvolution provides semi-quantitative information about the relative populations of OH groups engaged in different degrees of hydrogen bonding (Table 3.2).^[246, 247] In the PVA granules, most of the hydroxyl groups are engaged in either one or no hydrogen bonds whilst in electrospun PVA and silica-PVA nanofibres, significantly more OH groups are doubly hydrogen bonded. This shows that the electrospinning process causes conformational changes in the polymer.

Table 3.2. Relative areas of the deconvoluted C2 peaks from the ^1H - ^{13}C CP-MAS spectra.

	Proportion of Total C2 Peak Area (%)		
	PVA Granules	PVA Nanofibres	Silica-PVA Nanofibres
Peak 2a (Two H-bonds)	13 ± 0.1	22 ± 0.2	39 ± 2.4
Peak 2b (One H-bond)	54 ± 0.1	40 ± 0.1	28 ± 0.8
Peak 2c ^d (Zero H-bonds)	33 ± 0.1	38 ± 0.1	33 ± 0.8

^d The absolute area of this peak was multiplied by the polymer's degree of hydrolysis (88%) to discount the contribution of methine from the vinyl acetate monomer.

A ^{13}C spectrum was also recorded for silica nanofibres after calcination at 700 °C (Figure A2 in Appendix). As expected, no peaks were detected, verifying the nanofibres are inorganic.

3.3.5 Probing the Local Structure of Nanofibrous Silica using ^1H - ^{29}Si CP/MAS NMR

^1H - ^{29}Si CP/MAS NMR spectra for silica-PVA and silica nanofibres were recorded (Figure 3.17). The spectrum for the silica-PVA nanofibres exhibits three resonances at -89, -101 and -111 ppm, corresponding to Q^2 (geminal silanol), Q^3 (single/vicinal silanol) and Q^4 (siloxane bridge) sites, respectively.^[248]

Q^3 and Q^4 peaks are also present in the silica nanofibres; however, their intensities are significantly reduced compared to the silica-PVA spectrum. The spectral change is likely due to the absence of the ^1H -rich polymer, resulting in a lower density of proximal protons needed for the cross-polarisation of the ^{29}Si nuclei. Furthermore, the Q^3 peak intensity appears to decrease more than the Q^4 resonance, indicating a lower population of silanols in the silica nanofibres.^[249] It must be noted, however, that cross polarisation in solid state NMR is semi-quantitative. Whilst similar materials can be compared, the actual population size of each magnetic environment cannot be accurately quantified.

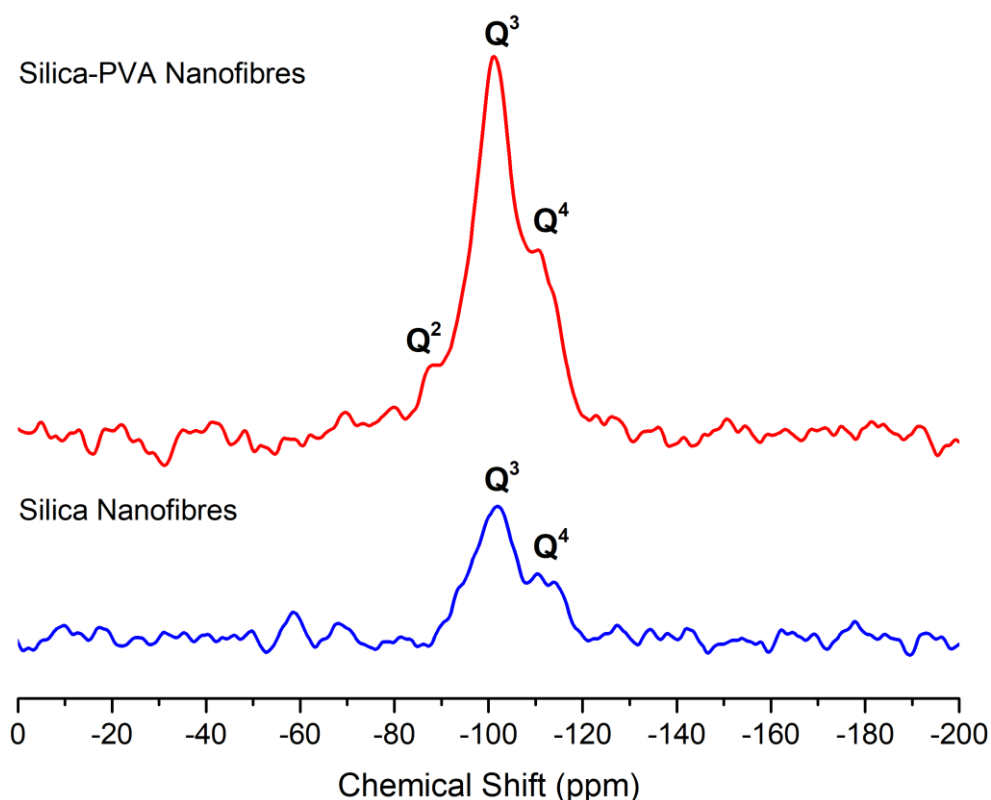
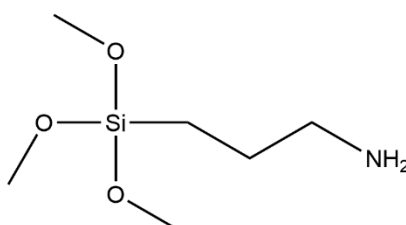


Figure 3.17. ^1H - ^{29}Si CP-MAS NMR spectra for as-spun silica-PVA nanofibres (top) and silica nanofibres (bottom). The spectra were acquired using identical experimental conditions (4 k scans, 2 ms contact pulse, 10 s recycle delay).

3.4 Surface Functionalisation of Nanofibrous Silica

A sample of silica nanofibres was grafted under hydrous conditions using APS as the grafting agent (Scheme 3.2), an aminosilane-to-silica ratio of 5 ml_{silane}/g_{silica} and the addition of 0.6 ml/g_{silica} of water. Prior to immersion, the silica mat had to be folded several times so that it could fit inside the round-bottomed flask in which the reaction mixture was prepared. As shown in Figure 3.18, the nanofibrous silica mat retained its self-standing structure after functionalisation.



Scheme 3.2. Chemical formula of 3-aminopropyltrimethoxysilane (APS).



Figure 3.18. A nanofibrous silica mat before (a) and after (b) amine functionalisation.

FTIR spectra were recorded for the material before and after grafting (Figure 3.19). Spectral changes can be seen in the Si-O-Si asymmetric stretching region (1250 - 1000 cm⁻¹). The strong peak associated with the transversal optical mode of a four-membered siloxane ring (TO₄) blueshifts after functionalisation, from 1066 to 1084 cm⁻¹. It has been reported that the shifting of this band to a higher wavenumber is associated with the introduction of organic groups into siliceous materials.^[241]

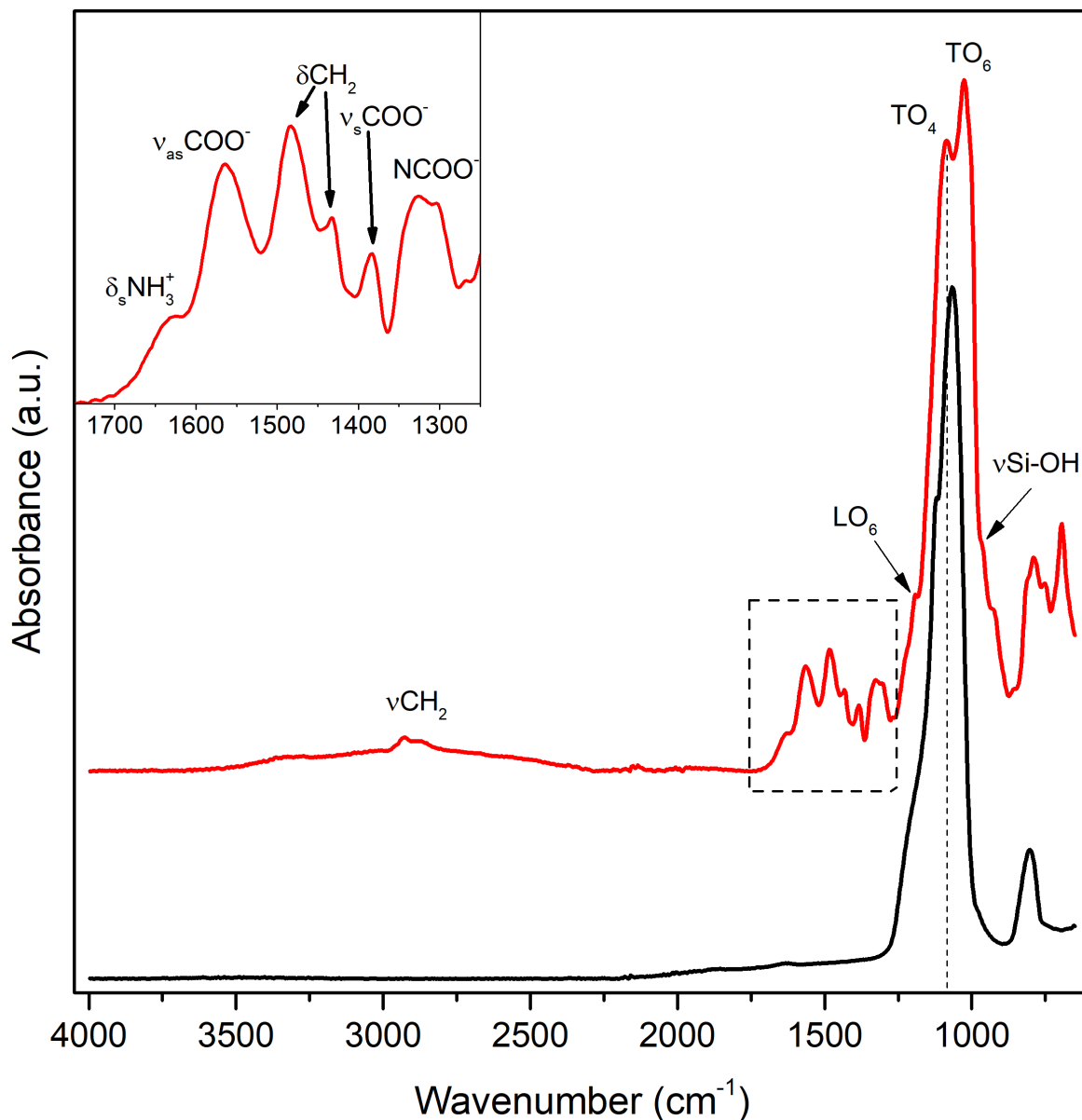
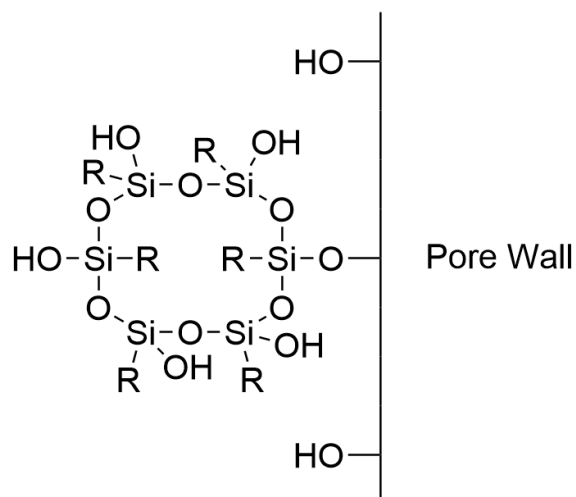


Figure 3.19. FTIR spectra of silica nanofibres before (black) and after (red) APS functionalisation.

The most significant change concerning the asymmetric Si-O-Si region is the appearance of a new peak at 1026 cm^{-1} , which has been tentatively assigned to the transverse optical mode of a six-membered siloxane ring (TO_6).^[250] The faint shoulder at 1190 cm^{-1} is assigned to the corresponding longitudinal optical mode of the six-membered siloxane unit (LO_6) whilst the faint sideband at 966 cm^{-1} is ascribed to a stretching mode of Si-OH^[243] from uncondensed silanol groups.

It has been reported that siliceous materials containing large amounts of organic moieties have a higher proportion of six-membered siloxane rings since their less-tensioned structure compared to four-membered rings allows them to better accommodate organic groups.^[250, 251] We propose that the $(\text{SiO})_6$ vibrations identified in the FTIR spectrum of the APS-functionalised material originated from tethered cyclical structures formed *via* the self-condensation of the coupling agent (Scheme 3.3).



Scheme 3.3. Schematic diagram of a six-membered siloxane structure grafted to a pore wall.

New absorption bands are also present in the material after surface modification due to bond vibrations from the aminopropyl groups grafted onto the nanofibres. Weak bands centred at *ca.* 2870 and 2930 cm^{-1} are assigned to symmetric and asymmetric stretching of CH_2 respectively, whilst IR absorption due to bending modes of CH_2 can be seen at 1383 and 1483 cm^{-1} .^[252-254]

There is also evidence of ionic ammonium carbamate formation, a product of CO_2 chemisorption. Asymmetric and symmetric stretching modes of COO^- from the carbamate ion are attributed to the peaks at 1564 and 1433 cm^{-1} respectively. Additionally, a peak at *ca.* 1327 cm^{-1} could be a skeletal vibration of NCOO^- . Lastly, an IR band at 1630 cm^{-1} is assigned to the symmetric bending of the ammonium counterion (NH_3^+).^[253, 255]

TGA thermograms were recorded for nanofibrous silica before and after APS functionalisation (Figure 3.20). Two prominent weight drops appear on the TGA trace for the grafted sample. The first, between 25 and *ca.* 150°C (7.5 wt%), is caused by the evolution of water (from entrapped moisture and condensation of silanol groups), entrapped solvent (from the grafting process) and carbon dioxide (from the decomposition of the carbamate salt identified in the FTIR analysis above). The second weight loss (15 wt%) between *ca.* 300 to 900°C is attributed to the decomposition of the organic component of the functionalised material. Namely, the aminopropyl branches from the tethered aminosilane. Based off the TGA data, the estimated aminosilane loading for the functionalised material is 3.4 $\text{mmol/g}_{\text{silica}}$.

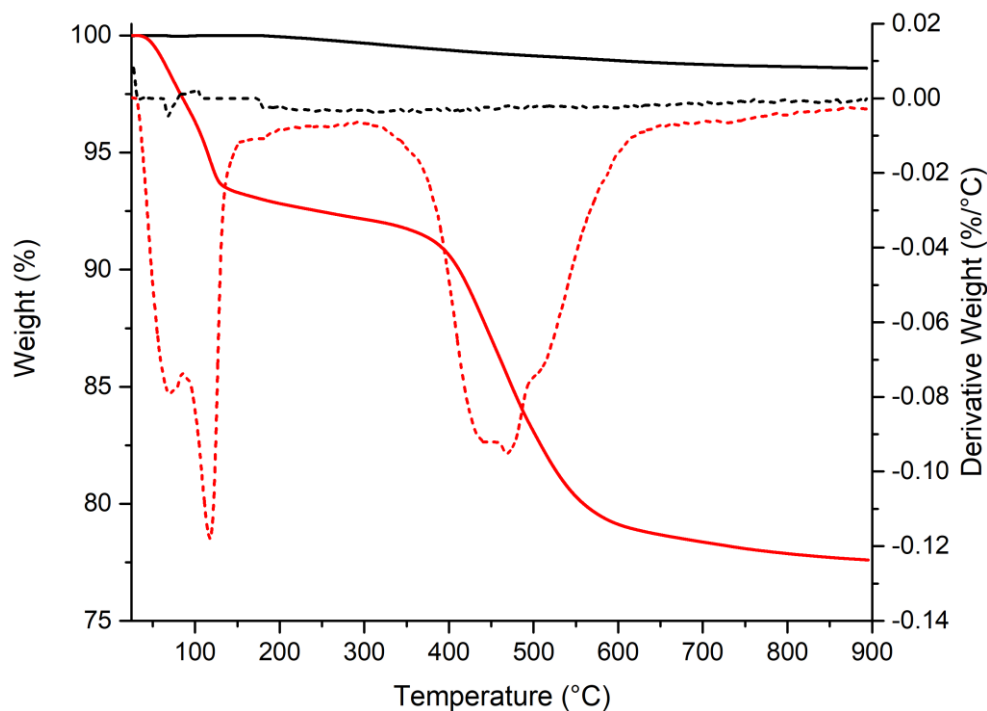


Figure 3.20. TGA thermograms of nanofibrous silica before (black) and after (red) APS functionalisation. Test conditions: 10°C/min ramp rate, Ar purge.

Silica mats before and after grafting were imaged using SEM (Figure 3.21). After functionalisation, the sample retains its nanofibrous structure, although some of the nanofibres are fragmented due to the harsh reaction conditions.

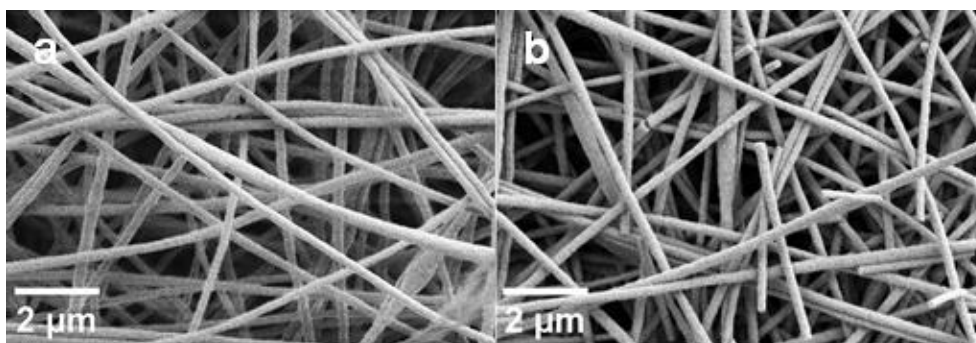


Figure 3.21. SEM images of nanofibrous silica before (a) and after (b) APS-functionalisation.

The ^1H - ^{13}C solid-state NMR spectrum for the APS-modified material (Figure 3.22) shows three tall peaks at 11.6, 23.1 and 43.5 ppm.^[256] These are all associated with the resonances of the methylene carbons in the aminosilane, verifying successful functionalisation of the silica nanofibers. The absence of a methoxy (OCH_3) resonance at *ca.* 51 ppm^[256] suggests that the aminosilane was fully hydrolysed prior to anchorage to the nanofibres. A small peak at 127.7 ppm is assigned to entrapped

solvent (toluene) from the grafting solution.^[257] The carbonyl (C=O) peak at 165 ppm corresponds to CO₂ adsorbed on the material.^[258]

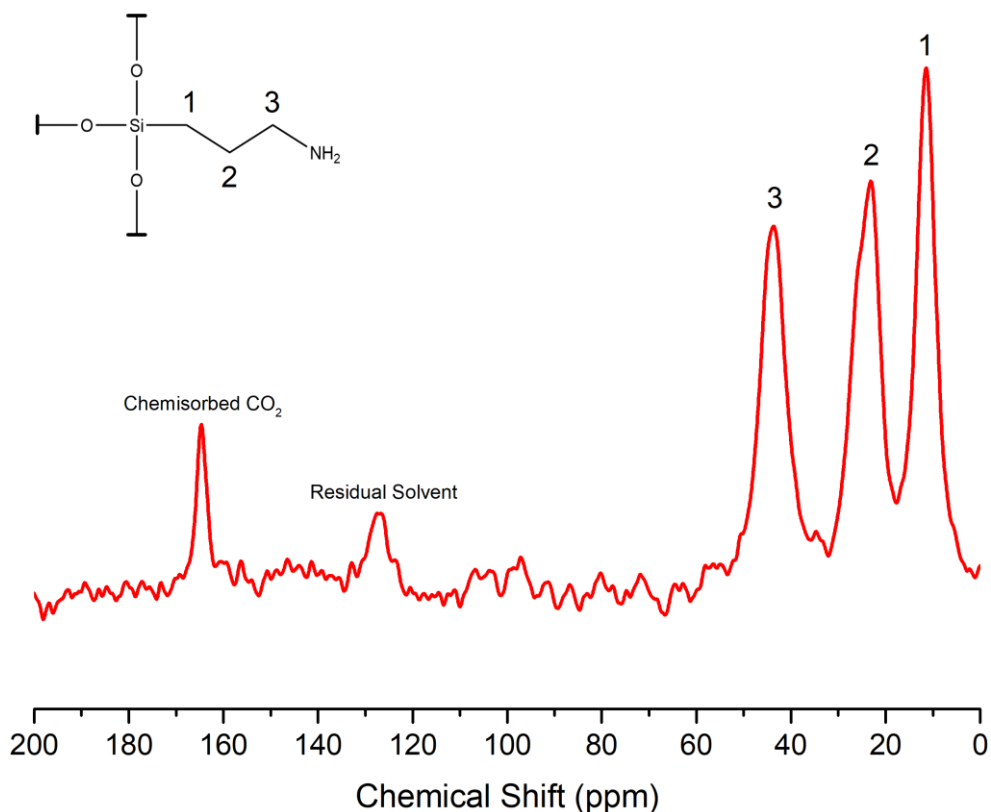


Figure 3.22. ¹H-¹³C CP-MAS NMR spectrum of APS-functionalised nanofibrous silica.

¹H-²⁹Si CP-MAS NMR spectra were recorded before and after surface functionalisation of silica nanofibres (Figure 3.23). In both spectra, Q³ (isolated/vicinal silanol) and Q⁴ (siloxane) resonances are present at -101 and -111 ppm respectively. Two additional peaks in the functionalised nanofibres correspond to ²⁹Si populations from the grafted aminosilane (Tⁿ sites). The resonance at -60 ppm is assigned to partially condensed T² sites (R-Si(OSi)₂OH) whilst the second at -68 ppm corresponds to fully condensed T³ sites (R-Si(OSi)₃).^[259] The higher signal intensity of T³ signal compared to T² suggests that a greater amount of aminosilane is fully condensed on the silica substrate.

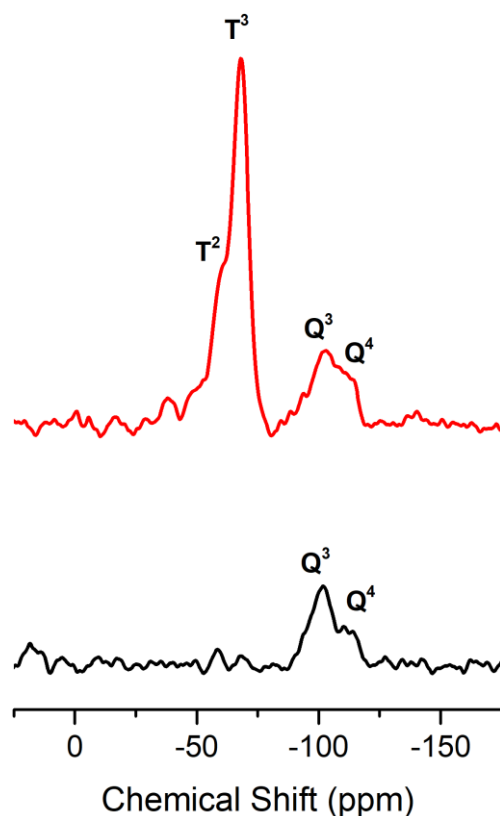


Figure 3.23. ^1H - ^{29}Si CP-MAS NMR spectra of nanofibrous silica before (black) and after (red) APS-functionalisation.

It is worth reiterating that CP experiments provide only semi-quantitative information about the different populations of ^{29}Si nuclei. As expected, ^{29}Si spectra obtained from direct polarisation (DP) experiments (Figure 3.24), which does provide quantitative information, show that the most abundant ^{29}Si population in the nanofibres is Q^4 . The silanols responsible for the Q^3 resonance are only present at the surface of silica and therefore have an extremely low relative population, as reflected by the fact that the Q^3 peak is indiscernible from the Q^4 resonance in the DP spectra. After functionalisation, the peaks associated with the T^n sites are shorter than the Q^4 resonance which is expected because silica makes up the bulk of the functionalised nanofibres.

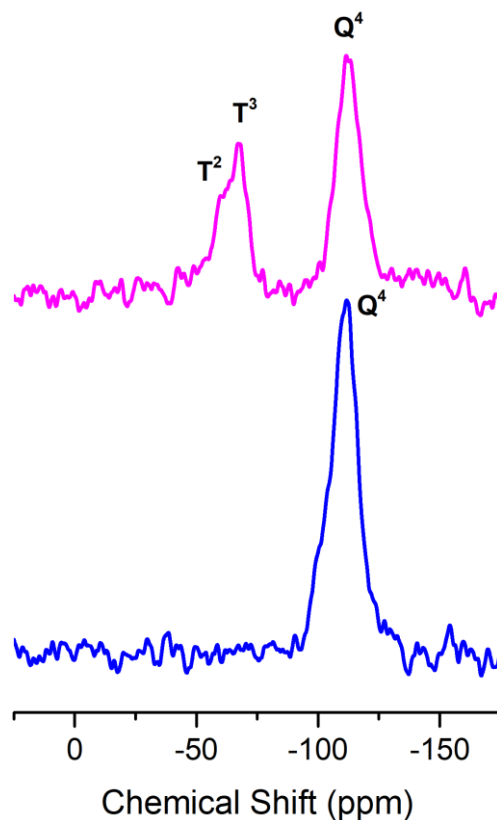


Figure 3.24 ^{29}Si DP NMR spectra of nanofibrous silica before (blue) and after (pink) APS-functionalisation.

There are multiple grafted structures that can give rise to the T^3 resonance.^[260] For example, during the grafting process, one aminosilane molecule can condense onto the silica surface *via* three siloxane bonds (Figure 3.25a). A partially-anchored aminosilane molecule can also cross-link with neighbouring tethered species, forming a monolayer (Figure 3.25b). Additionally, the grafting agent can self-condense longitudinally, resulting in the formation of ladder-like structures projecting from the silica surface (Figure 3.25c) It is likely that a combination of all three structures, together with more complex, disordered polyaminosiloxane species, contribute to the T^3 resonance.

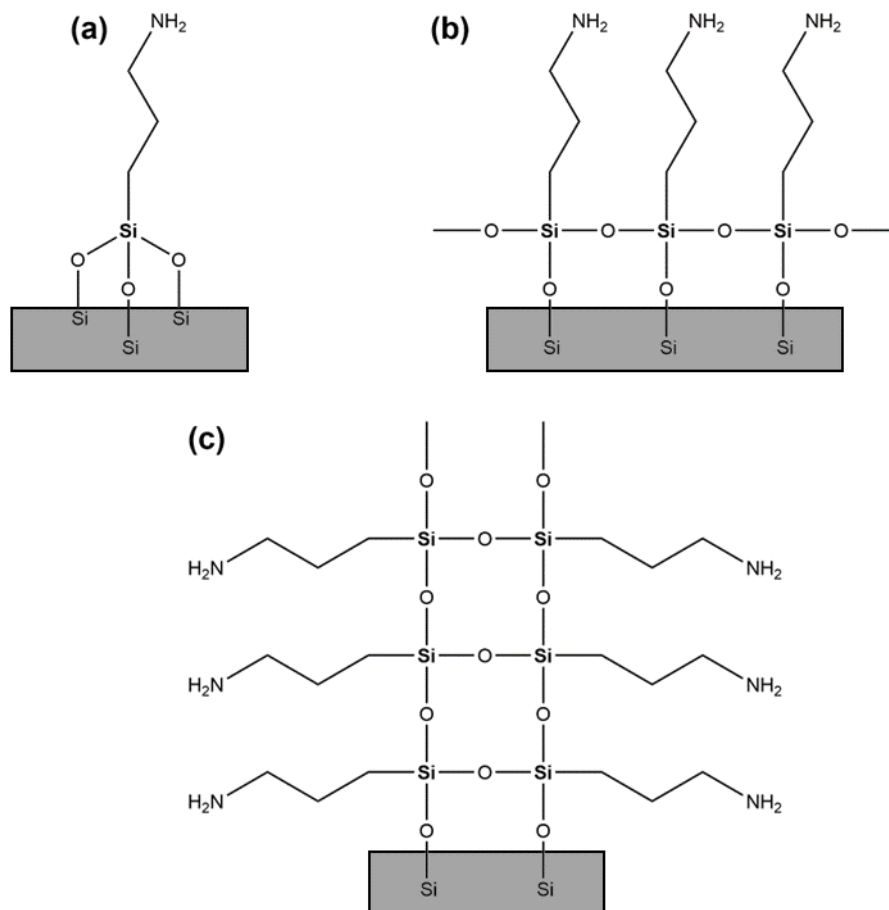


Figure 3.25. Three idealised aminosilane binding motifs that may contribute to the T^3 signal observed in ^{29}Si NMR analysis of the surface-modified silica. The grey rectangles represent the silica surface and the bold silicon atoms are the T^3 sites.

3.5 Effect of Silane Concentration on the Grafting Process

To investigate the influence of the concentration of silane on the grafting process, samples of nanofibrous silica were chemically modified using reaction mixtures with four different silane concentrations.

The silane loading increases with APS concentration whilst grafting efficiency decreases dramatically (Figure 3.26). Two factors may explain the reduction in grafting efficiency. Firstly, the grafting reaction consumes silanol functional groups on the surface of the nanofibres and thus the silica silanol density may limit the maximum attainable loading. Secondly, after the most energetically favourable grafting sites are occupied, steric hindrance may slow down the anchorage of additional silane.

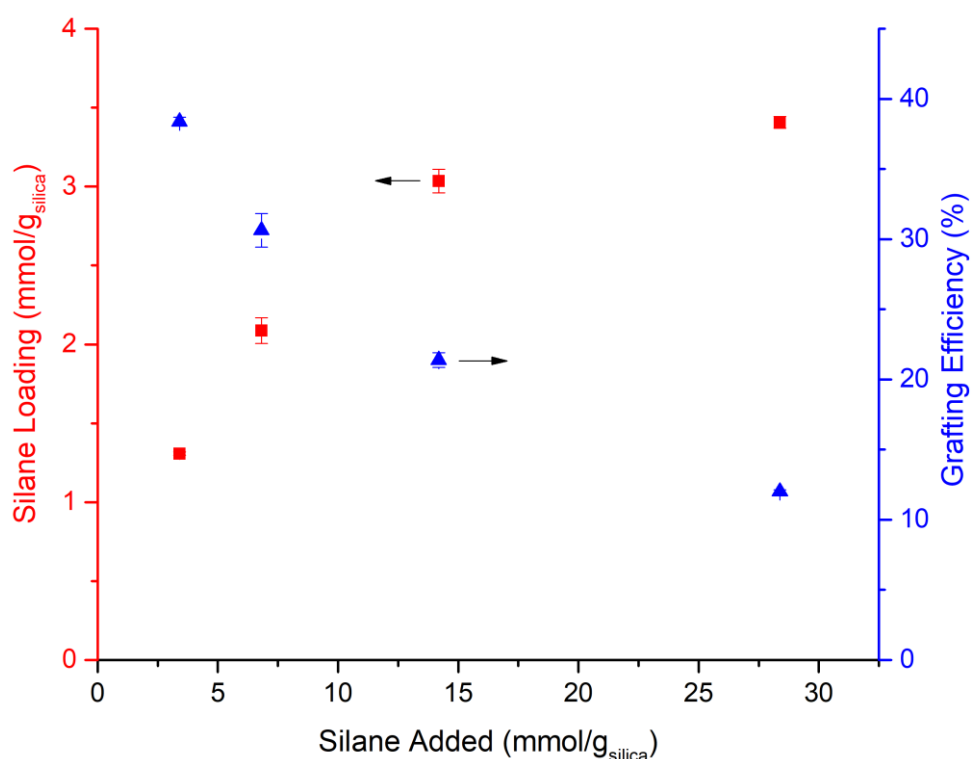


Figure 3.26. Silane loading and grafting efficiency *versus* silane added for APS-modified nanofibres.

TGA thermograms of functionalised silica nanofibres with differing APS loadings (Figure 3.27) exhibit two principal weight drops; one between 25 and 150°C (water, residual solvent and CO₂) and the other between 300 and 900°C (degradation of the grafted organic material). The height of the outgassing step increases with aminosilane loading. Furthermore, the onset of decomposition of the aminopropyl moieties appears to occur at a slightly lower temperature for the two higher loaded samples.

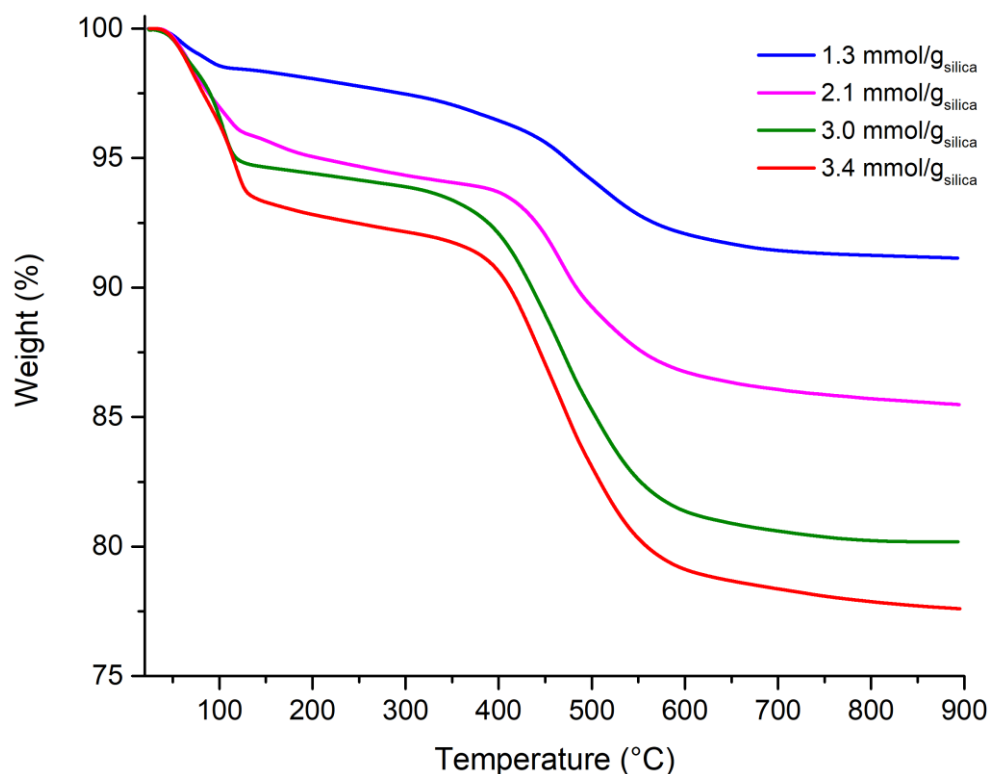


Figure 3.27. TGA thermograms of APS-modified nanofibrous silica of differing silane loadings. Test conditions: 10°C/min ramp rate, Ar purge.

FTIR spectra were recorded for the four APS-functionalised samples (Figure 3.28). The peaks in the wavenumber range of 1270 – 1720 cm^{-1} , assigned in Section 3.4 to bond vibrations in the aminopropyl branches and ammonium carbamate salt, are present in all four materials. The intensities of the six peaks in this region are considerably stronger in the highest loaded sample (3.4 mmol/g) than in the spectra of the middle two loadings (2.1 and 3.0 mmol/g) whilst the material with the lowest loading displays the weakest signals. Furthermore, there are two additional peaks in the material with a silane loading of 1.3 mmol/g at 1493 and 1452 cm^{-1} which are assigned to entrapped toluene from the grafting process.^[252, 261]

Regarding the IR bands in the siloxane (Si-O-Si) asymmetric vibration region (1250 – 1000 cm^{-1}), there is a slight increase in wavelength of the TO₄ Si-O-Si band with loading. For 1.3 and 2.1 mmol/g_{silica} materials, the TO₄ band is situated at *ca.* 1060 cm^{-1} . In contrast, for the higher loadings of 3.0 and 3.4 mmol/g_{silica}, the peak shifts to 1074 and 1084 cm^{-1} , respectively. The literature reports a shift of this peak to a higher wavenumber when organic groups are present in the silica.^[241] The fact there is progressive shift in this peak with silane loading indicates that the extent of blueshift of the band is linked to the degree of surface functionalisation.

The LO₆ and TO₆ bands on the spectrum for the highest APS-loaded material (3.4 mmol/g), which were previously assigned to six-membered cyclical structures from the grafted aminosilane, are not

visible on the spectra at lower loadings. These stretching modes may still exist but at lower intensities, causing them to be obscured by the dominant TO₄ band.

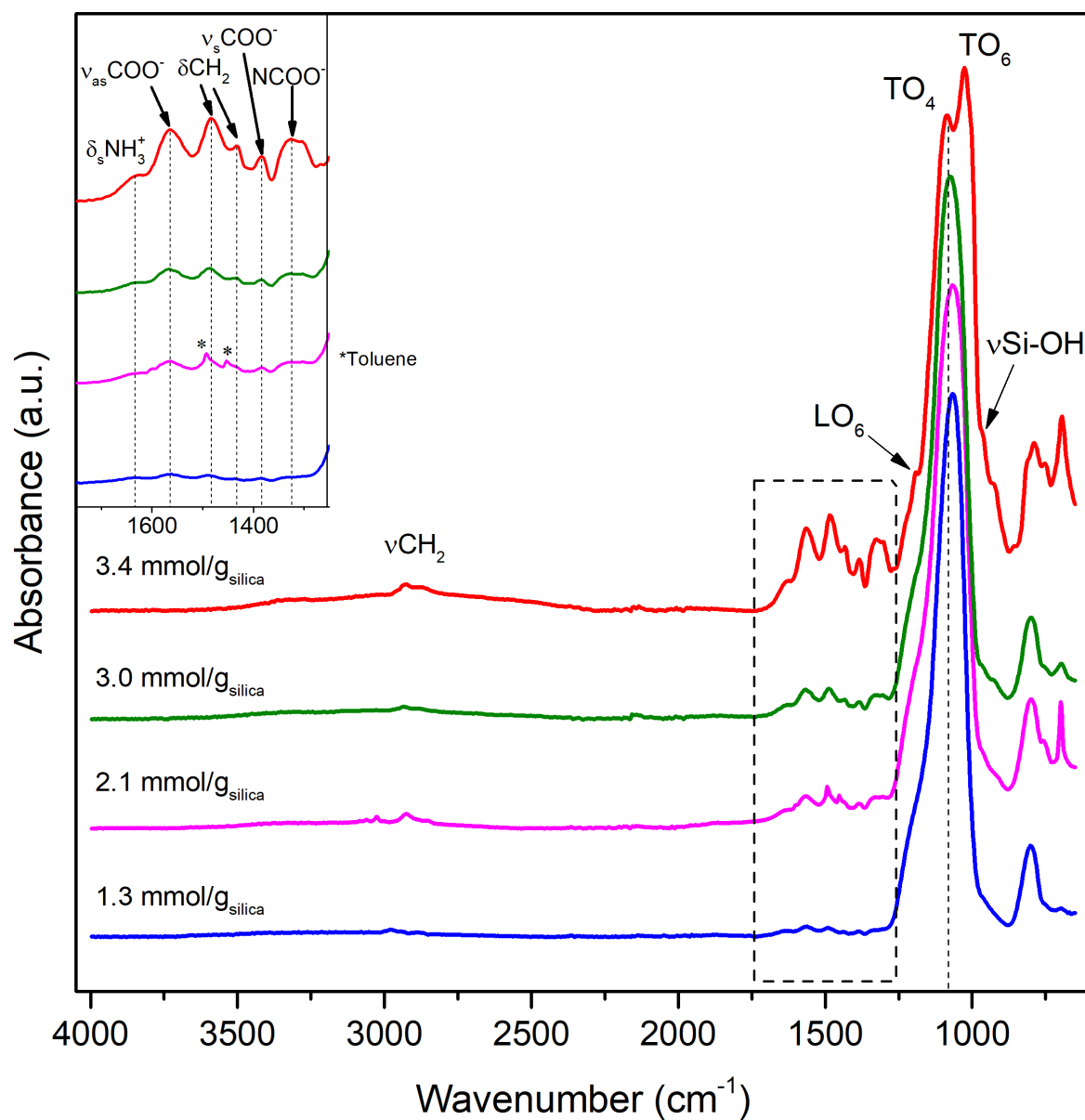


Figure 3.28. FTIR spectra of APS-modified silica nanofibres at various silane loadings.

¹³C solid-state NMR spectra were recorded for the four APS-modified materials (Figure 3.29). In all four spectra, it is clear that the C2 resonance is comprised of two overlapping peaks; one at 25 ppm (C2a) and the other at 23 ppm (C2b). A study from the literature by Chiang *et al.* also reported the occurrence of two chemical shifts for the middle carbon in aminopropyl moieties grafted onto silica. They proposed that the protonation of the amine group causes an electric field effect, resulting in an upfield shift of some of the C2 resonances. Therefore, C2a and C2b are associated with aminopropyl branches in which the amine group is non-protonated and protonated, respectively.^[262] The IR band

at 1630 cm^{-1} in Figure 3.28 above is ascribed to ammonium ions (NH_3^+) associated with a product of CO_2 chemisorption. Therefore, we propose that CO_2 adsorption is responsible for the C2b resonance. The ^{13}C spectra also show an increase in the intensity of the carbonyl peak at 165 ppm with aminosilane loading, which suggests that more CO_2 is chemisorbed on the fibres at higher grafting levels.

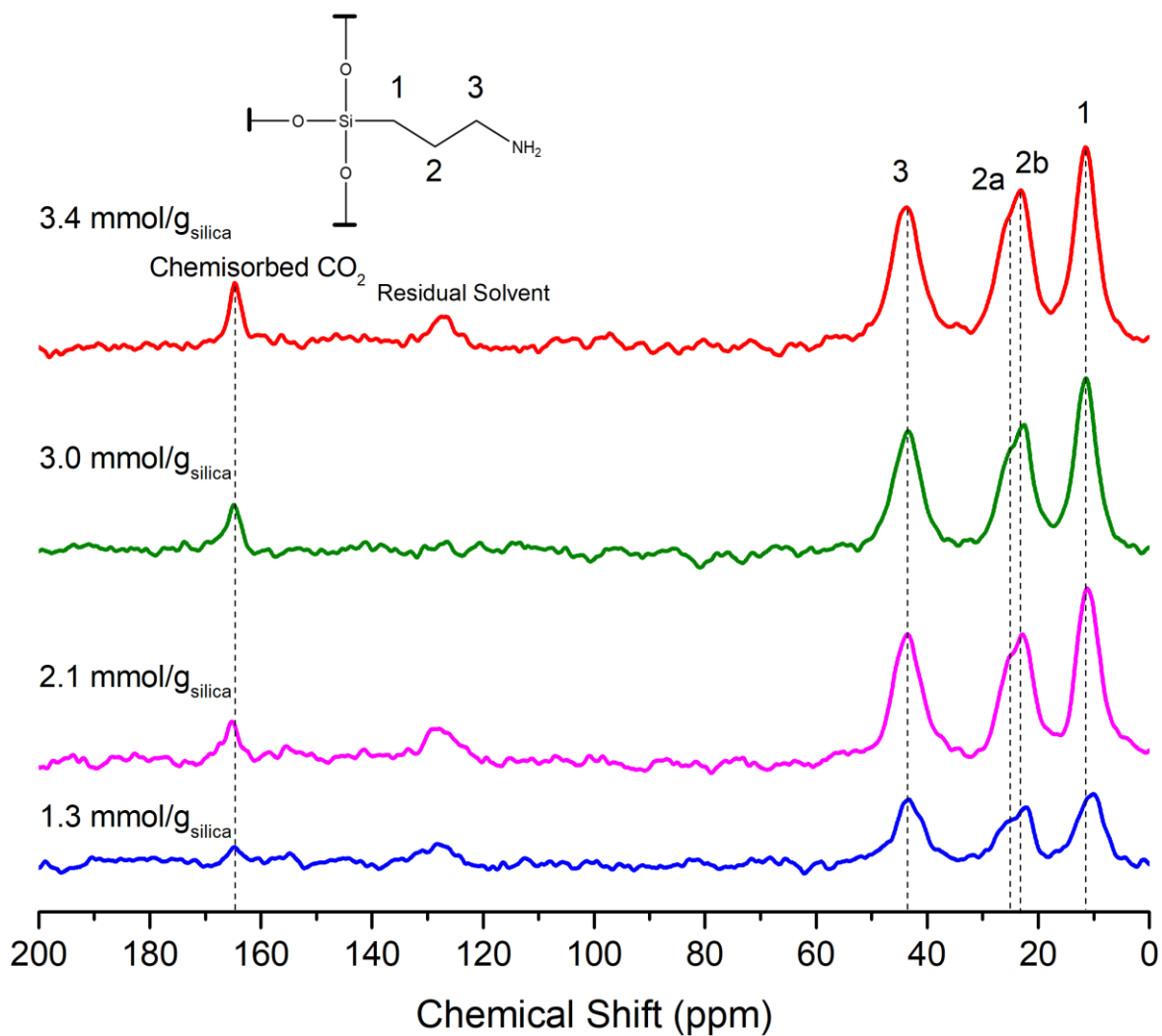


Figure 3.29. ^1H - ^{13}C CP-MAS NMR spectra for APS-functionalised nanofibrous silica at various silane loadings.

^{29}Si solid-state NMR spectra (Figure 3.30) all show resonances associated with the silica nanofibres (Q^3 at -101 ppm and Q^4 at -111 ppm) and the condensed silane (T^2 at -60 ppm and T^3 at -68 ppm).

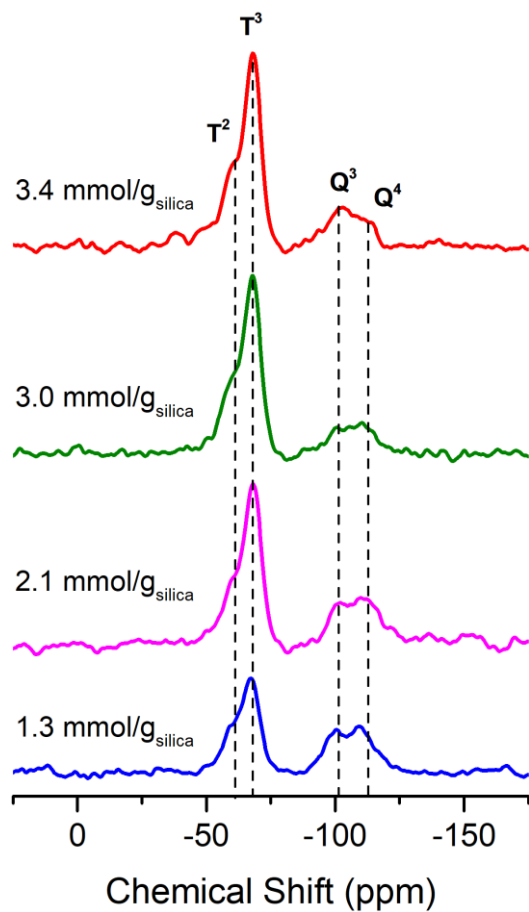
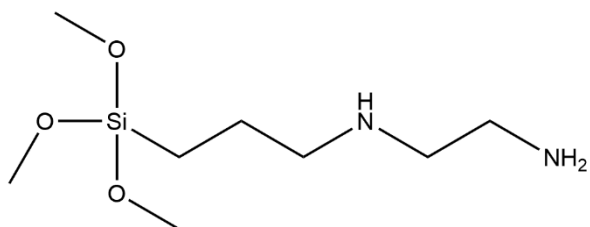


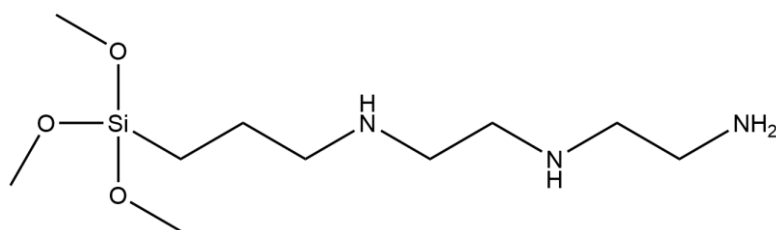
Figure 3.30. ^1H - ^{29}Si CP-MAS NMR spectra of APS-grafted nanofibrous silica at different silane loadings.

3.6 Effect of Silane Type on the Grafting Process

To investigate the impact of the silane type on the functionalisation of nanofibrous silica, additional silica samples were prepared and chemically modified with two other grafting agents; DAS (Scheme 3.4) and TAS (Scheme 3.5).



Scheme 3.4. Skeletal formula of N-[3-(Trimethoxysilyl)propyl]ethylenediamine (DAS).



Scheme 3.5. Skeletal formula of N1-(3-Trimethoxysilylpropyl)diethylenetriamine (TAS).

As with the APS-modified silicas, DAS and TAS-grafted materials exhibit an increase in silane loading with silane added (Figure 3.31a).

The grafting efficiencies of the DAS-modified nanofibres generally decreases with silane added in a similar fashion to the APS-loaded silicas (Figure 3.31b). At similar amounts of silane added, the grafting efficiency of DAS-loaded nanofibres is less than APS. The likely reason for this observation is steric hindrance; the bulkier R-group in the DAS reagent impedes the condensation of the grafting agent onto the surface of the nanofibres.

Like APS and DAS, TAS-grafted nanofibres show an initial large drop in grafting efficiency when the silane added is initially increased, from 37.5% at 2.1 mmol/g_{silica} to 24% at 4.2 mmol/g_{silica}. Yet increasing the silane added again to 8.7 mmol/g_{silica} causes no significant change in the grafting efficiency whilst at the highest amount of silane, the efficiency decreases slightly to 21.9%. Across the range of silane added, the efficiency of the TAS-modified nanofibres is generally higher than DAS but lower than APS. However, above 12.5 mmol/g_{silica}, the TAS efficiency slightly exceeds APS. The proposed reason for these unexpected observations with the TAS reagent is the interplay between steric hindrance and amine concentration on the grafting reaction. It has been reported that, under

hydrous conditions, amines catalyse the rate of hydrolysis of alkoxy silanes by deprotonating water molecules, forming nucleophilic hydroxyl anions which attack the alkoxy groups.^[263] APS, DAS and TAS contain one, two and three amine groups per molecule meaning that, at a fixed amount of silane added, the molar concentration of amines in the reaction mixture increases in the order TAS > DAS > APS. The initial drop in grafting efficiency of the TAS-functionalised nanofibres with silane added suggests that steric hindrance plays a bigger role in determining the final silane loading at low silane concentrations. However, at higher silane concentrations, the increasing amount of amine in the reaction mixture counteracts steric effects to some degree, resulting in a much smaller decrease in grafting efficiency. The exponential-like deterioration in grafting efficiency with silane loading for the APS and DAS-modified nanofibres suggests that the interplay between steric hindrance and amine concentration influences the grafting efficiency of these materials too.

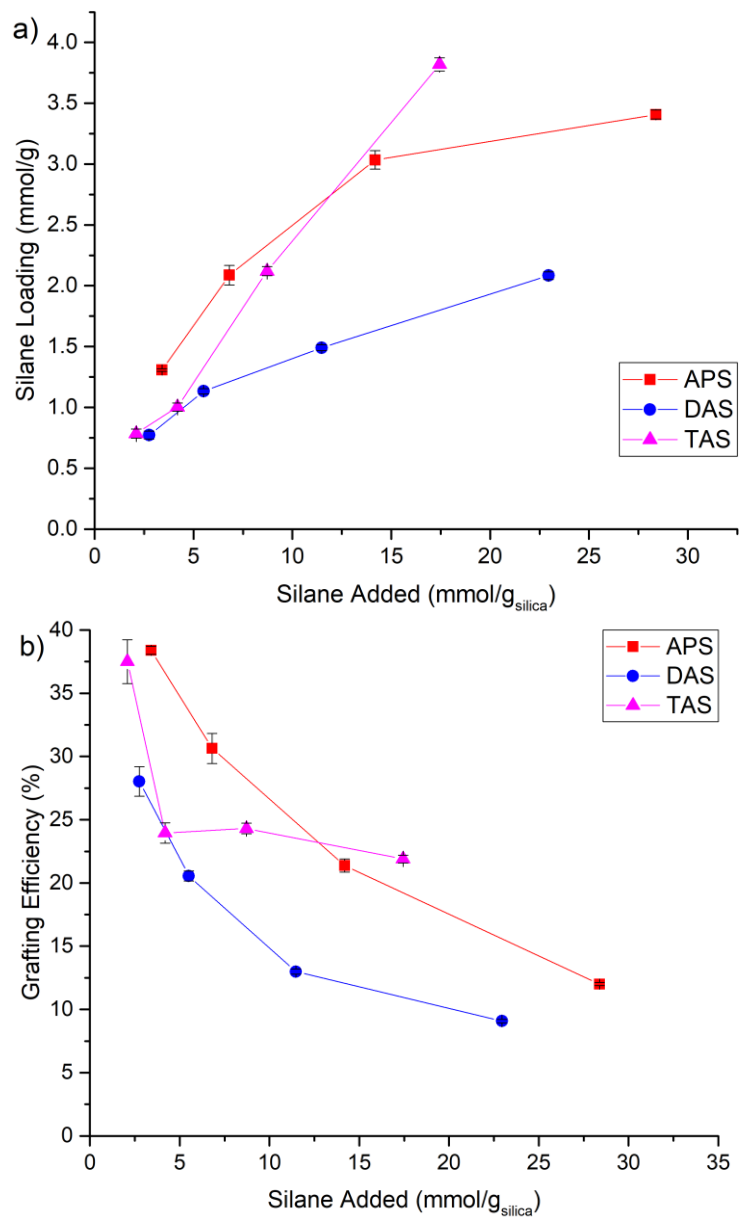


Figure 3.31. Silane loading (a) and grafting efficiency (b) *versus* silane added for silica nanofibres modified with three different silanes.

As with the APS-modified materials, two principal weight drops can be seen on the TGA isotherms of the diamine and triamine grafted materials (Figure 3.32 and Figure 3.33 respectively). The first (25 – 150°C) due to the outgassing of water, CO₂ and entrapped toluene from the reaction mixture and the second (300 – 900°C) from the decomposition of the tethered organic groups.

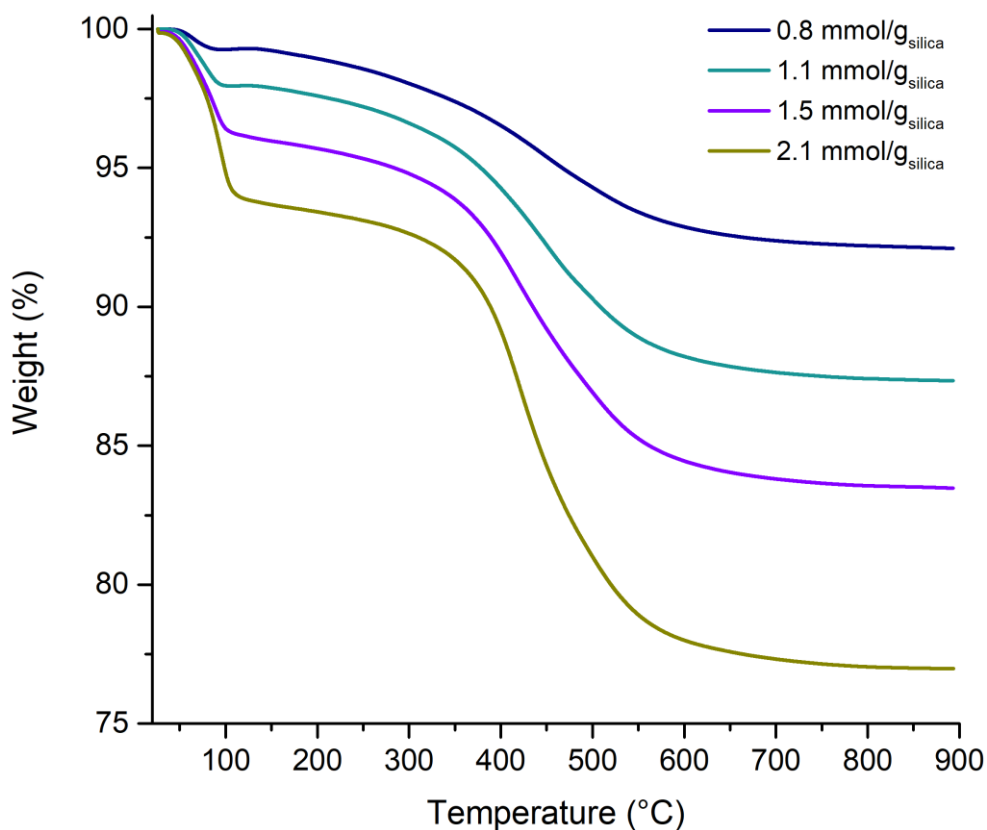


Figure 3.32. TGA thermograms of DAS-modified silica nanofibres prepared using different silane concentrations. Test conditions: 10°C/min ramp rate, Ar purge.

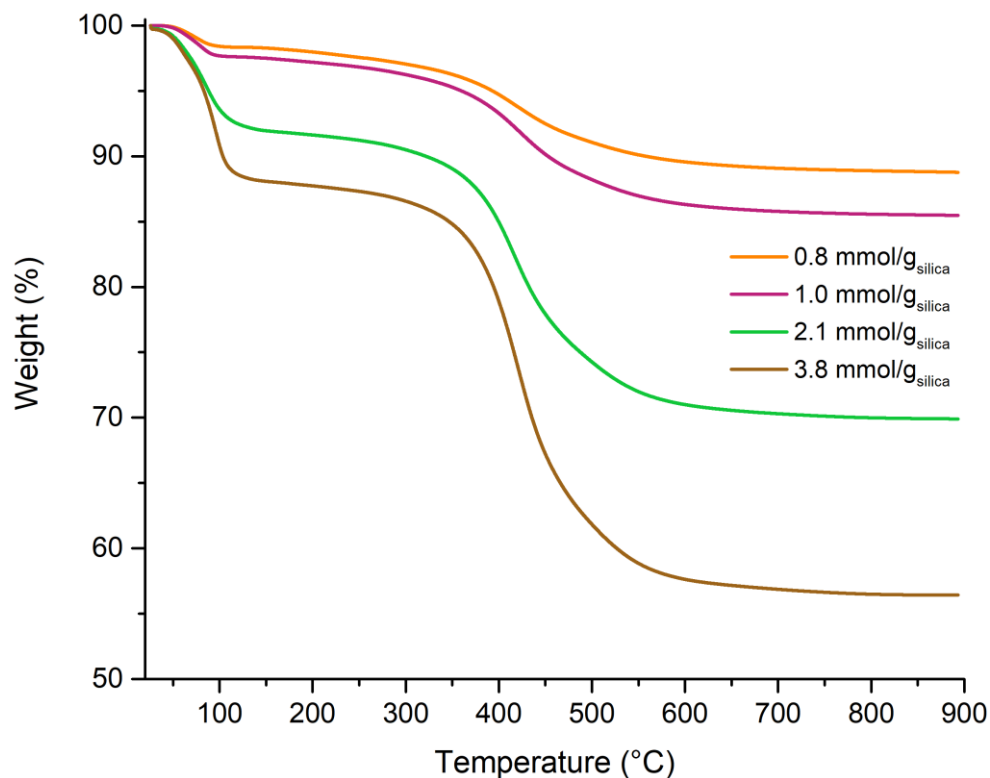


Figure 3.33. TGA thermograms of TAS-modified silica nanofibres prepared using different silane concentrations. Test conditions: 10°C/min ramp rate, Ar purge.

FTIR spectra of the DAS-modified silica nanofibres (Figure 3.34) show that, as with the APS-modified materials, infrared bands associated with the aminosilane are present between 1250 and 1750 cm^{-1} . The band at 1472 cm^{-1} corresponds to CH_2 scissoring, the peak at 1281 cm^{-1} is due to symmetric deformation of Si-CH_2 and the band at 1410 cm^{-1} is also attributed to the aminosilane, however, the exact assignment for this vibration cannot be identified.^[252, 264, 265] Silane peak intensities in this region are significantly higher for the material with the greatest loading of silane (2.1 mmol/g) compared to the other DAS-grafted materials. Two additional peaks at 1493 and 1452 cm^{-1} in the material with a DAS loading of 1.1 mmol/g are due to vibrations originating from entrapped toluene.^[252, 261] The highest-loaded material also shows two faint stretching peaks at *ca.* 2870 and 2930 cm^{-1} , corresponding to vibrations of the methylene groups (CH_2).^[252, 264, 265]

Evidence of CO_2 adsorption in the form of ammonium carbamate adducts is exhibited by the peaks at 1620, 1562 and 1310 cm^{-1} , corresponding respectively to the asymmetric deformation of ammonium ions (NH_{x+1}^+), asymmetric stretching of COO^- and a skeletal vibration of NCOO^- .^[253, 266, 267]

In the siloxane asymmetric stretching region (1250 – 1000 cm^{-1}), the DAS-modified spectra show similar features to those for the APS-functionalised materials studied in the previous sub-section. The wavenumber for the TO_4 Si-O-Si stretching mode increases with DAS loading from 1064 cm^{-1} at 0.8 mmol/g to 1082 cm^{-1} at 2.1 mmol/g. TO_6 and LO_6 siloxane stretching modes, previously

ascribed to cyclical aminosiloxane structures tethered to the nanofibres, are visible on the spectrum for the highest DAS-modified material.^[250]

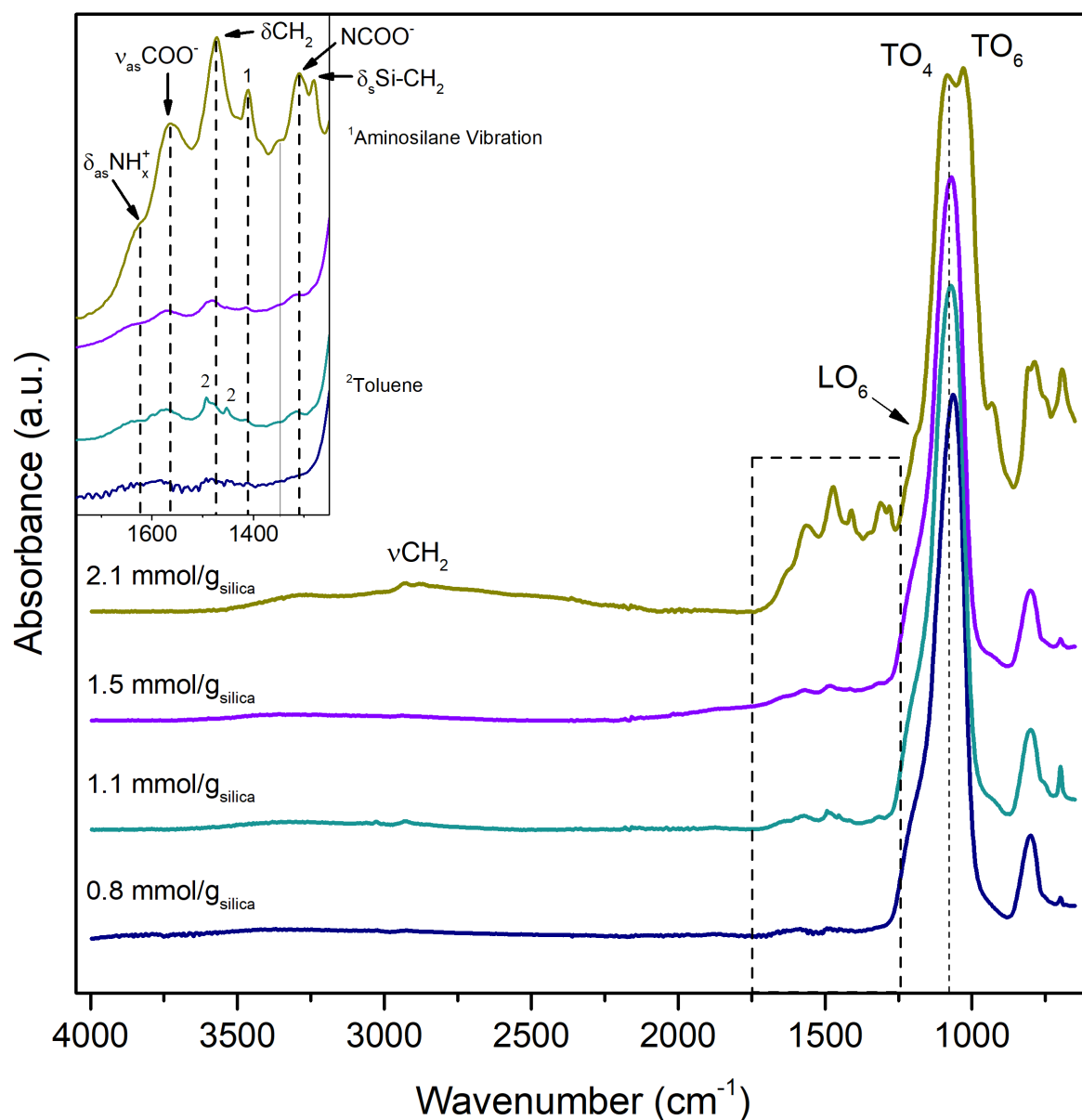


Figure 3.34. FTIR spectra of DAS-functionalised silica nanofibres..

FTIR spectra were also recorded for the four TAS-functionalised materials (Figure 3.35). The region between 1250 and 650 cm^{-1} is spectrally similar to APS and DAS-modified materials, with CH_2 scissoring at 1474 cm^{-1} , an aminosilane vibration at 1412 cm^{-1} and Si-CH_2 symmetric bending at 1410 cm^{-1} .^[252, 264, 265, 268] Ammonium carbamate bands can be seen at *ca.* 1630, 1558 and 1310 cm^{-1} , corresponding to NH_x^+ asymmetric bending, COO^- asymmetric stretching and NCOO^- skeletal vibration respectively.^[253, 266, 267] As expected, all aforementioned IR bands increase in intensity with silane loading.

In the material with the highest TAS loading, additional absorption bands at 2864 and 2930 cm^{-1} correspond to symmetric and asymmetric stretching of C-H respectively.^[252] Stretching of O-H and N-H bonds contribute to the broad absorption band between 3000 and 3500 cm^{-1} of this spectrum.^[269]

Similar spectral features to those seen in the APS and DAS materials are present in the siloxane asymmetric stretching region. First, the TO_4 peak shifts from 1063 cm^{-1} for the material with the lowest TAS loading to *ca.* 1074 cm^{-1} for the highest. Furthermore, at the highest TAS loading, TO_6 and LO_6 bands are discernible.^[250]

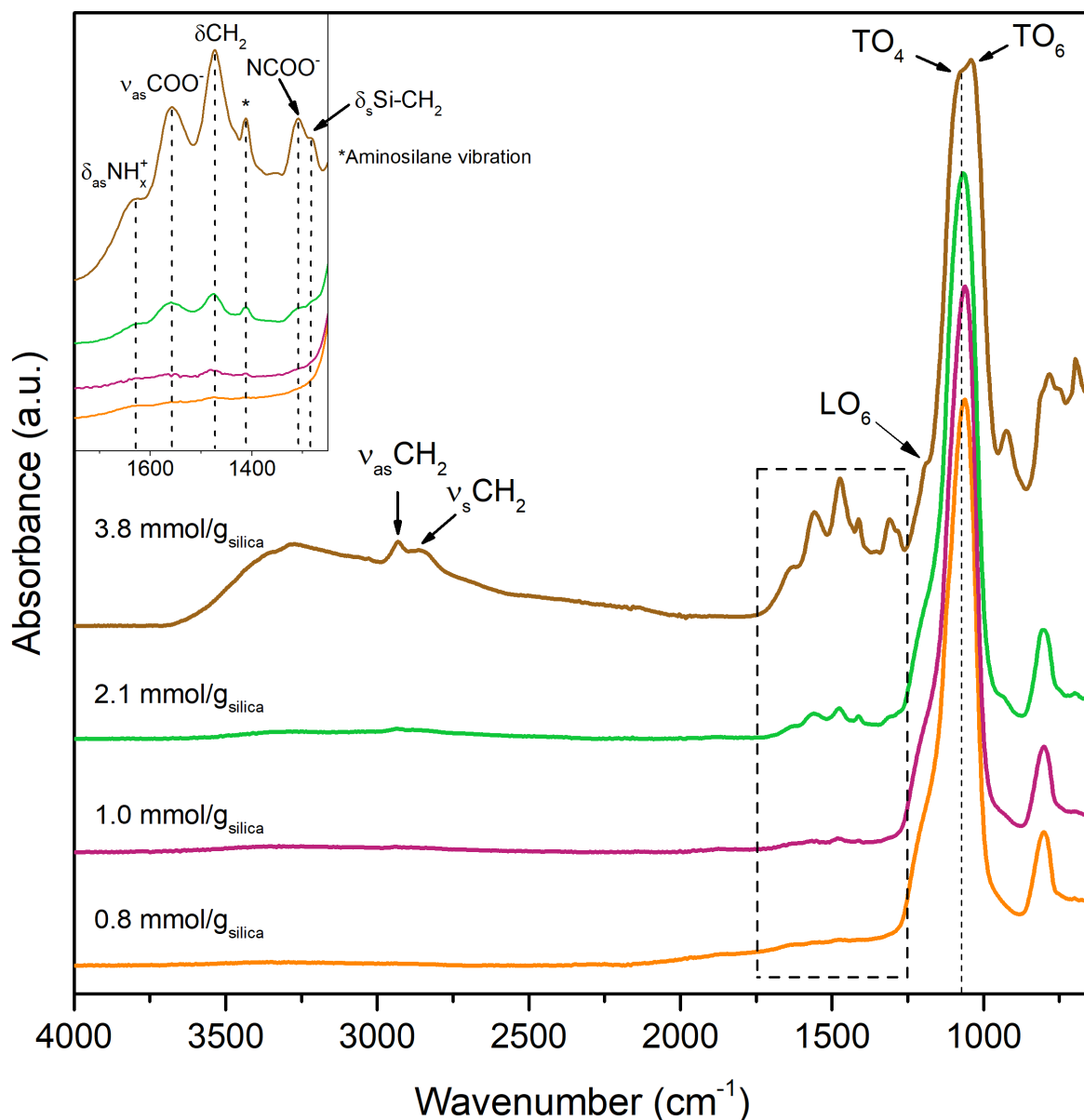


Figure 3.35. FTIR spectra of TAS-functionalised silica nanofibres.

^{13}C solid-state NMR spectra were recorded for the four DAS-grafted materials (Figure 3.36). Resonances associated with the aminosilane are visible between 5 and 65 ppm. Methylene peaks are

present at 11.8, 22.1, 41.1 and 51.9 ppm. The intensity of the aminosilane resonances increases with the extent of functionalisation. There is also a carbonyl peak at 165 ppm associated with CO₂ chemisorption on the nanofibres. The intensity of this peak increases with silane loading, suggesting the presence of increasing amounts of CO₂-amine adducts.^[258]

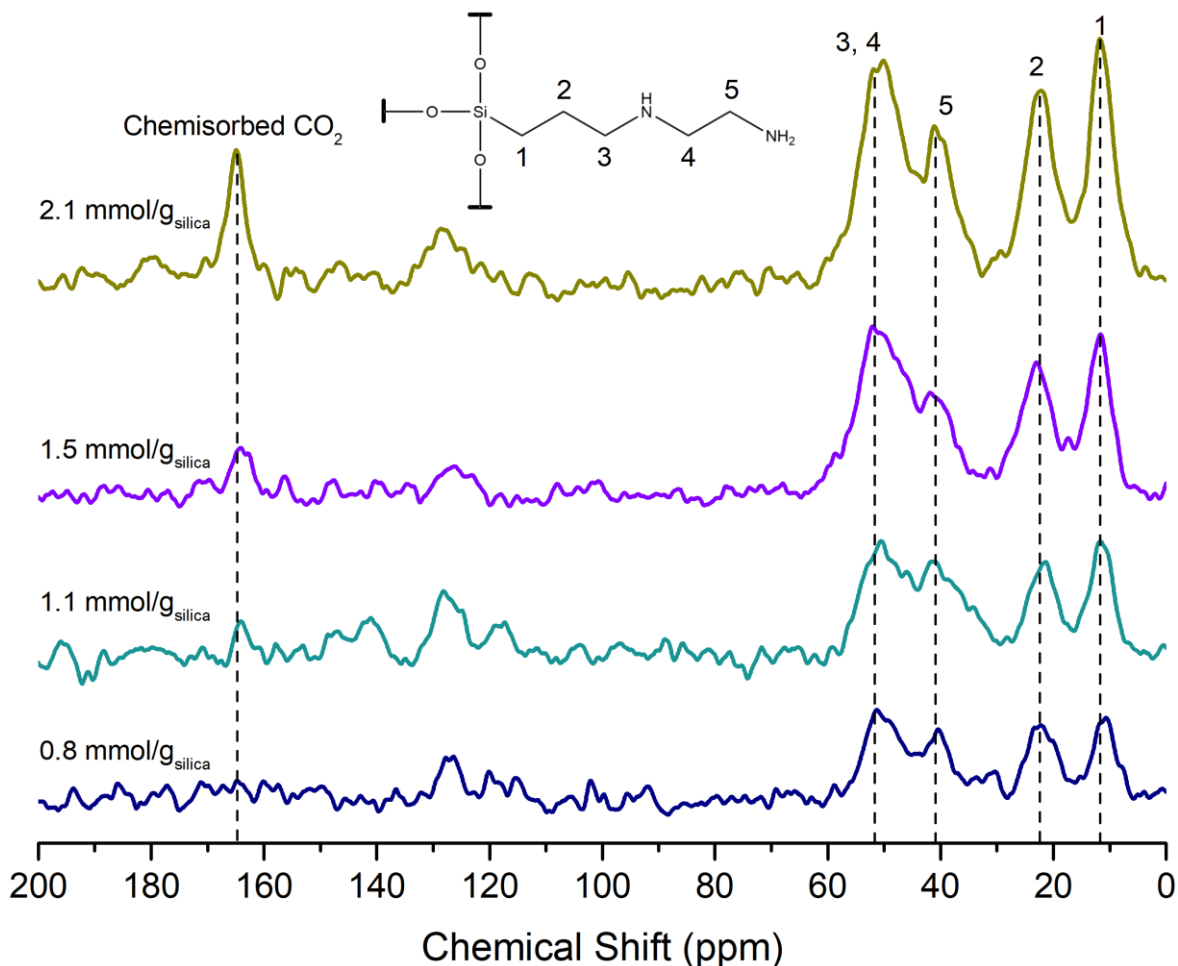


Figure 3.36. ¹H-¹³C CP-MAS NMR spectra for DAS-functionalised nanofibres at different silane loadings.

¹³C solid-state NMR spectra were also recorded for the TAS-functionalised materials (Figure 3.37). As with the other grafting agents, the TAS resonances are situated between 5 and 65 ppm. Methylene peaks are present at 12.2, 22.7, 41.7 and 48.6 ppm.^[270-272] As with the APS and DAS-functionalised materials, there is an additional resonance at 165 ppm due to the presence of chemisorbed CO₂.

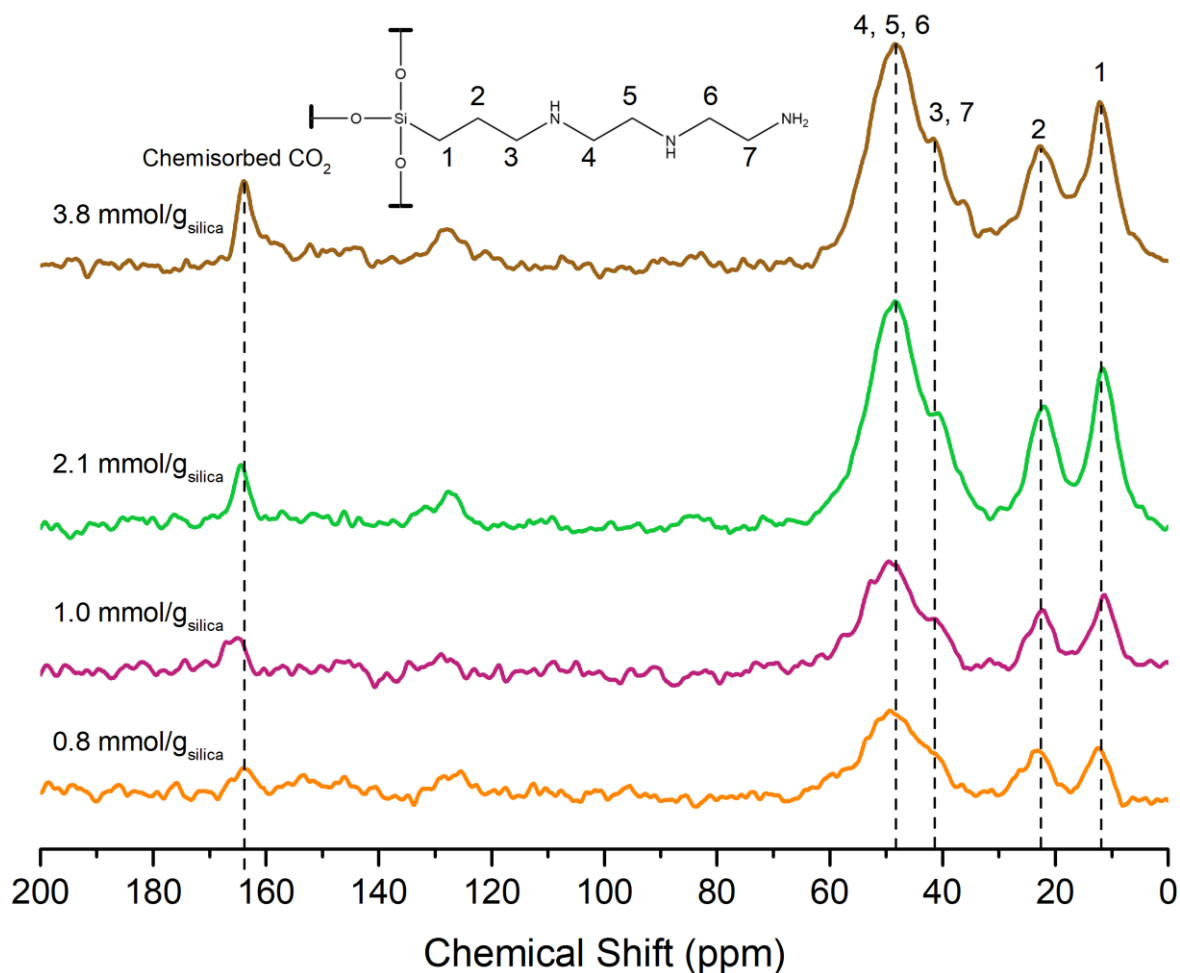


Figure 3.37. ^1H - ^{13}C CP-MAS NMR spectra for TAS-functionalised nanofibres at different silane loadings.

Similar resonances to those observed with the APS-grafted silicas are seen in the ^{29}Si spectra of the DAS and TAS functionalised materials (Figure 3.38 and Figure 3.39, respectively). For both DAS and TAS-functionalised materials, peaks at -101 ppm (Q^3) and -109 ppm (Q^4) originate from the silica substrate whilst those at -60 (T^2) and -68 ppm (T^3) are from the condensed aminosilane.

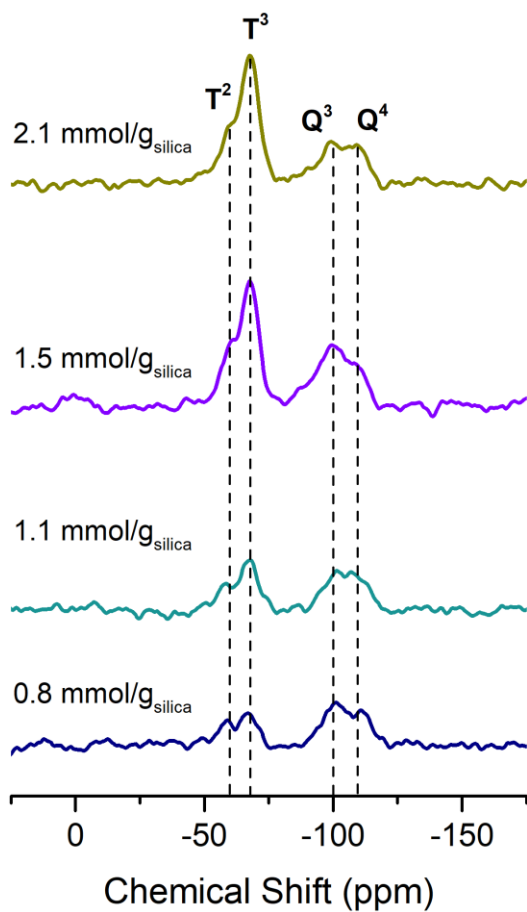


Figure 3.38. ^1H - ^{29}Si CP-MAS NMR spectra of DAS-grafted silica nanofibres at different loadings.

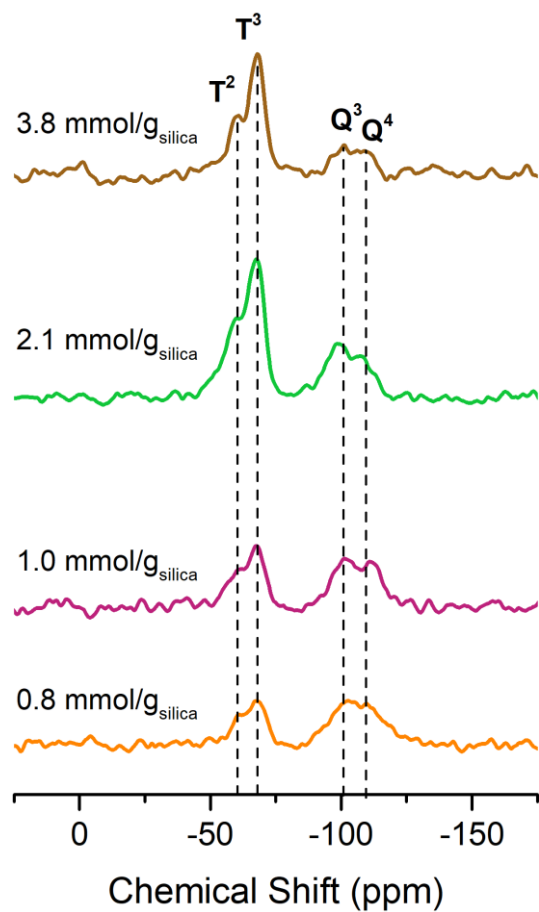


Figure 3.39. ^1H - ^{29}Si CP-MAS NMR spectra of TAS-grafted silica nanofibres at different loadings.

3.7 Effect of Water on the Grafting Process

To investigate how water affects the grafting process, two samples of nanofibrous silica were functionalised anhydrously using two different concentrations of APS (2.5 and 5.0 ml/g_{silica}, corresponding to molar concentrations of *ca.* 14 and 28 mmol/g_{silica} respectively). These were then compared to wet-grafted samples.

Under anhydrous conditions, doubling the APS concentration resulted in a small increase in silane loading from 1.5 to 1.8 mmol/g (Figure 3.40a). The absence of water in the reaction mixture should prevent cross-linking of silane molecules. In theory, this means that the extent of functionalisation is limited by the density of surface silanols on the silica surface. Therefore, the marginal enhancement in silane loading after doubling the silane concentration suggests that the majority of the silanols on the surface of the nanofibres have already been consumed at the lower concentration.

At a fixed APS concentration, grafting with the addition of water augments the silane loading. For example, in the reaction mixture with a silane concentration of 14 mmol/g_{silica}, the resulting silane loading is 1.5 mmol/g_{silica} for dry grafting compared to 3.0 mmol/g_{silica} for wet grafting. After doubling the aminosilane concentration, the grafting efficiency decreases regardless of the absence or presence of water in the reaction mixture (Figure 3.40b).

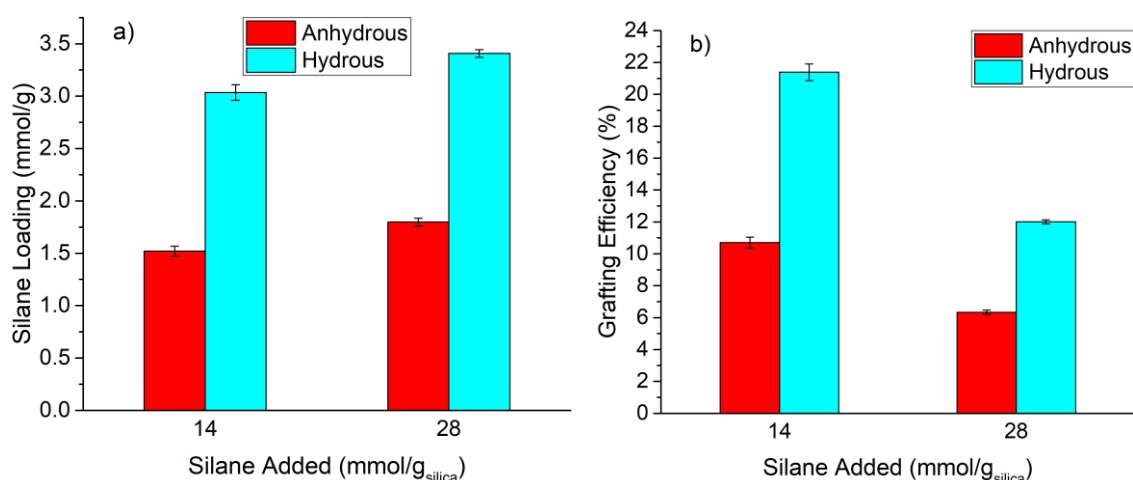


Figure 3.40. Silane loadings (a) and corresponding grafting efficiencies (b) of nanofibrous silica functionalised in anhydrous and hydrous conditions.

TGA, FTIR, and NMR analyses of a dry and wet-grafted material with similar silane loadings (1.5 and 1.3 mmol/g respectively) were carried out. The dry-grafted material has a similar TGA profile to the wet-grafted material with two principal weight drops, one between 25 and 150°C corresponding to the removal of adsorbed species (water, toluene and CO₂) and a second between 300 and 900°C

due to the decomposition of the organic content (Figure 3.41). Despite having similar silane loadings, the first weight drop in the dry-grafted trace is over twice that of the hydrous-grafted material (3.6 and 1.6 wt% respectively).

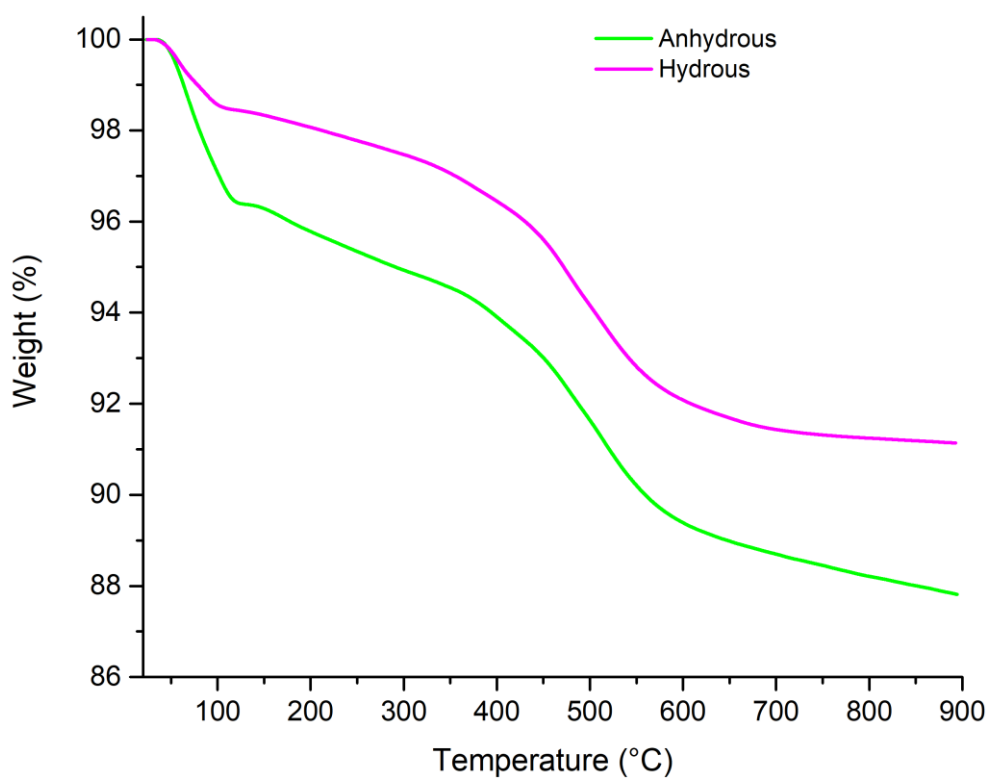


Figure 3.41. TGA traces of APS-modified silica grafted under anhydrous (green) and hydrous conditions (pink). Test conditions: 10°C/min ramp rate, Ar purge.

The anhydrous-grafted sample has the same infrared vibrational bands as the hydrous-grafted sample (Figure 3.42). This shows that the materials are chemically similar.

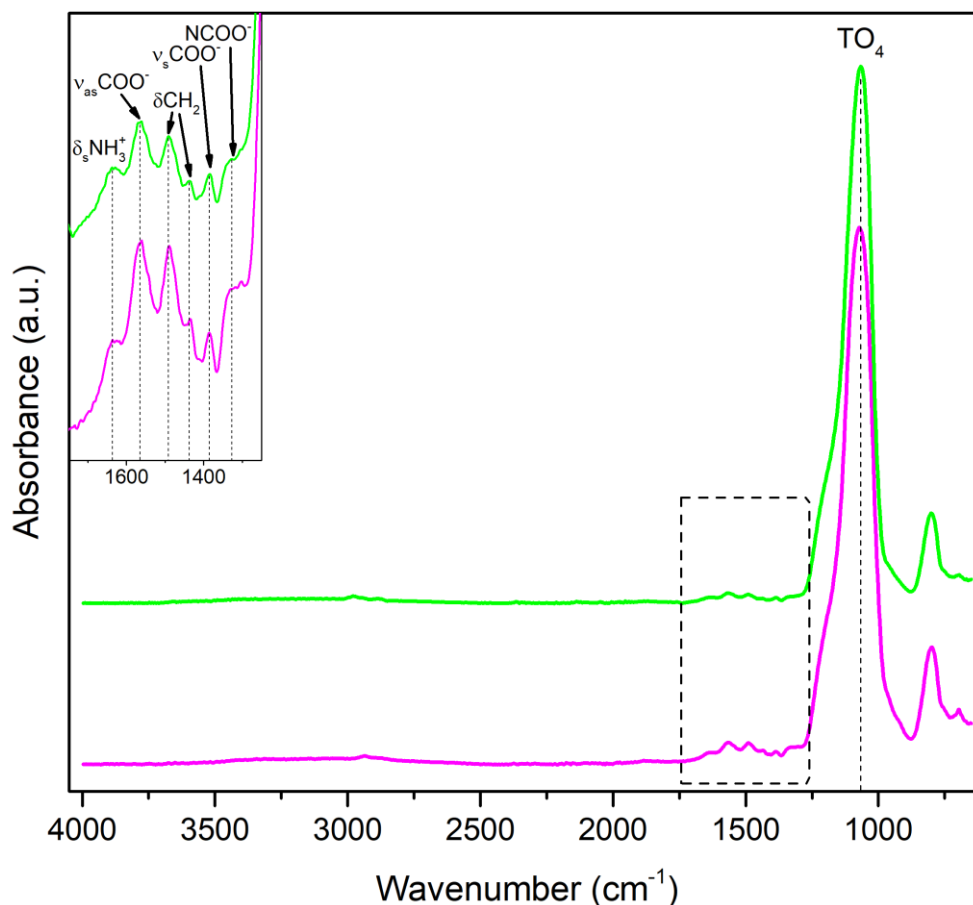


Figure 3.42. FTIR spectra of silica nanofibres grafted under anhydrous (pink) and hydrous (green) conditions with comparable silane loadings.

^{13}C solid-state NMR spectra were recorded for the two samples (Figure 3.43). The spectrum of the anhydrous-modified material exhibits four resonances assigned to the methylene groups in the grafting agent at 10.9 (C1), 22.9 (C2b), *ca.* 24.4 (C2a) and 43.5 ppm (C3). A small shoulder on the C3 peak at *ca.* 51 ppm might be a resonance from unreacted methoxy (O-CH₃) groups.^[256] The middle methylene peak associated with non-protonated amines (C2a) appears to have a higher relative intensity on the spectrum for the anhydrous-grafted nanofibres. This implies that less amines are protonated in this material compared to its hydrous-grafted counterpart.

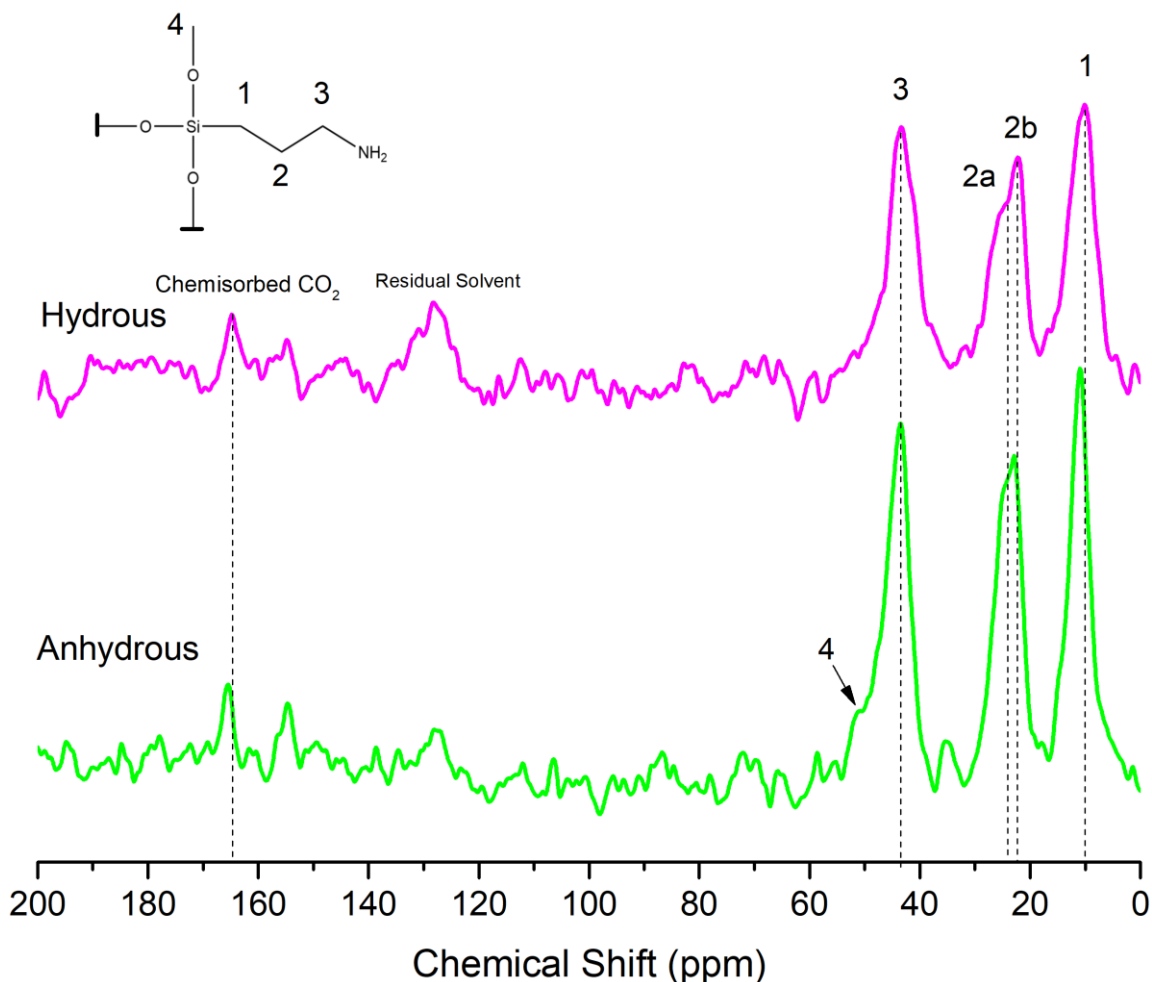


Figure 3.43. ^1H - ^{13}C CP-MAS NMR spectra of APS-functionalised silica nanofibres grafted under anhydrous and hydrous conditions with comparable silane loadings.

Unexpectedly, the ^{29}Si NMR spectrum of the anhydrous-grafted sample (Figure 3.44) reveals the presence of partially-condensed silane on the nanofibres, as evidenced by the T¹ (R-SiOSi(OH)₂) and T² (R-Si(OSi)₂OH) resonances at -49 and -60 ppm, respectively. In anhydrous conditions, the silane should react with the silica surface *via* a one-step solvolysis reaction, without the formation of silanol intermediates (see Section 2.1.4 for details). Thus, in theory, there should only be T³ sites (R-Si(OSi)₃) in the anhydrous-grafted nanofibres. The presence of T¹ and T² resonances suggests that at least some of the silanes have tethered onto the nanofibres *via* the hydrolysis-condensation mechanism underpinning hydrous grafting. In other words, there were likely trace amounts of water in the ‘anhydrous’ reaction mixture, possibly from the silica nanofibres.

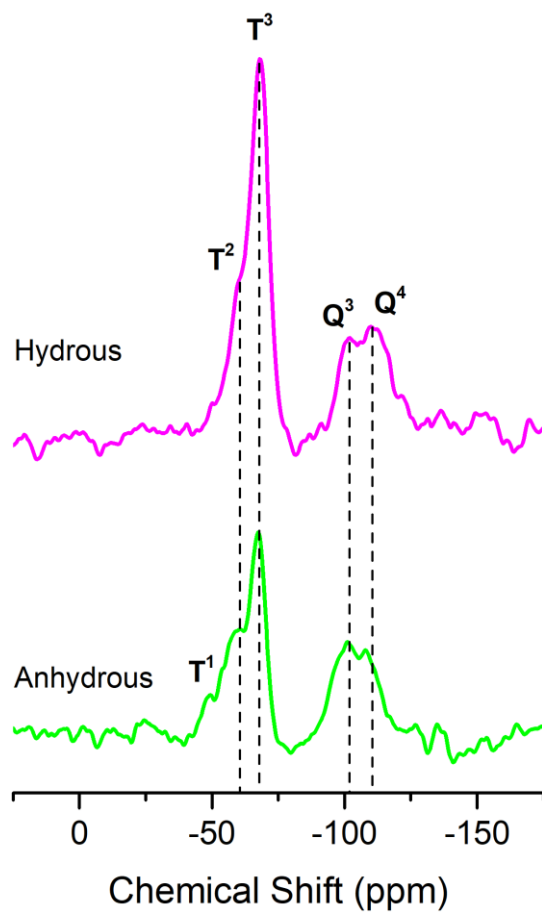


Figure 3.44. ^1H - ^{29}Si CP-MAS NMR spectra of silica nanofibres grafted under anhydrous (green) and hydrous (pink) conditions.

3.8 Comparison with Silane Grafting of SBA-15 Mesoporous Silica

To study how the physiochemical properties of amine-functionalised nanofibrous silica compare with other porous supports, SBA-15 mesoporous silica was prepared as a benchmark material. The SAXS diffraction pattern of the material (Figure 3.45) shows three interference peaks characteristic of the bidimensional hexagonal lattice of pores in SBA-15, thus verifying successful preparation of the mesoporous silica.^[164]

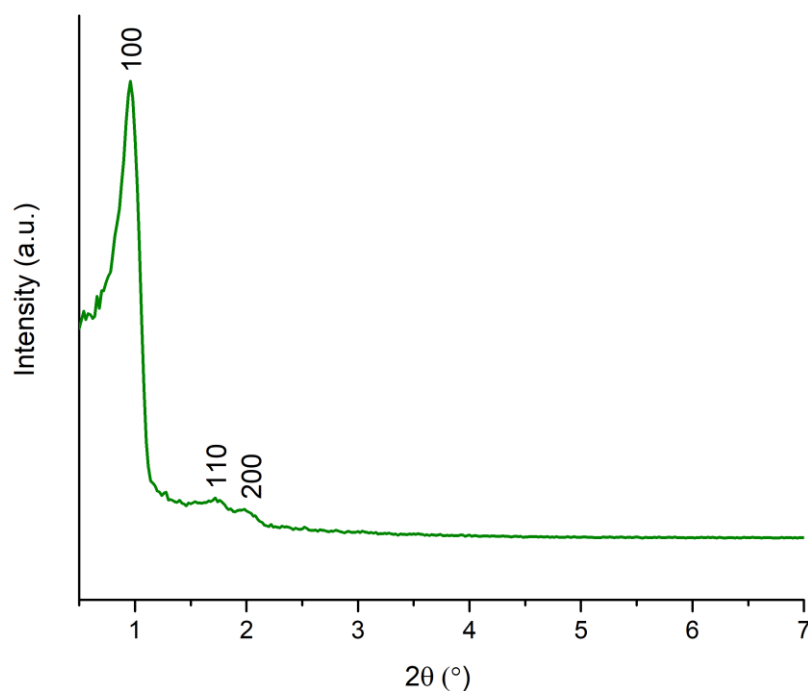


Figure 3.45. SAXS diffraction pattern of SBA-15 showing three interferences peaks indexed as (100), (110) and (200) Bragg reflections, characteristic of hexagonal mesoporous silica.^[164]

A TGA thermogram of the as-synthesised SBA-15 is compared to a sample of silica nanofibres (Figure 3.46). Unlike the nanofibres, the SBA-15 thermogram shows a significant decrease in weight between 25 and 900°C. There are two main weight drops: one between 25 and 120 °C (6.6 wt%) and another between 140°C and 900°C (6.1 wt%). These weight changes are attributed to moisture removal and silanol condensation, respectively.^[273] The weight drop associated with dehydroxylation is much bigger for SBA-15 compared to the silica nanofibres (6.1 and 1.4 wt% respectively). This implies that SBA-15 silica has a higher silanol content.

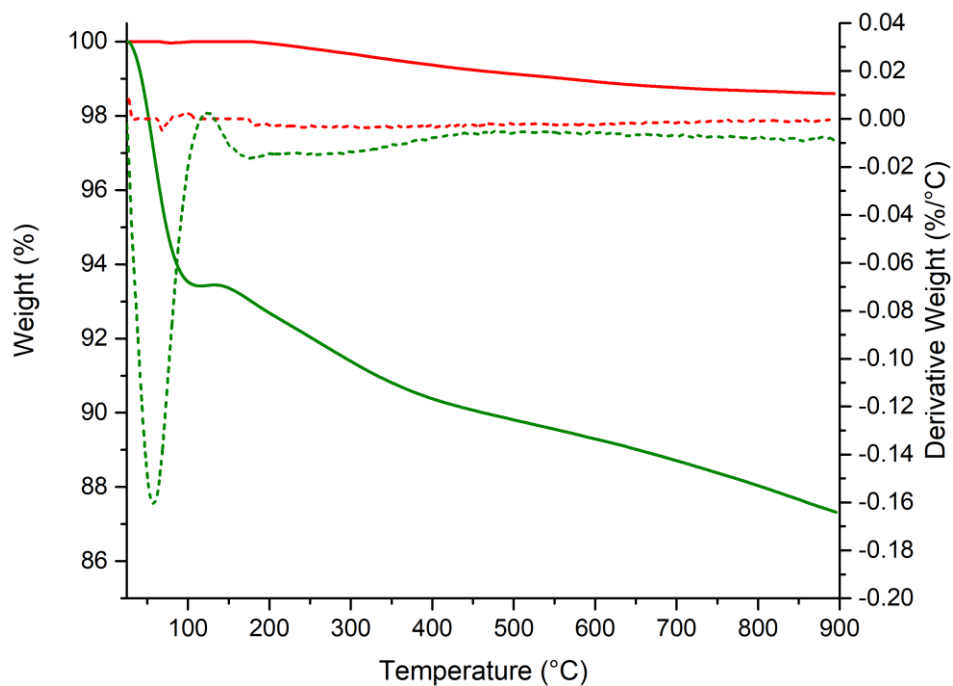


Figure 3.46. TGA/DTG thermograms of SBA-15 (green) and silica nanofibres (red). Test conditions: 10°C/min ramp rate, Ar purge.

The SBA-15 sample was functionalised with APS and its physiochemical properties were compared to APS-grafted nanofibrous silica prepared using the same grafting conditions (0.6 ml_{water}/g_{silica}, 5 ml_{silane}/g_{silica}). Both their TGA/DTG traces have similar profiles (Figure 3.47), comprising two outgassing events between 25 and 150°C (desorption of small molecular species such as water and CO₂) followed by decomposition of the grafted organic moieties between 300 and 900 °C.

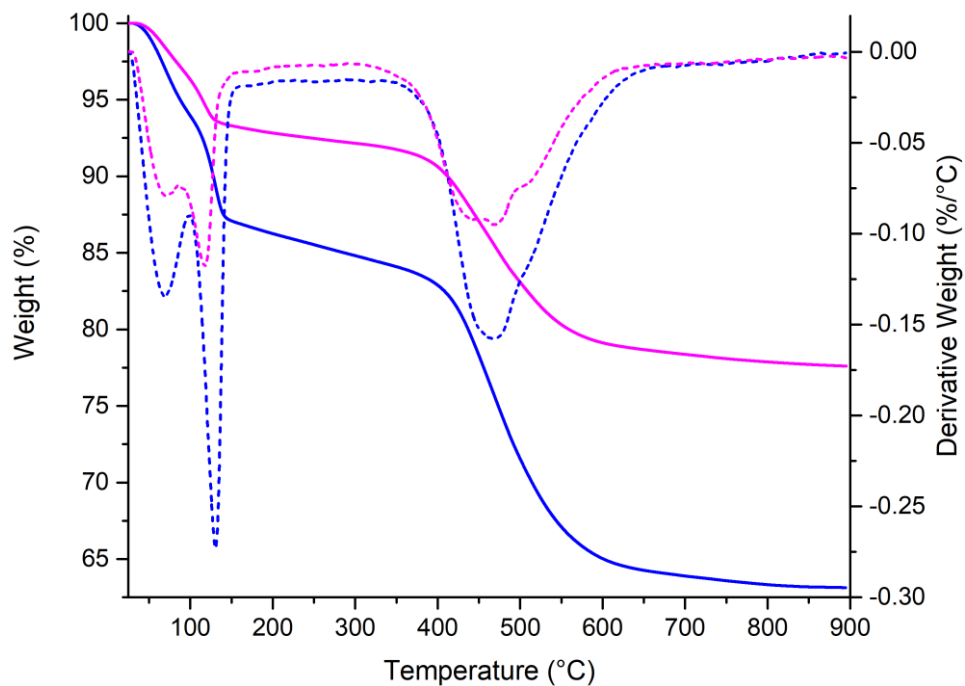


Figure 3.47. TGA/DTG thermograms of APS-modified silicas; SBA-15 (blue) and nanofibres (pink). Test conditions: 10°C/min ramp rate, Ar purge.

Based on the TGA results, the loading of condensed silane on the SBA-15 support was calculated. Under the same grafting conditions, the modified SBA material contains 6.2 mmol/g_{silica} of APS, 50% more than the silica nanofibres (Figure 3.48).

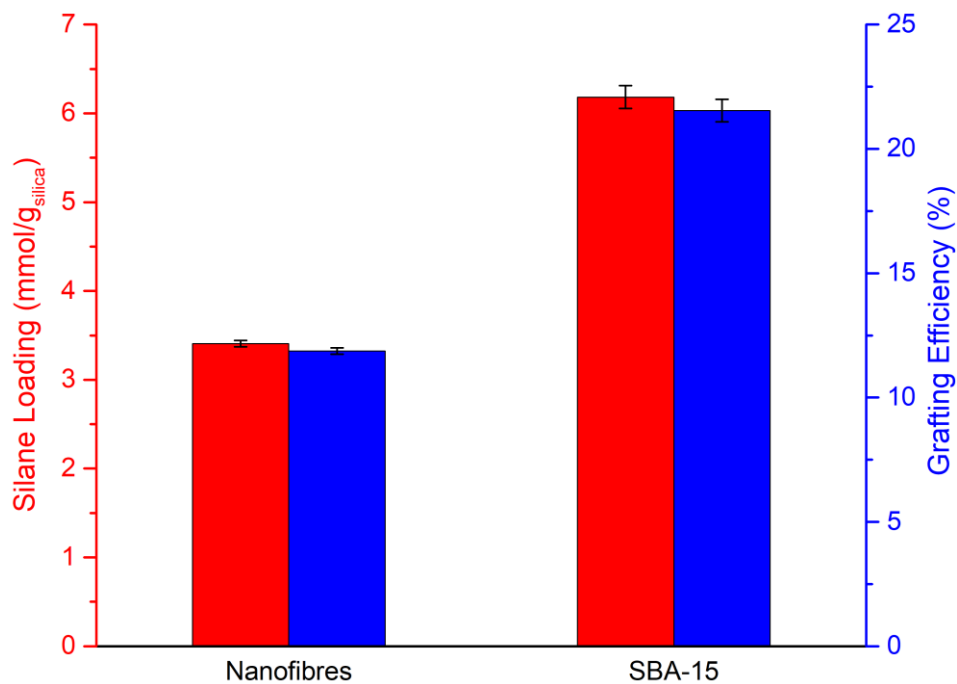


Figure 3.48. Aminosilane loading and efficiency for silica nanofibres and SBA-15 silica grafted under the same conditions (APS, 5 ml_{AS}/g_{silica}, 0.6 ml_{water}/g_{silica}).

Owing to technical difficulties with the instrumentation, the BET surface area of the as-synthesised SBA-15 could not be obtained. However, a paper which used the same recipe for the preparation of SBA-15 reported a specific surface area of 570 m²/g,^[274] over four times higher than the silica nanofibres. The higher specific surface area, together with the greater abundance of tethering sites (silanols) may explain the superior grafting efficiency of SBA-15.

The FTIR spectrum of SBA-15 was compared with that of the silica nanofibres (Figure 3.49). The main Si-O-Si asymmetric stretching vibration is at 1057 cm⁻¹ and is assigned to TO₄.^[240-242] A peak at 802 cm⁻¹ is attributed to the symmetrical stretching of siloxane bonds.^[243] Both of these peaks also appear in the spectrum of the silica nanofibres.

Several features on the SBA-15 spectrum are assigned to vibrational modes associated with the hydroxyl groups. Firstly, a stretching mode of silanol groups (Si-OH) is clearly visible at 970 cm⁻¹. This band is absent in the spectrum for the silica nanofibres supporting the theory that the SBA-15 material has a higher density of silanol groups. Secondly, a small peak at 1631 cm⁻¹ is assigned to a bending mode of water. Again, this is absent in the IR spectrum of the silica nanofibres, suggesting SBA-15 is more hygroscopic. TGA supports this hypothesis, as there is a considerable weight change between 25 and 120°C in SBA-15 which corresponds to the removal of surface-bound water. On the other hand, the silica nanofibres exhibit negligible weight loss in that temperature range. Lastly, a broad band between 3000 and 3750 cm⁻¹ in the SBA-15 spectrum is attributed to a stretching mode of O-H. Both hydroxyl groups on the silica surface and entrapped water contribute to infrared absorbance in this broad absorption band.^[241]

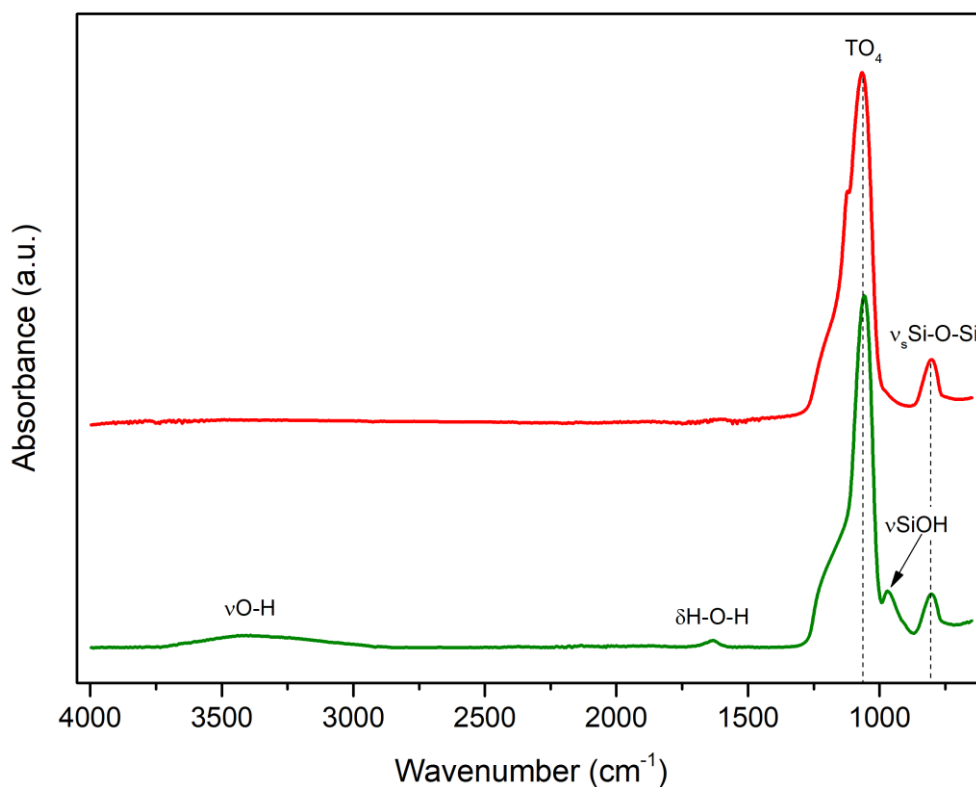


Figure 3.49. FTIR spectra of SBA-15 (green) and silica nanofibres (red).

An FTIR spectrum was recorded for the APS-functionalised SBA-15 and compared to its nanofibrous counterpart (Figure 3.50). After functionalisation, the dominant siloxane asymmetric peak is situated at 1028 cm^{-1} and is assigned to TO_6 .^[250] As with the TO_6 peak in the spectrum of the functionalised silica nanofibres, this vibration is theorised to originate from cross-linked aminosilane molecules. Between 1750 and 1250 cm^{-1} there are peaks associated with the R-group of the aminosilane, all at approximately the same wavenumbers as the APS-modified nanofibres. Stretching modes of the methylene groups in the aminopropyl branches are at 2870 and 2930 cm^{-1} .^[252-254] The TO_4 infrared band, clearly visible in the spectrum of the APS-functionalised nanofibres, cannot be discerned in the APS-SBA-15 spectrum and is probably overlapping with the TO_6 IR band.

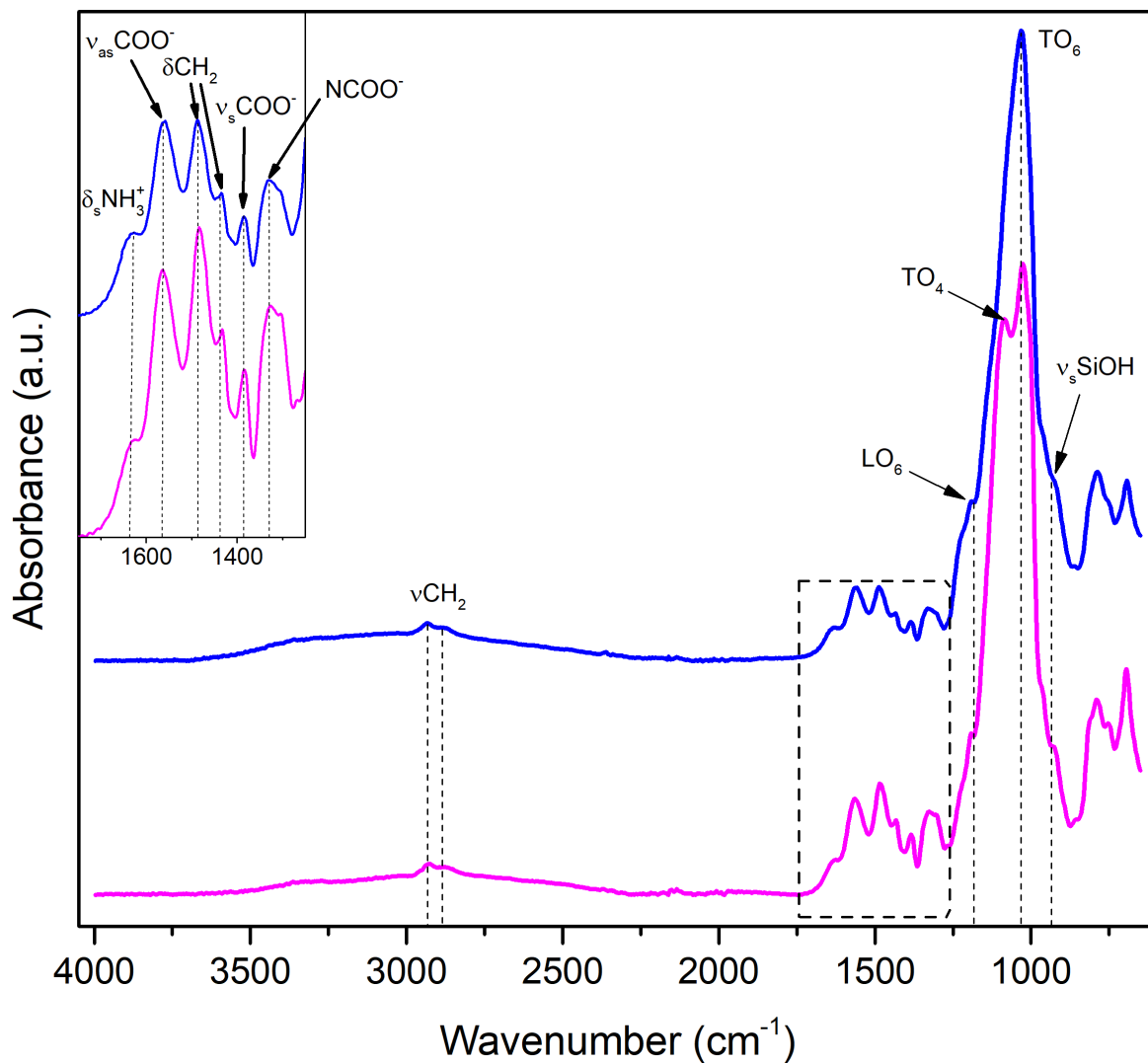


Figure 3.50. FTIR spectra of APS-functionalised SBA-15 (blue) and silica nanofibres (pink).

The 1H - ^{13}C CP/MAS NMR spectrum of the APS-modified SBA-15 shows methylene peaks at the same chemical shifts as the functionalised nanofibres. There is also a carbonyl resonance at 165 ppm due to chemisorbed CO_2 (Figure 3.51).^[258] The peak intensities of the methylene resonances are greater in the functionalised SBA-15 spectrum, likely due to the material's higher organic loading.

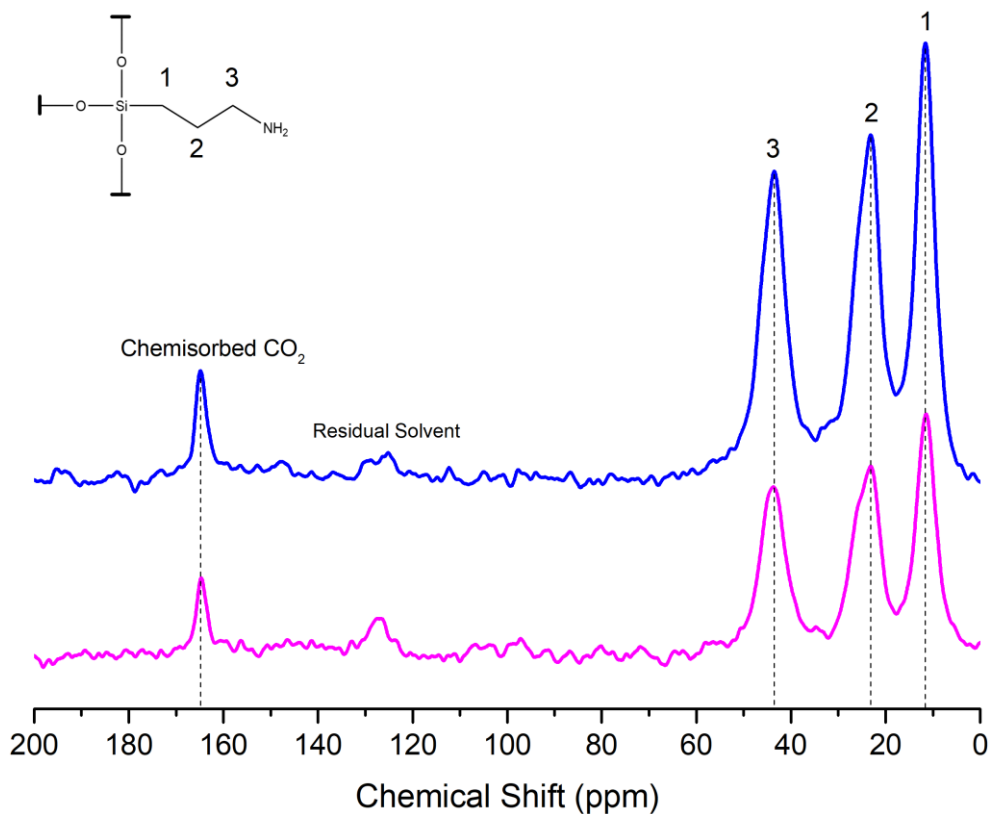


Figure 3.51. ^1H - ^{13}C CP-MAS NMR spectra of APS-functionalised SBA-15 (blue) and silica nanofibres (pink).

Concerning the ^{29}Si solid-state NMR spectrum of unmodified SBA-15 (Figure 3.52), the peak at -101 ppm is assigned to Q^3 (vicinal/isolated silanol) whilst the shoulders at -89 and -111 ppm are ascribed to Q^2 (geminal silanol) and Q^4 (siloxane) environments, respectively.^[248] The Q^n peaks are taller in the SBA-15 spectrum compared to those in the nanofibrous silica spectrum, which may reflect the higher content of ^1H nuclei in SBA-15.

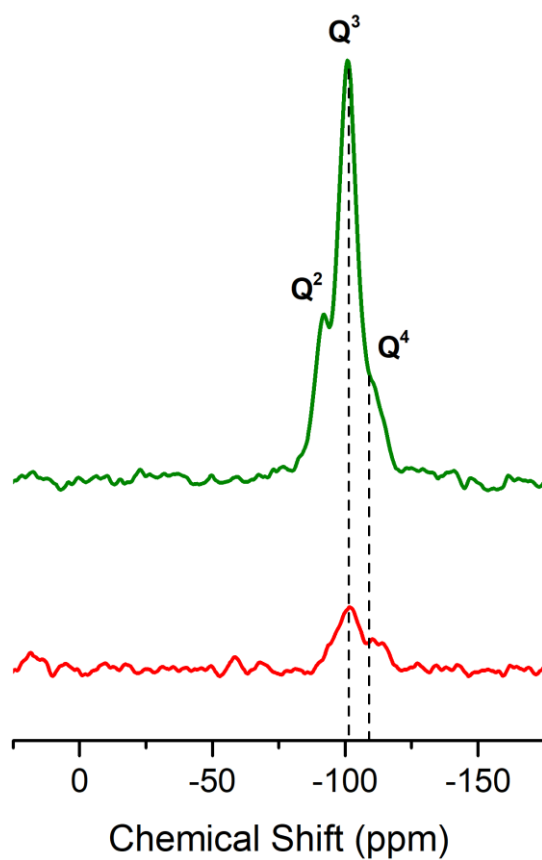


Figure 3.52. ^1H - ^{29}Si CP-MAS NMR spectra of SBA-15 (green) and silica nanofibres (red). The spectra were collected using the same experimental parameters (2 ms contact time, 10 s recycle delay, 4 k scans).

Similar to the functionalised nanofibres, the ^{29}Si spectrum of APS-modified SBA-15 silica (Figure 3.53). exhibits additional peaks at -60 ppm (T^2 , partially condensed silane) and -68 ppm (T^3 , fully condensed silane).^[259]

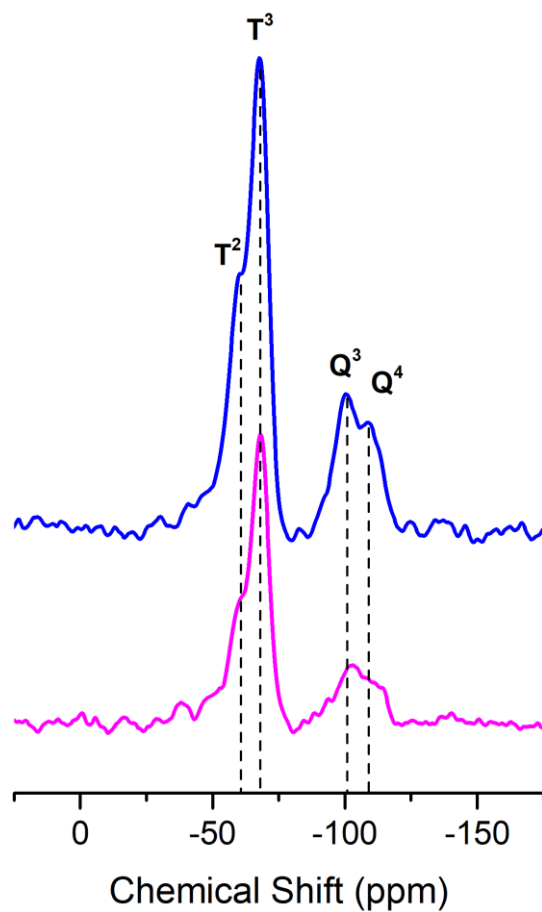


Figure 3.53. ^1H - ^{29}Si CP-MAS NMR spectra of APS-modified SBA-15 (blue) and functionalised silica nanofibres (pink). The spectra were collected using the same experimental parameters (2 ms contact time, 10 s recycle delay, 4 k scans).

3.9 Conclusions

Templated nanofibrous silica with a high specific surface area and mesoporosity have been successfully prepared through the optimisation of the electrospinning and calcination conditions (tip-to-collector distance, flow rate, silica-to-polymer ratio and calcination temperature). Varying the tip-to-collector distance and flow rate did not significantly impact the resulting mean nanofibre diameter. Meanwhile, using an electrospinning solution with a high silica-polymer ratio (3:1) resulted in a high density of beading due to its lower solution viscosity compared with the 1:1 and 2:1 formulations. Choosing the optimal calcination temperature involved balancing the trade-off between surface silanol density, which decreased with temperature, and nanofibre morphology, which generally improved with temperature. The physiochemical properties of the optimised material were studied using different characterisation techniques. Template removal was verified by TGA and FTIR. ^1H - ^{13}C CP/MAS NMR experiments revealed differences in tacticity of the polymer in the materials obtained after electrospinning compared to the polymer in its pristine state due to differing intramolecular bonding. Furthermore, TGA revealed that the polymer is less thermally stable in electrospun nanofibres. As expected, ^1H - ^{29}Si CP/MAS NMR experiments indicated a reduction in silanol group populations in the electrospun material after calcination due to thermally-induced dehydroxylation. Whilst as-spun silica-polymer nanofibres are non-porous, nitrogen physisorption analysis revealed that, after template removal, the nanofibres are mesoporous, with a specific surface area over 25 times that of the silica-polymer precursor material.

Multiple samples of nanofibrous silica were prepared using the optimal conditions and subsequently functionalised using various concentrations of grafting agent and different aminosilanes. Regardless of the grafting agent used, the degree of functionalisation increased as a function of the amount of silane added to the reaction mixture. Meanwhile, the grafting efficiency exhibits an exponential-like decrease with silane added. This was attributed to the interplay between the effects of steric hindrance and amine concentration on the grafting reaction. Furthermore, wet grafting of nanofibres yields significantly higher silane loadings and grafting efficiencies compared to anhydrous grafting. FTIR analysis revealed that the wavenumber of the TO_4 siloxane stretching band increases with the degree of functionalisation. Several peaks in the grafted materials were identified as being associated with formation of ammonium carbamate, a product of CO_2 chemisorption. At very high silane loadings, the appearance of a second strong siloxane stretching band implies the presence of larger siloxane ring structures from self-condensation of the grafting agent.

^{13}C and ^{29}Si CP/MAS NMR experiments provided further confirmation of the functionalisation of the nanofibers. Furthermore, ^{13}C NMR revealed additional evidence of chemisorbed CO_2 on the functionalised nanofibres. Lastly, a sample of SBA-15 silica was functionalised and compared to nanofibres modified under the same conditions. The SBA-15 material achieved a higher silane loading due to its higher specific surface area and silanol content.

4 Direct Air Capture Studies of Amine-Functionalised Nanofibrous Silica

4.1 Techniques for Studying CO₂ Capture on Solid Adsorbents

Having successfully developed a method for synthesising amine-functionalised nanofibrous silica, the next phase of the study will focus on investigating the CO₂ adsorption behaviour of these novel materials under direct air capture (DAC) conditions (400 ppm CO₂).

In the literature, there are three commonly used methods for quantifying CO₂ loading. The first is the volumetric or manometric method in which a sample is dosed with adsorbate inside a glass cell until a certain gas pressure is attained. The amount of adsorbed CO₂ at equilibrium is then deduced based on the volume of gas admitted into the sample cell. This process is repeated at multiple pressures to obtain a pressure-domain isotherm.^[275] Although this static approach provides information on the pressure dependence of the adsorption process, no kinetic information can be derived from the data as it only provides CO₂ loading values at equilibrium.

The second is the gravimetric approach wherein CO₂ uptake is quantified by monitoring the change in sample weight over time using thermogravimetric analysis (TGA).^[68] Such an experiment produces a time-domain isotherm which provides information about uptake kinetics in addition to the equilibrium capacity of the adsorbent. Although TGA provides useful preliminary information about the kinetics of CO₂ adsorption, there are limitations to using this method for fully characterising adsorbents for DAC. Firstly, TGA instruments are often limited to use of dry feed gases, meaning that materials cannot be tested in humid conditions. Since air invariably contains water, studying how moisture effects CO₂ sorption is essential for understanding how an adsorbent would perform in a real-world environment. Secondly, most TGA instruments cannot operate below 25°C. The majority of Earth's land surface has an average temperature below 20°C^[276], thus it is inevitable, given the scale of carbon dioxide removal needed (2.6 GtCO₂/yr by 2050 from novel CDR^{e[17]}), that many DAC plants will be processing air at a sub-ambient temperature. Therefore, studying the CO₂ removal performance of adsorbents below 25°C is essential. This is particularly pressing considering that there are only a small number of papers on DAC material development that have studied sub-ambient adsorption.^[25] Furthermore, understanding how a sorbent would perform on an industrial scale in such modalities as a fixed-bed requires the use of a proxy set-up such as a bench-scale system that mimics the CO₂ removal behaviour of a DAC reactor. Given the high flow rates used in TGA relative to the sample size, and the fact the feed gas flows over the sample rather than through it, the experimental set-up is highly inefficient with respect to CO₂ capture efficiency and is thus unrepresentative of industrial-scale capture systems.

To this effect, a third method has been commonly employed in the literature in which the feed gas is flown through a column packed with adsorbent (breakthrough testing).^[32, 51, 141] This technique is

^e Excludes well-established CDR strategies like afforestation/reforestation.

more representative of a practical adsorption-based separation process. Prior to testing, the adsorbent bed is outgassed under inert gas flow. Once the adsorbent bed has been regenerated, the gas source is switched to the CO₂ mixture. When CO₂ makes initial contact with the start of the fixed bed (t_1), it begins to travel to the active sites within the adsorbent via a series mass-transfer steps. In the case of amine adsorbents, the main steps are film diffusion, pore diffusion and removal *via* chemical reaction at the active sites.^[277] The adsorbate concentration decreases with the length of the bed, and the volume over which it varies is termed the mass transfer zone (Figure 4.1). The initial portion of the bed continues to remove CO₂ from the gas stream until it reaches equilibrium. After that, mass transfer within that section of adsorbent finishes and CO₂ penetrates further into the bed. The mass transfer zone moves through the fixed-bed as more of the adsorbent reaches equilibrium (t_2). Eventually, it reaches the end of the bed, which results in some unabsorbed CO₂ emerging from the column (t_3). The time at which this occurs is called the ‘breakthrough time’ and, hence-forth, the effluent concentration of CO₂ rises until the entire bed has reached equilibrium. At saturation, the concentration of adsorbate leaving the column is equal to that entering (t_4).^[278]

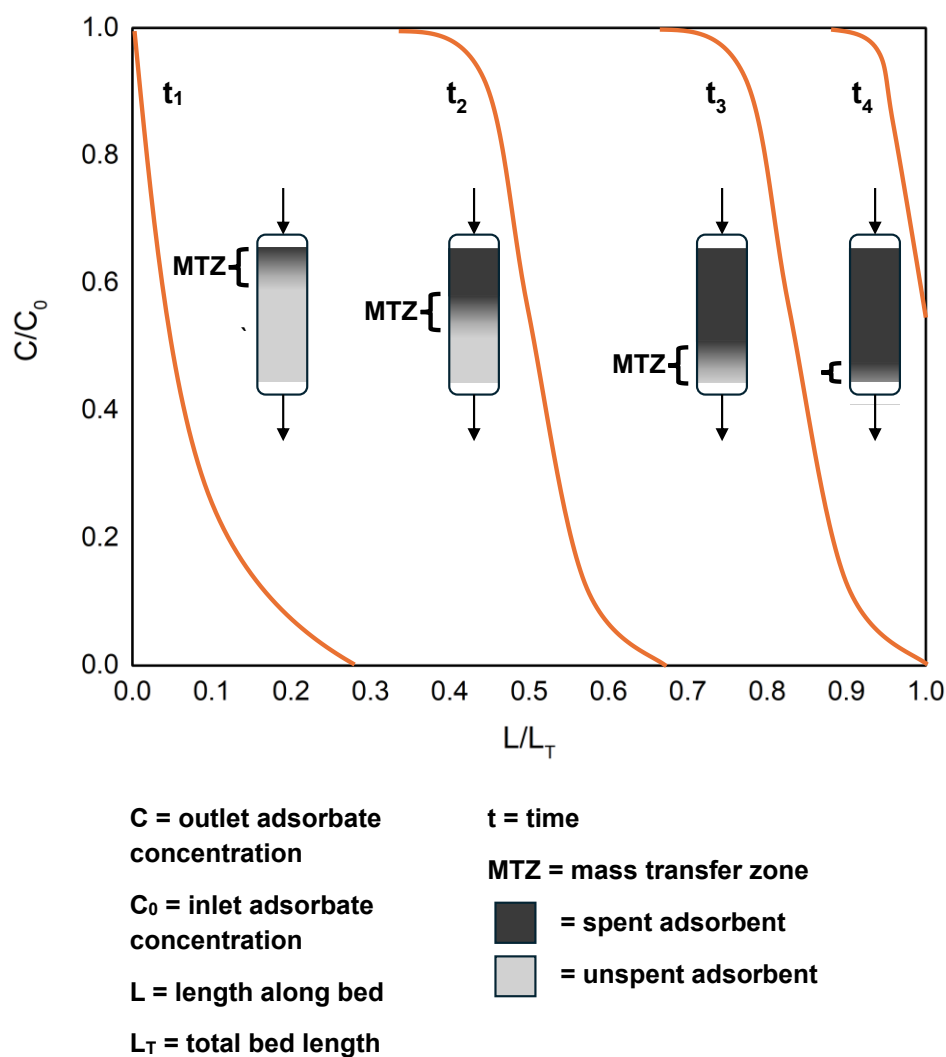


Figure 4.1. Movement of a mass transfer zone across a fixed bed reactor during a breakthrough test. Adapted with permission from: [279].

Throughout the experiment, the CO₂ concentration in the effluent is plotted against time and the CO₂ loading in the fixed bed at a given time can be derived from the area of the breakthrough curve (see Section 2.3.14 for details). Typically, the pseudo-equilibrium capacity, corresponding to the amount of adsorbed CO₂ at $C/C_0 = 0.95$, is used to denote the final adsorption capacity during a dynamic CO₂ experiment because it would be impractical to allow the adsorbent to reach true equilibrium during each cycle in a real-world DAC system.^[142, 207]

In this chapter, TGA is first used to for preliminary testing of amine-functionalised nanofibres with different amine loadings (expressed in mmol_N/g_{sample}) and amine types (APS, DAS and TAS). Next, a fixed-bed flow-through system is developed to assess the performance of some of these adsorbents in more realistic DAC conditions, including sub-ambient and humid testing.

4.2 TGA Studies

4.2.1 Bare versus Functionalised Nanofibrous Silica

TGA CO₂ isotherms were recorded at 25°C for samples of nanofibrous silica before and after amine-functionalisation under simulated DAC conditions (Figure 4.2). As expected, the unmodified silica adsorbs a negligible amount of CO₂ after three hours (< 0.01 mmol/g) due to the lack of basic sites for facilitating adsorption. After functionalisation with APS, the CO₂ affinity of the nanofibres improves dramatically, with 0.25 mmol/g of CO₂ bound to the material by the end of the experiment.

The uptake behaviour of the functionalised sample varies as a function of time, and this can be segmented into two distinct regions of adsorption. The first, up to *ca.* 10 minutes, exhibits rapid uptake of CO₂, with the adsorbate loading increasing linearly with time. This is due to formation of CO₂-amine adducts at readily accessible sites on the surface of the material. It has been proposed that, as more surface sites are occupied, ionic cross-links form between alkylamine moieties (Scheme 4.1). This creates a surface barrier which retards mass transfer of adsorbate into the bulk of the amine layer, leading to a second, slower region of CO₂ uptake.^[54] For the APS-loaded material, this occurs between 10 and 180 min. These observations agree with the reported kinetic behaviour of other amine-grafted silicas from the literature.^[280]

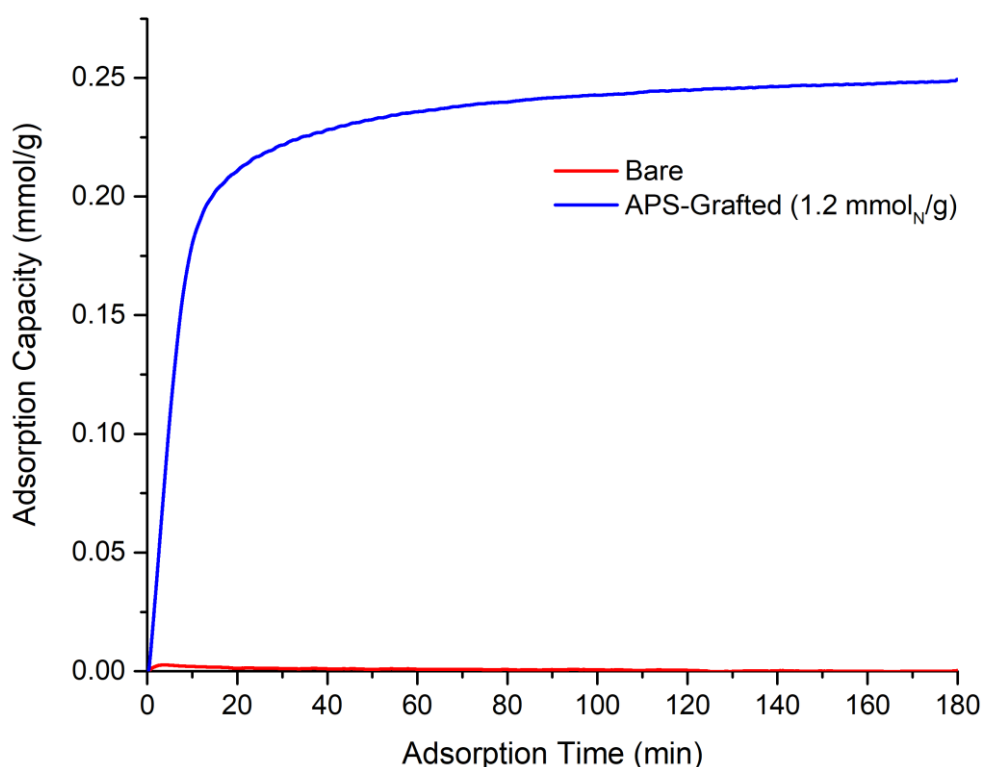
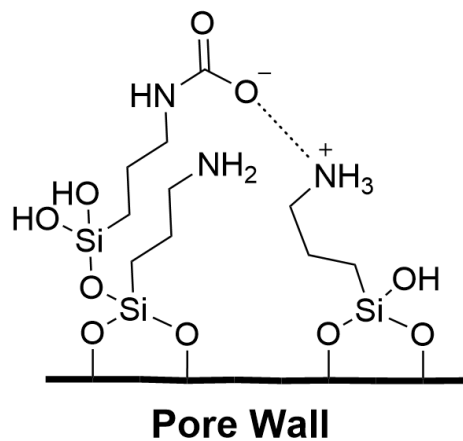


Figure 4.2. TGA CO₂ adsorption isotherms of bare and APS-functionalised nanofibrous silica during exposure to 400 ppm CO₂ at 25°C.



Scheme 4.1. Ionic cross-linking between alkyamine branches.

4.2.2 Effect of Amine Loading

The effect of active site density on the kinetic behaviour of CO₂ adsorption was assessed by recording isotherms for APS-modified nanofibres at two higher amine loadings (Figure 4.3). As with APS-low, the two samples with higher active site densities exhibit similarly shaped isotherms with rapid (linear) and slow uptake regions. All rapid segments are between 0 and 15 min whilst slow uptake is between 15 and 180 min. Unlike APS-low, the adsorption capacity of APS-medium and APS-high did not plateau out within the three-hour experimental time.

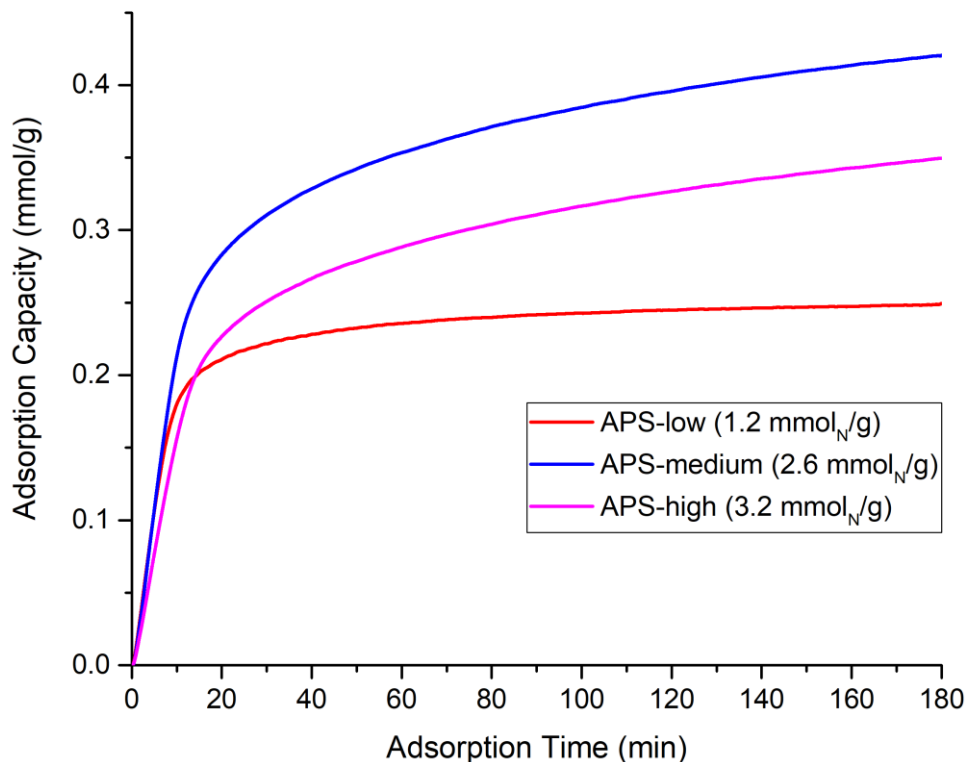


Figure 4.3. TGA CO₂ adsorption isotherms recorded at 25°C for APS-modified silica nanofibres of differing amine loadings.

Initially, increasing the amine content from 1.2 to 2.6 mmol_N/g results in an increase in the final adsorption capacity, from 0.25 to 0.42 mmol/g (Figure 4.4). However, upon further increasing the amine loading to 3.2 mmol_N/g, the final capacity reduces to 0.35 mmol/g. This observation shows that an initial increase in amine loading results in a higher number of accessible adsorption sites. Increasing the loading further may cause a net decrease in the number of available amine sites due to steric crowding of the grafted aminosilane in the pores of the nanofibres. Thus, there exists an optimal amine loading for achieving maximal capacity. Notwithstanding, the amine efficiency, which is the adsorption capacity divided by the amine loading, is lower for APS-medium compared to APS-low (0.16 and 0.21 mmolCO₂/mmol_N respectively) because a proportion of the added amines are inaccessible due to the reduction in pore volume and surface area that accompanies any increase in the degree of functionalisation. The amine efficiency of APS-high is lower still, at 0.11 mmolCO₂/mmol_N.

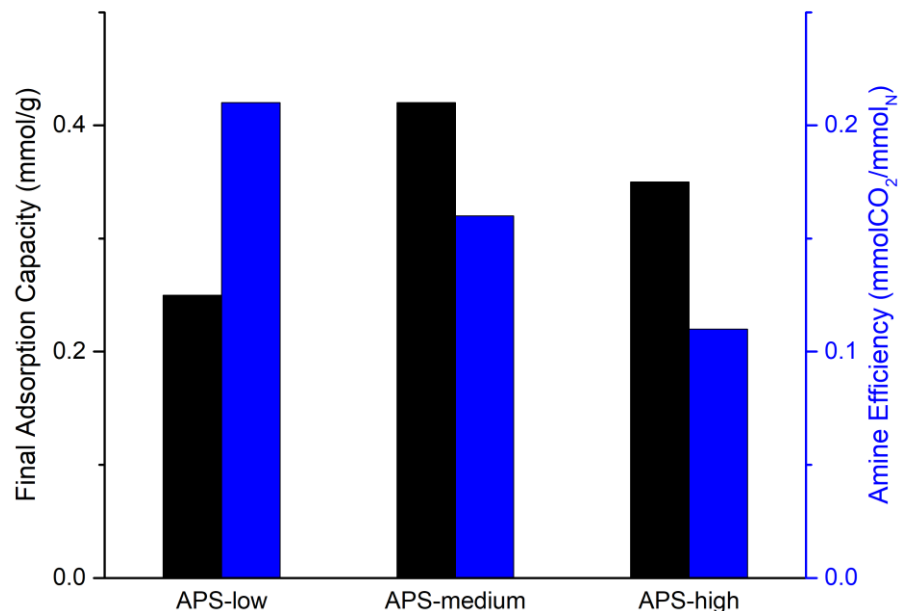


Figure 4.4. Final CO₂ adsorption capacities and amine efficiencies of the three APS-loaded nanofibrous silicas. Error: $\leq \pm 0.003$ mmol/g (adsorption capacity), $\leq \pm 0.015$ mmolCO₂/mmol_N (amine efficiency).

The initial adsorption rate (IAR) was computed to understand the uptake kinetics at the beginning of the TGA experiments. Understanding adsorption kinetics is important because, in a practical DAC system, optimising the CO₂ capture rate of the plant requires balancing kinetics with the material's time-dependent adsorption capacity.

The initial adsorption rate of APS-low is $23 \mu\text{mol}\cdot\text{g}^{-1}\cdot\text{min}^{-1}$ and increases slightly to $24.1 \mu\text{mol}\cdot\text{g}^{-1}\cdot\text{min}^{-1}$ for APS-medium (Figure 4.5). At the highest loading of APS, the IAR decreases to $17.5 \mu\text{mol}\cdot\text{g}^{-1}\cdot\text{min}^{-1}$.

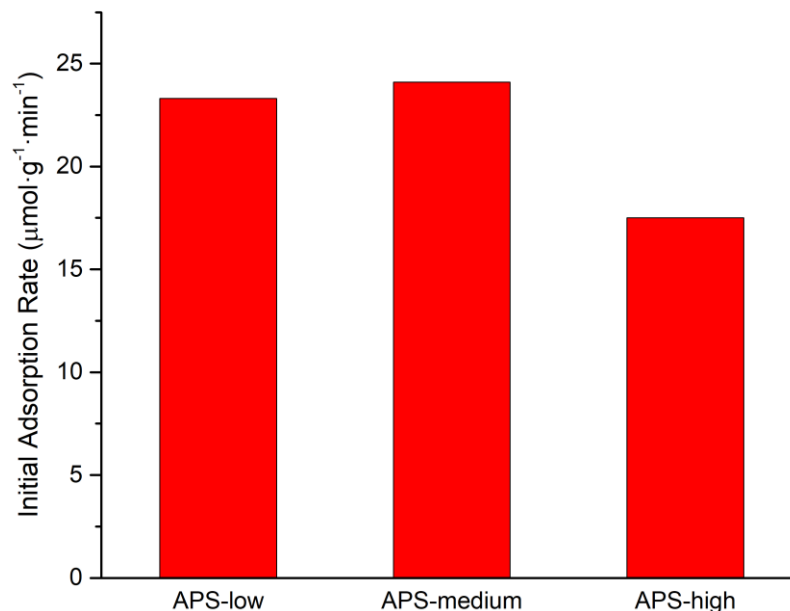


Figure 4.5. Initial adsorption rates of the three APS-loaded nanofibrous silicas.

4.2.3 Effect of Amine Type

To investigate the effect of amine type, adsorption experiments were carried out using samples of nanofibrous silica grafted with diamine (DAS) and triamine (TAS) grafting agents at different amine loadings.

The recorded isotherms for the DAS-modified samples (Figure 4.6) show that CO_2 adsorption on the low and medium-loaded materials reaches equilibrium by the end of the experiment whereas the adsorption capacity of high-DAS is still rising. Regarding the TAS isotherms (Figure 4.7), TAS-low shows a plateauing in its CO_2 loading after 3 h whereas CO_2 uptake on TAS-medium and TAS high is still rising considerably. Similarly to the APS-loaded silicas, the DAS and TAS samples show two distinct regions of rapid and slow adsorption.

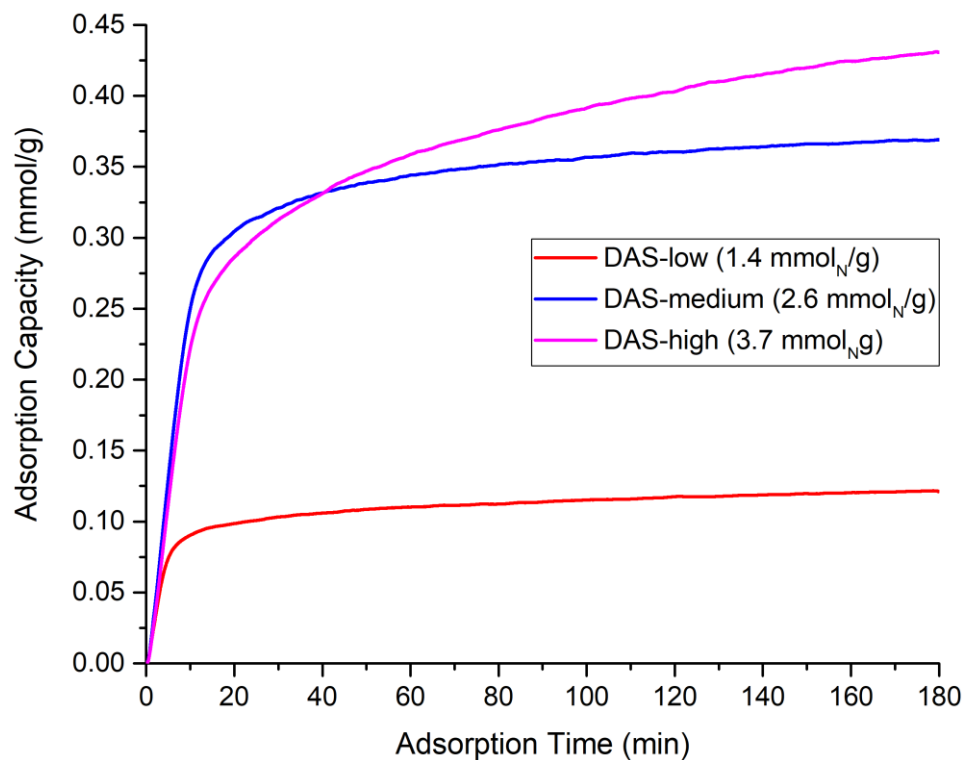


Figure 4.6. TGA CO₂ adsorption isotherms at 25°C of DAS-modified silica nanofibres with different amine loadings.

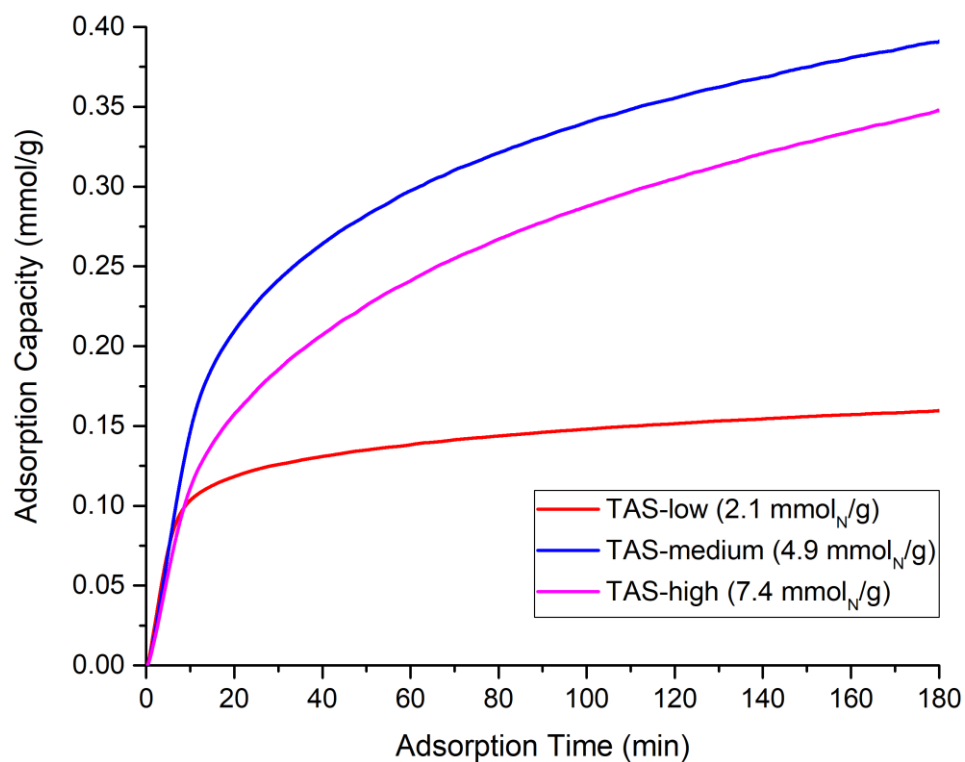


Figure 4.7. TGA CO₂ adsorption isotherms at 25°C of TAS-modified silica nanofibres with different amine loadings.

There is a significant difference in the final adsorption capacity between DAS-low and DAS-medium. An almost doubling of the amine content from 1.4 mmol_N/g for DAS-low to 2.6 mmol_N/g for DAS-medium causes a three-fold increase in the final adsorption capacity from 0.12 to 0.37 mmol/g, with a concomitant increase in the amine efficiency from 0.09 to 0.14 mmolCO₂/mmol_N (Figure 4.8). Increasing the degree of DAS functionalisation further results in an additional, albeit moderate, increase in final adsorption capacity to 0.43 mmol/g.

A more than two-fold increase of the amine loading from 2.1 mmol_N/g for TAS-low to 4.9 mmol_N/g for TAS-medium resulted in an increase in final adsorption capacity from 0.16 to 0.39 mmol/g respectively (Figure 4.9). As seen with the APS-modified nanofibres, the highest capacity is at the middling amine content, with a further increase in degree of functionalisation causing a slight decrease in capacity to 0.35 mmol/g for TAS-high. The amine efficiencies are similar for TAS-low and TAS-medium materials, whilst the amine efficiency of TAS-high is slightly lower (0.08 mmolCO₂/mmol_N for the former two and 0.05 mmolCO₂/mmol_N for the latter, respectively).

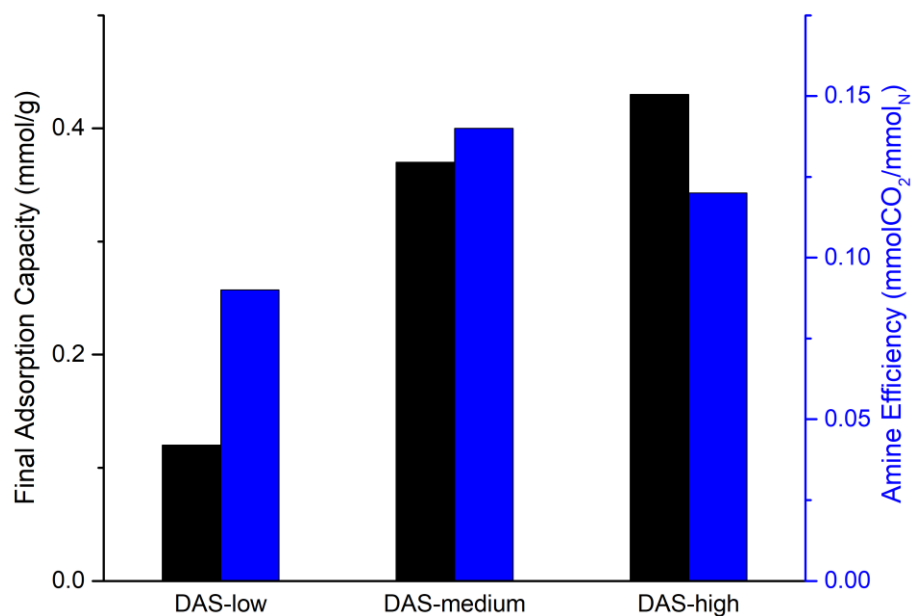


Figure 4.8. Final CO₂ adsorption capacities and amine efficiencies of the three DAS-loaded nanofibrous silicas. Error: $\leq \pm 0.003$ mmol/g (adsorption capacity), $\leq \pm 0.015$ mmolCO₂/mmol_N (amine efficiency).

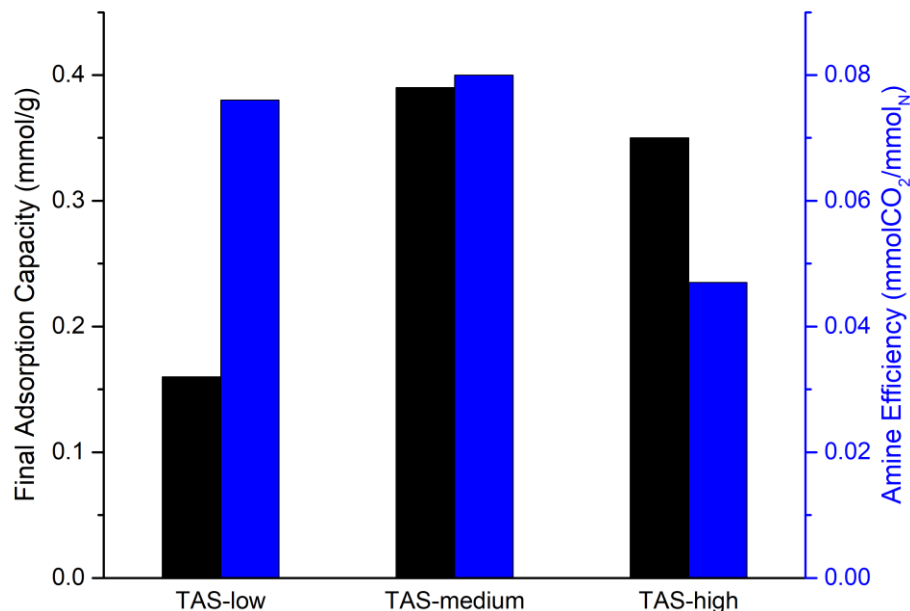


Figure 4.9. Final CO₂ adsorption capacities and amine efficiencies of the three TAS-loaded nanofibrous silicas. Error: $\leq \pm 0.003$ mmol/g (adsorption capacity), $\leq \pm 0.015$ mmolCO₂/mmolN (amine efficiency).

This could be due to lower sorbent surface areas and pore volumes at high amine loadings which impeded inter-fibre and pore diffusion of CO₂ during the experiments.

Concerning capture kinetics, the initial adsorption rate increases from $18.3 \mu\text{mol}\cdot\text{g}^{-1}\cdot\text{min}^{-1}$ for DAS-low to $30.2 \mu\text{mol}\cdot\text{g}^{-1}\cdot\text{min}^{-1}$ for DAS-medium, followed by a decrease to $25.9 \mu\text{mol}\cdot\text{g}^{-1}\cdot\text{min}^{-1}$ for DAS-high (Figure 4.10). Likewise, increasing the loading of TAS causes a slight increase of the IAR from 16.6 to $17.1 \mu\text{mol}\cdot\text{g}^{-1}\cdot\text{min}^{-1}$ for TAS-low and TAS-medium respectively (Figure 4.11). The IAR then decreases to $13.9 \mu\text{mol}\cdot\text{g}^{-1}\cdot\text{min}^{-1}$ for TAS-high. This study proposes that the decrease in IAR at high loadings of grafting agent is due to diffusion limitations as a result of pore blockage in the nanofibres. To verify the reduction in surface area and pore volume with loading, the textural properties of the TAS-grafted materials were measured using nitrogen physisorption (Figure A3 and Table A1). As expected, the specific surface area and total pore volume decreases with loading from 81 to $9 \text{ m}^2/\text{g}$ and from 0.18 to $0.02 \text{ cm}^3/\text{g}$, respectively. Unfortunately, surface area and pore volume data could not be collected for the APS and DAS-functionalised adsorbents owing to technical difficulties with the apparatus used for measuring nitrogen sorption isotherms.

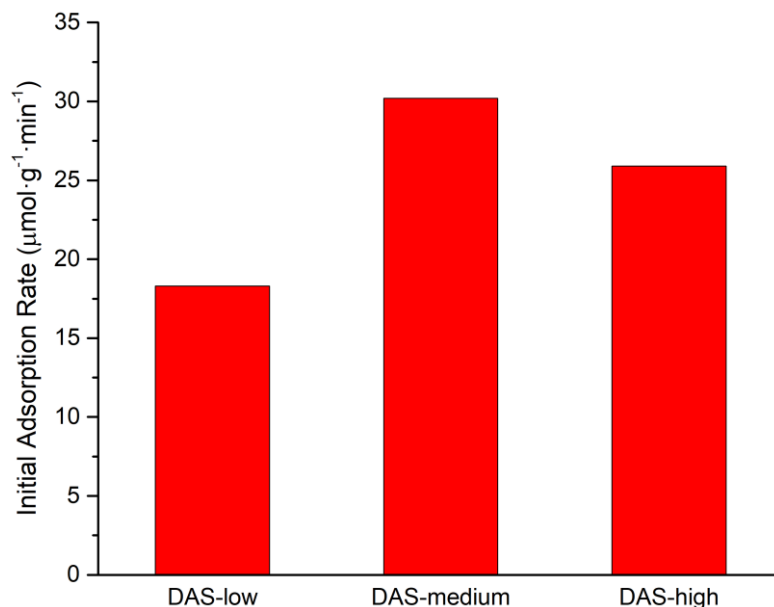


Figure 4.10. Initial adsorption rates of the three DAS-loaded nanofibrous silicas.

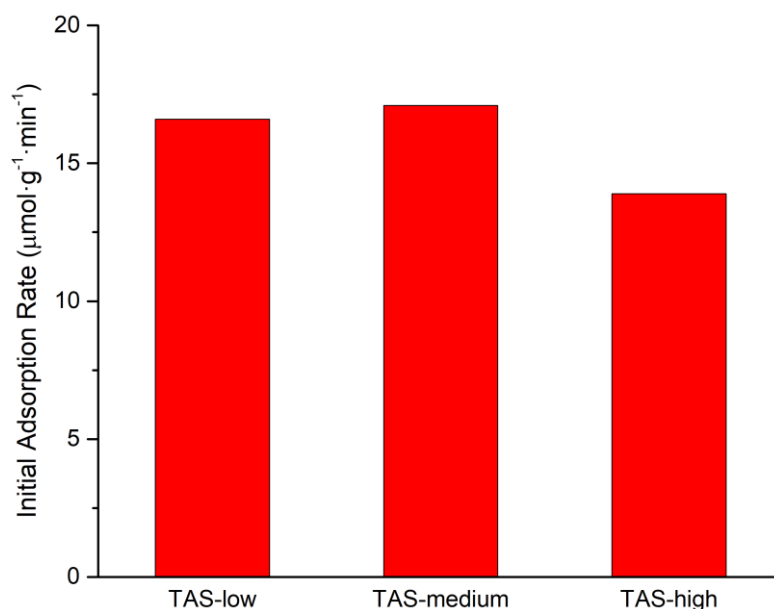


Figure 4.11. Initial adsorption rates of the three TAS-loaded nanofibrous silicas.

APS, DAS and TAS-modified samples of similar amine loadings were compared. At similar amine loadings, the final adsorption capacity and amine efficiency decreases in the order: APS < DAS < TAS (Figure 4.12). Whilst the APS-loaded material contains only primary amines, DAS and TAS samples contain primary and secondary amine groups. Primary amine groups are more basic and therefore have a higher reactivity towards CO_2 compared to secondary amines^[63], which may explain the inferior adsorption capacities and amine efficiencies of DAS and TAS. The ratio of primary to secondary amine groups in the DAS and TAS grafting agents is 1:1 and 1:2 respectively

and hence the higher abundance of secondary amines in the TAS-grafted material is probably responsible for its lower adsorption capacity and efficiency compared to the DAS-grafted adsorbent.

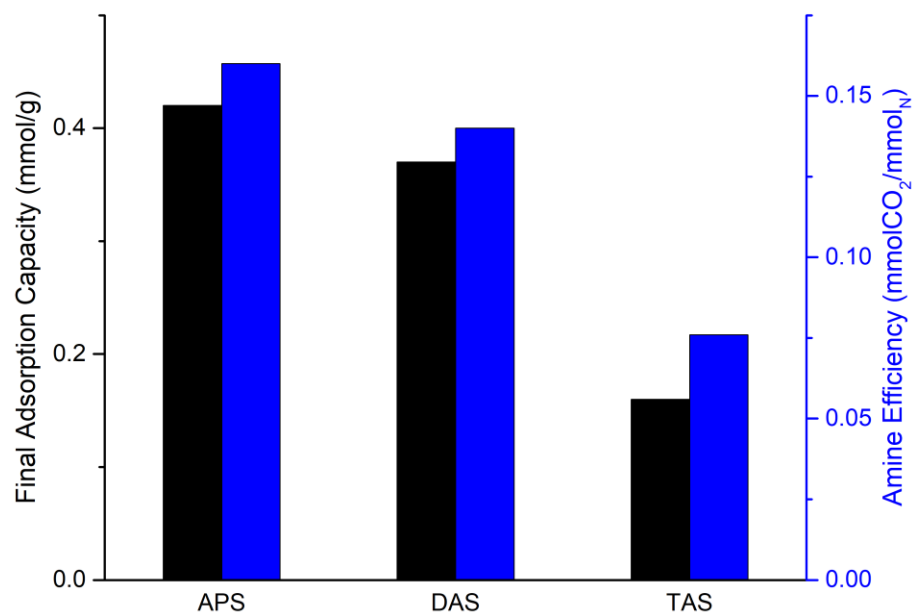


Figure 4.12. Final CO₂ adsorption capacities and amine efficiencies of APS, DAS and TAS functionalised nanofibrous silicas with similar amine loadings (2.6, 2.6 and 2.1 mmol_N/g, respectively). Error: $\leq \pm 0.003$ mmol/g (adsorption capacity), $\leq \pm 0.015$ mmolCO₂/mmol_N (amine efficiency).

The DAS adsorbent has the highest IAR of $30.2 \mu\text{mol}\cdot\text{g}^{-1}\cdot\text{min}^{-1}$ (Figure 4.13), followed by APS ($24.1 \mu\text{mol}\cdot\text{g}^{-1}\cdot\text{min}^{-1}$) then TAS ($16.6 \mu\text{mol}\cdot\text{g}^{-1}\cdot\text{min}^{-1}$).

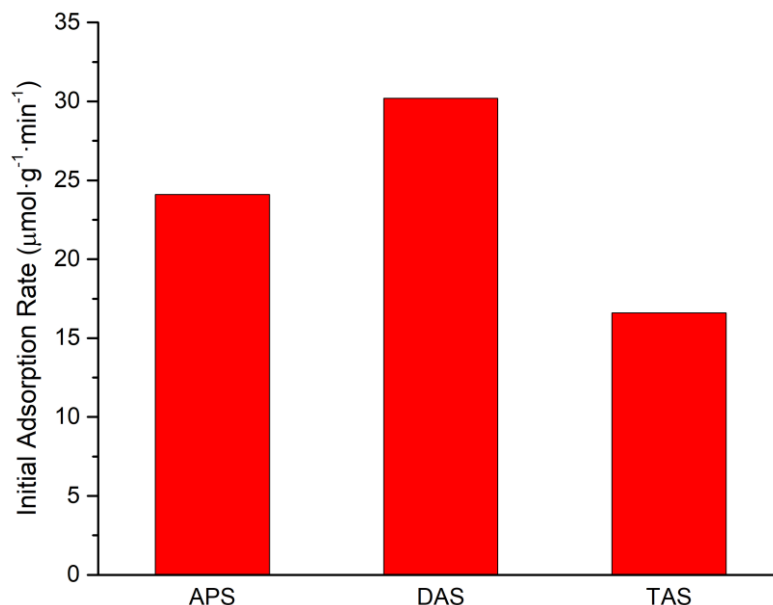


Figure 4.13. Initial adsorption rates of APS, DAS and TAS functionalised nanofibrous silicas with similar amine loadings.

4.2.4 Effect of Adsorption Temperature

The effect of temperature on the CO₂ uptake behaviour of amine-functionalised nanofibrous silicas was investigated by recording isotherms between 25 and 65°C for APS, DAS and TAS functionalised nanofibrous silicas of comparable amine loadings (Figure A4, Figure A5 and Figure A6). The effect of the temperature on the final adsorption capacity of functionalised nanofibres after 3 h of CO₂ exposure varied depending on the amine type (Figure 4.14). For APS, the final adsorption capacity increases with temperature between 25 and 45°C from 0.40 to 0.61 mmol/g. However, the CO₂ loading decreases slightly at 55°C (0.59 mmol/g) then dropped significantly at 65°C (0.33 mmol/g). As with APS, the TAS-grafted material shows an initial increase in adsorption capacity from 0.27 mmol/g at 25°C to 0.33 mmol/g at 35°C. Thereafter, the final CO₂ loading depreciates with temperature, with a value of 0.03 mmol/g recorded at 65°C. The initial increase in CO₂ loading with temperature for APS and TAS seems counterintuitive since the exothermic nature of the adsorption process should theoretically lead to an inverse relationship between final adsorption capacity and temperature.

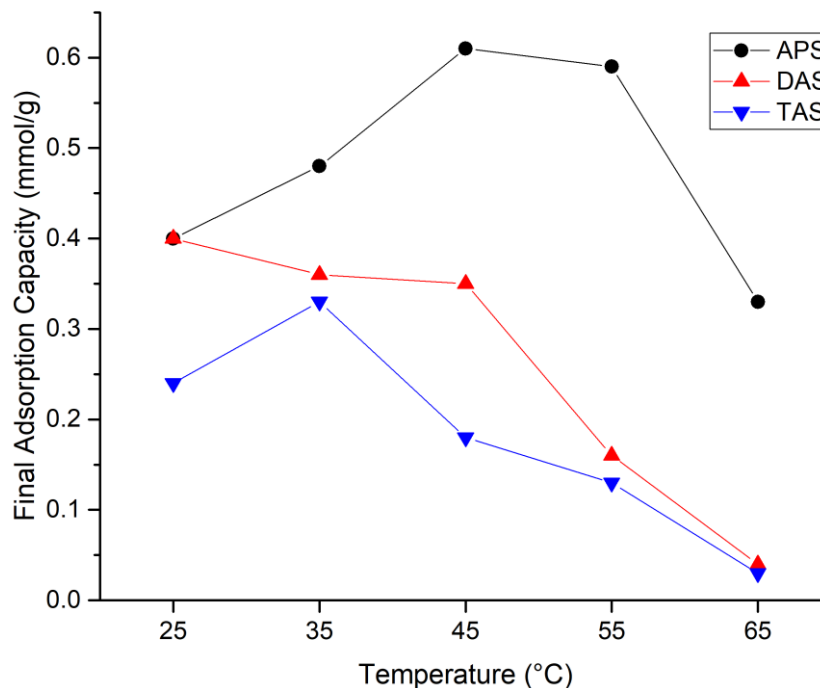


Figure 4.14. Final adsorption capacities of silica nanofibres functionalised with APS (2.6 mmol_N/g), DAS (2.2 mmol_N/g) and TAS (2.6 mmol_N/g) aminosilanes after three hours of CO₂ exposure at different temperatures. Error: $\leq \pm 0.003$ mmol/g.

Other studies have also reported a ‘peak and decline’ trend between CO₂ uptake and temperature for wet grafted silicas. Anyanwu *et al.* speculated that during hydrous amine functionalisation of silica, the silane polymerises on the pore walls of the support. Initially increasing the temperature increases the mobility of the polymer-like aminosiloxane layer, rendering more amine groups accessible for adsorption and hence a higher CO₂ uptake capacity. Beyond a certain temperature, CO₂ capture becomes thermodynamically-driven and the final CO₂ loading proceeds to decrease.^[66, 281]

In contrast to the APS and TAS samples, the final adsorption capacity of the DAS-grafted adsorbent decreases across the entire temperature range from 0.4 mmol/g at 25°C to 0.04 mmol/g at 65°C. The observed trend implies that adsorption is thermodynamically driven for this material. However, it may be the case that adsorption is kinetically-controlled at temperatures lower than 25°C.

All three materials show an initial increase in initial adsorption rate with temperature because of the positive effect of temperature on the CO₂ diffusion rate (Figure 4.15). However, after a certain temperature (55°C for APS and 35°C for DAS and TAS), IAR decrease due to a reduction in the affinity between CO₂ and the adsorption sites as a result of the desorption reaction becoming more thermodynamically favourable.

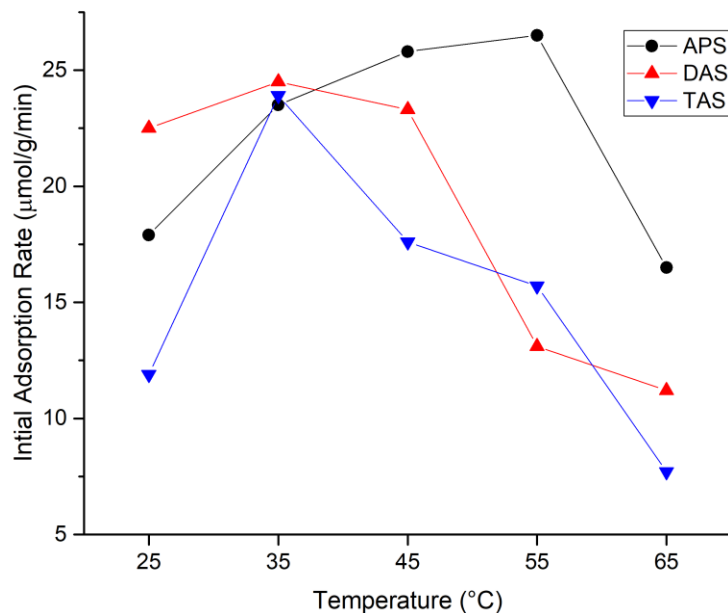


Figure 4.15. Initial adsorption rates of three amine-grafted nanofibrous silicas of similar amine loadings after three hours of CO₂ exposure at different temperatures.

4.2.5 Regenerability Testing

The economic viability of a sorbent for DAC depends not only on its adsorption behaviour but also its regenerability. The more times the capture medium can be cycled before replacement, the lower the capture cost.^[23, 24]

As a preliminary assessment of regenerability, APS-functionalised nanofibrous silicas were subjected to five consecutive temperature-swing cycles. Each cycle consisted of 1 h of 400 ppm CO₂ exposure at 25°C and 1 h of reactivation at 110°C. During the first cycle, the sample weight increases as a result of CO₂ adsorption (Figure 4.16). After an hour of adsorption at 25°C, the purge gas was switched to nitrogen and the furnace was heated to 110°C. The sample mass decreases precipitously during the heating step, indicating rapid removal of CO₂. The desorption rate is so quick that the sample had fully desorbed by the time the furnace temperature had equilibrated at 110°C. The sample mass at the start of each subsequent cycle is approximately the same (5.29 mg), indicating that the desorption conditions are sufficient to fully regenerate the material.

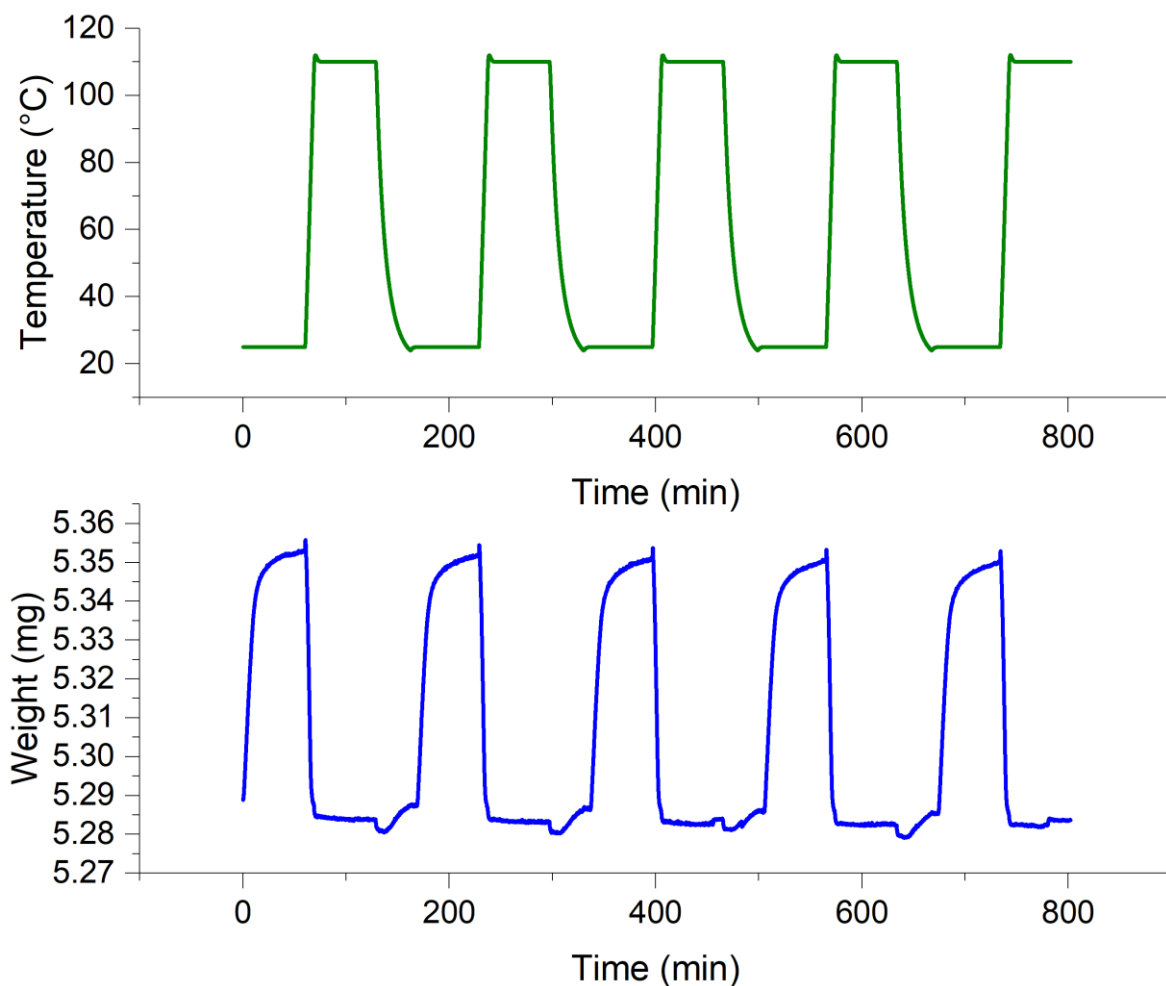


Figure 4.16. Temperature and weight variation during five adsorption-desorption cycles for an APS-grafted material (amine loading = 2.4 mmol_N/g).

The final adsorption capacity barely changed after each cycle (Figure 4.17). This indicates the material is fully regenerable and that no deactivation of adsorption sites occurred during the experiment.

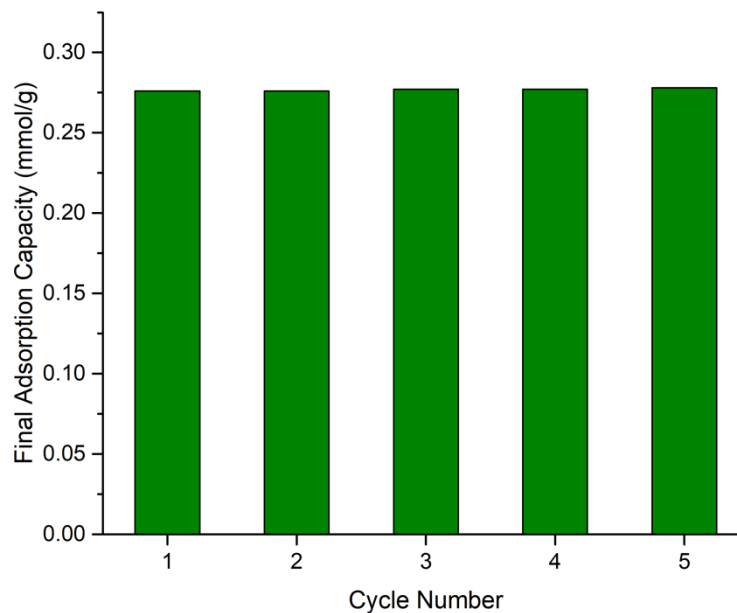


Figure 4.17. Final adsorption capacity of APS-grafted silica ($2.4 \text{ mmol}_N/\text{g}$) after each cycle.
Error: $\leq \pm 0.003 \text{ mmol/g}$.

The five adsorption isotherms obtained from the test (Figure 4.18) have identical CO_2 uptake profiles, which shows that the adsorption kinetics did not change during the experiment. This in turn suggests that there were no significant changes to the physical structure of the adsorbent during the five adsorption-desorption cycles. To verify the latter remark, SEM images of the sample were taken before and after the cycling experiment (Figure 4.19). The micrographs show the nanofibres retained their structure after cycling.

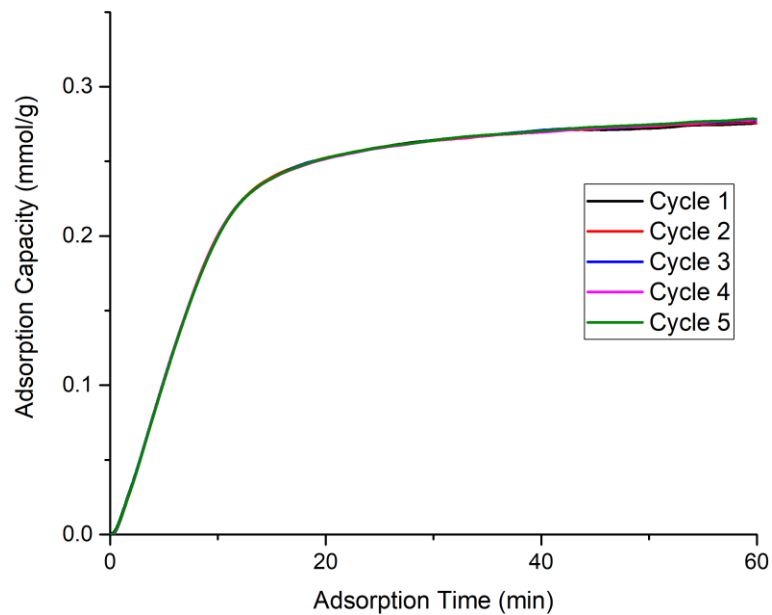


Figure 4.18. Overlaid adsorption isotherms of APS-grafted silica ($2.4 \text{ mmol}_N/\text{g}$) obtained from each cycle during regeneration testing.

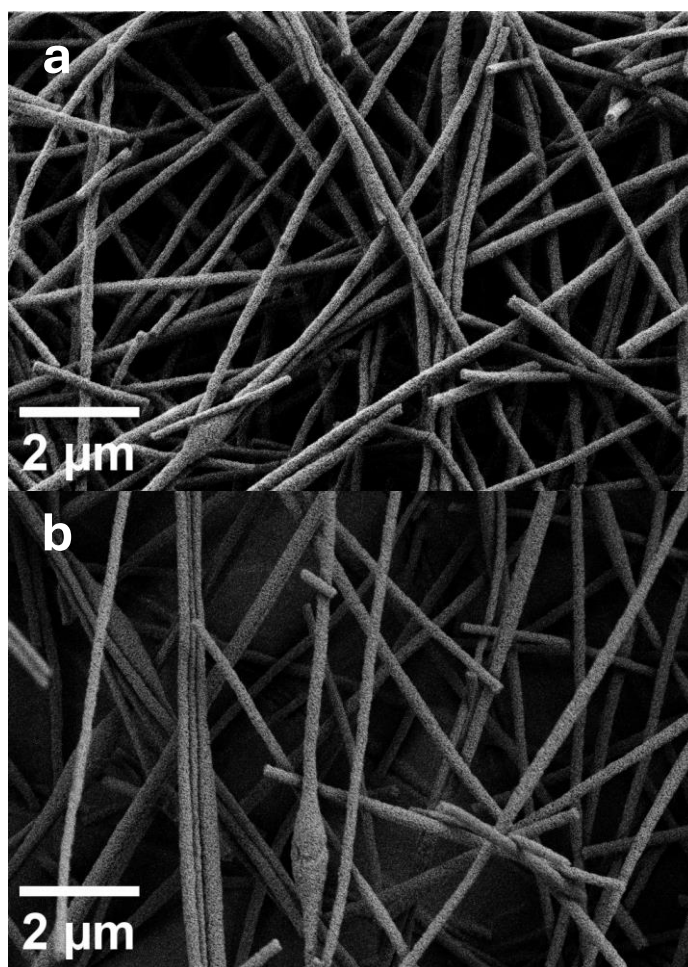


Figure 4.19. SEM images of APS-grafted nanofibres ($2.4 \text{ mmol}_N/\text{g}$) before (a) and after (b) five adsorption-desorption cycles.

A TAS-functionalised sample of similar amine loading was also subjected to five consecutive adsorption-desorption cycles. Like the APS adsorbent, the final adsorption capacity and uptake behaviour changed negligibly during the experiment (Figure 4.20).

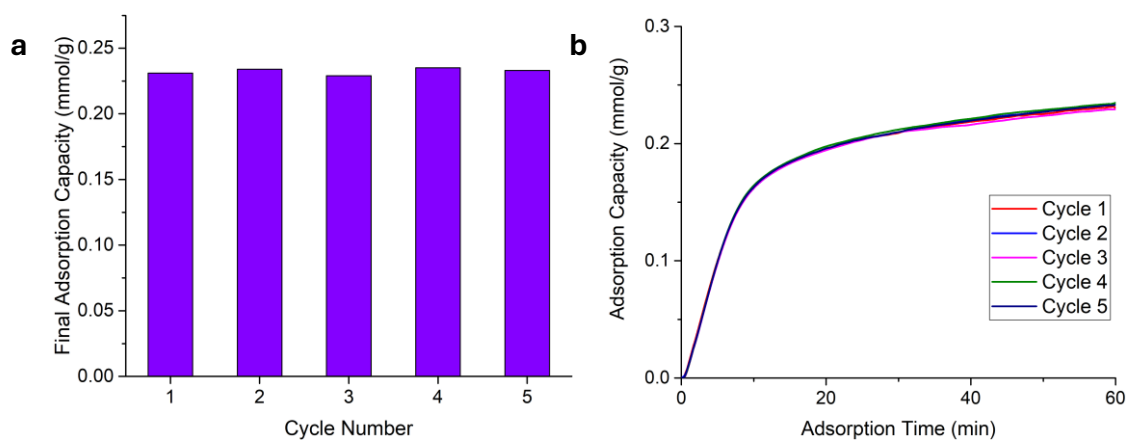


Figure 4.20. Final adsorption capacity (a) and overlaid CO₂ uptake profiles (b) of TAS-grafted nanofibrous silica (2.6 mmol_N/g) during regeneration testing. Error: $\leq \pm 0.003$ mmol/g.

4.3 Fixed-Bed Tests

4.3.1 Dynamic CO₂ Adsorption Behaviour of an APS-modified Nanofibrous Silica

The first material to be tested in the fixed-bed flow-through system was a sample of APS-grafted nanofibrous silica with an amine content of 2.6 mmol_N/g (APS-2.6) using an adsorption temperature and flow rate of 25°C and 100 SCCM^f, respectively. After activation of the adsorbent, the gas source was switched from nitrogen to 400 ppm CO₂ and the concentration of adsorbate from the column outlet was recorded.

The change in relative CO₂ concentration (C/C_0) was plotted against time (Figure 4.21). The breakthrough time (defined as the time at which $C/C_0 = 0.05$) is 5.2 minutes. After breakthrough, C/C_0 increases rapidly before plateauing out at $C/C_0 = 1$ due to adsorbent saturation. A blank run with no adsorbent was also recorded. During this run, there is a short delay of 0.2 min before adsorbate reached the analyser, after which, there is a step change in column outlet CO₂ concentration. This shows that feed gas advection has a negligible effect on the breakthrough profile of the adsorbent. The pseudo-equilibrium capacity of the material, defined as the adsorption capacity at $C/C_0 = 0.95$, is 0.32 mmol/g.

^f SCCM – standard cubic centimeters per minute (1 SCCM = 1 cm³STP/min)

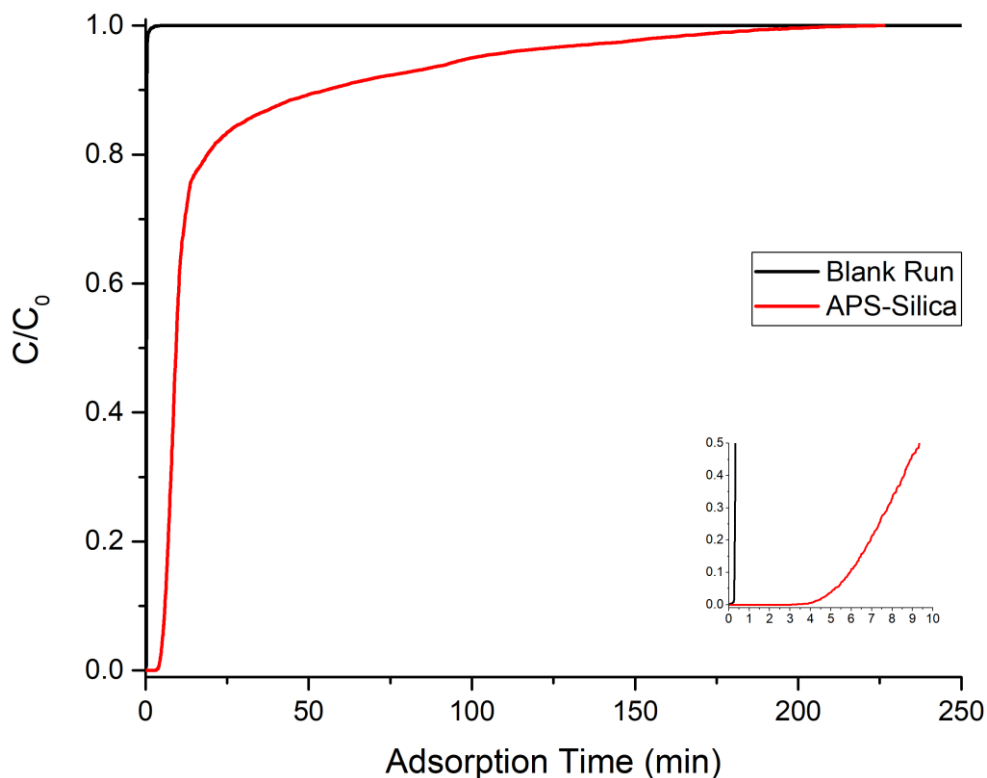


Figure 4.21. Relative CO₂ concentration in the column effluent during dynamic DAC testing of APS-2.6 (red) and a blank run with no adsorbent (black) at 25°C (100 SCCM flow rate).

To elucidate the mechanism of adsorption on APS-2.6, ¹³C solid state NMR spectra were recorded of the sample before and after CO₂ exposure (Figure 4.22). The spectrum of the outgassed material shows three peaks, previously assigned to the methylene groups in the grafting agent, at 11.8, 28.2 and 45.9 ppm.^[256] No peaks linked with CO₂ adsorption are visible, verifying that the outgassing procedure is sufficiently rigorous in removing pre-adsorbed CO₂ from the material. After CO₂ exposure, an additional ¹³C resonance appears at 165 ppm and is assigned to ionic ammonium carbamate involving a pair of amine groups on adjacent silane molecules.^[282-284] This species was previously identified from FTIR analysis of the as-synthesised functionalised silicas in Chapter 3. The hypothesised adsorption pathway involves two steps (Scheme 4.2). Firstly, the formation of carbamic acid *via* a zwitterionic mechanism. Secondly, the reaction of the unstable adduct with a second amine, forming an ammonium carbamate.^[283] There is no indication of physisorbed CO₂ on the material as evidenced by the absence of a peak at 125 ppm. This is in agreement with an NMR study which reported that physisorbed CO₂ is only present at much higher partial pressures (>1.3 kPa).^[285, 286]

The appearance of the methylene peaks also changed after CO₂ adsorption. Most notable is the appearance of a shoulder at *ca.* 23.5 ppm on the middle methylene peak. As discussed in Section 3.5, this second resonance occurs in aminopropyl branches in which the amine group is protonated.^[262] In other words, the appearance of C2b is the result of the formation of ammonium ions during CO₂

adsorption on the material. On that basis, the outgassed spectrum shows that all the amine groups are unprotonated prior to CO₂ exposure, providing further evidence that the outgassing conditions are sufficient to fully degas the adsorbent. To the author's best knowledge, no previous CO₂ capture studies on APS-functionalised materials have remarked on this spectral change.

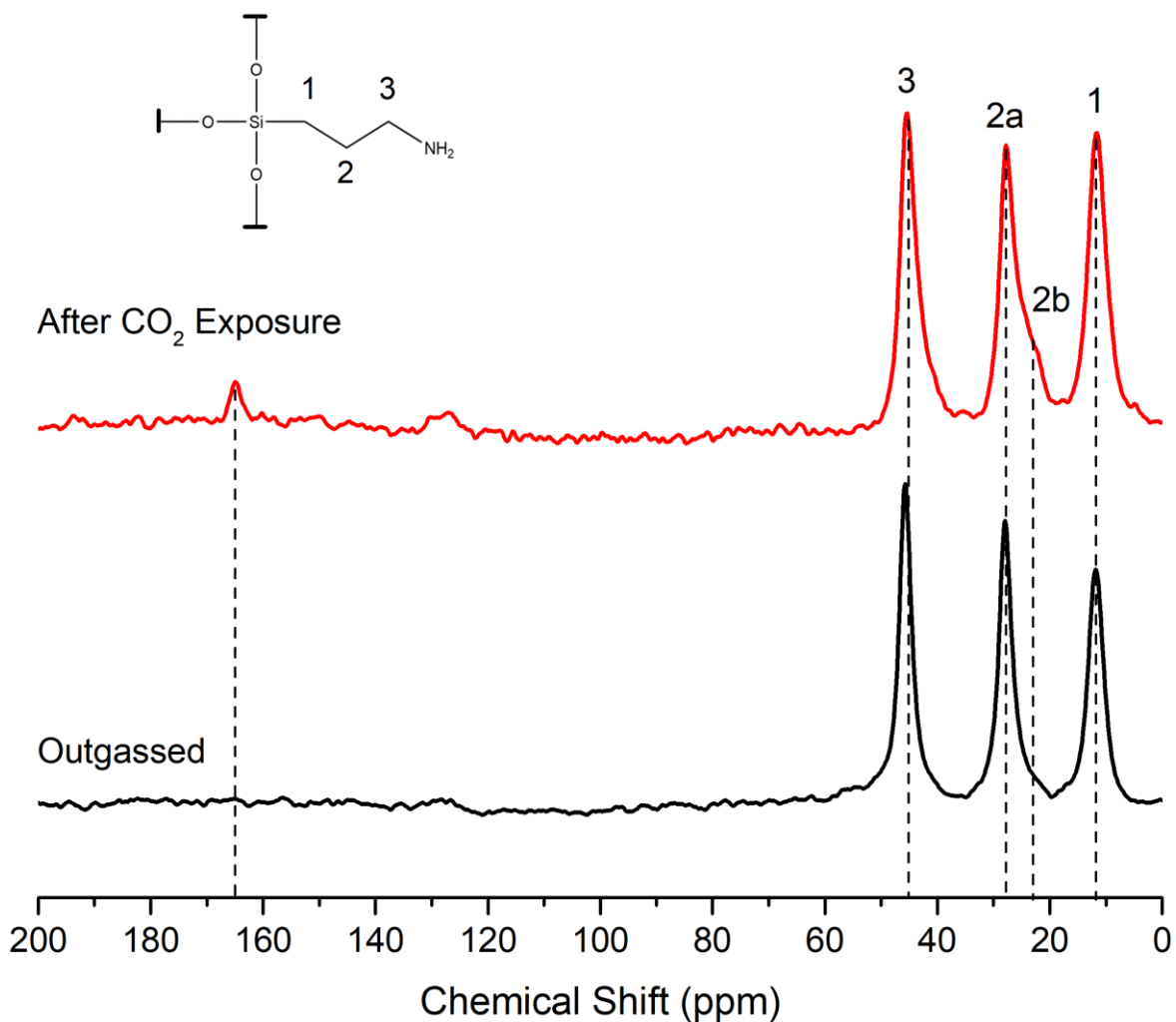
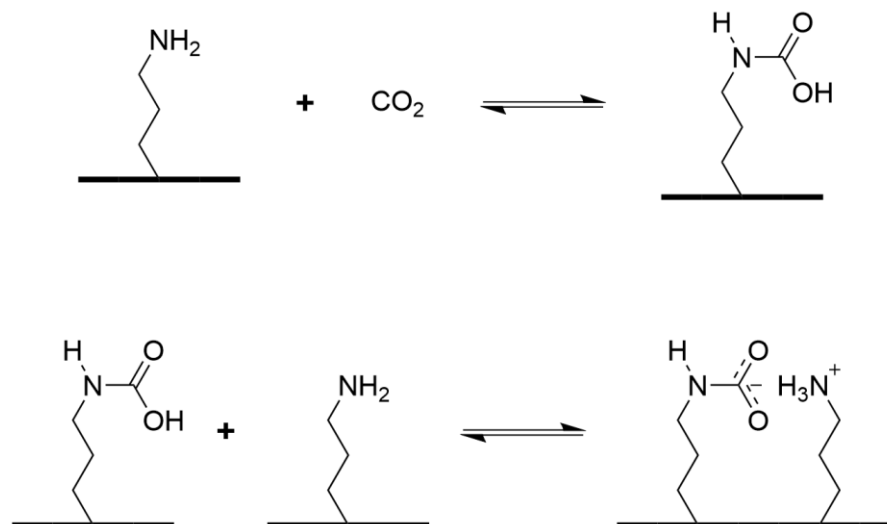


Figure 4.22. ¹H-¹³C CP/MAS NMR spectra of outgassed APS-2.6 and the same material after exposure to 400 ppm CO₂ (25°C). The dashed line corresponds to the chemical shift at which the chemisorbed CO₂ resonance is located.



Scheme 4.2. Hypothesised two-step reaction mechanism of CO₂ chemisorption on APS-2.6.^[283]

4.3.2 Effect of Amine Type

To investigate the effect of amine type on the column breakthrough behaviour of functionalised nanofibrous silica, a breakthrough curve for a triamine-grafted sample (TAS-2.6) with the same nitrogen loading as APS-2.6 was recorded under the same adsorption conditions (Figure 4.23). The breakthrough time (t_b) of TAS-2.6 is 4 min compared to 5.2 min for APS-2.6. One of the reasons for this could be the fact that, despite having similar amine loadings, the monoamine-grafted material contains only primary amines whereas the TAS-modified nanofibres contains primary and secondary moieties. Since secondary amines have a lower heat of adsorption than primary amines^[63], the lower density of primary amines in TAS-2.6 means that it is less selective in removing CO₂ from the feed gas, leading to a quicker breakthrough time.

Similarly to APS-2.6, TAS-2.6 exhibits a steep rise in outlet concentration after breakthrough. TAS-2.6 reached pseudo-equilibrium sooner than APS-2.6 (79 *versus* 100 min). This is because less aminosilane is grafted on TAS-2.6 compared to APS-2.6 resulting in more rapid diffusion of CO₂ to the adsorption sites through the former material. The pseudo-equilibrium capacity of TAS-2.6 under the conditions tested is 0.31 mmol/g.

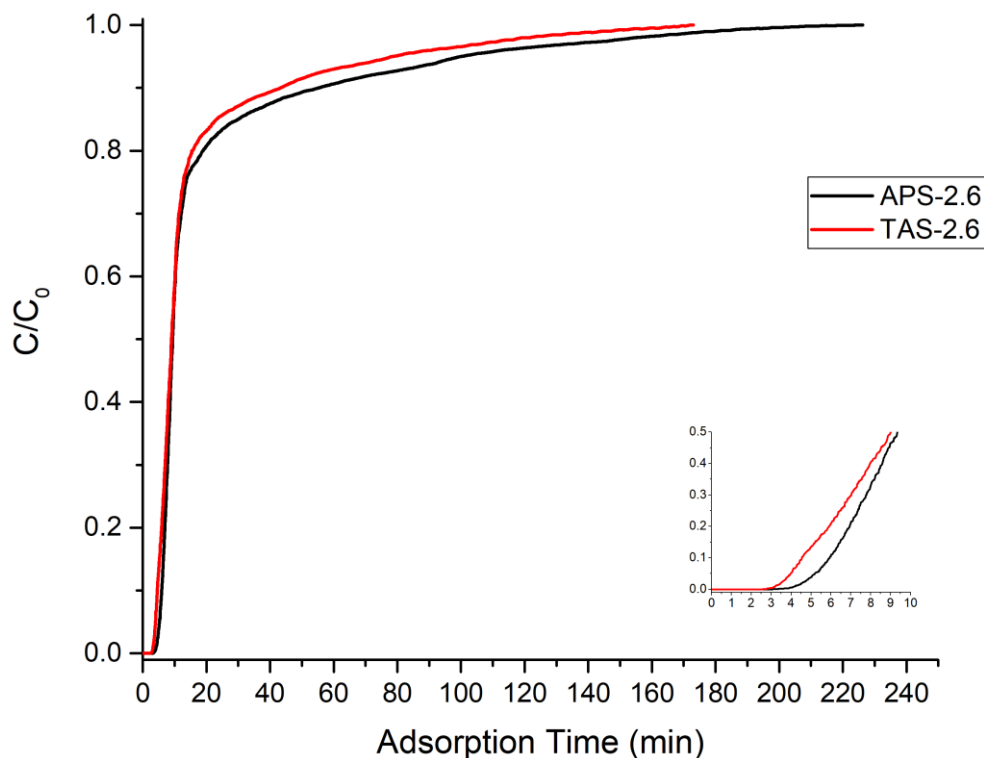


Figure 4.23. Breakthrough profiles of APS-2.6 and TAS-2.6 (100 SCCM, 25°C).

4.3.3 Effect of Amine Loading

Three materials were tested with loadings of 2.6, 4.9 and 6.4 mmol_N/g (TAS-2.6, TAS-4.9 and TAS-6.4, respectively). Breakthrough curves of the three materials were recorded using a flow rate of 100 SCCM and adsorption temperature of 25°C (Figure 4.24).

TAS-4.9 has the quickest breakthrough time of 5.5 min, followed by TAS-2.6 (4 min) and TAS-6.4 (3.3 min). Subsequently, all three profiles show a step-like rise in outlet CO₂ concentration up to 80% of the column inlet concentration. For the remainder of the experiments, the concentration tailed off, with all three materials reaching pseudo-equilibrium ($C/C_0 = 0.95$) between 75 and 84 min.

Initially, increasing the amine loading slightly increases the pseudo-equilibrium capacity from 0.31 mmol/g for TAS-2.6 to 0.33 mmol/g for TAS-4.9 (Figure 4.25). Increasing the loading further results in a marginal reduction in CO₂ uptake to 0.31 mmol/g for TAS-high. Thus, under the conditions tested, the density of adsorption sites did not significantly influence the CO₂ loading on the nanofibres at pseudo-equilibrium. Because of this, the amine efficiency decreases appreciably with loading, from 0.13 mmol_{CO2}/mmol_N for TAS-2.6 to 0.05 mmol_{CO2}/mmol_N for TAS-6.4. The material with the middle amine loading (TAS-4.9) has the highest extraction rate and capture fraction at $C/C_0 = 0.95$ of 0.26 mmol·g⁻¹·h⁻¹ and 25%, respectively (Figure 4.26).

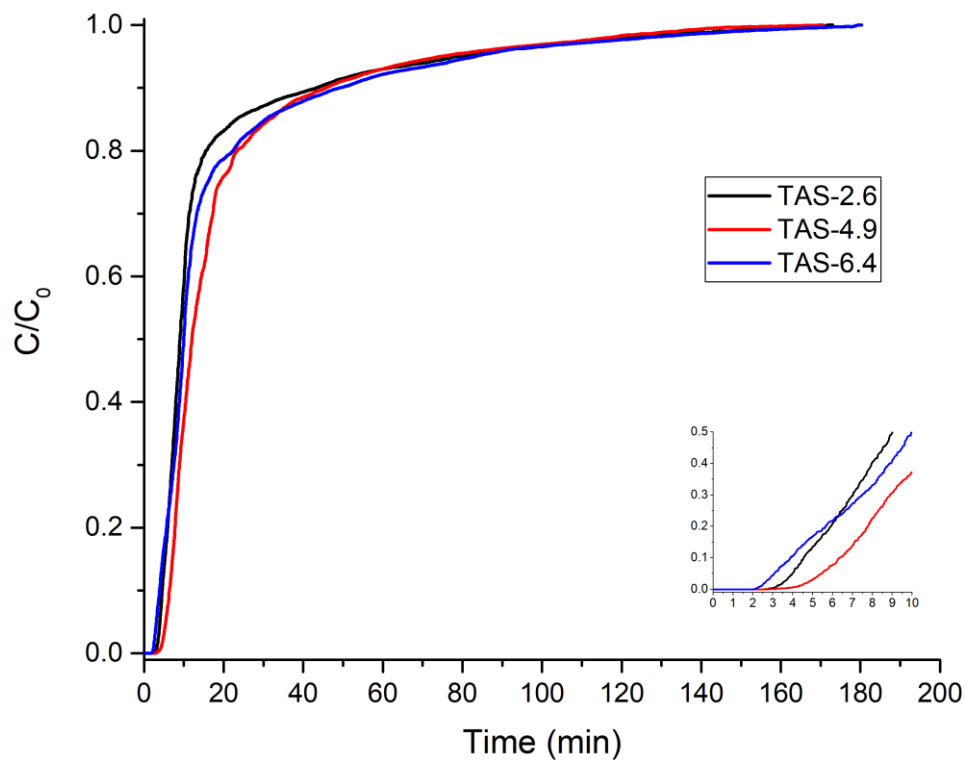


Figure 4.24. Breakthrough profiles of TAS-grafted nanofibrous silicas with different amine loadings (100 SCCM, 25°C).

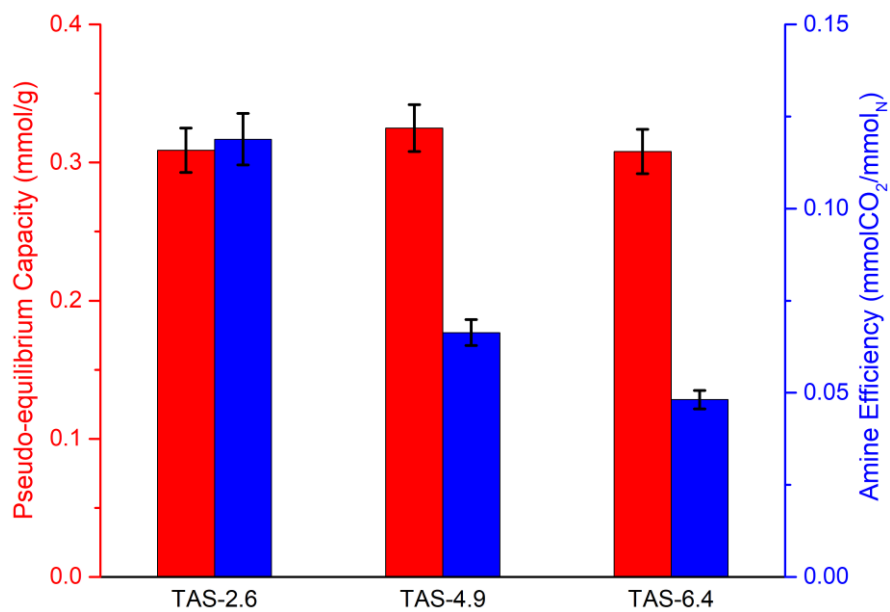


Figure 4.25. Pseudo-equilibrium capacity and amine efficiency of the three TAS-grafted materials (25°C, 100 SCCM).

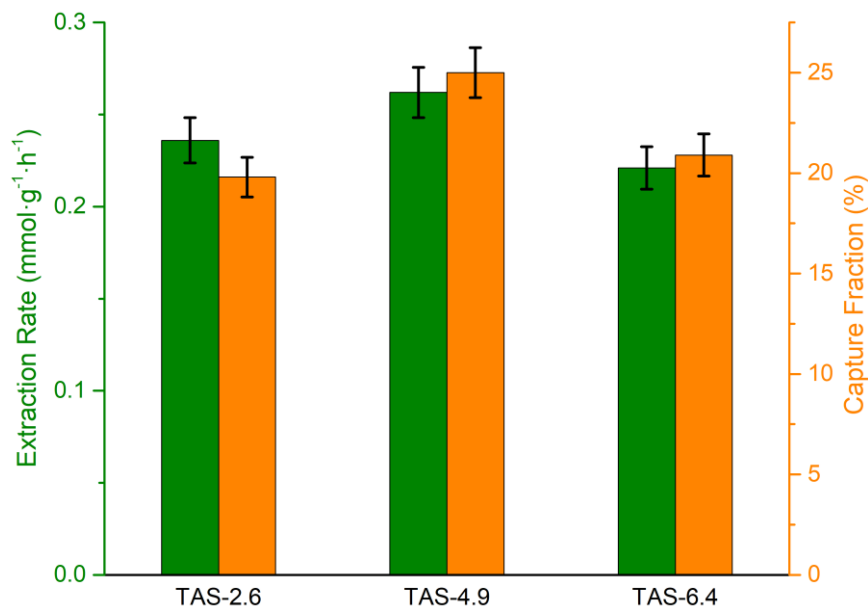


Figure 4.26. CO₂ extraction rate and capture fraction of the three TAS-grafted adsorbents at $C/C_0 = 0.95$.

4.3.4 Effect of Flow Rate

Feed gas flow rate is an important consideration when optimising a carbon capture system. To understand the impact of this factor on the adsorption behaviour of functionalised nanofibrous silica, four materials (APS-2.6, TAS-2.6, TAS-4.9 and TAS-6.4) were studied using the fixed-bed column apparatus at three flow rates (25, 50 and 100 SCCM).

The recorded breakthrough curves of APS-2.6 show that flow rate has a remarkable impact on the CO₂ uptake behaviour of the material (Figure 4.27). As expected, the breakthrough time (t_b) is inversely related to the flow rate; doubling the flow rate from 25 SCCM resulted in t_b decreasing from 41 to 15 min. Increasing the flow rate again to 100 SCCM caused a further shortening of the breakthrough time to 5 min. After breakthrough, all three test conditions exhibit a sharp rise in outlet concentration with time, followed by a slow tailing off up to the point of adsorbent saturation (i.e. $C/C_0 = 1$).

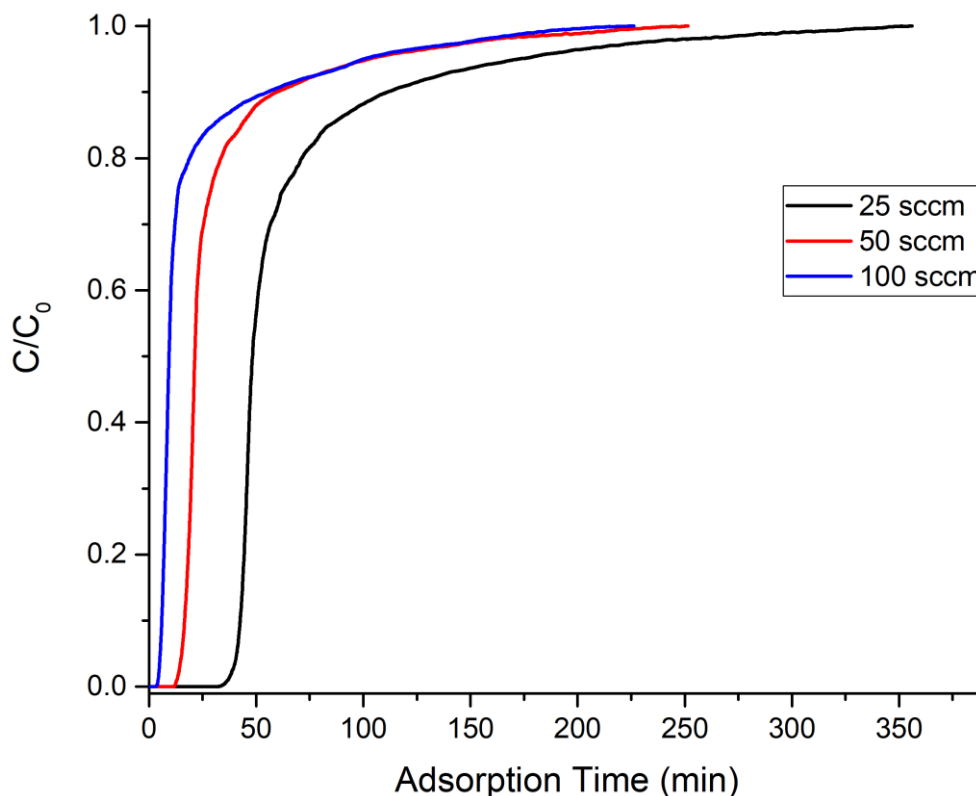


Figure 4.27. Breakthrough curves for APS-2.6 under various flow rates at 25°C.

The same trend is seen with the breakthrough curves of the TAS-grafted materials (Figure A7, Figure A8 and Figure A9). All three exhibit a decrease in breakthrough time with flow rate (Figure 4.28). Despite having similar amine loadings, TAS-2.6 has a shorter t_b in comparison to APS-2.6, regardless of flow rate. This can be explicated by the differing amounts of primary amines in the two materials (see Section 4.3.2). The difference in breakthrough time between APS-2.6 and TAS-2.6 is more pronounced at lower flow rates. For instance, at 25 SCCM, the difference is 5 min, whilst at 100 SCCM, it is 0.5 min. The same trend in t_b with amine loading as observed in Section 4.3.3 is maintained at lower flow rates too, with TAS-4.9 having the longest, followed by TAS-2.6 then TAS-6.4. As with the performance comparison between APS-2.6 and TAS-2.6, the differences in breakthrough time between the three TAS-graft materials is accentuated at lower flow rates.

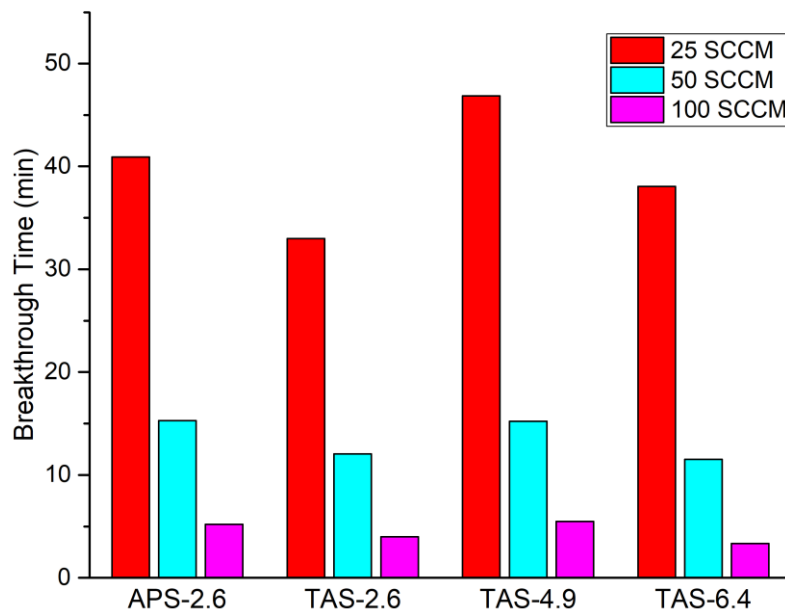


Figure 4.28. Breakthrough times of the four adsorbents under various flow rates at 25°C.

Increasing the flow rate resulted in an increase in CO₂ extraction rate of all four adsorbents (Figure 4.29). For example, when the flow rate was increased from 25 to 100 SCCM, the capture rate of APS-2.6 increases from 0.09 to 0.19 mmol·g⁻¹·h⁻¹. The improvement in capture rate is attributed to the reduction in the boundary layer thickness with flow rate. In fluid dynamics, the boundary layer is the thin region of fluid flow above a solid surface within which the velocity of the fluid varies from zero at the gas-solid interface to the free stream velocity of the fluid outside the boundary layer. The region creates resistance to CO₂ flux into the adsorbent (also known as film diffusion). Increasing the flow rate reduces the thickness of the boundary layer, thereby reducing film diffusion resistance.^[277]

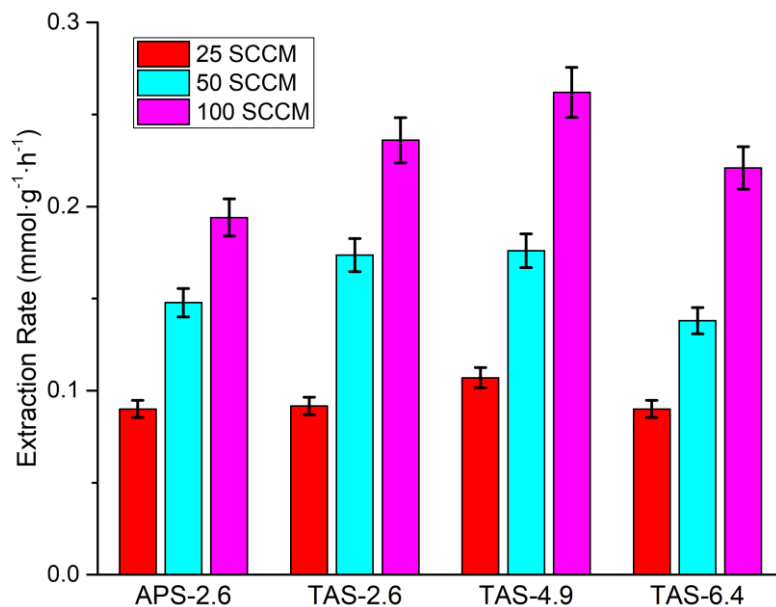


Figure 4.29. CO₂ extraction rates of the four adsorbents at various flow rates.

As expected, the capture fraction is inversely related to the flow rate for the four adsorbents (Figure 4.30). For example, when the flow rate was increased from 25 SCCM to 50 SCCM, the capture fraction of APS-2.6 decreases from 36% to 29%, respectively. It then decreases by a further 10% when the flow rate was doubled again to 100 SCCM. The reduction in capture fraction can be explained by the shortening of the residency time of the gas stream in the adsorption column as the flow rate increases. This results in less time for diffusion of CO₂ to the active sites inside the nanofibres.

The triamine-grafted material with the lowest amine density, TAS-2.6, has a capture fraction of 30% at the lowest flow rate, six percentage points smaller than APS-2.6. However, at the higher flow rates of 25 and 50 SCCM, the two adsorbents have similar capture fractions. Compared to the other adsorbents, TAS-4.9 has the highest capture efficiency at all three flow rates.

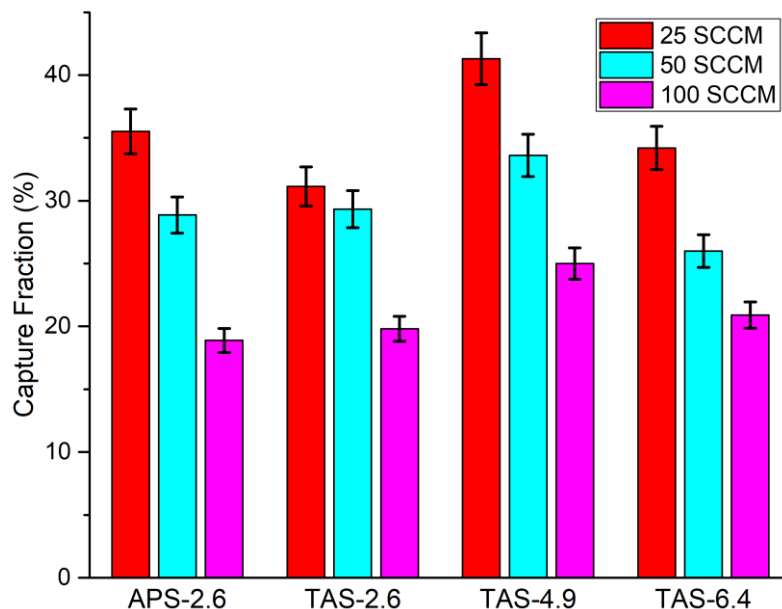


Figure 4.30. Capture fraction of the four amine-modified nanofibrous silicas at various flow rates.

The above observations show there is a trade-off between CO₂ extraction rate and capture efficiency. This has practical implications for the use of these adsorbent in a DAC plant. Whilst low flow rates favour high capture fractions, poor capture rates necessitate the installation of more reactors to achieve a certain daily CO₂ removal rate. This in turn will add to the plant's capital expenditure. Conversely, high flows rates endow adsorbents with high extraction rates, however, this comes at the expense of capture efficiency. More air must be processed to achieve a certain daily removal rate which adds to the energy and financial cost of operating the fans and pumps that supply air to the reactor.

4.3.5 Effect of Temperature

Since the terrestrial surface temperature of air varies spatially and temporally between -25 and 45°C^[276], it is important to understand how the performance of potential adsorbents for DAC is impacted by the feed gas temperature. Of particular importance is sub-ambient testing, which is seldom reported in the literature.^[25] To this effect, the CO₂ capture performance of the four amine-grafted nanofibrous silicas was investigated at temperatures between -5 and 45°C using the fixed-bed column set-up.

The profile of the breakthrough curve for APS-2.6 varied depending on the adsorption temperature (Figure 4.31). The breakthrough time consistently increases with temperature from 3.5 min at -5°C to 11 min at 45°C. After breakthrough, the CO₂ concentration recorded at -5 and 5°C increases rapidly before plateauing out. The breakthrough profiles are less sharp at adsorption temperatures above 5°C.

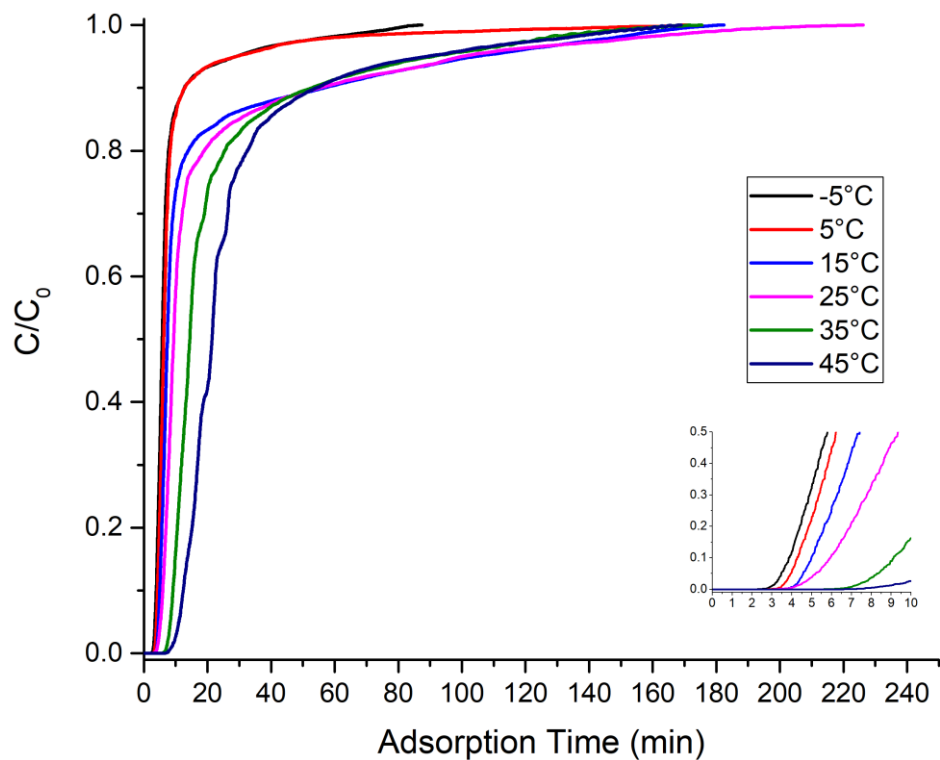


Figure 4.31. Breakthrough curves for APS-2.6 at various temperatures (100 SCCM flow rate).

Increasing the adsorption temperature from -5 to 5°C resulted in a marginal increase in pseudo-equilibrium capacity from 0.12 to 0.13 mmol/g, respectively (Figure 4.32). Raising the temperature again to 15°C caused over a doubling in the capacity to 0.3 mmol/g. The capacity continued to increase with temperature, reaching 0.46 mmol/g at 45°C . The fact that temperature has a positive effect on the pseudo-equilibrium capacity of APS-2.6 shows that CO_2 uptake in this temperature range is kinetically controlled.

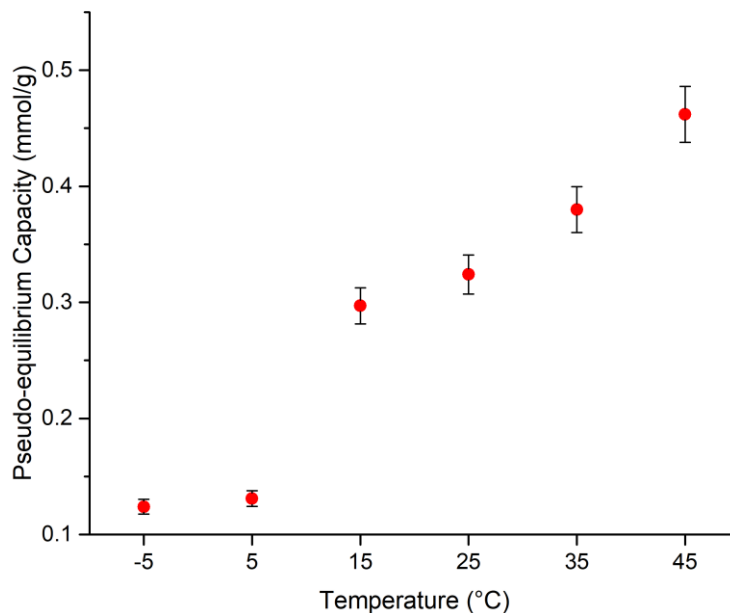


Figure 4.32. Pseudo-equilibrium adsorption capacity of APS-2.6 at various temperatures (100 SCCM).

^1H - ^{13}C CP/MAS NMR spectra were collected for APS-2.6 after exposure to 400 ppm CO_2 at adsorption temperatures between -5 and 45°C (Figure 4.33). As the adsorption temperature was increased, the intensity of the carbonyl resonance at 165 ppm, previously assigned to carbamate adducts, increases. This implies that increasing the temperature promotes the formation of ammonium carbamate on the nanofibres.

The appearance of the middle methylene resonances from the aminopropyl groups at 27.8 ppm (C2a) and 23.5 ppm (C2b) changes above 15°C . As discussed in Section 4.3.1, these two environments are associated with aminopropyl branches bearing non-protonated and protonated amine groups, respectively. The intensity of the C2b peak, relative to C2a, increases with adsorption temperature due to a higher abundance of protonated amines from CO_2 chemisorption.

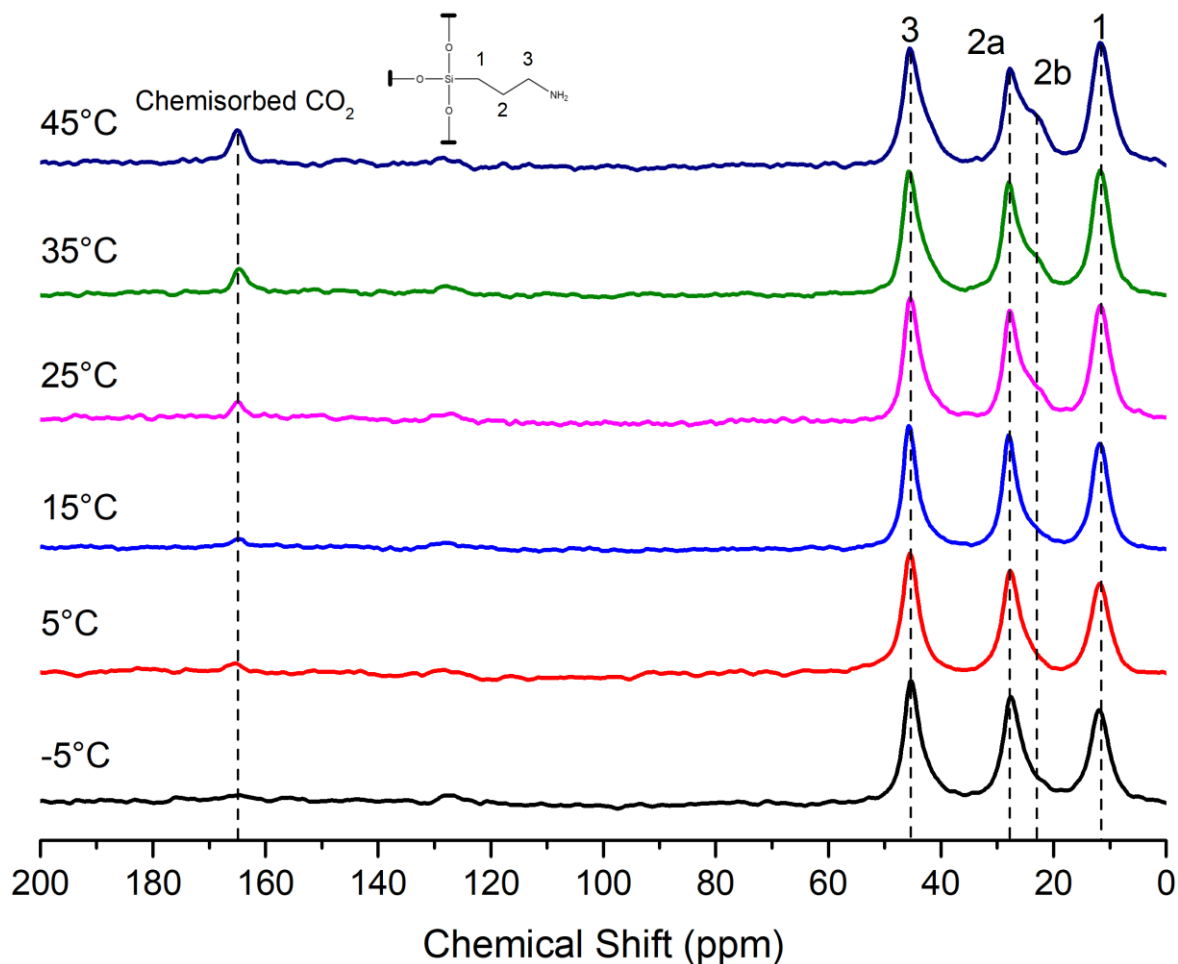


Figure 4.33. ^1H - ^{13}C CP-MAS NMR spectra of APS-2.6 after 400 ppm CO_2 exposure at various temperatures.

The impact of temperature on the process performance of APS-2.6 was also evaluated by calculating the CO_2 extraction rate and capture fraction (Figure 4.34). Between -5 and 5°C , the rate of CO_2 extraction marginally increases from 0.26 to $0.27 \text{ mmol}\cdot\text{g}^{-1}\cdot\text{h}^{-1}$. Likewise, the capture fraction improves from 25 to 27% (Figure 4.35). Yet, when the column temperature is increased to 15°C , there is a decrease in capture performance, with adsorption rate and capture fraction decreasing to respective values of $0.17 \text{ mmol}\cdot\text{g}^{-1}\cdot\text{h}^{-1}$ and 17% . This may be due to the extra amines rendered accessible for adsorption at 15°C having longer diffusion pathlengths compared with the other active sites. Above 15°C , the rate of CO_2 extraction and capture fraction improves with temperature, reaching $0.31 \text{ mmol}\cdot\text{g}^{-1}\cdot\text{h}^{-1}$ and 30% at 45°C due to the promotive effect of temperature on CO_2 transfer to the adsorption sites.

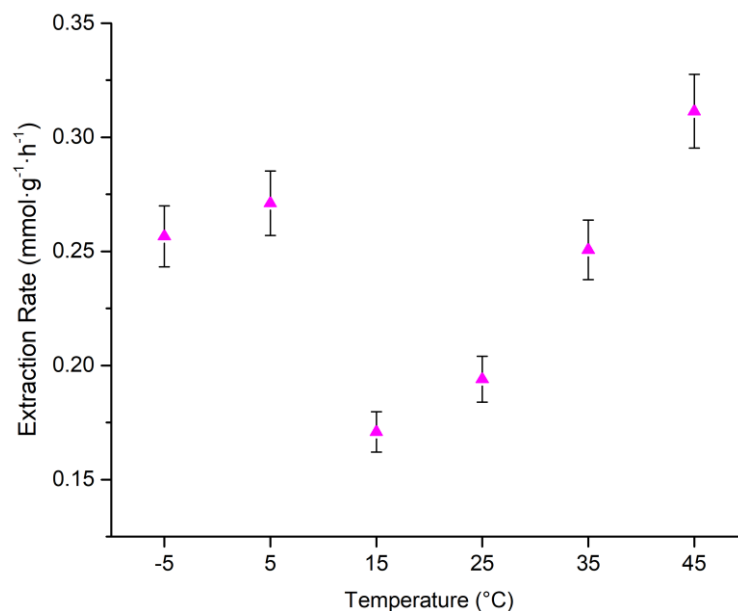


Figure 4.34. CO₂ extraction rate for APS-2.6 at different temperatures.

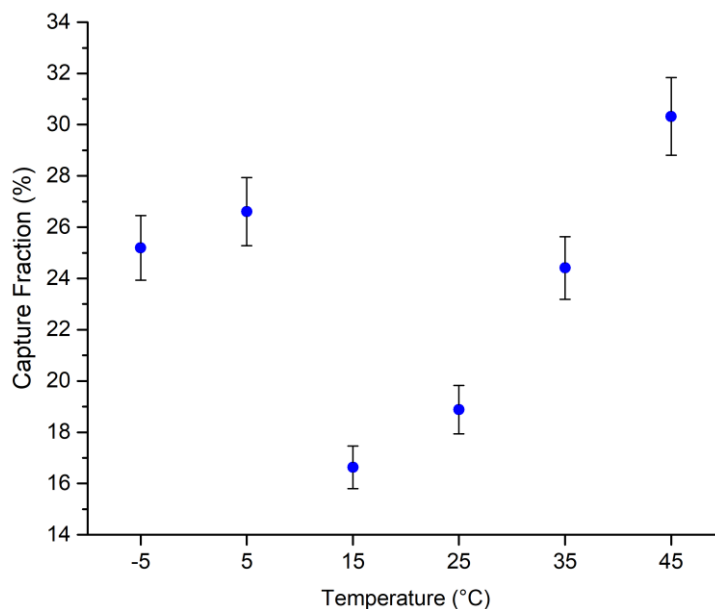


Figure 4.35. Capture fraction for APS-2.6 at different temperatures.

Next, breakthrough experiments were carried out for triamine-grafted nanofibrous silica (TAS-2.6, TAS-4.9 and TAS-6.4) at various temperatures (for breakthrough curves, see Figure A10, Figure A11 and Figure A12 in Appendix). TAS-4.9 and TAS-6.4 show an increase in breakthrough time with temperature (Figure 4.36). On the other hand, the breakthrough time of TAS-2.6 initially decreases from 3.6 min at -5°C to 3.2 min at 5°C, before increasing to 5 min at 35°C and remaining at that time at 45°C.

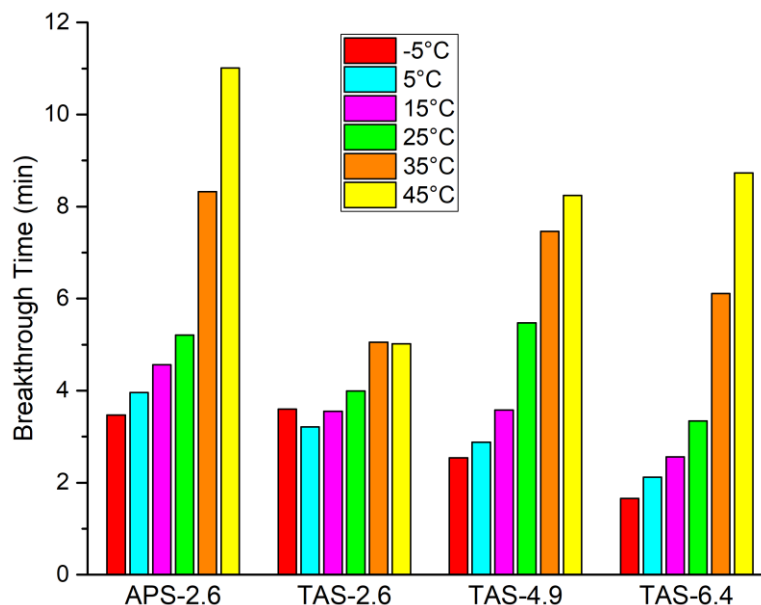


Figure 4.36. Variation in breakthrough time with temperature of four amine-functionalised nanofibrous silicas (100 SCCM flow rate).

Despite having the same amine loading as APS-2.6, the pseudo-equilibrium capacity of TAS-2.6 initially decreases between -5 and 5°C from 0.18 to 0.12 mmol/g (Figure 4.37), suggesting that the adsorption process is thermodynamically controlled at these two temperatures. However, above 5°C, the adsorption temperature has a positive effect on CO₂ uptake of TAS-2.6, indicating that adsorption transitioned to a kinetically limited process. At 15°C, the CO₂ loading of TAS-2.6 jumps to 0.26 mmol/g and continues to rise with temperature, reaching a maximum value of 0.41 mmol/g at 45°C. Excluding the materials' performance at -5°C, APS-2.6 has a higher pseudo-equilibrium capacity compared to TAS-2.6 regardless of the column temperature. As previously discussed, primary amines have a higher heat of adsorption compared to secondary amines and since only primary amines are tethered to the nanofibres in APS-2.6, it is more selective in removing CO₂ than TAS-2.6, which contains both 1° and 2° amines.

For TAS-4.9 and TAS-6.4, the pseudo-equilibrium capacity increases across the entire temperature range corresponding to adsorption that is kinetically limited. The enhancement in CO₂ uptake is modest between -5 to 15°C from 0.13 to 0.17 mmol·g⁻¹·h⁻¹ and 0.06 to 0.11 mmol·g⁻¹·h⁻¹ for TAS-4.9 and TAS-6.4, respectively. In contrast, between 15 and 45°C, there is a considerable improvement in CO₂ uptake by both materials, with respective values of 0.52 and 0.71 mmol/g at 45°C.

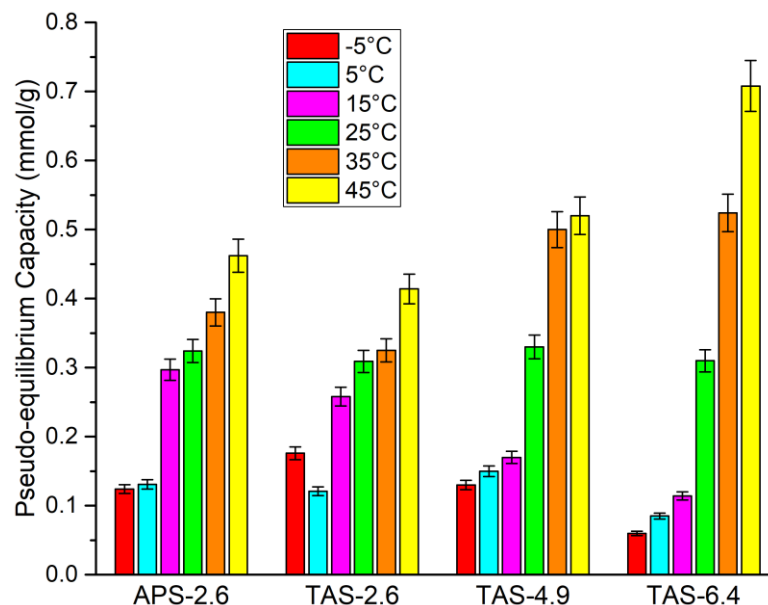


Figure 4.37. Variation in pseudo-equilibrium adsorption capacity with temperature of the four adsorbents.

To investigate whether there is a mechanistic cause for the enhancement in CO₂ uptake on the triamine-functionalised materials, ¹³C CP/MAS solid-state NMR spectra of TAS-4.9 were recorded after exposure to CO₂ at temperatures between -5 and 45°C (Figure 4.38). Peaks associated with the functional groups of the grafting agent are visible between 6 and 62 ppm (see Section 3.6 for their assignments)^[270-272] whilst the resonance at 128 ppm is assigned to entrapped toluene from the grafting process.^[257] As with the monoamine-functionalised APS-2.6 adsorbent, there is a single peak at 165 ppm associated with carbamate formation which grows in intensity with temperature. Therefore, the increase in CO₂ uptake is attributed to enhanced ammonium carbamate formation. As with APS-2.6, we propose that raising the adsorption temperature increases the mobility of the polymer-like aminosiloxane layer on the nanofibres in TAS-4.9, rendering more amines accessible for CO₂ chemisorption.

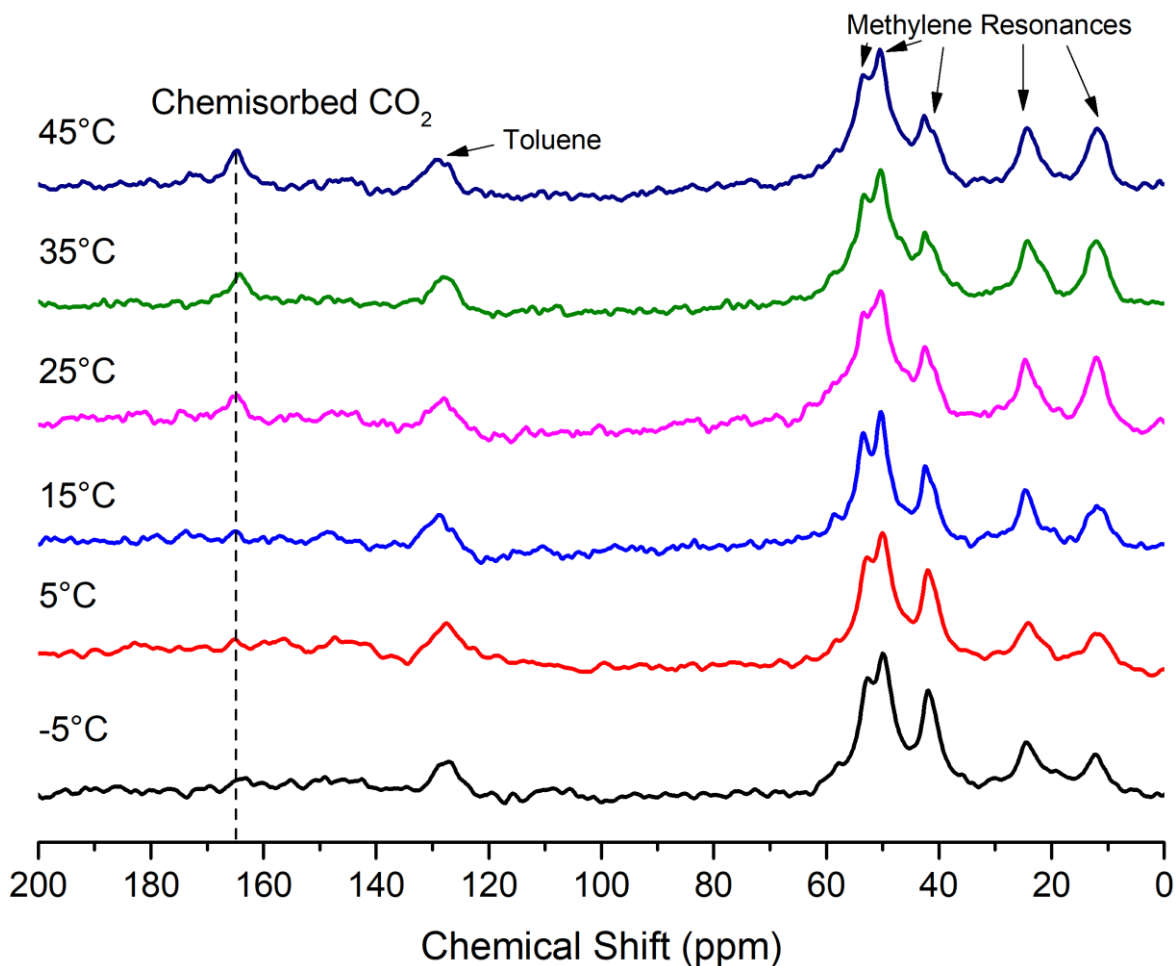


Figure 4.38. ^1H - ^{13}C CP-MAS NMR spectra of TAS-4.9 after exposure to dry 400 ppm CO_2 at four adsorption temperatures.

The rate of CO_2 extraction was computed to understand the effect of temperature on adsorption kinetics (Figure 4.39). Similarly to APS-2.6, there is an initial increase in capture rate for TAS-2.6 between -5 and 5°C from 0.25 to $0.34 \text{ mmol}\cdot\text{g}^{-1}\cdot\text{h}^{-1}$ respectively. This can be attributed to the enhanced diffusion rate of CO_2 to the active sites in the adsorbent. Raising the adsorption temperature to 15°C resulted in the rate of CO_2 uptake of TAS-2.6 decreasing to $0.2 \text{ mmol}\cdot\text{g}^{-1}\cdot\text{h}^{-1}$. As with APS-2.6, this might be caused by amines with significantly longer diffusion path lengths becoming available for adsorption. From 15 to 35°C , the CO_2 extraction rate of TAS-2.6 increases. This suggests that the promotive effect of temperature on the CO_2 mass transfer rate outweighs the effect of the longer diffusion path lengths to the extra amines made available for chemisorption.

A similar non-monotonic trend to TAS-2.6 is observed for TAS-6.4. There is an initial increase in capture rate to $0.27 \text{ mmol}\cdot\text{g}^{-1}\cdot\text{h}^{-1}$ at 5°C followed by a decrease to $0.22 \text{ mmol}\cdot\text{g}^{-1}\cdot\text{h}^{-1}$ at 25°C and then an uptick to $0.31 \text{ mmol}\cdot\text{g}^{-1}\cdot\text{h}^{-1}$ at 45°C . Meanwhile, for TAS-4.9, the CO_2 removal rate barely changes between -5 and 5°C whilst above 5°C , the capture rate continually improves with temperature. Since the flow rate was not varied, the variation in capture fraction with temperature follows the same trend as the CO_2 extraction rate (Figure 4.40).

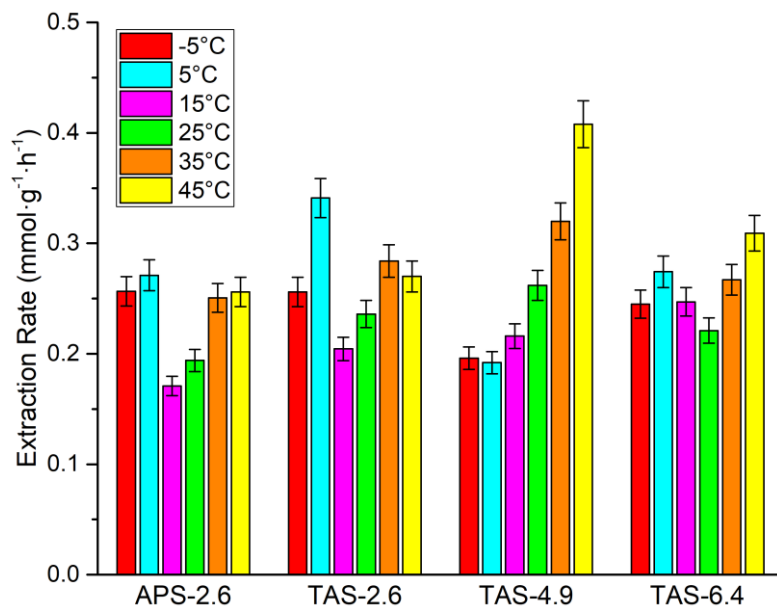


Figure 4.39. CO₂ extraction rates at different temperatures for the four amine-functionalised nanofibrous silicas.

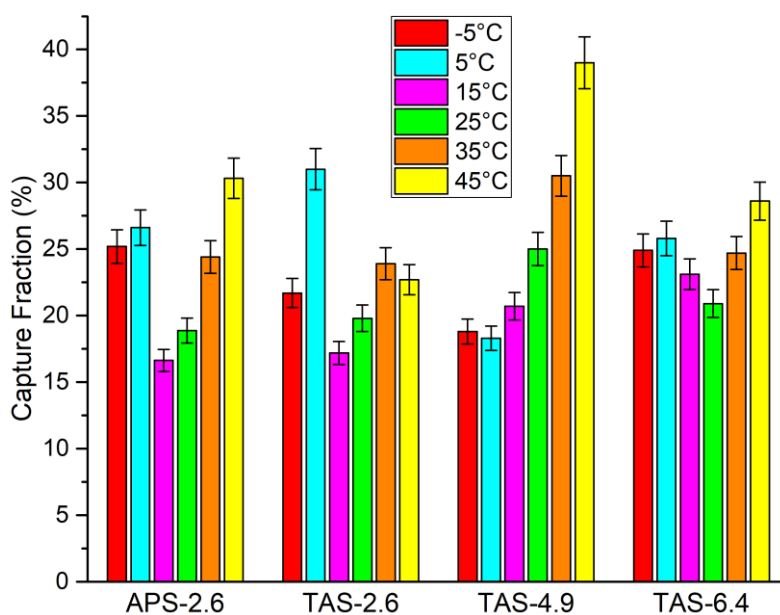


Figure 4.40. CO₂ capture fraction at different temperatures for the four amine-functionalised nanofibrous silicas.

4.3.6 Effect of Humidity

Given that ambient air contains a certain amount of moisture, it is crucial to understand how water affects adsorption of CO₂ on potential materials for DAC. To this effect, breakthrough experiments were carried out using the three TAS-grafted materials under humid conditions by directing the CO₂

feed through a gas bubbler maintained at a temperature of 15°C prior to the gas stream entering the adsorption column. For TAS-2.6, the breakthrough profile during humid adsorption is less sharp compared to that recorded under dry conditions (Figure 4.41). This is also the case for TAS-4.9 and TAS-6.4 (Figure 4.42 and Figure 4.43, respectively). Furthermore, the time to reach adsorbent saturation, when the outlet concentration is equal to that of the inlet, is longer, particularly for the two higher loaded TAS materials, increasing from 75 to 180 min and 83 to 212 min for TAS-4.9 and TAS-6.4, respectively. The less-steep breakthrough curves, along with the prolonged experimental time, indicates that humidity has a negative impact on CO₂ uptake kinetics, perhaps due to the co-adsorption of water.

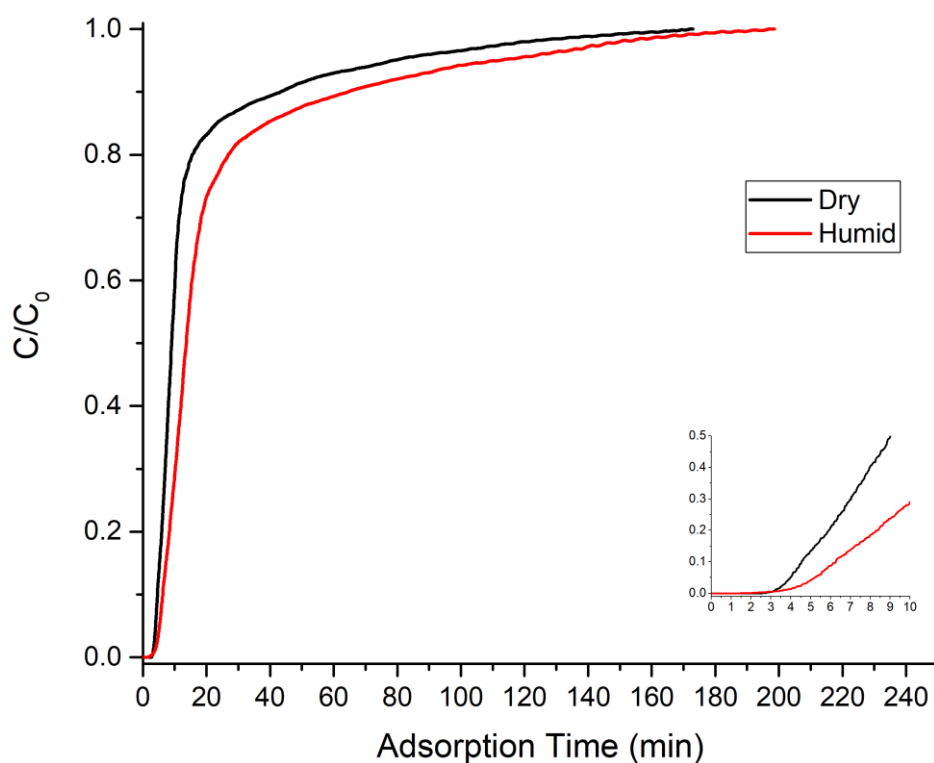


Figure 4.41. Breakthrough curves for TAS-2.6 under dry and humid conditions (25°C, 100 SCCM).

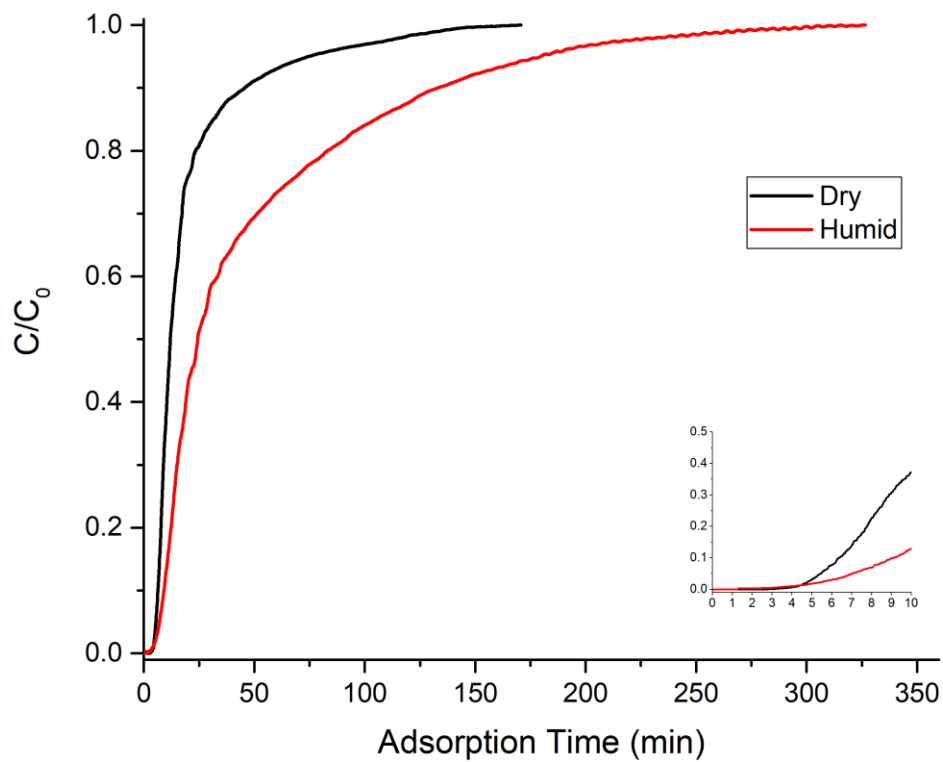


Figure 4.42. Breakthrough curve for TAS-4.9 under dry and humid conditions (25°C, 100 SCCM).

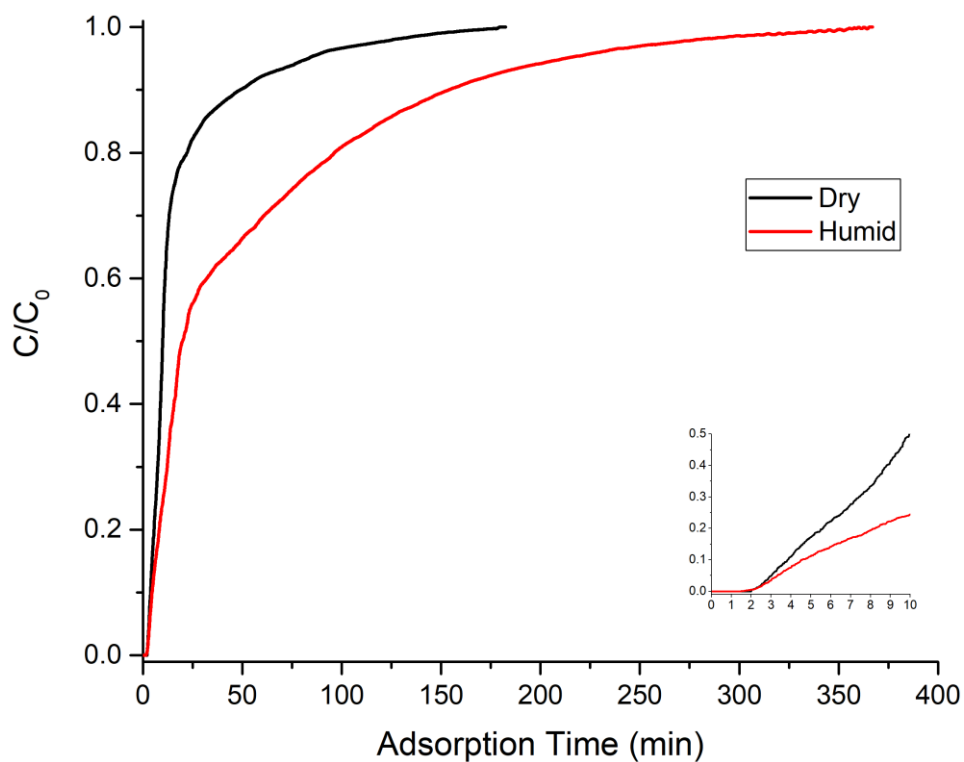


Figure 4.43. Breakthrough curves for TAS-6.4 under dry and humid conditions (25°C, 100 SCCM).

Humidity increases the breakthrough times of TAS-2.6 and TAS-4.9 whilst there is no change in t_b for TAS-6.4 (Figure 4.44).

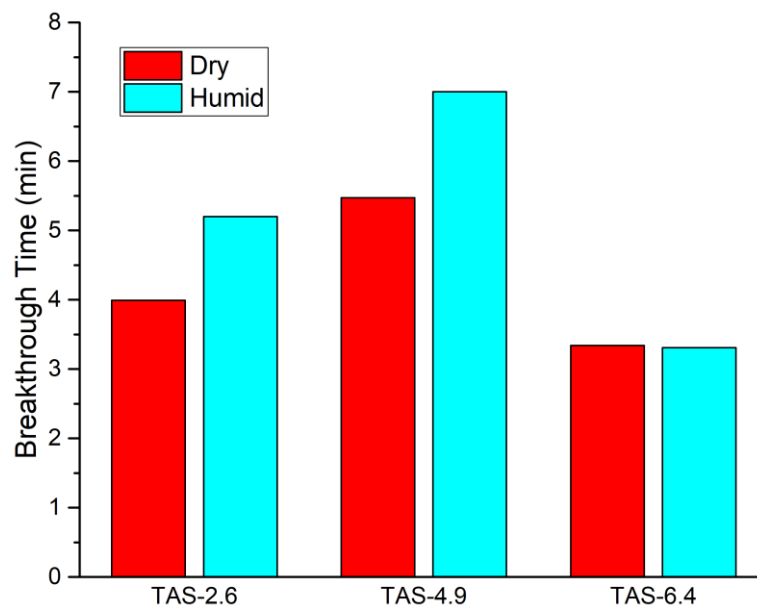


Figure 4.44. Breakthrough times of the three triamine-grafted materials under dry and humid conditions.

Water enhanced the pseudo-equilibrium capacity of all three materials (Figure 4.45). The adsorption capacity of TAS-2.6 increases by over 50% from 0.31 to 0.47 mmol/g. Meanwhile the promotive effect of CO_2 adsorbed on TAS-4.9 and TAS-6.4 is more pronounced, with their respective pseudo-equilibrium capacities rising from 0.33 to 0.83 mmol/g and 0.31 to 0.91 mmol/g.

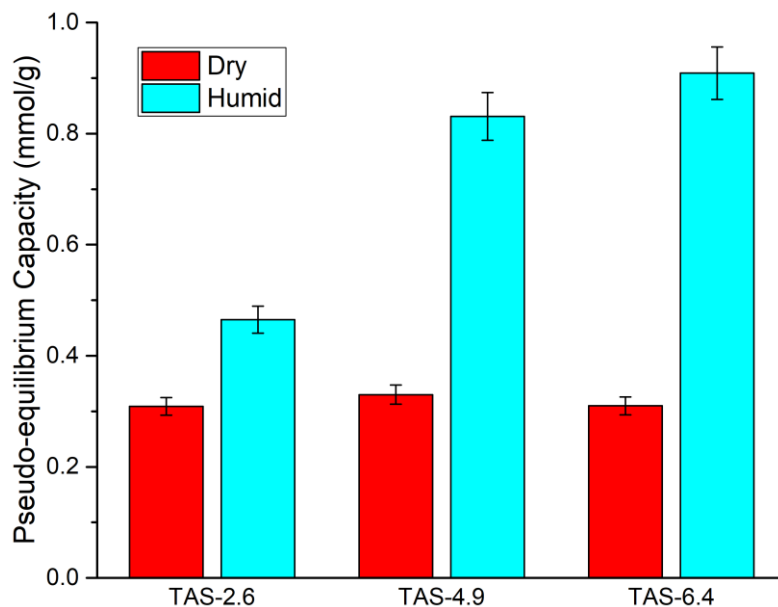


Figure 4.45. Pseudo-equilibrium capacities of the three triamine-grafted nanofibrous silicas after exposure to dry and humid CO₂.

Most DAC studies from the literature on amine-functionalised sorbents have reported an enhancement in CO₂ loading with the introduction of moisture in the feed gas.^[25] There are two theories for this observation. Firstly, the presence of humidity during CO₂ adsorption opens the possibility of bicarbonate formation. Unlike the ammonium carbamate mechanism, which requires two amines for every molecule of adsorbed CO₂ (see Section 4.3.1), the bicarbonate pathway has an amine-CO₂ reaction stoichiometry of 1:1. This results in humid adsorption having a maximum theoretical adsorption capacity twice that of the ammonium carbamate route. Some papers speculated bicarbonate formation as the cause for the positive effect of moisture on CO₂ uptake without any spectroscopic evidence^[287-289]. However, an FTIR study reported an absorption band associated with the bicarbonate ion on monoamine-functionalised silica with a low amine loading.^[275] The second explanation for the positive effect of humidity on CO₂ adsorption is an increase in ammonium carbamate formation, particularly on amine adsorbents with a high surface coverage.^[253, 275]

To elucidate the possible mechanistic cause of the adsorption capacity increase on amine-functionalised nanofibrous silica, a ¹³C solid-state NMR spectrum of moderately-loaded, TAS-modified nanofibres (TAS-4.9) was recorded after moist CO₂ exposure and compared with a spectrum of the material tested under dry conditions (Figure 4.46). Despite using the same experimental parameters, the signal-to-noise ratio of the methylene resonances in the grafting agent (between 5 and 70 ppm) is poorer in the material after humid CO₂ exposure. This could be due to surface-bound water reducing the cross-polarisation efficiency of the experiment. The ammonium carbamate resonance at 165 ppm in the dry spectrum also appears in the spectrum of the adsorbent exposed to humidity. Its signal-to-noise is also attenuated by moisture in the samples. No other resonances associated with CO₂-amine adducts are present, such as carbamic acid

(153 – 161 ppm^[284]) or physisorbed CO₂ (125 ppm^[286]). Therefore, it is probable that moisture promoted the production of more ammonium carbamate. This agrees with Mafra and co-workers, who found that ammonium carbamate formation was the most abundant adduct formed on amine-grafted SBA-15 silica after adsorption of moist ¹³CO₂ under controlled partial pressures. They supported these spectral findings with computed Gibbs Free energy calculations of all the possible chemisorption products, which revealed that ammonium carbamate is the most energetically stable adduct.^[290] The reason for enhanced ammonium carbamate formation could be due to adsorbed water disrupting hydrogen bonding between the alkylamine moieties, thereby increasing the number of accessible amines for adsorption.^[253]

Yet a different study argued that bicarbonate formation cannot be discounted based purely from ¹³C NMR work. In one study, they ran a ¹⁵N{¹³C} REDOR NMR experiment for monoamine-grafted SBA-15 after exposure to ¹³CO₂. The intensity of the peak at 165 ppm, which they had initially assigned to carbamate based on CP/MAS data, reached only 90% of its anticipated maximum. The missing 10% was deemed to be a result of a ¹³C magnetic environment not directly coupled to ¹⁵N from the amine groups and they postulated that the adduct responsible was bicarbonate.^[283] However, the amine content of the adsorbent used in that publication was less than the lowest loaded adsorbent used in this study, and the group had already established from previous work that bicarbonate formation did not occur in adsorbents with higher amine contents.^[275] Therefore, the positive effect of moisture on CO₂ uptake on the TAS-functionalised nanofibrous silicas is attributed predominantly to an increase in ammonium carbamate adducts, although some bicarbonate formation cannot be fully ruled out.

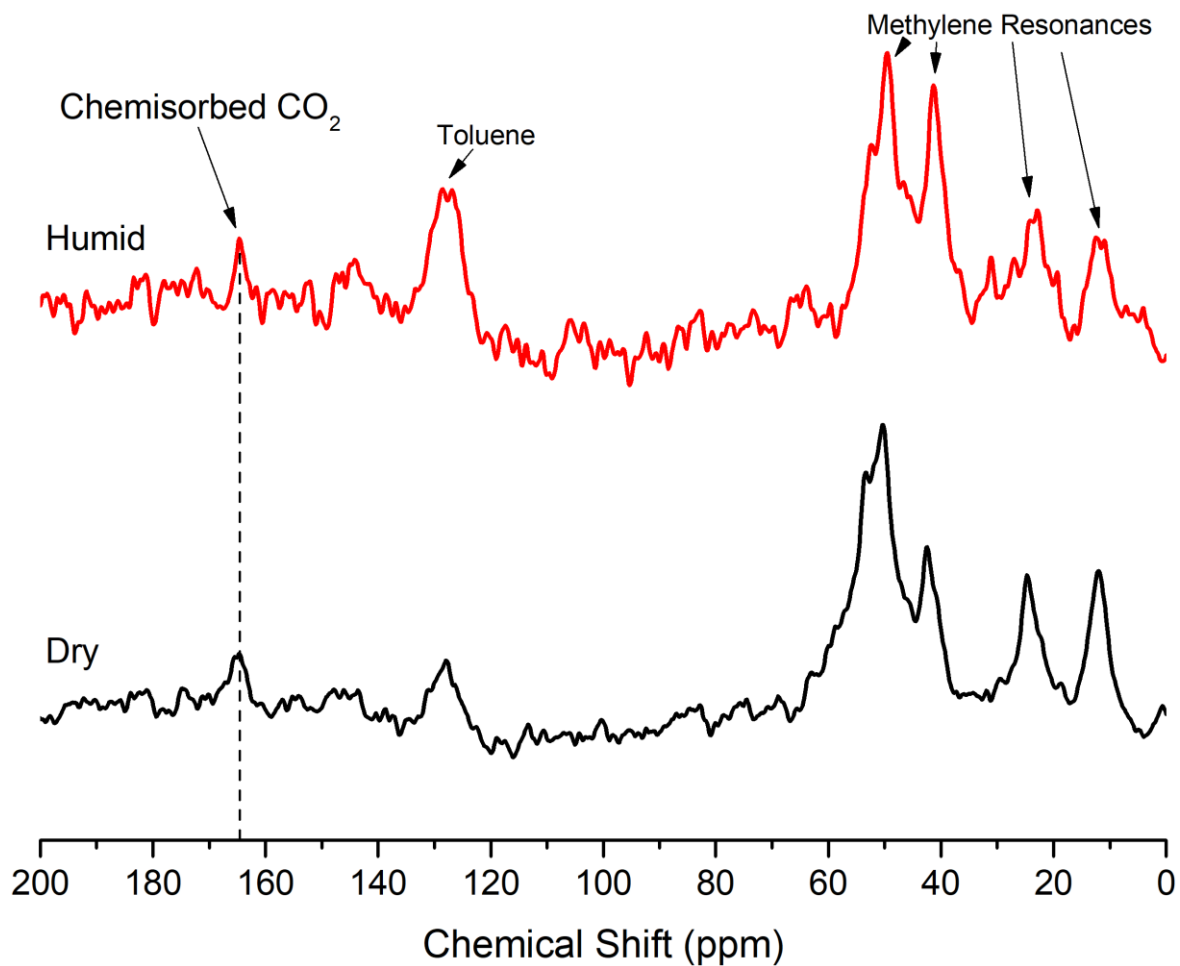


Figure 4.46. ^1H - ^{13}C CP-MAS NMR spectra of TAS-functionalised silica nanofibre after 3 h of exposure to dry and humid CO_2 gas feeds. The spectra are normalised with respect to the tallest methylene peak.

The CO_2 extraction rate and capture fractions of the materials marginally improved under humid conditions (Figure 4.47 and Figure 4.48). TAS-6.4 exhibits the greatest improvement in process performance, with the capture rate increasing from 0.22 to $0.26 \text{ mmol}\cdot\text{g}^{-1}\cdot\text{h}^{-1}$ and capture fraction rising by three percentage points from 21 to 24%.

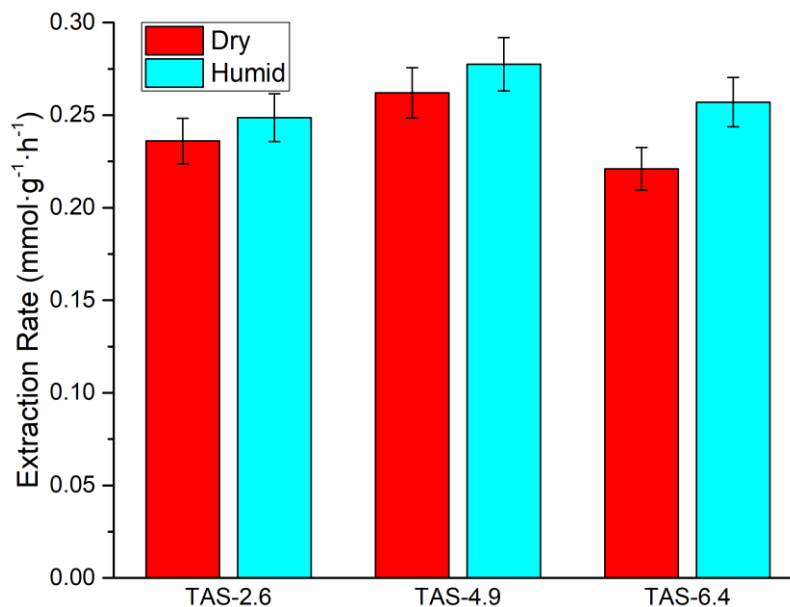


Figure 4.47. Extraction rate of the triamine-grafted materials under dry and humid conditions.

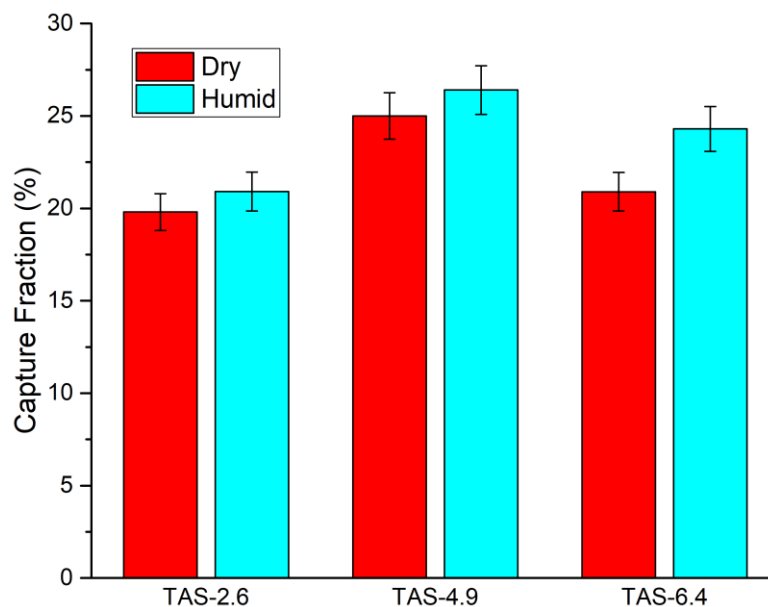


Figure 4.48. Capture fraction of the triamine-grafted materials under dry and humid conditions.

4.3.7 Kinetic Modelling

To gain insight into the mechanisms underpinning CO₂ mass transfer, three kinetic models were fitted to adsorption data from the 35 fixed-bed tests: pseudo-first order (PFO), pseudo-second order (PSO) and Avrami.

Based on the R² values, the PFO model provides the worst fit to the adsorption data, regardless of the flow rate (Table A2 to Table A5), temperature (Table A6 to Table A9) and humidity (Table A10 to Table A12). This is expected since PFO is reported to represent adsorption in which physisorption

is the mechanism responsible for adsorbate-adsorbent interactions.^[291, 292] As reported in this chapter, ¹³C NMR results show no evidence of physisorbed CO₂ on amine-functionalised nanofibrous silica.

PSO models adsorption better than PFO, achieving an R² greater than 0.99 in 49% of the fixed-bed experiments, compared to 26% for PFO (Figure 4.49). The pseudo-second order model assumes that there is a strong affinity between the adsorbate and adsorbent during adsorption and, as a result, is appropriate for modelling CO₂ uptake driven by chemisorption.^[197, 293] However, Avrami performs even better, producing a fit with an R² greater than 0.99 in 74% of the fixed-bed tests. In the remaining 26% of the experiments, this kinetic model has a corresponding R² of 0.98. Therefore, the Avrami kinetic model provides the best simulation of adsorption uptake on amine-functionalised nanofibrous silica using the fixed-bed set-up. It has been reported that, in the context of adsorption, the Avrami model accounts for complex reaction mechanisms or the occurrence of multiple adsorption pathways such as simultaneous chemisorption and physisorption.^[291, 294]

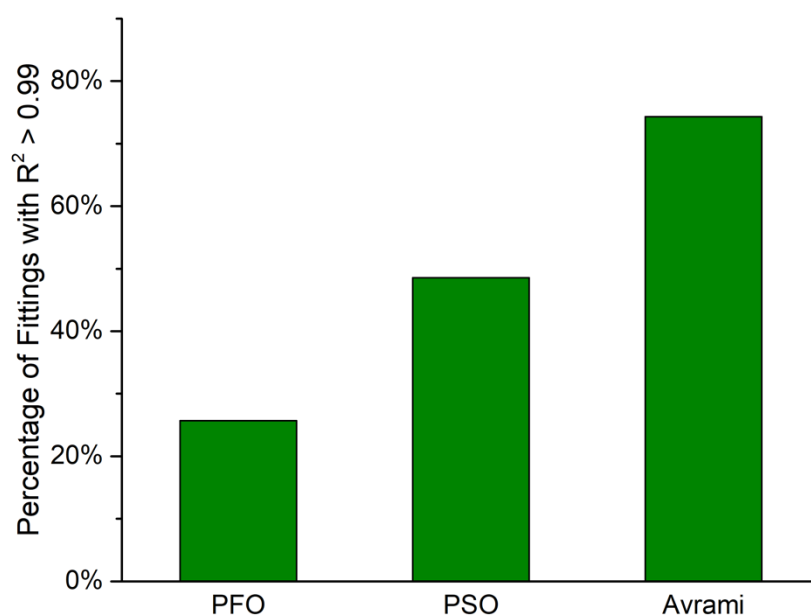


Figure 4.49. Percentage of fittings that yielded an R² greater than 0.99 for the different kinetic models.

For the adsorption data in this study, the value of the Avrami exponent (n_a) varies between 0.47 and 1.2 depending on the material and test conditions, with most experiments yielding exponents less than 1. The most commonly cited interpretation of the physical significance of n_a from the standpoint of CO₂ adsorption is that by Liu *et al.*^[201] They speculated that the value of n_a is related to the ‘dimensionality’ of adsorption sites. A value of 1 equates to homogeneous adsorption whilst higher orders of 2, 3 and 4 correspond to one-, two- and three-dimensional growth of occupied sites, respectively.

This interpretation is extrapolated from the physical basis of the Avrami equation in the context of phase changes, its original application. Phase changes are commonly described as two-step processes. The first stage is nucleation, which is the start of the formation of a new phase with lower free energy inside a parent phase with a higher free energy. The second stage is growth of the new phase, in up to three dimensions. Growth of new phases can be interface-controlled or diffusion-controlled. Lui *et al.*'s analogy is an extrapolation of an interface-controlled phase change, wherein, the growth of the new phase is solely dependent on the attachment of atoms or molecules from the surrounding parent phase onto the new phase at the interface.^[295]

Liu *et al.*'s interpretation of the Avrami equation is problematic in two ways. Firstly, there is no experimental evidence to support their analogy. Secondly, it does not allow for values of n_a less than one. For phase changes, the only scenario where n_a can be less than one is when the growth process is diffusion-controlled. This type of phase change can have an Avrami exponent as low as 0.5.^[295, 296] Since the values of n_a from the Avrami fits in this work are mostly below 1, a new interpretation of the Avrami exponent is presented to understand the kinetics of CO₂ adsorption on the nanofibrous adsorbents.

The new interpretation of the Avrami exponent assumes that there are three main steps to CO₂ uptake by the adsorbents: film diffusion, pore diffusion and the chemical reaction at the accessible active sites. When n_a is close to 0.5, it is posited that pore diffusion is the rate-limiting step to CO₂ uptake whereas when n_a is close to 1, a different stage of CO₂ transport limits the uptake of adsorbate. Therefore, increases in n_a imply a reduction in the dependability of CO₂ uptake on pore diffusion.

Avrami modelling of experiments carried out at different flow rates revealed that n_a decreases with flow rate (Figure 4.50). Based on the new interpretation of the Avrami model, the high n_a values at 25 SCCM correspond to CO₂ uptake in which film diffusion is the rate limiting step. As the flow rate is increased, film diffusion resistance decreases, and CO₂ mass transfer becomes more dependent on pore diffusion kinetics.

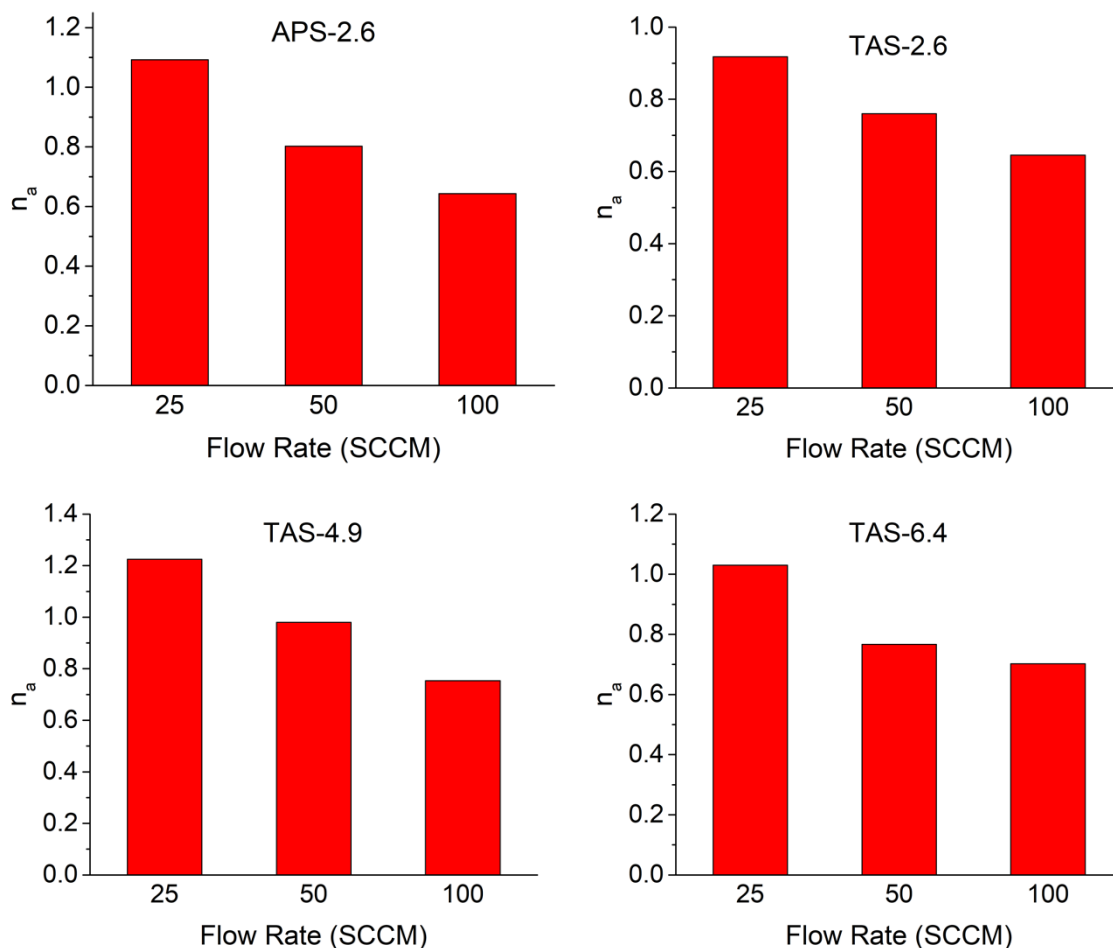


Figure 4.50. Avrami exponents (n_a) from fixed-bed tests at different flow rates (25°C).

As discussed in Section 4.3.5, the column temperature increases the effective diffusivity of CO_2 . Concerning the fixed-bed experiments, apart from APS-2.6, the Avrami exponent is relatively constant up to 15°C, implying CO_2 transport is limited by pore diffusion (Figure 4.51). Above this temperature, n_a increases for all four adsorbents. Since film diffusion is not strongly influenced by adsorption temperature, the increase in n_a is attributed to a shift in the rate limiting step from pore diffusion to the CO_2 -amine reaction.

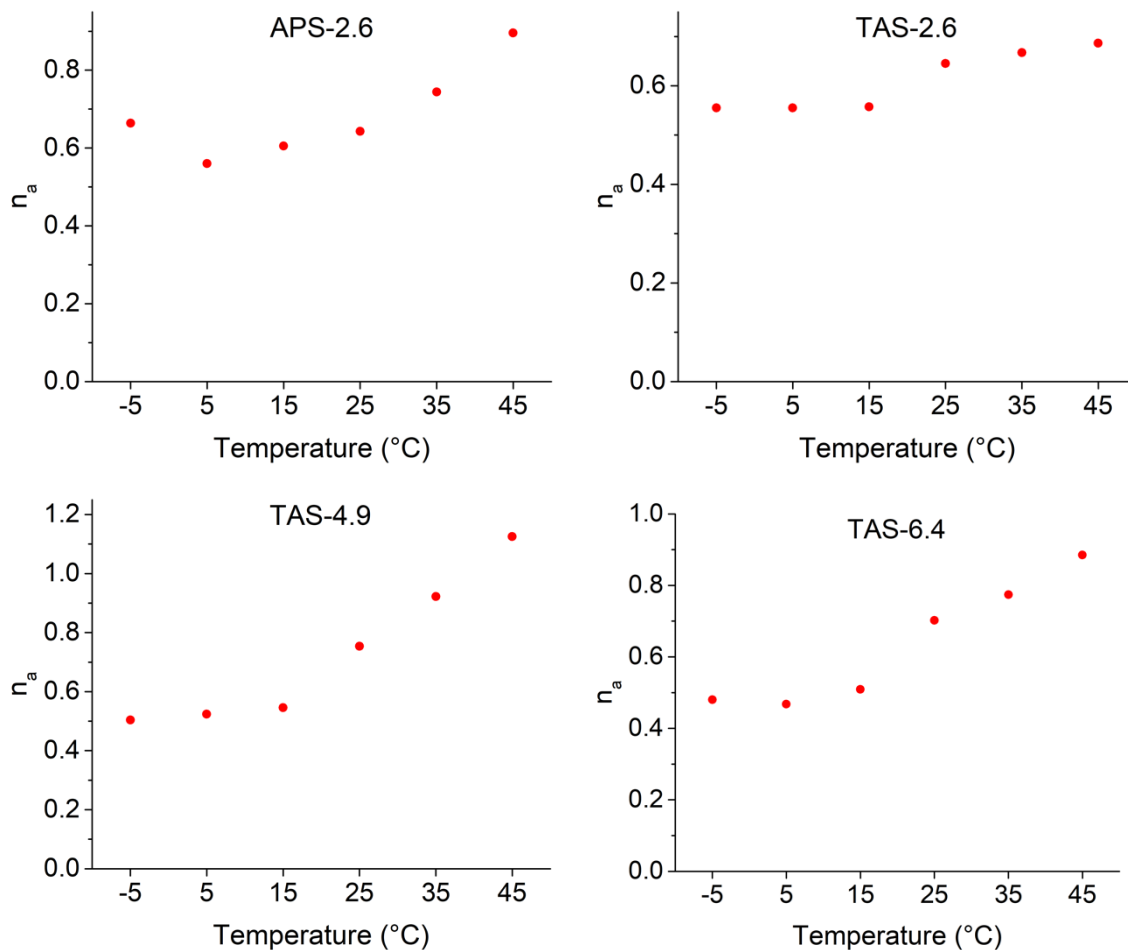


Figure 4.51. Avrami exponents (n_a) from fixed-bed tests at different temperatures (100 SCCM).

Concerning the humid adsorption tests, the increase in n_a under moist conditions (Figure 4.52) suggests that CO_2 mass transfer is limited less by pore diffusion and more by the rate of the chemisorption reaction. In amine-functionalised silicas, water is thought to disrupt hydrogen-bonding between amine functionalities, increasing the number of accessible active sites and improving the effective diffusivity of CO_2 within the layer of grafted amines.^[253]

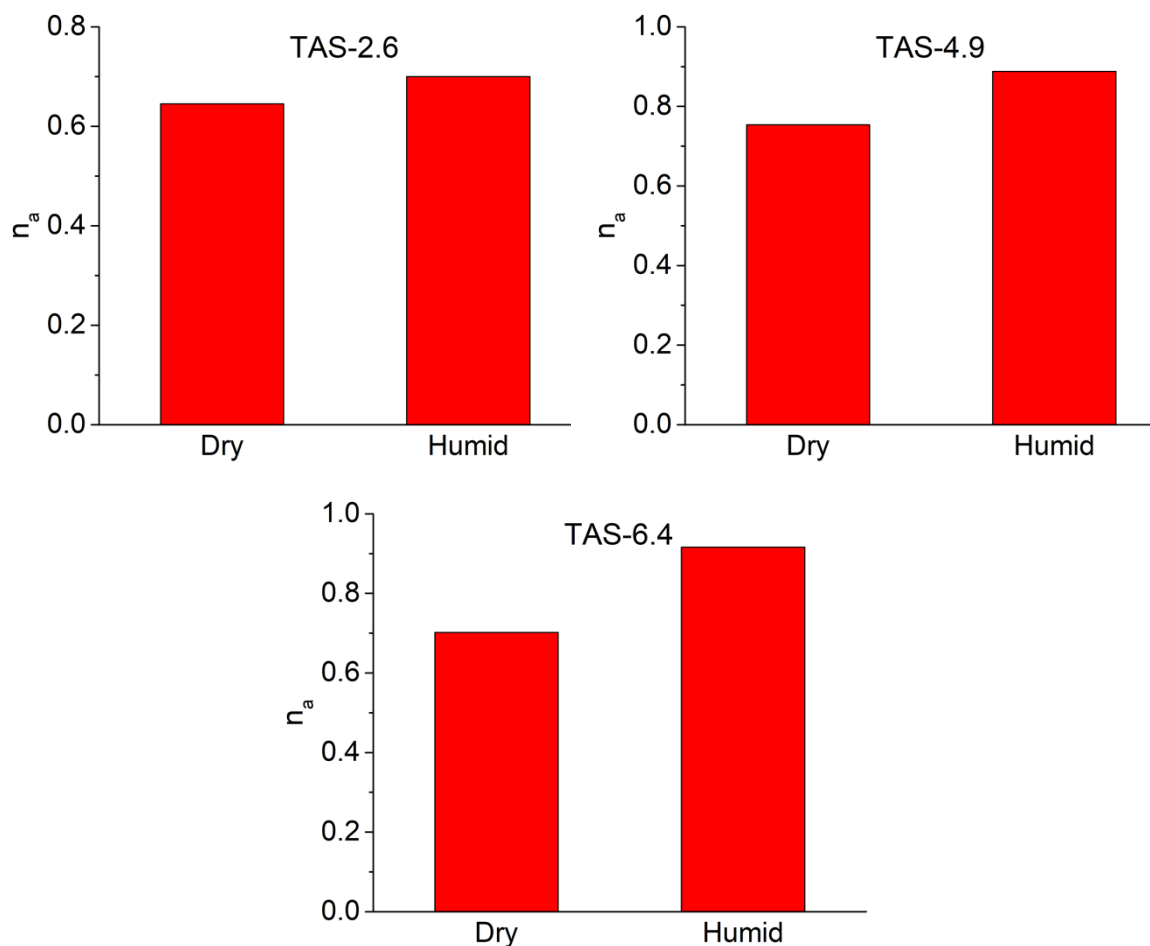


Figure 4.52. Avrami exponents (n_a) from fixed-bed tests under dry and humid conditions (25°C, 100 SCCM).

Unlike the pseudo first-order constant (k_s), the pseudo second-order constant (k_s) is not the kinetic constant of adsorption *per se*, rather a bulk constant that is influenced by various factors like the desorption rate constant, and equilibrium adsorption capacity.^[291, 297] Likewise, the Avrami constant k_a is likely an overall constant that is a complex function of various parameters such as the desorption rate constant, film and pore diffusion rates, the rate of different reaction steps and the number of accessible adsorption sites.^[291] This is reflected by the values of k_a obtained from the fittings in this study, which did not always follow a clear trend. When the flow rate increases between 25 and 100 SCCM, the Avrami constant changes non-monotonically for APS-2.6 and TAS-2.6, whereas k_a increases for TAS-4.9 and TAS-6.4 (Figure 4.53). As the adsorption temperature is increased, k_a decreases for TAS-6.4 whereas there is no correlation for the other three materials (Figure 4.54). The constant is consistently lower for the tests carried out under humid conditions compared to dry CO₂ exposure (Figure 4.55).

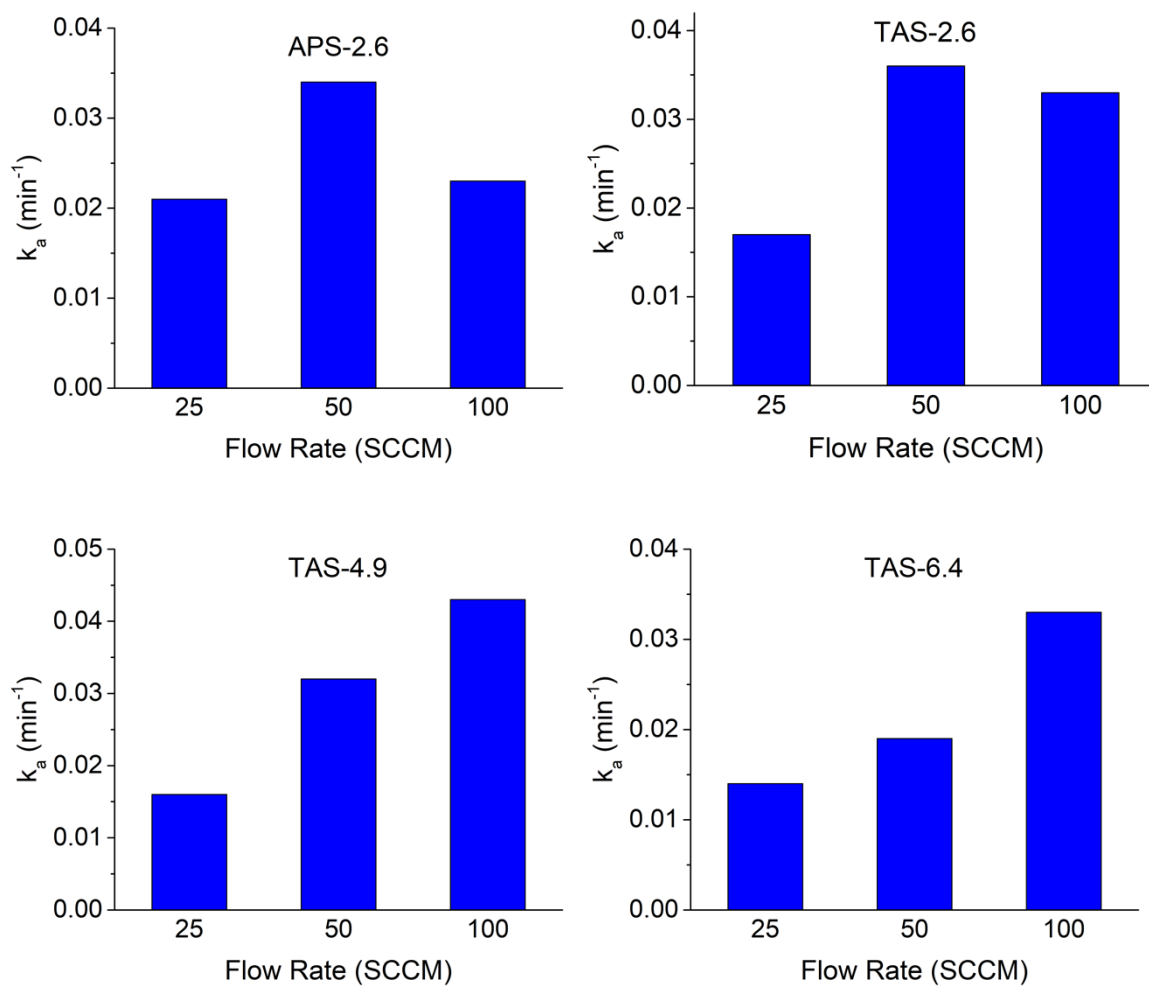


Figure 4.53. Avrami constants (k_a) from fixed-bed tests at different flow rates (25°C).

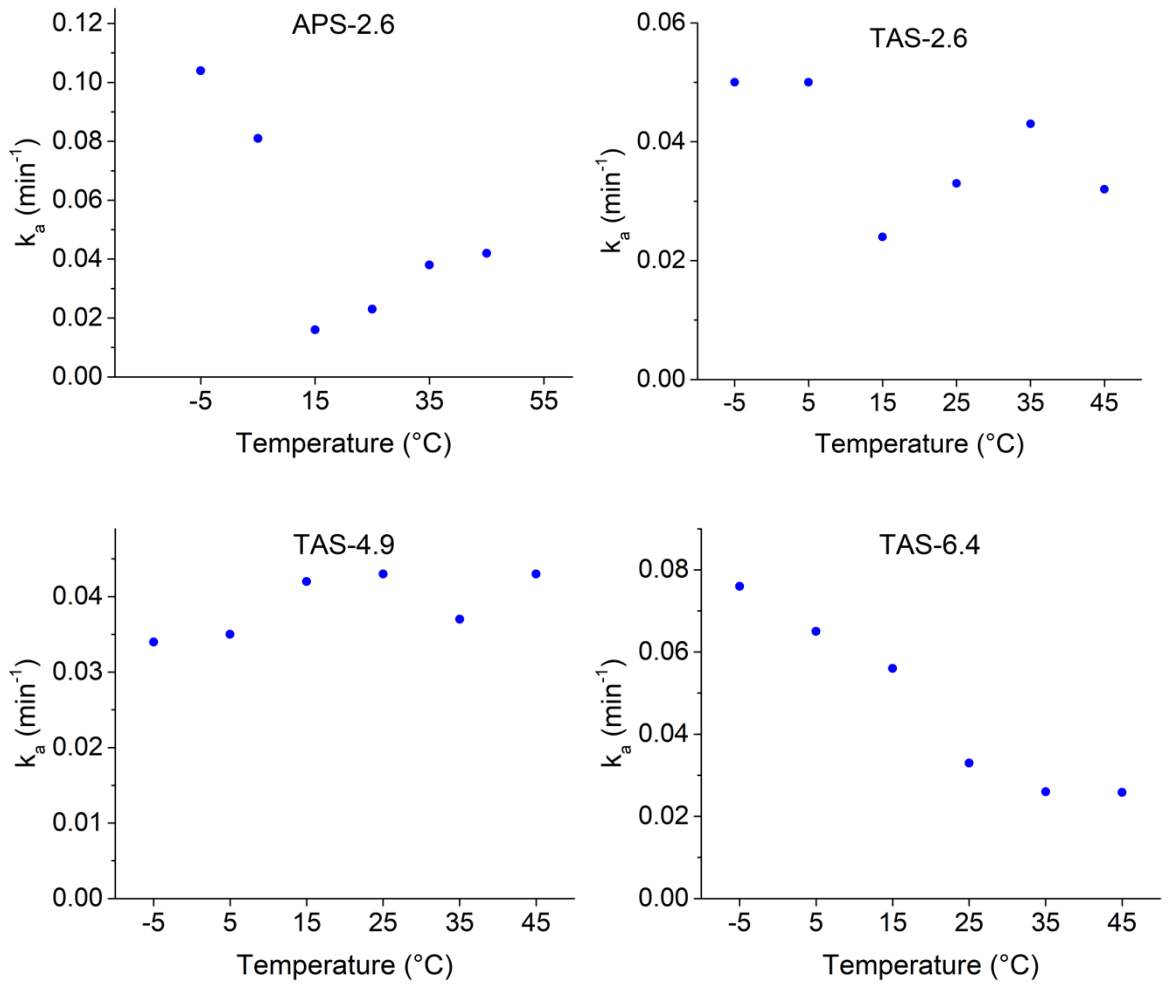


Figure 4.54. Avrami constants (k_a) from fixed-bed tests at different temperatures (100 SCCM).

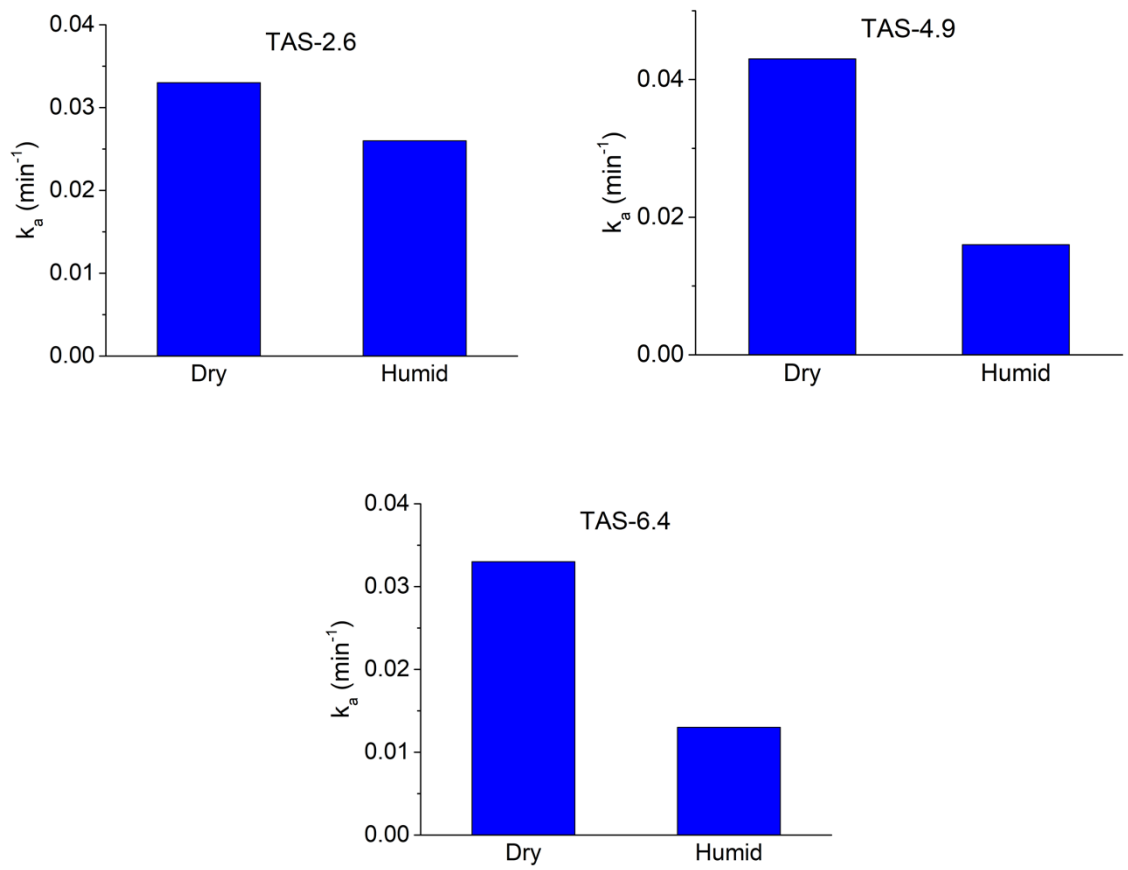


Figure 4.55. Avrami constants (k_a) from fixed-bed tests under dry and humid conditions (25°C, 100 SCCM).

4.4 Conclusions

This chapter has covered the testing of amine-functionalised nanofibrous silicas, produced via electrospinning and silane grafting, under simulated direct air capture conditions (400 ppm CO₂).

Preliminary testing of nanofibrous materials was conducted using the TGA method. Bare silica nanofibres adsorbed negligible amounts of CO₂ at room temperature. Upon functionalisation with monoamine (APS), diamine (DAS) and triamine (TAS) grafting agents at different loading levels, the silica nanofibres became effective adsorbents for CO₂. The amount of CO₂ adsorbed was dependent not only on the amine loading but also the choice of grafting agent. At comparable loadings, TGA CO₂ uptake and amine efficiency were in the order APS > DAS > TAS due to the decreasing density of highly-reactive primary amine groups. Uptake kinetics were also affected by the amine content, with the initial adsorption rate decreasing at high amine loadings. This was attributed to steric crowding of the grafting agent in the nanofibre pores which impeded CO₂ diffusion. Furthermore, the adsorption temperature influenced the TGA adsorption capacity of the functionalised nanofibres between 25 and 65°C. Whilst the final adsorption capacity of a DAS-grafted material decreased with temperature due to the exothermic nature of the adsorption process, the CO₂ loading on the APS and TAS-modified adsorbents showed a ‘peak and decline’ trend. The initial capacity enhancement was attributed to an increase in the mobility of the polymer-like aminosiloxane layer on the pore walls which increased the number of accessible adsorption sites. Finally, the amine-modified nanofibres were found to be fully regenerable after five temperature-swing cycles. Importantly, the microscopic structure of the nanofibres did not change during the cycling tests.

The fixed-bed experiments revealed that flow rate had a significant impact on the CO₂ capture performance, with capture efficiency deteriorating and extraction rate improving with flow rate. Temperature had a mostly positive effect on the pseudo-equilibrium capacity between -5 and 45°C, due to increased ammonium carbamate formation. The degree of enhancement was material dependent; adsorbents with higher amine loadings exhibited the biggest improvement in CO₂ loading with temperature. The fixed-bed pseudo-equilibrium capacities of the triamine-modified adsorbents were enhanced during humid CO₂ adsorption due to the formation of more ammonium carbamate.

The Avrami model provided the best simulation of CO₂ uptake during the fixed-bed tests. This study proposed a new interpretation of the Avrami exponent (n_a) to understand how the mechanisms underpinning CO₂ mass transfer change in response to alterations of the adsorption conditions. Values that are *ca.* 0.5 reflect conditions in which pore diffusion is the rate-limiting step, whilst values close to 1 or higher suggest another step of CO₂ mass transfer, such as film diffusion or the CO₂-amine reaction, limit the rate of CO₂ uptake by the adsorbent.

5 Discussion and Future Work

5.1 Comparison of Nanofibrous Silica with Other Silicas from the Literature

The textural properties of the nanofibrous silica (NFS) prepared using the optimised synthesis protocol in this work were compared with those of mesoporous silicas from the literature (Figure 5.1). The BET surface area of the nanofibrous silica is much lower than for the conventional mesoporous supports. For example, SBA-15, a widely used support for direct air capture studies,^[24] has a surface area over seven times that of NFS. This is because conventional templated silicas are powders which naturally have higher specific surface areas compared to nanofibres. Similarly, the total pore volume (TPV) of NFS is lower than the powdered silicas. However, the difference in TPV is much less stark compared to the difference in surface areas for conventional silicas with similar pore sizes to NFS. For instance, pore-expanded SBA-15 with the closest pore diameter to NFS, has a surface area of 766 m²/g, almost six times larger than that of NFS, yet its TPV of 1.3 cm³/g is only three times bigger. Meanwhile, pore-expanded MCM-41 which has by far the largest pore size of the listed materials (30 nm), has a surface area and TPV of 1045 m²/g and 2.58 cm³/g, respectively which are correspondingly seven and eight times greater than the surface area and TPV of NFS.

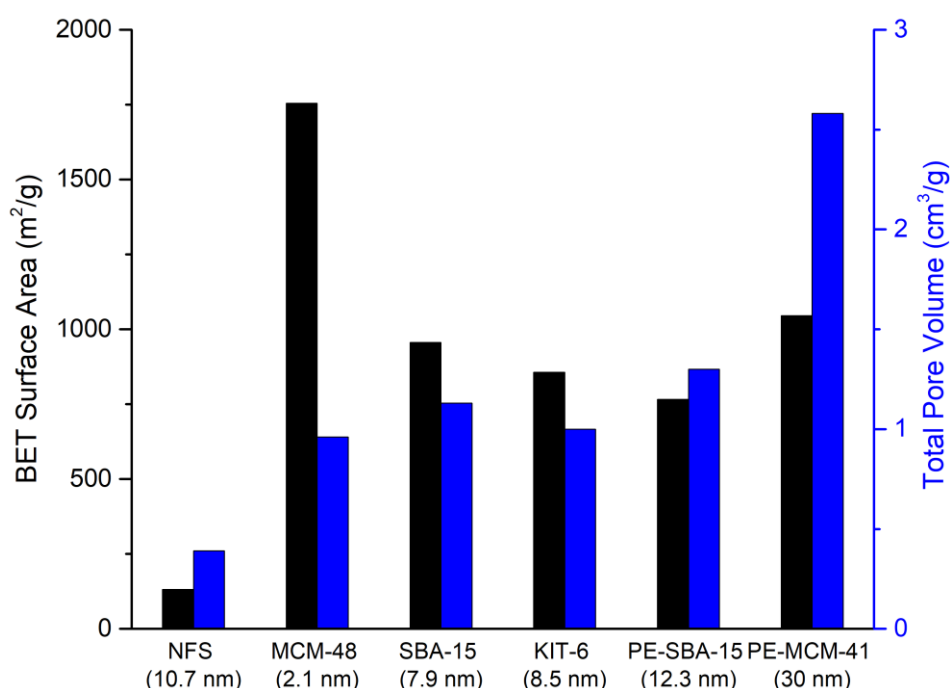


Figure 5.1. Surface area and total pore volume of nanofibrous silica (NFS) synthesised in this work compared to other mesoporous silicas from the literature: SBA-15^[298], pore-expanded SBA-15 (PE-SBA-15)^[298], KIT-6^[299], MCM-48^[299] and pore-expanded MCM-41 (PE-MCM-41).^[281] The average pore diameter of each support is shown in brackets.

Whilst conventional mesoporous silicas have superior textural characteristics to NFS, the latter's properties are comparable to other nanofibrous silicas from the literature. Kanehata *et al.* synthesised nanofibrous silica using a similar protocol to that used in this study (electrospinning of a precursor poly(vinyl alcohol)-sol solution, followed by removal of the organic template *via* calcination). They used three different colloidal silicas containing dispersed silica nanoparticles with average diameters of 15, 50 and 100 nm (K15, K50 and K100 respectively). Their results showed a decrease in surface area and pore volume of the nanofibres with particle size. NFS, with an average particle diameter of 23 nm, fits in with the decreasing trend in surface area with particle diameter (Figure 5.2). However, it does not fit in with the decreasing trend in TPV with particle size. This may be due to differences in the synthesis conditions.

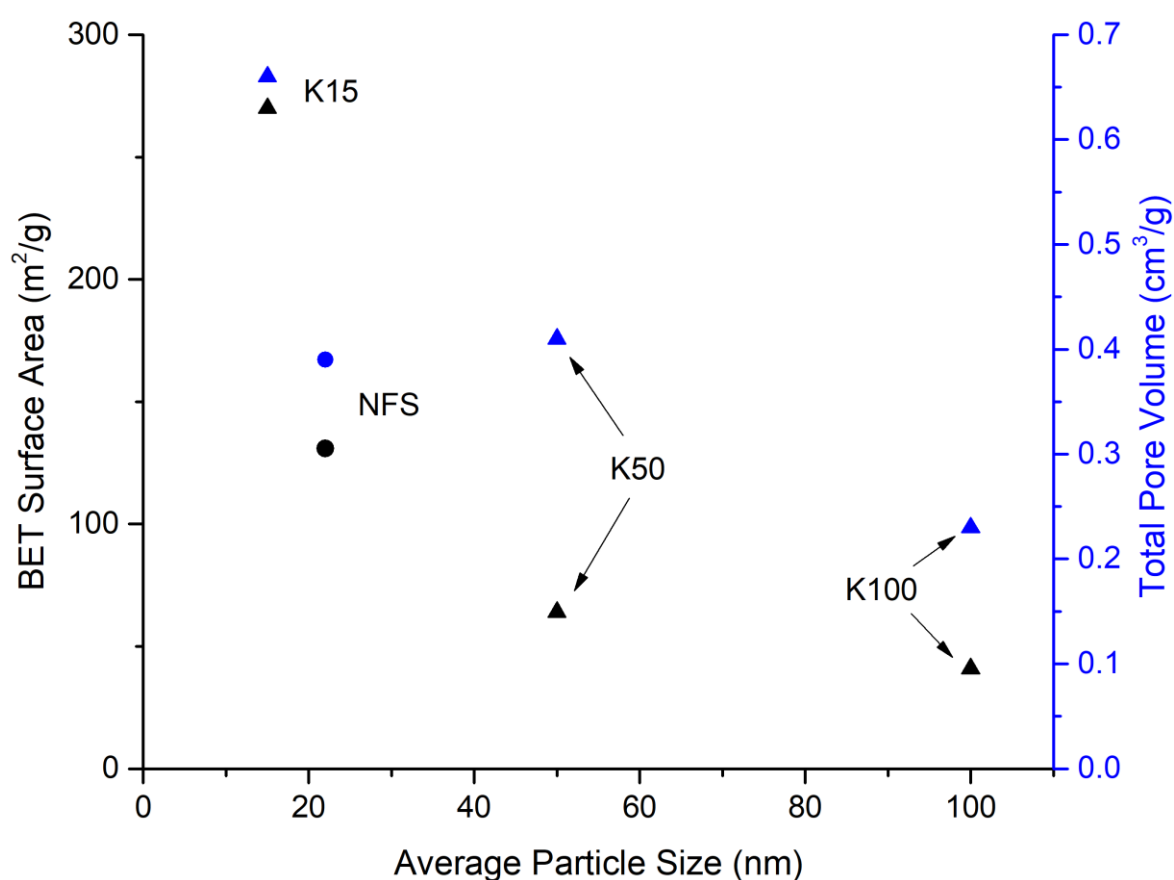


Figure 5.2. Surface area and total pore volume against average particle size of nanofibres synthesised from colloidal silica. NFS (this work), K15, K50 and K100 from the study by Kanehata *et al.*^[231]

5.2 Comparison of Functionalised Materials

The physiochemical properties of four triamine-modified NFS materials from this work (TAS-2.1, TAS-2.6, TAS-4.9 and TAS-7.4) were compared to other silicas functionalised with the same grafting agent under hydrous conditions. The data used in the comparison can be found in Table A13 of the Appendix.

The grafting efficiency was plotted against the amount of silane added to the grafting solution (Figure 5.3). The other functionalised silicas align with the general trend found with the amine-modified nanofibrous materials in Chapter 3, wherein grafting efficiency declines in an exponential-like fashion as the amount of silane added is increased. However, at similar amounts of added silane, the silicas from the literature have higher grafting efficiencies compared to the NFS materials. For example, the amount of amine added for TAS-4.9 is similar to that used in the functionalisation of the MCM-41 material, yet the former has a grafting efficiency of 24% whilst the latter 40%.

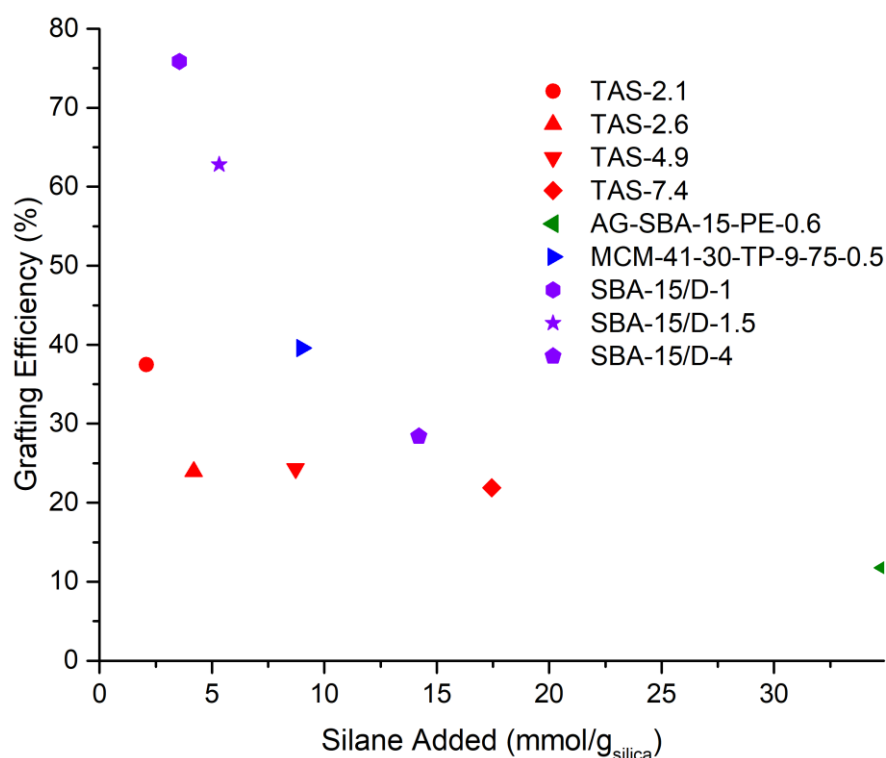


Figure 5.3. Grafting efficiency *versus* silane added to the reaction mixture of various triamine-modified silicas: TAS-2.1, TAS-2.6, TAS-4.9 and TAS-7.4 (own work), AG-SBA-15-PE-0.6^[298], MCM-41-30-TP-9-75-0.5^[281], and SBA-15/D-1, D-1.5 and D-4.^[300]

The effect of amine loading on pore filling was also investigated (Figure 5.4). As expected, higher amine loadings resulted in greater filling of the mesopores. The four materials with the highest amine loadings, including one of the functionalised nanofibrous silicas (TAS-7.4), have pore fill fractions greater than 90%. Considering the small range of amine loadings amongst these four silicas

(7 – 7.6 mmol_N/g), the amine loading at high pore fill fractions is not strongly influenced by the silica type. This seems counterintuitive when taking into consideration the high variation in total pore volume and pore size of the supports (0.37 – 2.58 cm³/g and 6.8 – 30 nm, respectively). It would be expected that silicas with lower pore volumes and pore sizes would have lower amine loadings at 100% pore filling.

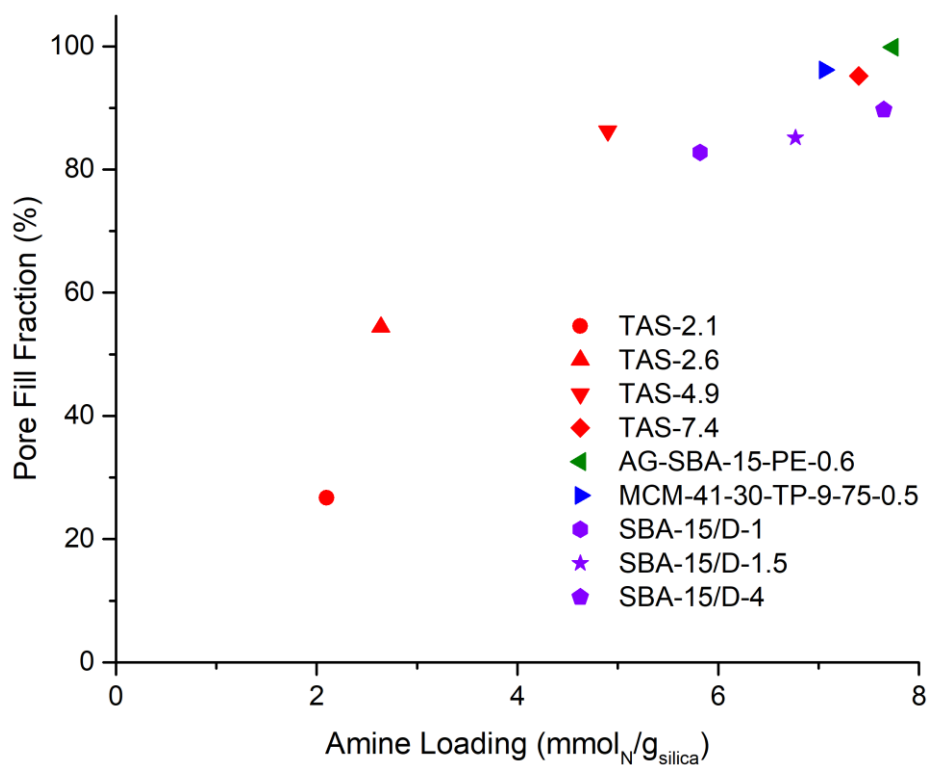


Figure 5.4. Pore fill fraction *versus* amine loading of various triamine-modified silicas.

Lastly, amine coverage (amount of nitrogen per unit surface area of bare silica) was plotted against amine loading (Figure 5.5). The nanofibrous silicas have much higher amine coverages compared to the other functionalised materials. For example, TAS-7.4 and SBA-15/D-4 have similar amine loadings and yet the former has an amine coverage of 57 m²/g compared to 11 m²/g for the latter.

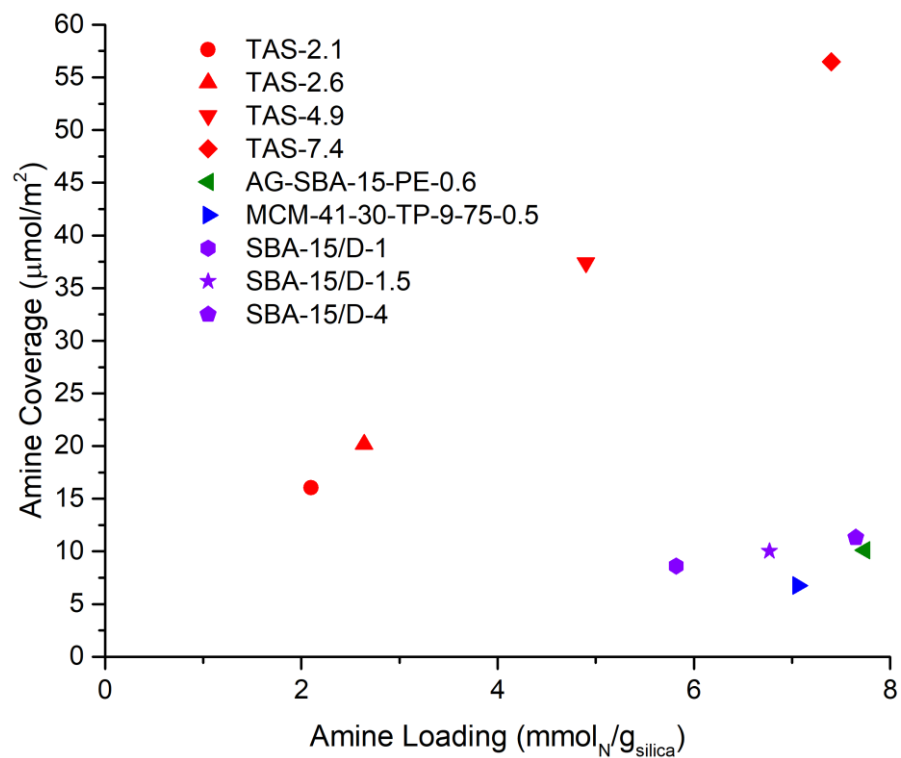


Figure 5.5. Amine coverage *versus* amine loading of various triamine-modified silicas.

5.3 Comparison of CO₂ Capture Performance of Functionalised Nanofibrous Silicas with Other Adsorbents from the Literature

The DAC performance of the functionalised nanofibrous silicas synthesised in this work were compared with other materials from the literature. Adsorbents were evaluated based on their maximum adsorption capacities, kinetic half-times and the average uptake rate (AUR). AUR unifies adsorption capacity with kinetics and provides a better overall picture on the adsorption performance of a material.^[133] This assumes a CO₂ capture process in which the adsorption step is stopped when the material's CO₂ loading reaches half of its maximum capacity, and the desorption step is equal in duration to the adsorption step, meaning the total cycle time is double the half-time.

$$AUR = 60 \times \frac{0.5q_{max}}{2t_{\frac{1}{2}}} \quad (5.1)$$

Where: q_{max} is the maximum adsorption capacity and $t_{1/2}$ is the adsorption half-time (the time taken for the adsorption capacity to reach 50% of its final value). The factor of 60 is added to convert the AUR into CO₂ uptake per gram per hour.

A literature search was carried out to find adsorbents tested under DAC-like conditions with similar amine loadings to the functionalised nanofibres used in the fixed-bed experiments (*i.e.* 2.6-6.4 mmol_N/g). Four adsorbents were found for the dry adsorption comparison and a further four for the humid comparison. Most of them have amine loadings close to that of TAS-4.9, therefore, we compared the performance of the literature adsorbents to that of TAS-4.9.

5.3.1 Dry Adsorption Comparison

The five adsorbents from the literature used in the dry adsorption comparison were: an amine-appended metal organic framework (Mg₂[dobdc][N₂H₄]₂, shortened to amino-MOF)^[92], monoamine and triamine-grafted hierarchical silica (HSA-50 and HST-30, respectively)^[68], polyamine-impregnated SBA-15 (20TEPA)^[35] and triamine-grafted SBA-15 (S-T-4.6).^[280] Amine loadings and test conditions can be found in Table A14 of the Appendix.

The amine-appended MOF possesses the largest maximum CO₂ uptake of 3.7 mmol/g, roughly an order of magnitude greater than the other amine adsorbents (Figure 5.6). The unusually high adsorption capacity of this material was attributed to molecular interactions between the support and appended amines, which favour the formation of carbamic acid.^[92] This reaction has an amine-CO₂ reaction stoichiometry of 1:1. In contrast, ammonium carbamate formation, which is the dominant

mechanism for dry CO₂ adsorption on amine-functionalised silica^[301, 302], has an amine-CO₂ stoichiometry of 2:1.

The monoamine-grafted hierarchical silica (HSA-50) has the second highest CO₂ uptake, with a final adsorption capacity of 0.6 mmol/g. All the remaining adsorbents have lower capacities owing to the fact they contain a mixture of primary and secondary amines. As previously discussed, secondary amines are less reactive towards CO₂.^[63] The polyamine-impregnated silica (20TEPA) has the worst adsorption capacity of 0.16 mmol/g. Meanwhile, TAS-4.9 has a comparable CO₂ loading to the other two triamine-grafted silicas, S-T-4.6 and HST-30, with respective maximum uptakes of 0.36, 0.33 and 0.28 mmol/g.

Despite the very high adsorption capacity of the amino-MOF, it has the slowest uptake kinetics, with an adsorption half-time of 310 min. In contrast, the functionalised silicas have much shorter adsorption half-times, with 20TEPA having the lowest of 2 min. This shows that there is a trade-off amongst these materials between maximum adsorption capacity and kinetics.

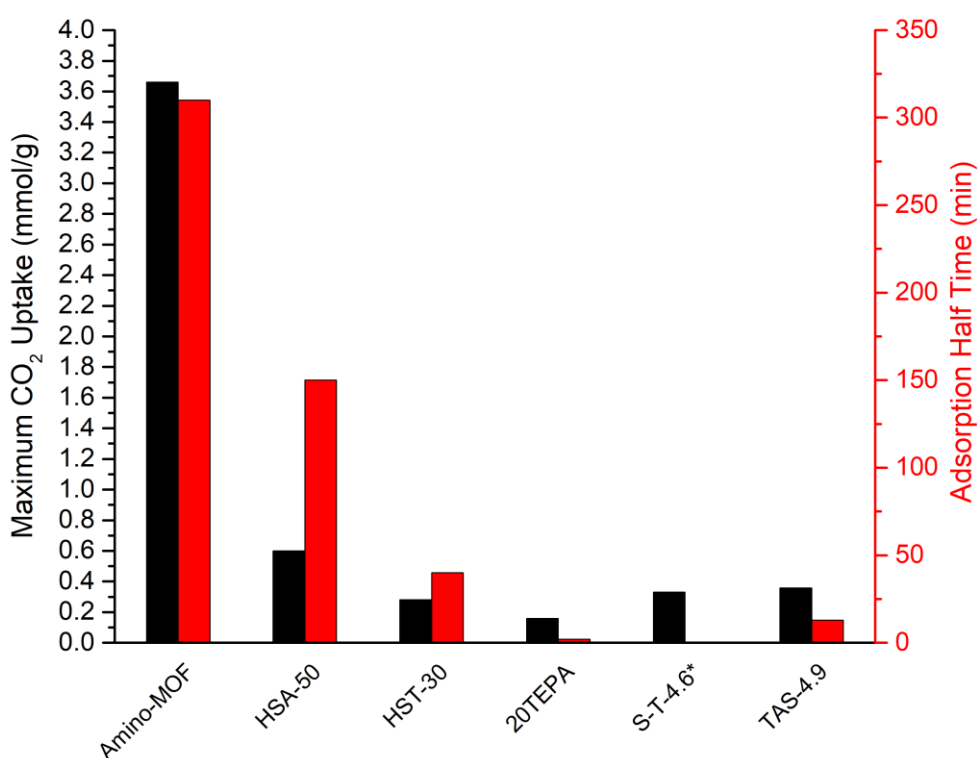


Figure 5.6. Maximum CO₂ uptake and adsorption half-times of amine-functionalised materials with similar amine loadings to TAS-4.9 under dry DAC conditions. *No kinetic data was available for S-T-4.6.

The average uptake provides a different picture of the performance of the adsorbents (the AUR of S-T-4.6 could not be calculated owing to the unavailability of kinetic data). Because of the slow uptake kinetics of the amino-MOF, it has a comparatively small AUR of 0.18 mmol·g⁻¹·h⁻¹ (Figure

5.7). Likewise, the monoamine and triamine modified hierarchical silicas (HSA-50 and HST-30) have slow AURs of 0.06 and 0.11 $\text{mmol}\cdot\text{g}^{-1}\cdot\text{h}^{-1}$ due to their long half-times. On the other hand, because of the rapid kinetics of 20TEPA, it has the highest AUR of all the materials of 1.2 $\text{mmol}\cdot\text{g}^{-1}\cdot\text{h}^{-1}$. The triamine-grafted nanofibrous silica TAS-4.9 has the second-highest AUR of 0.42 $\text{mmol}\cdot\text{g}^{-1}\cdot\text{h}^{-1}$, four times higher than the hierarchical silica grafted with the same amine (HST-30). These results show the importance of considering both adsorption capacity and uptake kinetics when evaluating the CO_2 capture performance of amine adsorbents.

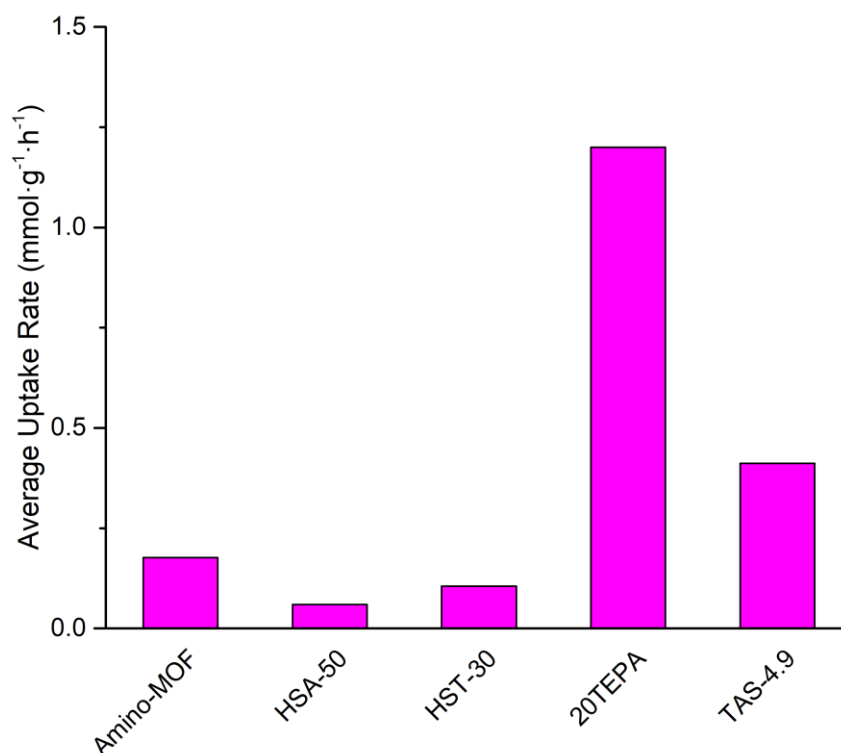


Figure 5.7. Average uptake rates of various amine-functionalised adsorbents tested under dry DAC conditions.

5.3.2 Humid Adsorption Comparison

The adsorption behaviour of TAS-4.9 was also compared with four adsorbents tested under humid conditions; monoamine-based hybrid silica (MAHSM)^[303], diamine-functionalised nanofibrillated cellulose (DAS-NFC)^[105], hyperbranched aminosilica (HAS4)^[73], and triamine-functionalised SBA-15 (S-T-4.6).^[280] Amine loadings and test conditions can be found in Table A15 of the Appendix.

MAHSM has the highest adsorption capacity of 1.68 mmol/g (Figure 5.8), followed by DAS-NFC (1.39 mmol/g) and HAS4 (1 mmol/g). Although TAS-4.9 has a lower final uptake capacity of 0.87 mmol/g , this exceeds that of S-T-4.6 (0.59 mmol/g). Of all the adsorbents used in the comparison,

S-T-4.6 is the most chemically comparable to TAS-4.9. Furthermore, the kinetics is faster for TAS-4.9 compared to S-T-4.9, with respective adsorption half-times of 39 and 59 min. The other adsorbents also have longer half-times than the functionalised nanofibrous silica, with HAS4 having the longest $t_{1/2}$ of 163 min.

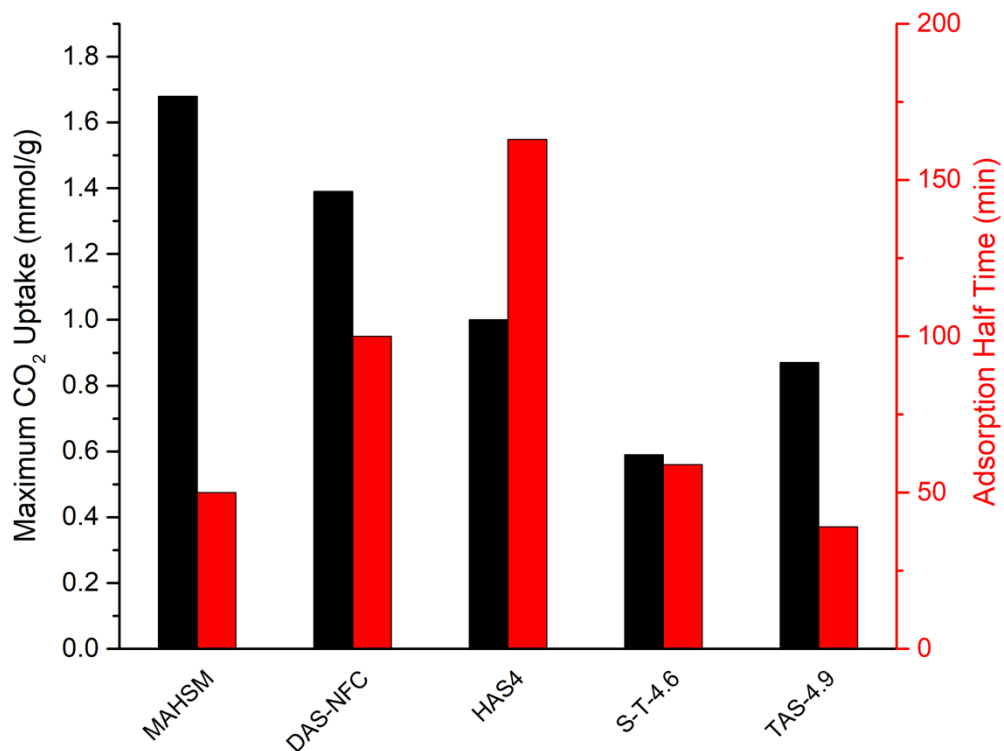


Figure 5.8. CO₂ uptake and adsorption half-times of amine-functionalised materials with similar amine loadings to TAS-4.9 tested under humid DAC conditions.

The amine-functionalised hybrid silica MAHSM has the highest average uptake rate of $0.5 \text{ mmol} \cdot \text{g}^{-1} \cdot \text{h}^{-1}$ (Figure 5.9). TAS-4.9 has the second highest ($0.34 \text{ mmol} \cdot \text{g}^{-1} \cdot \text{h}^{-1}$), over double that of its SBA-15 counterpart S-T-4.6 ($0.15 \text{ mmol} \cdot \text{g}^{-1} \cdot \text{h}^{-1}$).

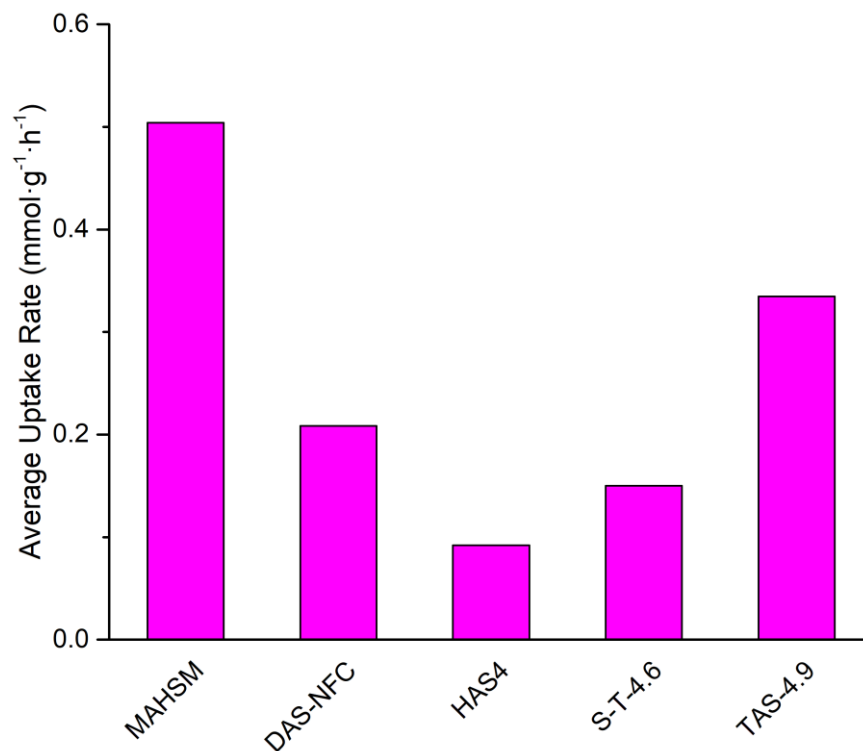


Figure 5.9. Average uptake rates of amine-functionalised adsorbents tested under humid DAC conditions.

5.3.3 Comparison with Other Nanofibrous Adsorbents

The humid CO₂ capture performance of TAS-4.9 was also compared with two other DAC sorbents synthesised using electrospinning: PVA/Arginine hybrid fibres^[229] and PVA nanofibres embedded with an ion exchange resin (IER).^[133] Test conditions can be found in Table A16 of the Appendix.

The PVA/IER nanofibres have the highest AUR of 1.4 mmol·g⁻¹·h⁻¹ (Figure 5.10), over four times the humid average uptake rate of TAS-4.9 (0.33 mmol·g⁻¹·h⁻¹). Meanwhile, the PVA/arginine nanofibres have the lowest AUR of 0.27 mmol·g⁻¹·h⁻¹. It must be noted that the two adsorbents from the literature were tested using significantly higher flow rates compared to that used in this study (0.5 and 1.0 L/min for PVA/arginine and PVA/IER respectively, compared to 0.1 L/min for TAS-4.9). As previously discussed, the rate of CO₂ uptake is affected by flow rate, with higher flow rates favouring more rapid adsorption kinetics.

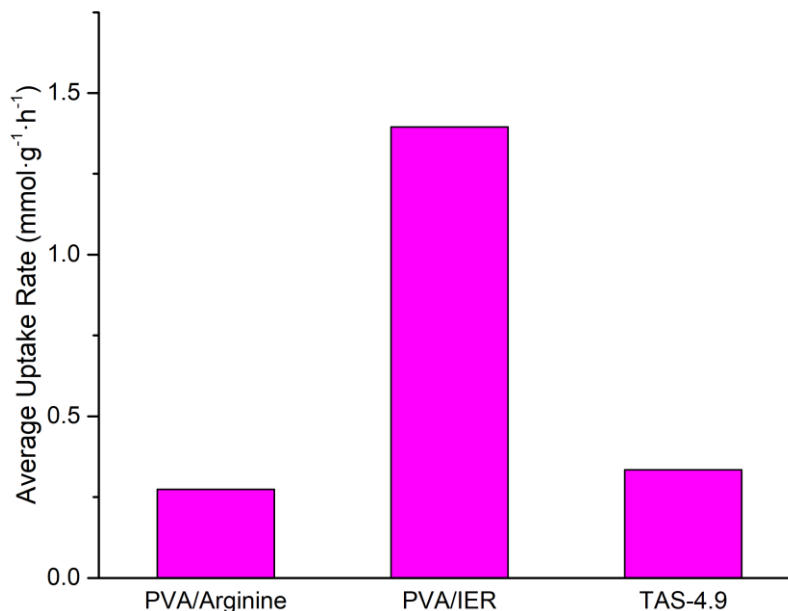


Figure 5.10. Average uptake rates of nanofibrous adsorbents tested under humid DAC conditions

5.3.4 Dynamic Performance Comparison at Various Flow Rates

The fixed-bed performance of TAS-6.4 at various flow rates was compared to data reported for an amine functionalised MOF tested using a similar method (mmen-Mg₂[dobpdc], shortened to mmen-MOF).^[26] The amine loading was not provided in the study, however, the recipe for the sorbent is from another publication in which the amine loading was estimated at 7.4 mmol_N/g.^[304] TAS-6.4, having the closest amine content to this MOF sorbent, is considered as the most appropriate amine-functionalised nanofibrous silica for this comparison.

As with TAS-6.4, increasing the flow rate augmented the rate of CO₂ extraction of mmen-MOF (Figure 5.11). Regardless of the flow rate, the rate of CO₂ extraction is higher for mmen-MOF, although the absolute difference between the two sorbent's performance is roughly the same at all three flow rates (0.06 – 0.07 mmol·g⁻¹·h⁻¹). As with TAS-6.4, flow rate has a negative effect on the CO₂ capture fraction of the MOF (Figure 5.12). At low flow rates, the capture fractions of the two materials are similar, whilst at 100 SCCM, there is a greater deterioration in mmen-MOF's performance with respect to this performance metric, with TAS-6.4 having a higher capture fraction (21% *versus* 17% for the MOF).

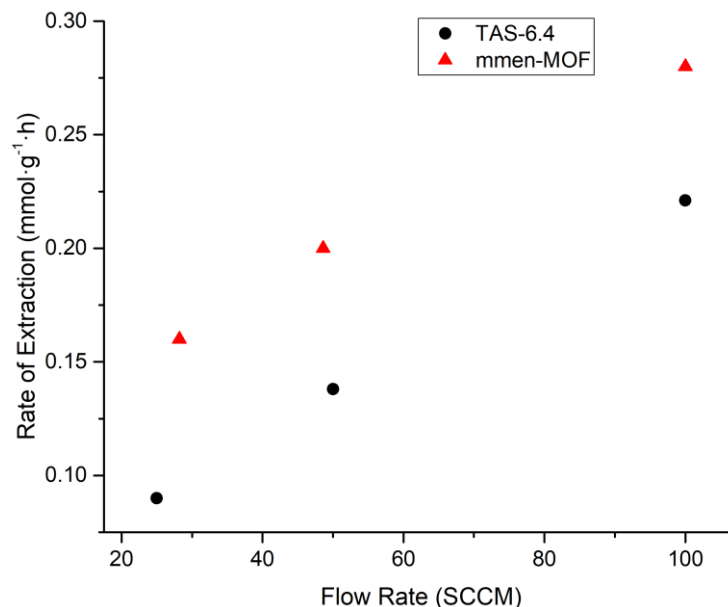


Figure 5.11. Rate of CO₂ extraction *versus* flow rate for TAS-6.4 and an amine-appended MOF at $C/C_0 = 0.95$ from fixed-bed experiments.

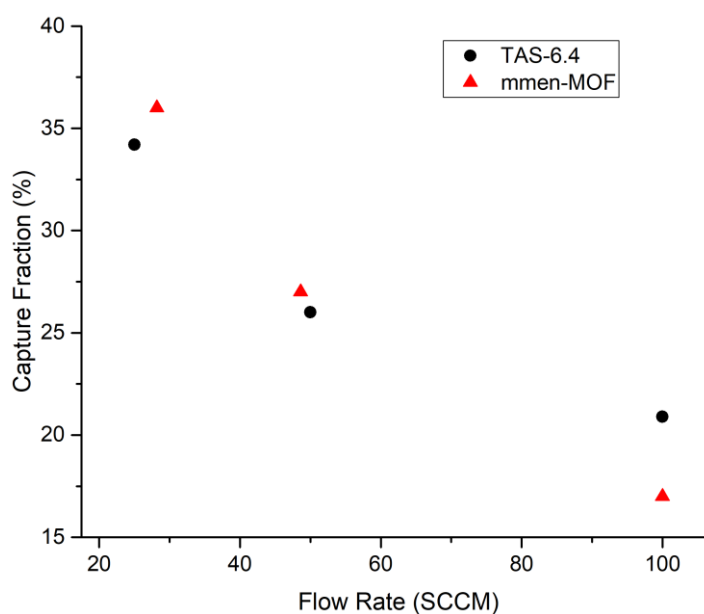


Figure 5.12. Capture fraction *versus* flow rate for TAS-6.4 and an amine-appended MOF at $C/C_0 = 0.95$ from fixed-bed experiments.

5.3.5 Summary

In summary, although TAS-4.9 did not have the best DAC adsorption capacity compared to other adsorbents from the literature, its average uptake rate is competitive under both dry and humid conditions. Meanwhile, the dynamic performance under various flow rates of TAS-6.4 is comparable to an amine-functionalised MOF of a similar amine loading. It is worth noting that there are some limitations with the comparisons. Although great care has been taken in selecting materials to make

the comparisons as meaningful as possible, the experimental set-ups and conditions varied from material to material. This is a particular problem for the adsorbents tested under humid conditions. For example, the humid capacity of S-T-4.6 was measured using ambient air with a relative humidity of 24%, compared to an RH of 60% for TAS-4.9. The feed gas composition also varied. Whilst some papers, like in this study, used a binary mixture of CO₂ and an inert gas, others used air. Such experimental differences impact the comparability of the adsorbents.

5.4 Future Work

Regarding material synthesis, it would be useful to prepare supports using colloidal silicas with dispersed nanoparticles of other sizes and investigate how the particle size impacts the grafting efficiency and CO₂ capture performance of the resulting silica nanofibres. It would be expected that smaller nanoparticles would yield higher specific surface area and pore volumes in the resulting composites, which may lead to higher achievable amine loadings before total pore filling is achieved. This could in turn enhance the CO₂ adsorption capacities of the resultant functionalised nanofibres. Using suspensions of classic mesoporous silicas like SBA-15 may offer an alternative route to producing high surface area nanofibres. Electrospun polymer-SBA-15 composite nanofibres have been reported in the literature^[305-307] although purely siliceous nanofibres made of SBA-15 have not been studied to the author's best knowledge.

An unanswered yet important question that needs addressing in future work is how the presence of oxygen in the gas feed impacts the capture performance of amine functionalised nanofibrous silicas. Oxygen is the second most abundant constituent in air (21 mol%) and may impact the performance of these novel materials through amine deactivation, particular during the desorption step at elevated temperatures.^[65,308] Furthermore, quantifying water adsorption during exposure to humid gas streams is important in the development of amine sorbents for DAC, with the reported ratio between water and CO₂ equilibrium adsorption capacities reaching as high as 12.4 mmolH₂O/mmolCO₂.^[107] Although water has a promotive effect on CO₂ capture on the adsorbents studied in this work, excessive water adsorption should be avoided as it increases the energy input necessary for sorbent regeneration both in terms of sensible heat and desorption enthalpy.^[207]

Future work should also endeavour to understand the long-term stability of these materials using tens, if not, hundreds of cycles, as the affordability of direct air capture depends greatly on how many cycles the adsorbent can be subjected to before it needs replacing.^[24] Furthermore, on an industrial scale, use of pure nitrogen gas during the desorption step is technically unfeasible since it produces a dilute CO₂ stream which is unsuitable for sequestration. It is therefore imperative to test the regenerability of these novel adsorbents using more realistic regeneration methods like combined temperature and vacuum swing, and steam stripping.^[142, 309] Studying how the number of cycles and regeneration conditions affect the physical integrity and morphology of the materials will also be

needed as it is envisaged that these mats would be scaled up and installed in industrial contactors with minimal mechanical reinforcement, and so their physical resilience to multiple cycling is as important as their chemical stability.

Although breakthrough testing using a fixed-bed flow-through system offers a simple way of monitoring the dynamic performance of materials under more realistic processing conditions, such a set-up would be impractical on an industrial scale due to the high pressure drops associated with packed-bed reactors. Furthermore, this experimental set-up does not exploit the self-standing nature of the amine-functionalised materials; the mats had to be cut up into smaller pieces in order for the adsorbent to be tightly packed inside the reactor. Therefore, testing of these novel materials in contactors that are both more practicable for industrial scale-up and can accommodate whole mats of functionalised nanofibres is crucial.

One reactor configuration worth exploring is a 'laminar' contactor in which sheets of adsorbent are stacked together with inert spacers between mats (Figure 5.13). Such a set-up was used by Min *et al.* for DAC testing of a self-standing material comprised of amine-functionalised silica embedded in a poly(tetrafluoroethylene) (PTFE) matrix. The obvious advantage of the sorbents developed in this work over that of Min *et al.*'s PTFE/silica composite adsorbent is that the silica support is free-standing in its as-synthesised form, without the need for an inert binder. In other words, the fact that the amine-functionalised nanofibrous silicas are themselves scalable means that their application in a laminar contactor would maximise the space occupied by CO₂-reactive material. To understand whether this translates into better adsorption performance would require testing of both the materials produced in this work and the hybrid mats created by Min *et al.*

The impact of grafting agent, amine loading, flow rate, temperature and humidity on the CO₂ capture performance of amine-functionalised nanofibrous silica in the laminar contactor will be necessary to ascertain whether their adsorption behaviour differs from that using the fixed-bed set-up. Humid testing of materials at various temperatures is also needed to ascertain the versatility of the adsorbents over a wide range of processing conditions. Sub-ambient humid testing of the adsorbents would be of particular value to the material development community, as such work is lacking for DAC sorbents in general.^[25]

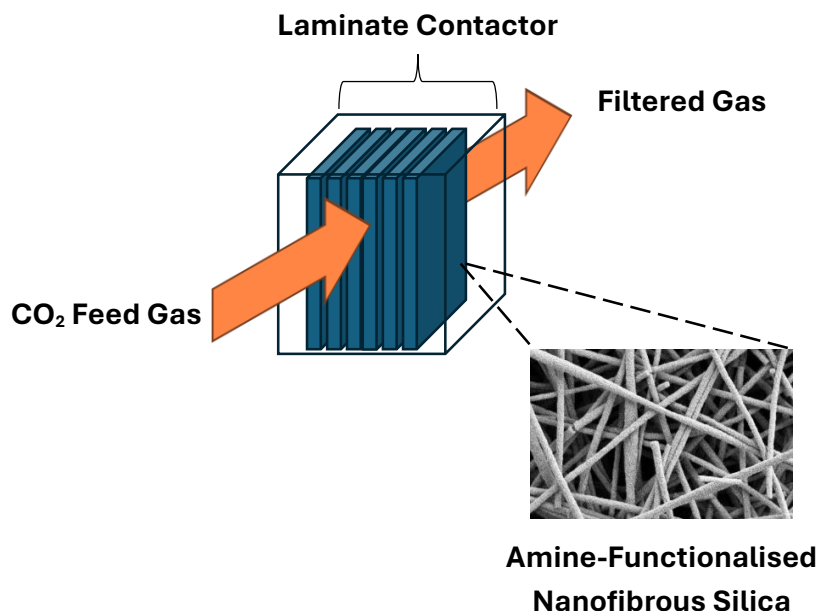


Figure 5.13. Proposed laminate DAC contactor for testing of functionalised nanofibrous silica under more realistic processing conditions. As-synthesised nanofibrous mats (blue) are stacked inside the contactor and the CO₂ feed is passed through it parallel to the adsorbent sheets. Adapted with permission from: [207]. Copyright 2022 American Chemical Society.

Finally, more advanced NMR studies of CO₂ speciation on the adsorbents is needed. It has been shown in this work that ammonium carbamate formation seems to be the dominant mechanism underpinning chemisorption on functionalised nanofibrous silica. However, the low natural abundance of the ¹³C isotope resulted in the ¹³C resonance assigned to the CO₂-amine adduct having a poor signal-to-noise ratio. Exposing the adsorbents to ¹³CO₂ would dramatically improve the signal-to-noise ratio, providing greater confidence in the assignment of the resonance associated with adsorption of CO₂ on the nanofibres. Furthermore, quantitative CP-MAS has recently been applied in the study of CO₂ adsorption on amine-functionalised SBA-15 silica to quantify the amounts of each chemisorption product at various adsorbate pressures.^[310] This technique would be invaluable in further investigating the effects of processing conditions (amine loading, amine type, humidity, temperature) on CO₂ speciation on amine-functionalised nanofibrous silicas.

6 Overall Conclusions

In this thesis, we explored the application of amine-modified nanofibrous silica for DAC. This approach combines the favourable CO₂ capture properties of functionalised silicas, which have been extensively researched in powdered form in the literature, with the scalability offered by the electrospinning of nanofibres.

The key findings are as follows:

1. We successfully optimised the protocol for synthesising porous silica nanofibres *via* electrospinning of colloidal silica and polymer blends, followed by calcination to remove the organic template. A silica-polymer weight ratio of 2:1 and calcination temperature of 700°C produces the best quality nanofibres with respect to morphology and durability.
2. Characterisation of as-spun silica-PVA mats showed that the polymer template is less thermally stable when electrospun compared to in its as-received granular form and that there are conformational differences with respect to intramolecular hydrogen bonding between the two forms of the polymer. Template removal causes a 26-fold increase in specific area of the nanofibres, together with the formation of mesopores.
3. We have successfully obtained amine functionalised nanofibrous silica *via* hydrous grafting of aminosilanes onto the support. Nanofibrous silica retains its self-standing nature after functionalisation. As the amount of silane added to the reaction mixture increases, the grafting efficiency decreases in an exponential-like manner due to the interplay of steric hindrance and amine concentration on the grafting reaction.
4. The CO₂ capture performance under simulated DAC conditions (400 ppm CO₂/N₂, 25°C) was assessed using TGA. The interplay between amine loading and active site accessibility results in moderately-loaded nanofibres having the highest final adsorption capacities. At similar amine loadings, CO₂ loading and amine efficiency decreases in the order: monoamine (APS) > diamine (DAS) > triamine (TAS) owing to the decreasing proportion of primary amines, which have a stronger affinity toward CO₂ compared to secondary amines.
5. The adsorption temperature significantly influences the TGA CO₂ uptake on nanofibrous silicas between 25 and 65°C. At similar loadings, monoamine and triamine-modified silica nanofibres show an unusual 'peak and decline' trend in adsorption capacity with temperature due to the interplay of kinetics and thermodynamics.
6. Amine-functionalised nanofibrous silica are fully regenerable after five temperature-swing cycles (adsorption at 25°C, desorption at 110°C), with no change in fibre morphology.
7. We successfully built a lab-scale fixed-bed flow-through system for assessing the dynamic performance of functionalised nanofibres. Increasing the flow rate reduces the capture efficiency whilst simultaneously increasing the CO₂ extraction rate at pseudo-equilibrium. Meanwhile, temperature has a positive effect on adsorption between -5°C and 45°C, regardless of the amine loading, showing that CO₂ capture is kinetically-controlled at

temperatures pertinent to DAC. Humidity also augments the pseudo-equilibrium capacity of triamine-loaded nanofibres, with an almost tripling of the adsorption capacity of the highest-loaded material compared to dry adsorption

8. ^1H - ^{13}C CP/MAS NMR experiments revealed that increasing the temperature and humidifying the gas stream promotes the formation of more ammonium carbamate adducts. An additional ^{13}C resonance associated with the aminopropyl moieties was identified on the spectrum for an APS-grafted silica after CO_2 adsorption and is attributed to amine protonation.
9. A moderately-grafted, triamine-modified nanofibrous adsorbent performs well against other similarly-loaded amine adsorbents from the literature, achieving the second highest average uptake rate in dry and humid conditions.
10. Kinetic modelling of the fixed-bed adsorption data revealed that the Avrami model provides the most robust fit to the data, regardless of the adsorption conditions. This study proposed a new interpretation of the Avrami exponent n_a to understand the underlying mechanism dictating CO_2 transfer through amine-functionalised nanofibres. When the exponent is close to 0.5, pore diffusion is the rate-determining step whereas when it increases to 1 or higher, another step of CO_2 transfer determines the speed of kinetics such as film diffusion or the CO_2 -amine reaction.

Future work should endeavour to understand the long-term chemical stability of these materials when subjected to gas streams containing oxygen, and to ascertain whether their performance with respect to adsorption capacity and kinetics changes over tens, if not hundreds of cycles. Such work should be carried out using a reactor design that exploits the scalability and self-standing nature of the adsorbents. This will allow process engineers to better understand how nanofibrous adsorbents perform under conditions more representative of industrial-scale DAC.

Appendix

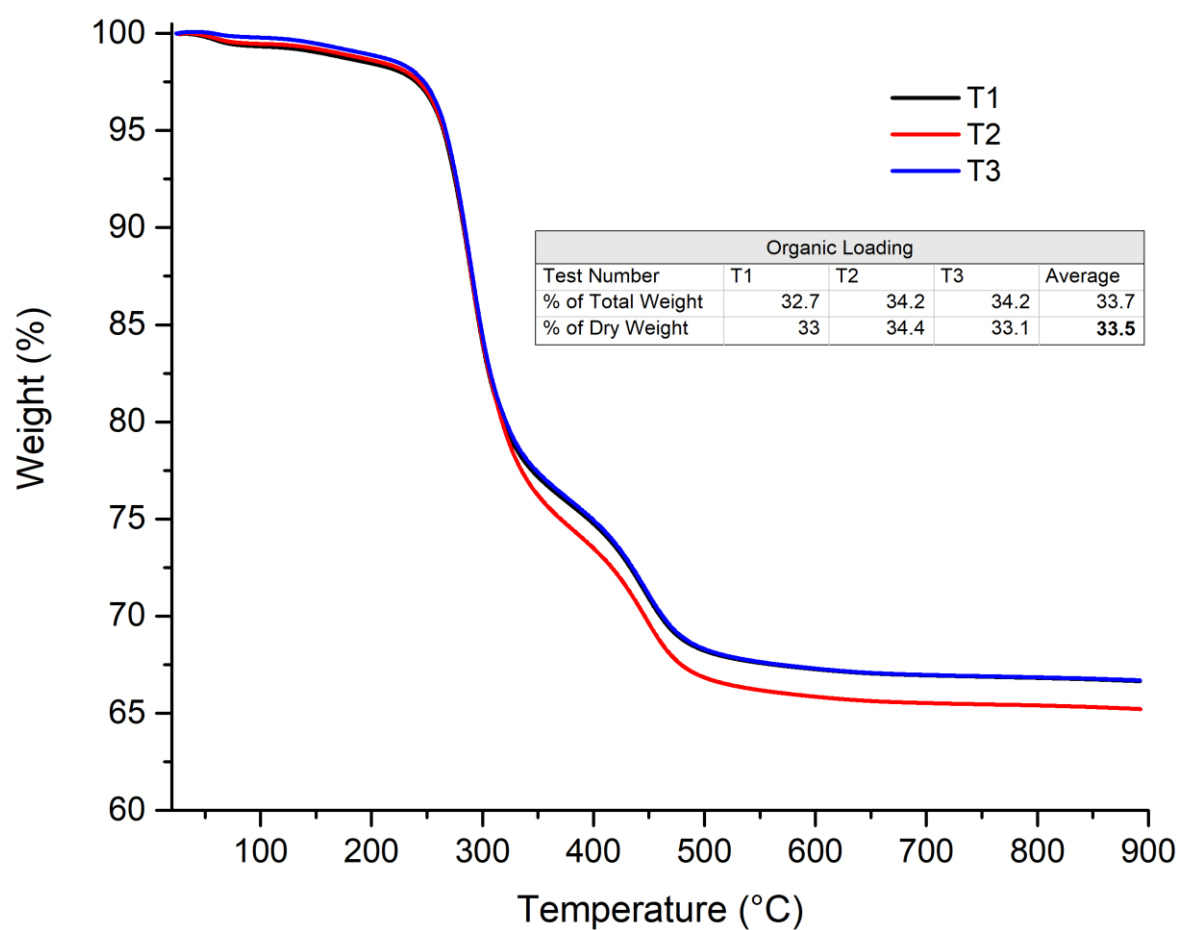


Figure A1. TGA traces of three samples of as-spun nanofibres fabricated from the 2:1 silica-PVA electrospinning blend.

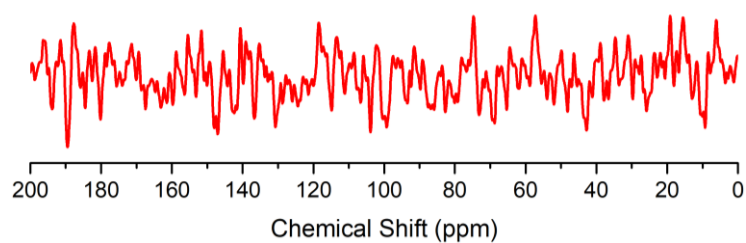


Figure A2. ^1H - ^{13}C CP-MAS NMR spectrum of nanofibrous silica (4 k scans, 1.1 ms contact pulse, 5 s recycle delay).

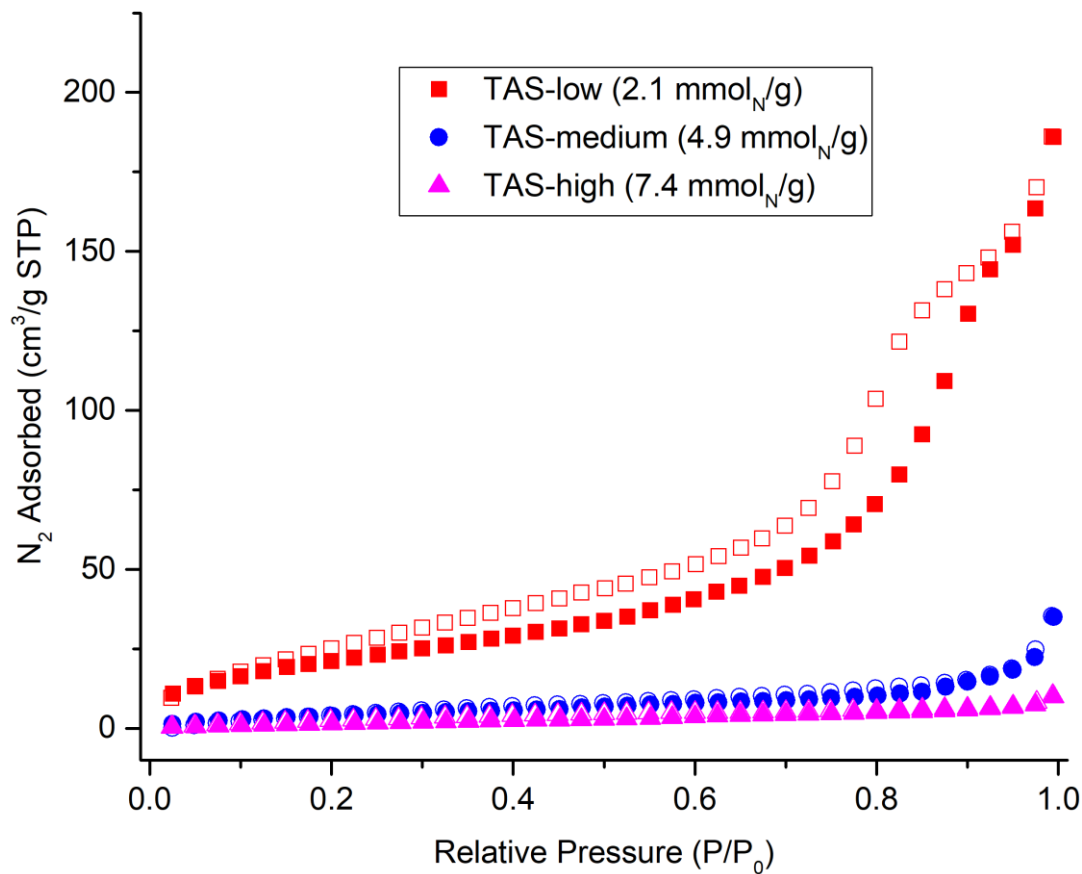


Figure A3. N₂ adsorption-desorption isotherms of TAS-grafted nanofibrous silicas.

Table A1. Textural properties of TAS-grafted nanofibrous silicas derived from N₂ adsorption-desorption isotherms.

Sample	Nitrogen Loading (mmol _N /g)	BET Surface Area (m ² /g)	Total Pore Volume (cm ³ /g)
TAS-low	2.1	81	0.288
TAS-medium	4.9	17	0.054
TAS-high	7.4	9	0.019

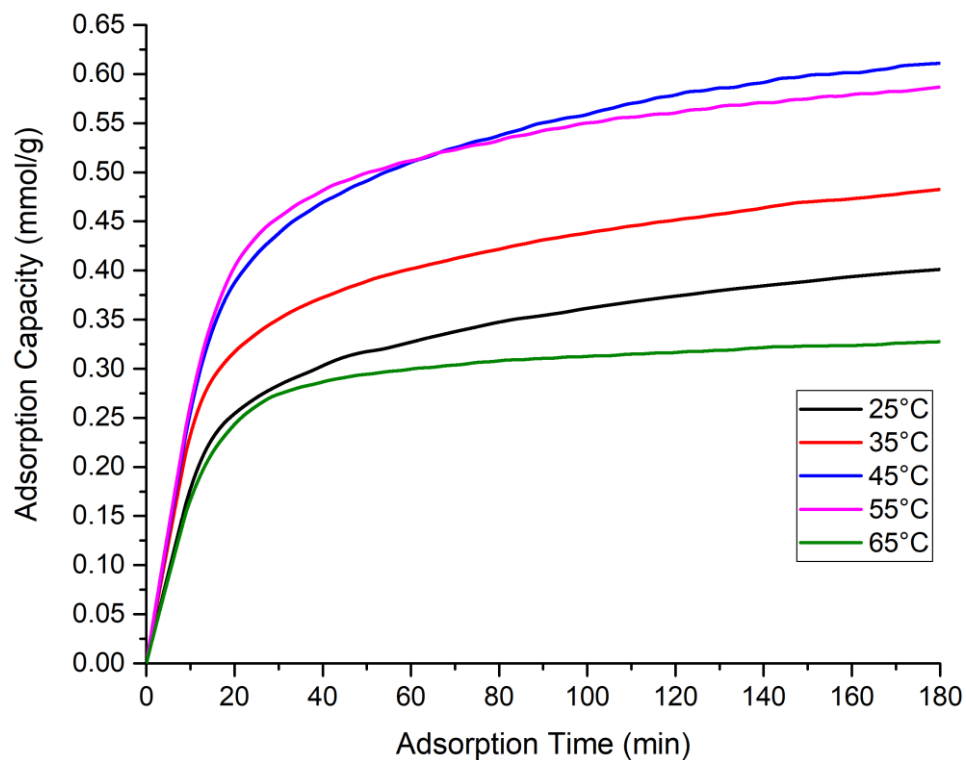


Figure A4. TGA CO₂ isotherms of APS-grafted nanofibrous silica (2.6 mmol_N/g) at different adsorption temperatures.

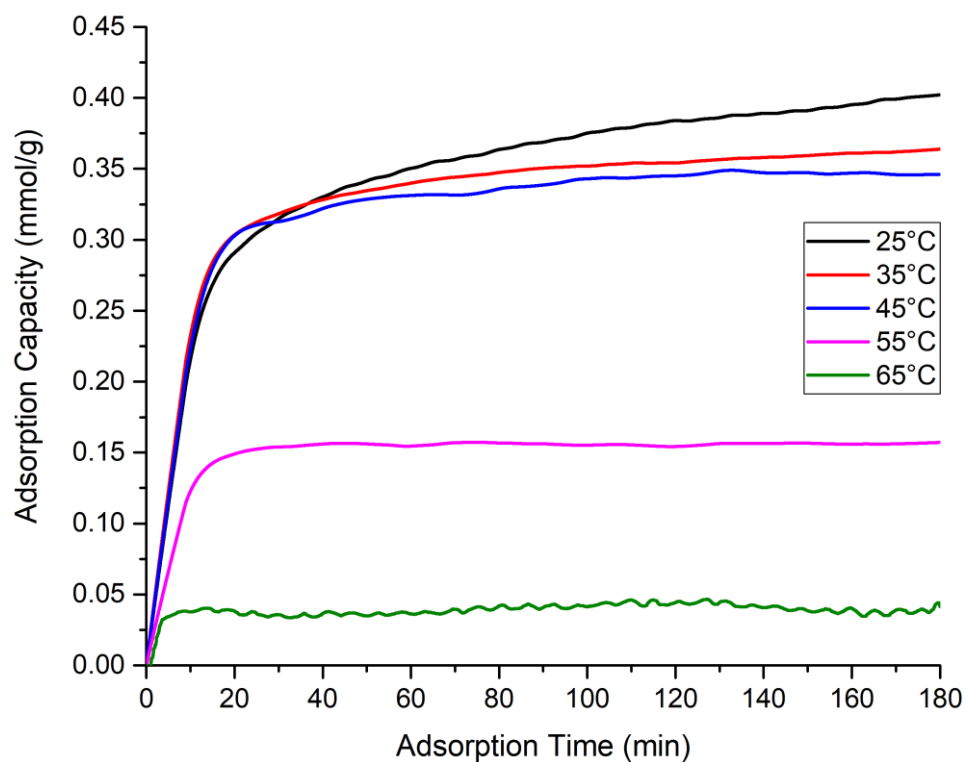


Figure A5. TGA CO₂ isotherms of DAS-grafted nanofibrous silica (2.6 mmol_N/g) at different adsorption temperatures.

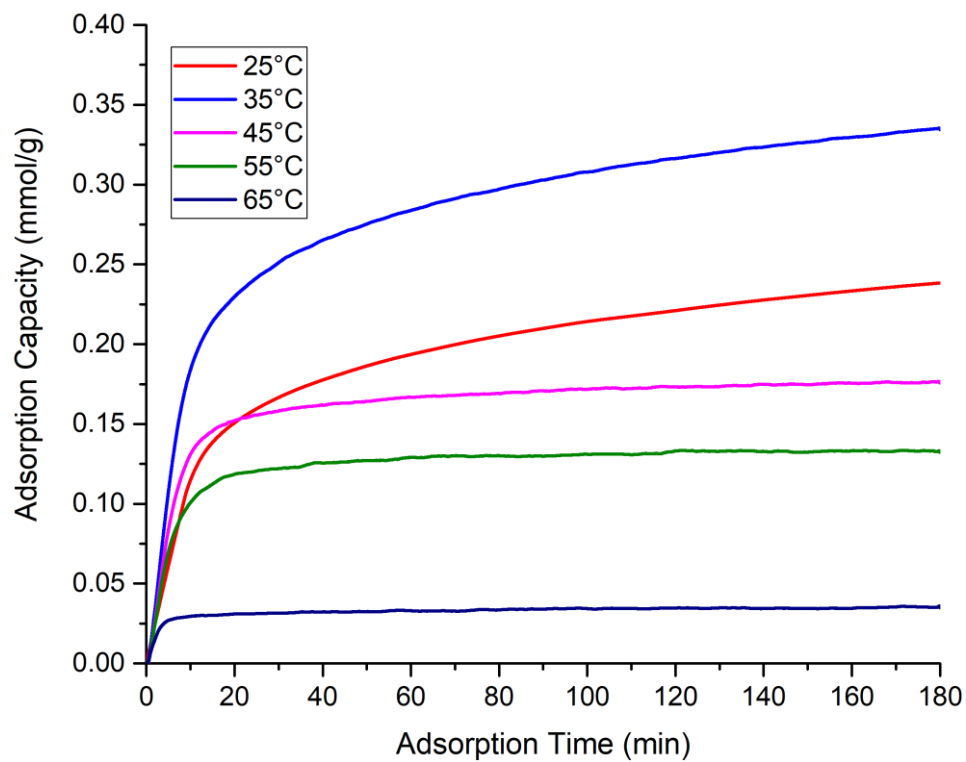


Figure A6. TGA CO₂ isotherms of TAS-grafted nanofibrous silica (2.1 mmol_N/g) at different adsorption temperatures.

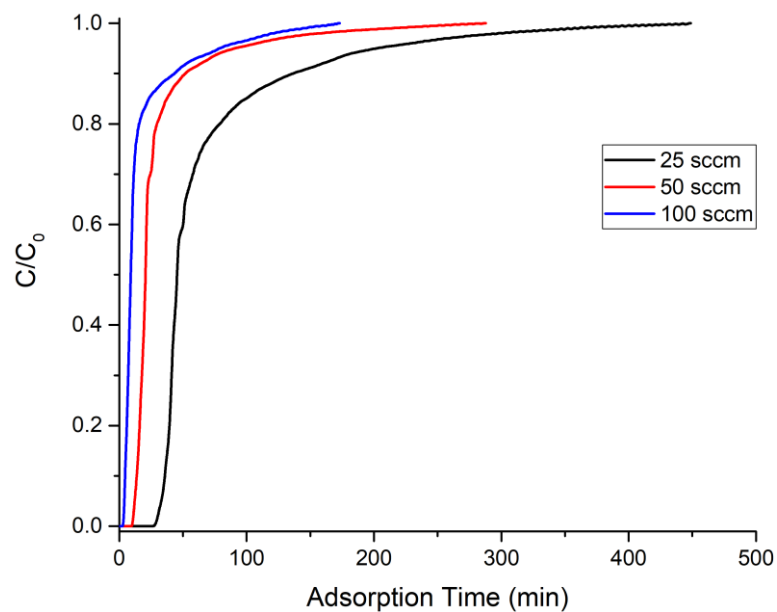


Figure A7. Breakthrough curves for TAS-2.6 under various flow rates at 25°C.

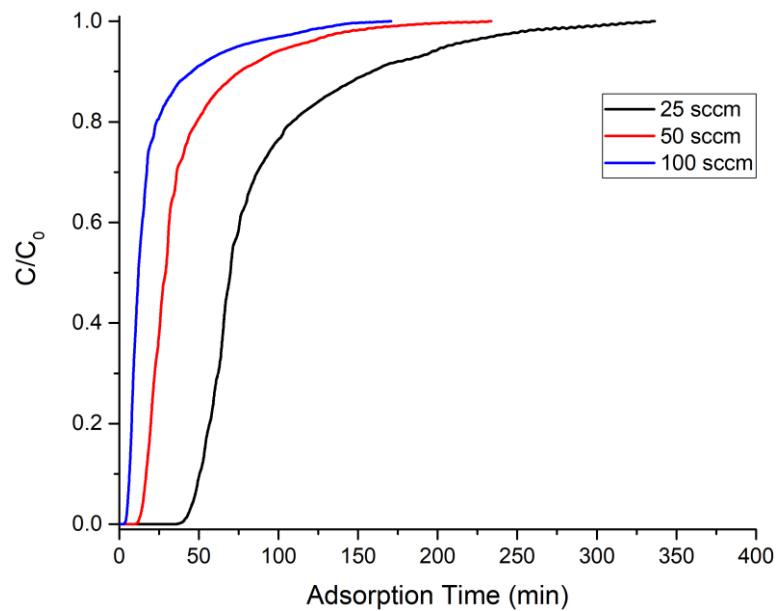


Figure A8. Breakthrough curves for TAS-4.9 under various flow rates at 25°C.

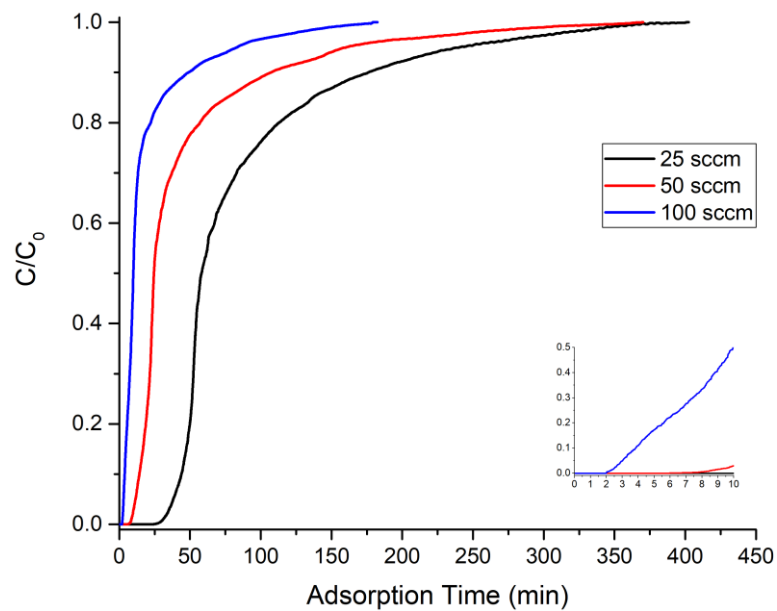


Figure A9. Breakthrough curves for TAS-6.4 under various flow rates at 25°C.

Table A2. Parameters derived from the fitting of kinetic models to fixed-bed adsorption data for APS-2.6 under different flow rates at 25°C. q_e = equilibrium CO₂ adsorption capacity, $k_{f/s/a}$ = rate constant of kinetic model, R^2 = coefficient of determination, n_a = Avrami exponent.

Model	Parameters	25 SCCM	50 SCCM	100 SCCM
Experimental	q_e (mmol/g)	0.274	0.277	0.365
Pseudo-first order	q_e (mmol/g)	0.270	0.269	0.356
	k_f (min ⁻¹)	0.021	0.035	0.028
	R^2	0.988	0.978	0.956
Pseudo-second order	q_e (mmol/g)	0.314	0.303	0.412
	k_s (g·mmol ⁻¹ ·min ⁻¹)	0.082	0.160	0.090
	R^2	0.971	0.992	0.990
Avrami	q_e (mmol/g)	0.268	0.275	0.393
	k_a (min ⁻¹)	0.021	0.034	0.023
	n_a	1.092	0.802	0.643
	R^2	0.989	0.988	0.996

Table A3. Parameters derived from the fitting of kinetic models to fixed-bed adsorption data for TAS-2.6 under different flow rates at 25°C. q_e = equilibrium CO₂ adsorption capacity, $k_{f/s/a}$ = rate constant of kinetic model, R^2 = coefficient of determination, n_a = Avrami exponent.

Model	Parameters	25 SCCM	50 SCCM	100 SCCM
Experimental	q_e (mmol/g)	0.331	0.295	0.347
Pseudo-first order	q_e (mmol/g)	0.325	0.286	0.336
	k_f (min ⁻¹)	0.017	0.037	0.039
	R^2	0.989	0.970	0.955
Pseudo-second order	q_e (mmol/g)	0.373	0.317	0.387
	k_s (g·mmol ⁻¹ ·min ⁻¹)	0.060	0.170	0.134
	R^2	0.986	0.992	0.992
Avrami	q_e (mmol/g)	0.327	0.292	0.368
	k_a (min ⁻¹)	0.017	0.036	0.033
	n_a	0.918	0.760	0.645
	R^2	0.991	0.986	0.995

Table A4. Parameters derived from the fitting of kinetic models to fixed-bed adsorption data for TAS-4.9 under different flow rates at 25°C. q_e = equilibrium CO₂ adsorption capacity, $k_{f/s/a}$ = rate constant of kinetic model, R^2 = coefficient of determination, n_a = Avrami exponent.

Model	Parameters	25 SCCM	50 SCCM	100 SCCM
Experimental	q_e (mmol/g)	0.377	0.335	0.357
Pseudo-first order	q_e (mmol/g)	0.382	0.332	0.348
	k_f (min ⁻¹)	0.016	0.032	0.045
	R²	0.991	0.996	0.978
Pseudo-second order	q_e (mmol/g)	0.467	0.382	0.397
	k_s (g·mmol ⁻¹ ·min ⁻¹)	0.036	0.109	0.152
	R²	0.970	0.984	0.998
Avrami	q_e (mmol/g)	0.373	0.333	0.361
	k_a (min ⁻¹)	0.016	0.032	0.043
	n_a	1.225	0.980	0.754
	R²	0.997	0.996	0.995

Table A5. Parameters derived from the fitting of kinetic models to fixed-bed adsorption data for TAS-6.4 under different flow rates at 25°C. q_e = equilibrium CO₂ adsorption capacity, $k_{f/s/a}$ = rate constant of kinetic model, R^2 = coefficient of determination, n_a = Avrami exponent.

Model	Parameters	25 SCCM	50 SCCM	100 SCCM
Experimental	q_e (mmol/g)	0.374	0.404	0.339
Pseudo-first order	q_e (mmol/g)	0.373	0.394	0.330
	k_f (min ⁻¹)	0.014	0.020	0.037
	R^2	0.996	0.982	0.971
Pseudo-second order	q_e (mmol/g)	0.446	0.452	0.382
	k_s (g·mmol ⁻¹ ·min ⁻¹)	0.037	0.058	0.126
	R^2	0.985	0.998	0.997
Avrami	q_e (mmol/g)	0.371	0.409	0.352
	k_a (min ⁻¹)	0.014	0.019	0.033
	n_a	1.030	0.767	0.702
	R^2	0.996	0.997	0.997

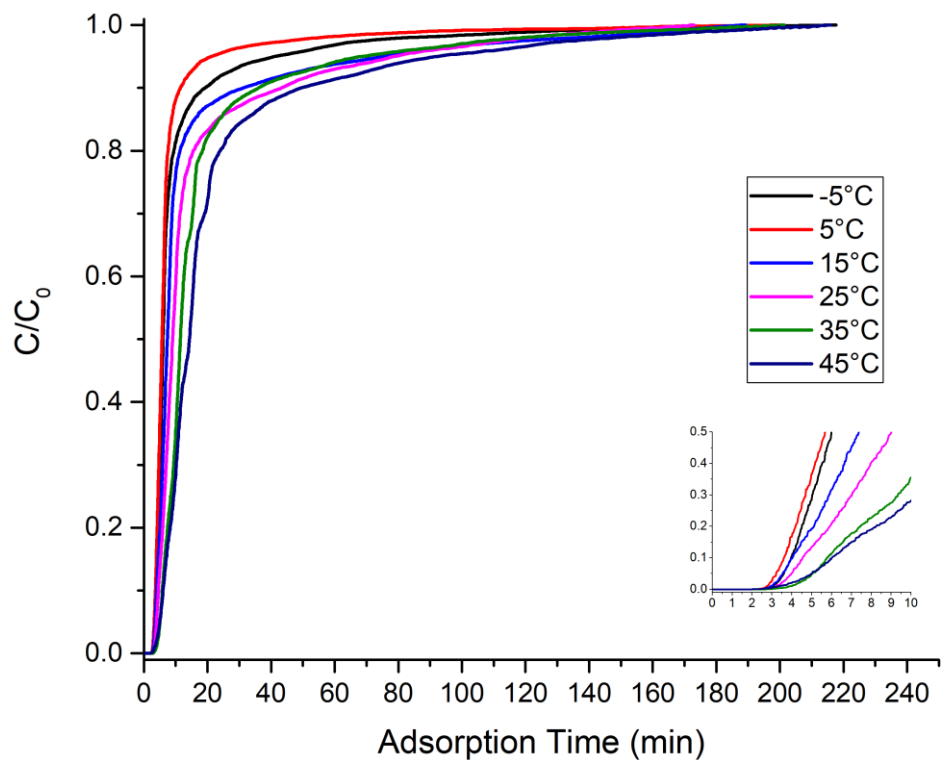


Figure A10. Breakthrough curves for TAS-2.6 at various temperatures (100 SCCM flow rate).

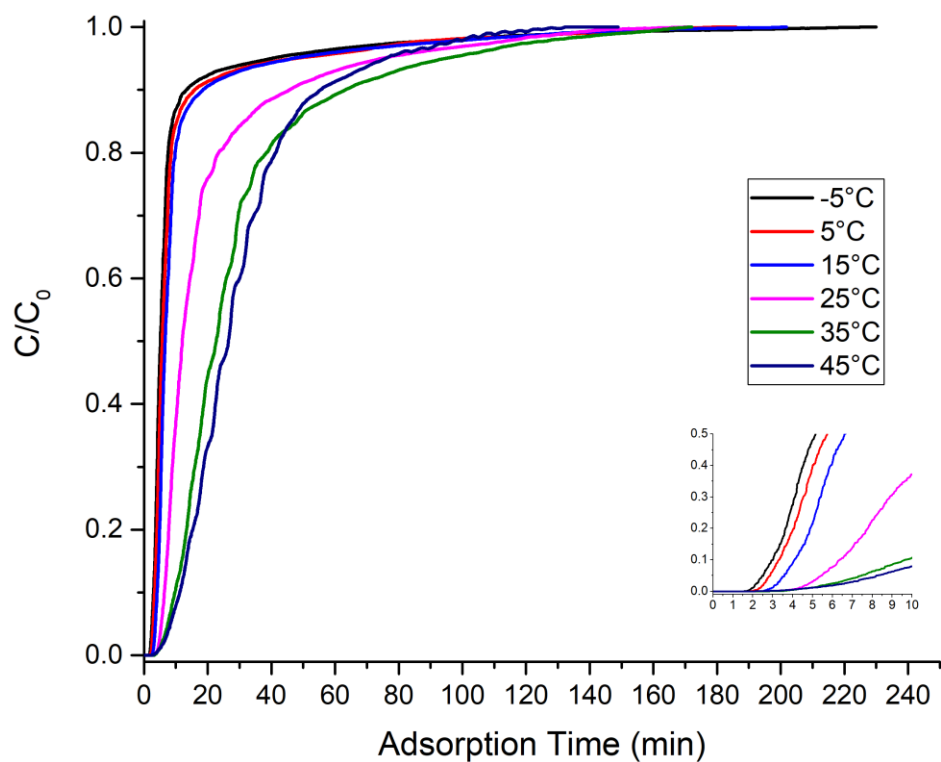


Figure A11. Breakthrough curves for TAS-4.9 at various temperatures (100 SCCM flow rate).

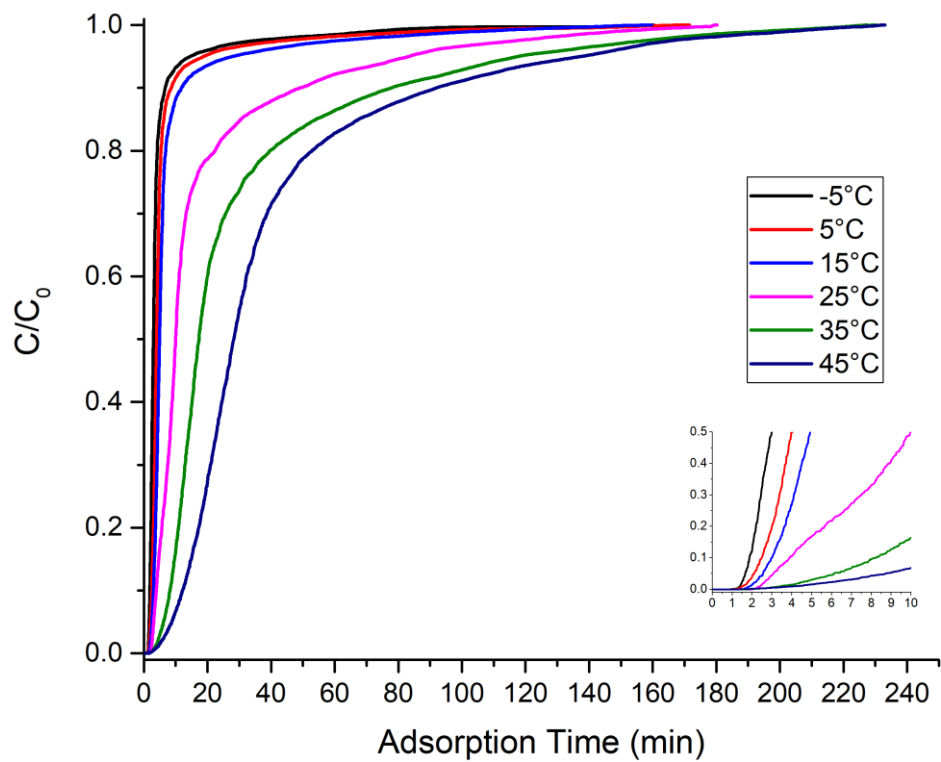


Figure A12. Breakthrough curves for TAS-6.4 at various temperatures (100 SCCM flow rate).

Table A6. Parameters derived from the fitting of kinetic models to fixed-bed adsorption data for APS-2.6 at various temperatures (100 SSCM).
 q_e = equilibrium CO₂ adsorption capacity, $k_{f/s/a}$ = rate constant of kinetic model, R^2 = coefficient of determination, n_a = Avrami exponent.

Model	Parameters	-5°C	5°C	15°C	25°C	35°C	45°C
Experimental	q_e (mmol/g)	0.145	0.164	0.328	0.365	0.408	0.493
Pseudo-first order	q_e (mmol/g)	0.138	0.156	19.300	0.356	0.397	0.481
	k_f (min ⁻¹)	0.113	0.087	0.027	0.028	0.041	0.043
	R²	0.942	0.895	0.956	0.956	0.974	0.990
Pseudo-second order	q_e (mmol/g)	0.154	0.169	0.386	0.412	0.457	0.557
	k_s (g·mmol ⁻¹ ·min ⁻¹)	1.054	0.821	0.082	0.090	0.118	0.098
	R²	0.988	0.983	0.983	0.990	0.996	0.990
Avrami	q_e (mmol/g)	0.145	0.165	0.395	0.393	0.416	0.488
	k_a (min ⁻¹)	0.104	0.081	0.016	0.023	0.038	0.042
	n_a	0.664	0.560	0.605	0.643	0.744	0.896
	R²	0.979	0.977	0.996	0.996	0.993	0.992

Table A7. Parameters derived from the fitting of kinetic models to fixed-bed adsorption data for TAS-2.6 at various temperatures (100 SSCM).
 q_e = equilibrium CO₂ adsorption capacity, $k_{f/s/a}$ = rate constant of kinetic model, R^2 = coefficient of determination, n_a = Avrami exponent.

Model	Parameters	-5°C	5°C	15°C	25°C	35°C	45°C
Experimental	q_e (mmol/g)	0.222	0.159	0.307	0.347	0.374	0.465
Pseudo-first order	q_e (mmol/g)	0.216	0.216	13.200	0.336	0.360	0.449
	k_f (min ⁻¹)	0.054	0.054	0.035	0.039	0.046	0.035
	R²	0.902	0.902	0.927	0.955	0.953	0.963
Pseudo-second order	q_e (mmol/g)	0.236	0.236	0.337	0.387	0.403	0.512
	k_s (g·mmol ⁻¹ ·min ⁻¹)	0.368	0.368	0.142	0.134	0.164	0.094
	R²	0.985	0.985	0.980	0.992	0.995	0.996
Avrami	q_e (mmol/g)	0.231	0.231	0.345	0.368	0.379	0.477
	k_a (min ⁻¹)	0.050	0.050	0.024	0.033	0.043	0.032
	n_a	0.555	0.555	0.557	0.645	0.667	0.686
	R²	0.991	0.991	0.995	0.995	0.991	0.994

Table A8. Parameters derived from the fitting of kinetic models to fixed-bed adsorption data for TAS-4.9 at various temperatures (100 SSCM).
 q_e = equilibrium CO₂ adsorption capacity, $k_{f/s/a}$ = rate constant of kinetic model, R^2 = coefficient of determination, n_a = Avrami exponent.

Model	Parameters	-5°C	5°C	15°C	25°C	35°C	45°C
Experimental	q_e (mmol/g)	0.180	0.194	0.213	0.357	0.532	0.535
Pseudo-first order	q_e (mmol/g)	0.172	0.186	0.204	0.348	0.524	0.538
	k_f (min ⁻¹)	0.043	0.047	0.050	0.045	0.038	0.043
	R²	0.877	0.895	0.898	0.978	0.995	0.997
Pseudo-second order	q_e (mmol/g)	0.189	0.207	0.225	0.397	0.614	0.635
	k_s (g·mmol ⁻¹ ·min ⁻¹)	0.357	0.337	0.340	0.152	0.075	0.080
	R²	0.968	0.973	0.979	0.998	0.992	0.975
Avrami	q_e (mmol/g)	0.193	0.212	0.224	0.361	0.530	0.532
	k_a (min ⁻¹)	0.034	0.035	0.042	0.043	0.037	0.043
	n_a	0.504	0.524	0.546	0.754	0.922	1.125
	R²	0.992	0.991	0.989	0.995	0.997	0.999

Table A9. Parameters derived from the fitting of kinetic models to fixed-bed adsorption data for TAS-6.4 at various temperatures (100 SSCM).
 q_e = equilibrium CO₂ adsorption capacity, $k_{f/s/a}$ = rate constant of kinetic model, R^2 = coefficient of determination, n_a = Avrami exponent.

Model	Parameters	-5°C	5°C	15°C	25°C	35°C	45°C
Experimental	q_e (mmol/g)	0.088	0.121	0.153	0.340	0.565	0.741
Pseudo-first order	q_e (mmol/g)	0.083	0.114	0.146	0.330	0.553	0.731
	k_f (min ⁻¹)	0.086	0.080	0.069	0.037	0.028	0.027
	R²	0.839	0.834	0.873	0.971	0.984	0.994
Pseudo-second order	q_e (mmol/g)	0.090	0.124	0.160	0.382	0.645	0.862
	k_s (g·mmol ⁻¹ ·min ⁻¹)	1.601	1.049	0.675	0.126	0.055	0.037
	R²	0.963	0.961	0.971	0.997	0.998	0.995
Avrami	q_e (mmol/g)	0.091	0.127	0.162	0.352	0.578	0.745
	k_a (min ⁻¹)	0.076	0.065	0.056	0.033	0.026	0.026
	n_a	0.480	0.468	0.509	0.702	0.774	0.885
	R²	0.986	0.983	0.986	0.997	0.998	0.997

Table A10. Parameters derived from the fitting of kinetic models to fixed-bed adsorption data for TAS-2.6 under dry and humid conditions (25°C, 100 SSCM).

q_e = equilibrium CO₂ adsorption capacity, $k_{f/s/a}$ = rate constant of kinetic model,

R^2 = coefficient of determination, n_a = Avrami exponent.

Model	Parameters	Dry	Humid
Experimental	q_e (mmol/g)	0.347	0.500
Pseudo-first order	q_e (mmol/g)	0.336	0.487
	k_f (min ⁻¹)	0.039	0.031
	R^2	0.955	0.971
Pseudo-second order	q_e (mmol/g)	0.387	0.570
	k_s (g·mmol ⁻¹ ·min ⁻¹)	0.134	0.068
	R^2	0.992	0.996
Avrami	q_e (mmol/g)	0.368	0.527
	k_a (min ⁻¹)	0.033	0.026
	n_a	0.645	0.700
	R^2	0.995	0.996

Table A11. Parameters derived from the fitting of kinetic models to fixed-bed adsorption data for TAS-4.9 under dry and humid conditions (25°C, 100 SSCM).
 q_e = equilibrium CO₂ adsorption capacity, $k_{f/s/a}$ = rate constant of kinetic model,
 R^2 = coefficient of determination, n_a = Avrami exponent.

Model	Parameters	Dry	Humid
Experimental	q_e (mmol/g)	0.360	0.874
Pseudo-first order	q_e (mmol/g)	0.348	0.874
	k_f (min ⁻¹)	0.045	0.017
	R^2	0.978	0.997
Pseudo-second order	q_e (mmol/g)	0.397	1.047
	k_s (g·mmol ⁻¹ ·min ⁻¹)	0.152	0.019
	R^2	0.998	0.995
Avrami	q_e (mmol/g)	0.361	0.893
	k_a (min ⁻¹)	0.043	0.016
	n_a	0.754	0.888
	R^2	0.995	0.999

Table A12. Parameters derived from the fitting of kinetic models to fixed-bed adsorption data for TAS-6.4 under dry and humid conditions (25°C, 100 SSCM).
 q_e = equilibrium CO₂ adsorption capacity, $k_{f/s/a}$ = rate constant of kinetic model,
 R^2 = coefficient of determination, n_a = Avrami exponent.

Model	Parameters	Dry	Humid
Experimental	q_e (mmol/g)	0.340	0.964
Pseudo-first order	q_e (mmol/g)	0.330	0.971
	k_f (min ⁻¹)	0.037	0.013
	R^2	0.971	0.998
Pseudo-second order	q_e (mmol/g)	0.382	1.189
	k_s (g·mmol ⁻¹ ·min ⁻¹)	0.126	0.012
	R^2	0.997	0.995
Avrami	q_e (mmol/g)	0.352	0.989
	k_a (min ⁻¹)	0.033	0.013
	n_a	0.702	0.916
	R^2	0.997	0.9995

Table A13. Physiochemical properties of triamine-grafted silicas. SA – specific surface area, TPV – total pore volume, GE – grafting efficiency, TW – this work.

Sample Name	Support	Support Properties		Functionalised Silica Properties							Ref
		SA (m ² /g)	TPV (cm ³ /g)	Silane Added (mmol/g _{silica})	Silane Loading (mmol/g _{silica})	GE (%)	Amine Loading (mmol _N /g)	TPV (cm ³ /g)	Pore Fill Fraction (%)	Amine Coverage (μmol/m ²)	
TAS-2.1	NFS	131	0.393	2.09	0.78	37	2.1	0.288	26.7	16.0	TW
TAS-2.6	NFS	131	0.393	4.19	1.00	24	2.6	0.179	54.5	20.2	TW
TAS-4.9	NFS	131	0.393	8.72	2.12	24	4.9	0.054	86.3	37.4	TW
TAS-7.4	NFS	131	0.393	17.44	3.82	22	7.4	0.019	95.2	56.5	TW
AG-SBA-15-PE-0.6	PE SBA-15	766	1.300	34.89	4.11	12	7.7	0.002	99.8	10.1	[298]
MCM-41-30-TP-9-75-0.5	PE MCM-41	1045	2.580	9.00	3.56	40	7.1	0.0998	96.1	6.8	[281]
SBA-15/D-1	SBA-15	676	1.184	3.55	2.69	76	5.8	0.204	82.8	8.6	[300]
SBA-15/D-1.5	SBA-15	676	1.184	5.33	3.35	63	6.8	0.176	85.1	10.0	[300]
SBA-15/D-4	SBA-15	676	1.184	14.20	4.03	28	7.7	0.122	89.7	11.3	[300]

Table A14. Dry CO₂ capture performance of amine-functionalised silicas.

Adsorbent Name	Description	Amine Loading (mmol _N /g)	Set-Up	Conditions	q _{max} (mmol/g)	t _{1/2} (min)	Average Uptake Rate (mmol·g ⁻¹ ·h ⁻¹)	Ref
Mg ₂ (dobdc)	Hydrazine-Appended Metal Organic Framework	6.01	TGA	Dry Air 25°C	3.66	310	0.18	[92]
HSA-50	Monoamine-Functionalised Hierarchical Silica	3.7	TGA	400 ppm CO ₂ /He 30°C	0.60	150	0.06	[68]
HST-30	Triamine-Functionalised Hierarchical Silica	4.4	TGA	400 ppm CO ₂ 30°C	0.28	40	0.11	[68]
20TEPA	TEPA-Impregnated SBA-15	5.3	TGA	400 ppm CO ₂ /He 30°C	0.16	2	1.20	[35]
S-T-4.6	Triamine-grafted SBA-15	4.6	Volumetric	0.04 kPa CO ₂ 25°C	0.33	-	-	[280]

Adsorbent Name	Description	Amine Loading (mmol _N /g)	Set-Up	Conditions	q _{max} (mmol/g)	t _{1/2} (min)	Average Uptake Rate (mmol·g ⁻¹ ·h ⁻¹)	Ref
TAS-4.9	Triamine-grafted Nanofibrous Silica	4.9	Fixed Bed	400 ppm CO ₂ /N ₂ , 25°C, Dry	0.36	13	0.41	This work

Table A15. Humid CO₂ capture performance of amine-functionalised silicas.

Adsorbent Name	Description	Amine Loading (mmol _N /g)	Set-Up	Conditions	q _{max} (mmol/g)	t _{1/2} (min)	Average Uptake Rate (mmol·g ⁻¹ ·h ⁻¹)	Ref
MAHSM	Monoamine-Based Hybrid Silica	4.5	TGA	Air (400 ppm CO ₂) 60% RH 30°C	1.68	50	0.50	[303]
DAS-NFC	Diamine-Functionalized Nanofibrillated Cellulose	4.9	Fixed-Bed	Air (506 ppm CO ₂) 40% RH 25°C	1.39	100	0.21	[105]
HAS4	Hyperbranched Aminosilica	5.3	Fixed Bed	400 ppm CO ₂ Humid	1	163	0.09	[73]
S-T-4.6	Triamine-Functionalised SBA-15	4.6	TGA	Ambient Air 24% RH	0.59	59	0.15	[280]

Adsorbent Name	Description	Amine Loading (mmol _N /g)	Set-Up	Conditions	q _{max} (mmol/g)	t _{1/2} (min)	Average Uptake Rate (mmol·g ⁻¹ ·h ⁻¹)	Ref
TAS-4.9	Triamine-Functionalised Nanofibrous Silica	4.9	Fixed Bed	400 ppm CO ₂ /N ₂ 60% RH 25°C	0.87	39	0.33	Own Work

Table A16. Humid CO₂ capture performance of nanofibrous adsorbents.

Adsorbent Name	Description	Nitrogen Loading (mmol _N /g)	Set-Up	Conditions	q _{max} (mmol/g)	t _{1/2} (min)	Average Uptake Rate (mmol·g ⁻¹ ·h ⁻¹)	Ref
PVA/Arginine	Poly(vinyl alcohol) and arginine hybrid nanofibres	5.7	Open circuit system (sorbent chamber loosely packed)	Lab air (400 – 450 ppm CO ₂) 80% RH 0.5 L/min	0.31	17	0.27	[229]
PVA/IER	Porous poly(vinyl alcohol) nanofibres with an embedded ion exchange resin	-	Closed circuit system	Moist air 1 L/min	0.93	10	1.40	[133]
TAS-4.9	Triamine-grafted nanofibrous silica	4.9	Fixed bed	400 ppm CO ₂ /N ₂ 25°C 60% RH 0.1 L/min	0.87	39	0.33	Own work

List of References

1. Mitchell, J.F.B., *The “Greenhouse” effect and climate change*. Reviews of Geophysics, 1989. **27**(1): p. 115-139.
2. IPCC, *Summary for Policymakers*. In: *Climate Change 2021: The Physical Science Basis. Contribution of Working Group I to the Sixth Assessment Report of the Intergovernmental Panel on Climate Change* [Masson-Delmotte, V., P. Zhai, A. Pirani, S.L. Connors, C. Péan, S. Berger, N. Caud, Y. Chen, L. Goldfarb, M.I. Gomis, M. Huang, K. Leitzell, E. Lonnoy, J.B.R. Matthews, T.K. Maycock, T. Waterfield, O. Yelekçi, R. Yu, and B. Zhou (eds.)]. 2021: Cambridge University Press, Cambridge, United Kingdom and New York, NY, USA. p. 3-32.
3. IPCC, *Summary for Policymakers*. In: *Climate Change 2022: Impacts, Adaptation, and Vulnerability. Contribution of Working Group II to the Sixth Assessment Report of the Intergovernmental Panel on Climate Change* [H.-O. Pörtner, D.C. Roberts, M. Tignor, E.S. Poloczanska, K. Mintenbeck, A. Alegría, M. Craig, S. Langsdorf, S. Löschke, V. Möller, A. Okem, B. Rama (eds.)]. 2022: Cambridge University Press, Cambridge, UK and New York, NY, USA. p. 3-33.
4. Le Treut, H., R. Somerville, U. Cubasch, Y. Ding, C. Mauritzen, A. Mokssit, T. Peterson and M. Prather, *Historical Overview of Climate Change*. In: *Climate Change 2007: The Physical Science Basis. Contribution of Working Group I to the Fourth Assessment Report of the Intergovernmental Panel on Climate Change* [Solomon, S., D. Qin, M. Manning, Z. Chen, M. Marquis, K.B. Averyt, M. Tignor and H.L. Miller (eds.)]. 2007: Cambridge University Press, Cambridge, United Kingdom and New York, NY, USA.
5. Tyndall, J., *XXIII. On the absorption and radiation of heat by gases and vapours, and on the physical connexion of radiation, absorption, and conduction.—The bakerian lecture*. The London, Edinburgh, and Dublin Philosophical Magazine and Journal of Science, 1861. **22**(146): p. 169-194.
6. Callendar, G.S., *The artificial production of carbon dioxide and its influence on temperature*. Quarterly Journal of the Royal Meteorological Society, 1938. **64**(275): p. 223-240.
7. Keeling, C.D., *The concentration and isotopic abundances of carbon dioxide in rural and marine air*. Geochimica et Cosmochimica Acta, 1961. **24**(3-4): p. 277-298.
8. Ramanathan, V., *Greenhouse effect due to chlorofluorocarbons: Climatic implications*. Science, 1975. **190**(4209): p. 50-52.
9. Wang, W., et al., *Greenhouse Effects due to Man-Made Perturbations of Trace Gases: Anthropogenic gases may alter our climate by plugging an atmospheric window for escaping thermal radiation*. Science, 1976. **194**(4266): p. 685-690.
10. WMO, *Report of the International conference of the Assessment of the role of carbon dioxide and of other greenhouse gases in climate variations and associated impacts*. 1986: Geneva.
11. Agrawala, S., *Context and Early Origins of the Intergovernmental Panel on Climate Change*. Climatic Change, 1998. **39**(4): p. 605-620.
12. IPCC. *History of the IPCC*. [cited 2024 6th March]; Available from: <https://www.ipcc.ch/about/history/>.
13. UNFCCC. *What is the Kyoto Protocol?* [cited 2024 6th March]; Available from: https://unfccc.int/kyoto_protocol.
14. UNFCCC. *The Paris Agreement*. [cited 2024 6th March]; Available from: <https://unfccc.int/process-and-meetings/the-paris-agreement#:~:text=The%20Paris%20Agreement%20is%20a,force%20on%204%20November%202016>.
15. IPCC, *Global warming of 1.5°C. An IPCC Special Report on the impacts of global warming of 1.5°C above pre-industrial levels and related global greenhouse gas emission pathways, in the context of strengthening the global response to the threat of climate change, sustainable development, and efforts to eradicate poverty* [V. Masson-Delmotte, P. Zhai, H. O. Pörtner, D. Roberts, J. Skea, P.R. Shukla, A. Pirani, W. Moufouma-Okia, C. Péan, R. Pidcock, S. Connors, J. B. R. Matthews, Y. Chen,

- X. Zhou, M. I. Gomis, E. Lonnoy, T. Maycock, M. Tignor, T. Waterfield (eds.)). 2018: In Press.
16. Luderer, G., et al., *Residual fossil CO₂ emissions in 1.5–2 C pathways*. Nature Climate Change, 2018. **8**(7): p. 626-633.
 17. Smith, S.M., et al., *The State of Carbon Dioxide Removal - 1st Edition*. 2023, The State of Carbon Dioxide Removal.
 18. Ritchie, H.R., M. . *CO₂ Emissions*. 2020 [cited 2024 7th March]; Available from: <https://ourworldindata.org/co2-emissions>.
 19. Agency, I.E., *Direct Air Capture: A key technology to net zero*. 2022.
 20. Erans, M., et al., *Direct air capture: process technology, techno-economic and socio-political challenges*. Energy & Environmental Science, 2022. **15**(4): p. 1360-1405.
 21. Energy, U.S.D.o. *Secretary Granholm Launches Carbon Negative Earthshots to Remove Gigatons of Carbon Pollution from the Air by 2050*. 2021 [cited 2024 7th March]; Available from: <https://www.energy.gov/articles/secretary-granholm-launches-carbon-negative-earthshots-remove-gigatons-carbon-pollution>.
 22. National Academies of Sciences, D.o.E., Life Studies, Ocean Studies Board, Board on Chemical Sciences, Board on Earth Sciences, Board on Energy, Environmental Systems, Board on Atmospheric Sciences, Committee on Developing a Research Agenda for Carbon Dioxide Removal and Reliable Sequestration, *Negative emissions technologies and reliable sequestration: a research agenda*. 2019.
 23. Azarabadi, H. and K.S. Lackner, *A sorbent-focused techno-economic analysis of direct air capture*. Applied Energy, 2019. **250**: p. 959-975.
 24. Shi, X., et al., *Sorbents for the Direct Capture of CO₂ from Ambient Air*. Angewandte Chemie International Edition, 2020. **59**(18): p. 6984-7006.
 25. Kong, F.H., et al., *Research needs targeting direct air capture of carbon dioxide: Material & process performance characteristics under realistic environmental conditions*. Korean Journal of Chemical Engineering, 2022. **39**(1): p. 1-19.
 26. Darunte, L.A., et al., *Moving Beyond Adsorption Capacity in Design of Adsorbents for CO₂ Capture from Ultradilute Feeds: Kinetics of CO₂ Adsorption in Materials with Stepped Isotherms*. Industrial & Engineering Chemistry Research, 2019. **58**(1): p. 366-377.
 27. Elfving, J., et al., *Experimental comparison of regeneration methods for CO₂ concentration from air using amine-based adsorbent*. Chemical Engineering Journal, 2021. **404**: p. 13.
 28. Xu, X.C., et al., *Novel polyethylenimine-modified mesoporous molecular sieve of MCM-41 type as high-capacity adsorbent for CO₂ capture*. Energy & Fuels, 2002. **16**(6): p. 1463-1469.
 29. Xu, X.C., et al., *Adsorption separation of carbon dioxide from flue gas of natural gas-fired boiler by a novel nanoporous "molecular basket" adsorbent*. Fuel Processing Technology, 2005. **86**(14-15): p. 1457-1472.
 30. Son, W.J., J.S. Choi, and W.S. Ahn, *Adsorptive removal of carbon dioxide using polyethyleneimine-loaded mesoporous silica materials*. Microporous and Mesoporous Materials, 2008. **113**(1-3): p. 31-40.
 31. Goeppert, A., et al., *Nanostructured silica as a support for regenerable high-capacity organoamine-based CO₂ sorbents*. Energy & Environmental Science, 2010. **3**(12): p. 1949-1960.
 32. Goeppert, A., et al., *Carbon Dioxide Capture from the Air Using a Polyamine Based Regenerable Solid Adsorbent*. Journal of the American Chemical Society, 2011. **133**(50): p. 20164-20167.
 33. Holewinski, A., M.A. Sakwa-Novak, and C.W. Jones, *Linking CO₂ Sorption Performance to Polymer Morphology in Aminopolymer/Silica Composites through Neutron Scattering*. Journal of the American Chemical Society, 2015. **137**(36): p. 11749-11759.
 34. Holewinski, A., et al., *Aminopolymer Mobility and Support Interactions in Silica-PEI Composites for CO₂ Capture Applications: A Quasielastic Neutron Scattering Study*. Journal of Physical Chemistry B, 2017. **121**(27): p. 6721-6731.

35. Moon, H.J., R.S. Sekiya, and C.W. Jones, *Probing the Morphology and Mobility of Amines in Porous Silica CO₂ Sorbents by 1H T₁-T₂ Relaxation Correlation NMR*. Journal of Physical Chemistry C, 2023: p. 14.
36. Goeppert, A., et al., *Oxidation-Resistant, Cost-Effective Epoxide-Modified Polyamine Adsorbents for CO₂ Capture from Various Sources Including Air*. Chemsuschem, 2019. **12**(8): p. 1712-1723.
37. Srikanth, C.S. and S.S.C. Chuang, *Spectroscopic Investigation into Oxidative Degradation of Silica-Supported Amine Sorbents for CO₂ Capture*. Chemsuschem, 2012. **5**(8): p. 1435-1442.
38. Ahmadalinezhad, A. and A. Sayari, *Oxidative degradation of silica-supported polyethylenimine for CO₂ adsorption: insights into the nature of deactivated species*. Physical Chemistry Chemical Physics, 2014. **16**(4): p. 1529-1535.
39. Bali, S., et al., *Oxidative Stability of Amino Polymer-Alumina Hybrid Adsorbents for Carbon Dioxide Capture*. Energy & Fuels, 2013. **27**(3): p. 1547-1554.
40. Pang, S.H., R.P. Lively, and C.W. Jones, *Oxidatively-Stable Linear Poly(propylenimine)-Containing Adsorbents for CO₂ Capture from Ultradilute Streams*. Chemsuschem, 2018. **11**(15): p. 2628-2637.
41. Sujan, A.R., et al., *Poly(glycidyl amine)-Loaded SBA-15 Sorbents for CO₂ Capture from Dilute and Ultradilute Gas Mixtures*. Acs Applied Polymer Materials, 2019. **1**(11): p. 3137-3147.
42. Kumar, D.R., et al., *Alkyl-Aryl Amine-Rich Molecules for CO₂ Removal via Direct Air Capture*. Acs Sustainable Chemistry & Engineering, 2020. **8**(29): p. 10971-10982.
43. Park, S.J., et al., *Silica supported poly(propylene guanidine) as a CO₂ sorbent in simulated flue gas and direct air capture*. Adsorption-Journal of the International Adsorption Society, 2020. **26**(1): p. 89-101.
44. Sakwa-Novak, M.A., S. Tan, and C.W. Jones, *Role of Additives in Composite PEI/Oxide CO₂ Adsorbents: Enhancement in the Amine Efficiency of Supported PEI by PEG in CO₂ Capture from Simulated Ambient Air*. Acs Applied Materials & Interfaces, 2015. **7**(44): p. 24748-24759.
45. Rosu, C., et al., *Sequential polymer infusion into solid substrates (SPISS): Impact of processing on sorbent CO₂ adsorption properties*. Separation and Purification Technology, 2022. **292**: p. 12.
46. He, Z.J., et al., *Mixed polyamines promotes CO₂ adsorption from air*. Journal of Environmental Chemical Engineering, 2022. **10**(2): p. 11.
47. Miao, Y.H., et al., *Mixed Diethanolamine and Polyethyleneimine with Enhanced CO₂ Capture Capacity from Air*. Advanced Science, 2023. **10**(16): p. 8.
48. Chaikittisilp, W., H.J. Kim, and C.W. Jones, *Mesoporous Alumina-Supported Amines as Potential Steam-Stable Adsorbents for Capturing CO₂ from Simulated Flue Gas and Ambient Air*. Energy & Fuels, 2011. **25**(11): p. 5528-5537.
49. Kuwahara, Y., et al., *Dramatic Enhancement of CO₂ Uptake by Poly(ethyleneimine) Using Zirconosilicate Supports*. Journal of the American Chemical Society, 2012. **134**(26): p. 10757-10760.
50. Kuwahara, Y., et al., *Enhanced CO₂ Adsorption over Polymeric Amines Supported on Heteroatom-Incorporated SBA-15 Silica: Impact of Heteroatom Type and Loading on Sorbent Structure and Adsorption Performance*. Chemistry-a European Journal, 2012. **18**(52): p. 16649-16664.
51. Sayari, A., Q. Liu, and P. Mishra, *Enhanced Adsorption Efficiency through Materials Design for Direct Air Capture over Supported Polyethylenimine*. Chemsuschem, 2016. **9**(19): p. 2796-2803.
52. Qi, L.M., et al., *Role of brush-like additives in CO₂ adsorbents for the enhancement of amine efficiency*. Journal of Environmental Chemical Engineering, 2021. **9**(6): p. 11.
53. Al-Absi, A.A., et al., *CO₂ capture using in-situ polymerized amines into pore-expanded-SBA-15: Performance evaluation, kinetics, and adsorption isotherms*. Fuel, 2023. **333**: p. 13.

54. Kwon, H.T., et al., *Aminopolymer-Impregnated Hierarchical Silica Structures: Unexpected Equivalent CO₂ Uptake under Simulated Air Capture and Flue Gas Capture Conditions*. *Chemistry of Materials*, 2019. **31**(14): p. 5229-5237.
55. Kulkarni, V., D. Panda, and S.K. Singh, *Direct Air Capture of CO₂ over Amine-Modified Hierarchical Silica*. *Industrial & Engineering Chemistry Research*, 2023. **62**(8): p. 3800-3811.
56. Leal, O., et al., *Reversible adsorption of carbon dioxide on amine surface-bonded silica gel*. *Inorganica Chimica Acta*, 1995. **240**(1): p. 183-189.
57. Harlick, P.J. and A. Sayari, *Applications of pore-expanded mesoporous silicas. 3. Triamine silane grafting for enhanced CO₂ adsorption*. *Industrial & Engineering Chemistry Research*, 2006. **45**(9): p. 3248-3255.
58. Harlick, P.J.E. and A. Sayari, *Applications of Pore-Expanded Mesoporous Silica. 5. Triamine Grafted Material with Exceptional CO₂ Dynamic and Equilibrium Adsorption Performance*. *Industrial & Engineering Chemistry Research*, 2007. **46**(2): p. 446-458.
59. Belmabkhout, Y., R. Serna-Guerrero, and A. Sayari, *Adsorption of CO₂ Containing Gas Mixtures over Amine-Bearing Pore-Expanded MCM-41 Silica: Application for Gas Purification*. *Industrial & Engineering Chemistry Research*, 2010. **49**(1): p. 359-365.
60. Belmabkhout, Y., R. Serna-Guerrero, and A. Sayari, *Amine-bearing mesoporous silica for CO₂ removal from dry and humid air*. *Chemical Engineering Science*, 2010. **65**(11): p. 3695-3698.
61. Wurzbacher, J.A., C. Gebald, and A. Steinfeld, *Separation of CO₂ from air by temperature-vacuum swing adsorption using diamine-functionalized silica gel*. *Energy & Environmental Science*, 2011. **4**(9): p. 3584-3592.
62. Lee, J.J., et al., *Effect of Humidity on the CO₂ Adsorption of Tertiary Amine Grafted SBAL15*. *Journal of Physical Chemistry C*, 2017. **121**(42): p. 23480-23487.
63. Didas, S.A., et al., *Role of Amine Structure on Carbon Dioxide Adsorption from Ultradilute Gas Streams such as Ambient Air*. *Chemsuschem*, 2012. **5**(10): p. 2058-2064.
64. Alkhabbaz, M.A., et al., *Important Roles of Enthalpic and Entropic Contributions to CO₂ Capture from Simulated Flue Gas and Ambient Air Using Mesoporous Silica Grafted Amines*. *Journal of the American Chemical Society*, 2014. **136**(38): p. 13170-13173.
65. Yoo, C.J., S.J. Park, and C.W. Jones, *CO₂ Adsorption and Oxidative Degradation of Silica-Supported Branched and Linear Aminosilanes*. *Industrial & Engineering Chemistry Research*, 2020. **59**(15): p. 7061-7071.
66. Anyanwu, J.T., Y.R. Wang, and R.T. Yang, *Amine-Grafted Silica Gels for CO₂ Capture Including Direct Air Capture*. *Industrial & Engineering Chemistry Research*, 2020. **59**(15): p. 7072-7079.
67. Anyanwu, J.T., Y.R. Wang, and R.T. Yang, *CO₂ capture (including direct air capture) and natural gas desulfurization of amine-grafted hierarchical bimodal silica*. *Chemical Engineering Journal*, 2022. **427**: p. 10.
68. Kulkarni, V., J. Parthiban, and S.K. Singh, *Direct CO₂ capture from simulated and Ambient Air over aminosilane-modified hierarchical silica*. *Microporous and Mesoporous Materials*, 2024. **368**: p. 112998.
69. Wang, Y.R. and R.T. Yang, *Template Removal from SBA-15 by Ionic Liquid for Amine Grafting: Applications to CO₂ Capture and Natural Gas Desulfurization*. *Acs Sustainable Chemistry & Engineering*, 2020. **8**(22): p. 8295-8304.
70. Wang, Y.R., et al., *Significantly enhancing CO₂ adsorption on Amine-Grafted SBA-15 by boron doping and acid treatment for direct air capture*. *Separation and Purification Technology*, 2023. **309**: p. 8.
71. Potter, M.E., et al., *Role of Alumina Basicity in CO₂ Uptake in 3-Aminopropylsilyl-Grafted Alumina Adsorbents*. *Chemsuschem*, 2017. **10**(10): p. 2192-2201.
72. Hicks, J.C., et al., *Designing adsorbents for CO₂ capture from flue gas-hyperbranched aminosilicas capable of capturing CO₂ reversibly*. *Journal of the American Chemical Society*, 2008. **130**(10): p. 2902-2903.

73. Choi, S., et al., *Application of Amine-Tethered Solid Sorbents for Direct CO₂ Capture from the Ambient Air*. Environmental Science & Technology, 2011. **45**(6): p. 2420-2427.
74. Chaikittisilp, W., et al., *Poly(L-lysine) Brush-Mesoporous Silica Hybrid Material as a Biomolecule-Based Adsorbent for CO₂ Capture from Simulated Flue Gas and Air*. Chemistry-a European Journal, 2011. **17**(38): p. 10556-10561.
75. Al-Absi, A.A., et al., *Development of in situ polymerized amines into mesoporous silica for direct air CO₂ capture*. Chemical Engineering Journal, 2022. **447**: p. 14.
76. Li, L., et al., *Review on applications of metal-organic frameworks for CO₂ capture and the performance enhancement mechanisms*. Renewable and Sustainable Energy Reviews, 2022. **162**: p. 112441.
77. Kumar, A., et al., *Direct Air Capture of CO₂ by Physisorbent Materials*. Angewandte Chemie-International Edition, 2015. **54**(48): p. 14372-14377.
78. Andirova, D., et al., *Functionalization of Metal-Organic Frameworks for Enhanced Stability under Humid Carbon Dioxide Capture Conditions*. Chemsuschem, 2015. **8**(20): p. 3405-3409.
79. Shekhah, O., et al., *Made-to-order metal-organic frameworks for trace carbon dioxide removal and air capture*. Nature Communications, 2014. **5**: p. 7.
80. Bhatt, P.M., et al., *A Fine-Tuned Fluorinated MOF Addresses the Needs for Trace CO₂ Removal and Air Capture Using Physisorption*. Journal of the American Chemical Society, 2016. **138**(29): p. 9301-9307.
81. Guo, M.Z., et al., *A Highly Efficient and Stable Composite of Polyacrylate and Metal-Organic Framework Prepared by Interface Engineering for Direct Air Capture*. Acs Applied Materials & Interfaces, 2021. **13**(18): p. 21775-21785.
82. Darunte, L.A., et al., *Direct Air Capture of CO₂ Using Amine Functionalized MIL-101(Cr)*. Acs Sustainable Chemistry & Engineering, 2016. **4**(10): p. 5761-5768.
83. Yang, R.A., et al., *Investigation of storage environments on aminopolymer stabilization within UiO-67(Zr) for CO₂ capture*. Materials Advances, 2023. **4**(3): p. 901-909.
84. Rim, G., et al., *Sub-Ambient Temperature Direct Air Capture of CO₂ using Amine-Impregnated MIL-101(Cr) Enables Ambient Temperature CO₂ Recovery*. Jacs Au, 2022. **2**(2): p. 380-393.
85. Rim, G., et al., *Support Pore Structure and Composition Strongly Influence the Direct Air Capture of CO₂ on Supported Amines*. Journal of the American Chemical Society, 2023. **145**(13): p. 7190-7204.
86. Choi, S., et al., *Modification of the Mg/DOBDC MOF with Amines to Enhance CO₂ Adsorption from Ultradilute Gases*. Journal of Physical Chemistry Letters, 2012. **3**(9): p. 1136-1141.
87. Lee, W.R., et al., *Diamine-functionalized metal-organic framework: exceptionally high CO₂ capacities from ambient air and flue gas, ultrafast CO₂ uptake rate, and adsorption mechanism*. Energy & Environmental Science, 2014. **7**(2): p. 744-751.
88. Dong, H., et al., *Amine-Functionalized Quasi-MOF for Direct Air Capture of CO₂*. Acs Materials Letters, 2023. **5**(10): p. 2656-2664.
89. Liu, F.S., et al., *Modified metal-organic framework by a novel coordinatively unsaturated amine grafting mechanism for direct air capture of CO₂*. Chemical Engineering Journal, 2023. **454**: p. 9.
90. McDonald, T.M., et al., *Capture of Carbon Dioxide from Air and Flue Gas in the Alkylamine-Appended Metal-Organic Framework mmen-Mg₂(dobpdc)*. Journal of the American Chemical Society, 2012. **134**(16): p. 7056-7065.
91. Bose, S., et al., *Suitability of a diamine functionalized metal-organic framework for direct air capture*. Chemical Science, 2023. **14**(35): p. 9380-9388.
92. Liao, P.Q., et al., *Putting an ultrahigh concentration of amine groups into a metal-organic framework for CO₂ capture at low pressures*. Chemical Science, 2016. **7**(10): p. 6528-6533.
93. Boer, D.G., J. Langerak, and P.P. Pescarmona, *Zeolites as Selective Adsorbents for CO₂ Separation*. ACS Applied Energy Materials, 2023. **6**(5): p. 2634-2656.

94. Wilson, S.M.W. and F.H. Tezel, *Direct Dry Air Capture of CO₂ Using VTSA with Faujasite Zeolites*. *Industrial & Engineering Chemistry Research*, 2020. **59**(18): p. 8783-8794.
95. Bari, G. and J.H. Jeong, *Porous Carbon for CO₂ Capture Technology: Unveiling Fundamentals and Innovations*. *Surfaces*, 2023. **6**(3): p. 316-340.
96. Song, M.Y., et al., *Cold-Temperature Capture of Carbon Dioxide with Water Coproduction from Air Using Commercial Zeolites*. *Industrial & Engineering Chemistry Research*, 2022: p. 11.
97. Fu, D.L., Y. Park, and M.E. Davis, *Zinc Containing Small-Pore Zeolites for Capture of Low Concentration Carbon Dioxide*. *Angewandte Chemie-International Edition*, 2022. **61**(5): p. 6.
98. Liu, S.S., et al., *Regulating Extra-Framework Cations in Faujasite Zeolites for Capture of Trace Carbon Dioxide*. *Chemistry-a European Journal*, 2022. **28**(50): p. 8.
99. Wilson, S.M.W., *High purity CO₂ from direct air capture using a single TVSA cycle with Na-X zeolites*. *Separation and Purification Technology*, 2022. **294**: p. 9.
100. Xiang, X.J., et al., *High Adsorption Capacity Fe@13X Zeolite for Direct Air CO₂ Capture*. *Industrial & Engineering Chemistry Research*, 2023. **62**(12): p. 5420-5429.
101. Tao, Z.Y., et al., *Direct air capture of CO₂ by metal cation-exchanged LTA zeolites: Effect of the charge-to-size ratio of cations*. *Aiche Journal*, 2023. **69**(8): p. 11.
102. Wilson, S.M.W., *The potential of direct air capture using adsorbents in cold climates*. *Iscience*, 2022. **25**(12): p. 21.
103. Thakkar, H., et al., *CO₂ Capture from Air Using Amine-Functionalized Kaolin-Based Zeolites*. *Chemical Engineering & Technology*, 2017. **40**(11): p. 1999-2007.
104. Short, G.N., et al., *Single-Walled Zeolitic Nanotubes: Advantaged Supports for Poly(ethylenimine) in CO₂ Separation from Simulated Air and Flue Gas*. *Jacs Au*, 2023. **3**(1): p. 62-69.
105. Gebald, C., et al., *Amine-Based Nanofibrillated Cellulose As Adsorbent for CO₂ Capture from Air*. *Environmental Science & Technology*, 2011. **45**(20): p. 9101-9108.
106. Gebald, C., et al., *Stability of Amine-Functionalized Cellulose during Temperature-Vacuum-Swing Cycling for CO₂ Capture from Air*. *Environmental Science & Technology*, 2013. **47**(17): p. 10063-10070.
107. Sehaqui, H., et al., *Fast and Reversible Direct CO₂ Capture from Air onto All-Polymer Nanofibrillated Cellulose-Polyethylenimine Foams*. *Environmental Science & Technology*, 2015. **49**(5): p. 3167-3174.
108. Chen, Z.H., et al., *Polyethylenimine-Impregnated Resin for High CO₂ Adsorption: An Efficient Adsorbent for CO₂ Capture from Simulated Flue Gas and Ambient Air*. *Acs Applied Materials & Interfaces*, 2013. **5**(15): p. 6937-6945.
109. Wang, J.T., et al., *Application of Polyethylenimine-Impregnated Solid Adsorbents for Direct Capture of Low-Concentration CO₂*. *Aiche Journal*, 2015. **61**(3): p. 972-980.
110. Yang, M., S.J. Wang, and L.Z. Xu, *Hydrophobic functionalized amine-impregnated resin for CO₂ capture in humid air*. *Separation and Purification Technology*, 2023. **315**: p. 11.
111. Wang, J.T., et al., *Direct Capture of Low-Concentration CO₂ on Mesoporous Carbon-Supported Solid Amine Adsorbents at Ambient Temperature*. *Industrial & Engineering Chemistry Research*, 2015. **54**(19): p. 5319-5327.
112. Lu, W.G., et al., *Carbon Dioxide Capture from Air Using Amine-Grafted Porous Polymer Networks*. *Journal of Physical Chemistry C*, 2013. **117**(8): p. 4057-4061.
113. Zhang, J.X., et al., *Direct capture of low concentration CO₂ using tetraethylenepentamine-grafted polyacrylonitrile hollow fibers*. *Separation and Purification Technology*, 2022. **287**: p. 9.
114. Zhang, J.X., et al., *Separation and capture of CO₂ from ambient air using TEPA-functionalized PAN hollow fibers*. *Separation and Purification Technology*, 2023. **324**: p. 9.
115. Veselovskaya, J.V., et al., *Direct CO₂ capture from ambient air using K₂CO₃/Al₂O₃ composite sorbent*. *International Journal of Greenhouse Gas Control*, 2013. **17**: p. 332-340.

116. Veselovskaya, J.V., et al., *K₂CO₃-Containing Composite Sorbents Based on Thermally Modified Alumina: Synthesis, Properties, and Potential Application in a Direct Air Capture/Methanation Process*. *Industrial & Engineering Chemistry Research*, 2020. **59**(15): p. 7130-7139.
117. Derevschikov, V.S., et al., *Direct CO₂ capture from ambient air using K₂CO₃/Y₂O₃ composite sorbent*. *Fuel*, 2014. **127**: p. 212-218.
118. Rodríguez-Mosqueda, R., et al., *Parametrical Study on CO₂ Capture from Ambient Air Using Hydrated K₂CO₃ Supported on an Activated Carbon Honeycomb*. *Industrial & Engineering Chemistry Research*, 2018. **57**(10): p. 3628-3638.
119. Masoud, N., et al., *Effect of Support Surface Properties on CO₂ Capture from Air by Carbon-Supported Potassium Carbonate*. *Industrial & Engineering Chemistry Research*, 2021. **60**(38): p. 13749-13755.
120. Derevschikov, V.S., et al., *Composite Sorbents Based on Carbon Nanotubes and K₂CO₃ for CO₂ Capture from Ambient Air*. *Industrial & Engineering Chemistry Research*, 2023. **62**(47): p. 20340-20351.
121. Veselovskaya, J.V., et al., *K₂CO₃-containing composite sorbents based on a ZrO₂ aerogel for reversible CO₂ capture from ambient air*. *Microporous and Mesoporous Materials*, 2021. **310**: p. 9.
122. Rodríguez-Mosqueda, R., et al., *Low temperature water vapor pressure swing for the regeneration of adsorbents for CO₂ enrichment in greenhouses via direct air capture*. *Journal of CO₂ Utilization*, 2019. **29**: p. 65-73.
123. Nikulshina, V., C. Gebald, and A. Steinfeld, *CO₂ capture from atmospheric air via consecutive CaO-carbonation and CaCO₃ calcination cycles in a fluidized-bed solar reactor*. *Chemical Engineering Journal*, 2009. **146**(2): p. 244-248.
124. Dott, A., et al., *Preparation, Characterization and Experimental Investigation of the Separation Performance of a Novel CaO-based CO₂ Sorbent for Direct Air Capture*. *Chemical Engineering & Technology*, 2023. **46**(5): p. 891-900.
125. Goldman, M., et al., *Parametric and laboratory aging studies of direct CO₂ air capture simulating ambient capture conditions and desorption of CO₂ on supported alkaline adsorbents*. *Carbon Capture Science & Technology*, 2023. **6**: p. 10.
126. Criado, Y.A. and J.C. Abanades, *Carbonation Rates of Dry Ca(OH)₂ Mortars for CO₂ Capture Applications at Ambient Temperatures*. *Industrial & Engineering Chemistry Research*, 2022. **61**(40): p. 14804-14812.
127. Abanades, J.C., Y.A. Criado, and H.I. White, *Direct capture of carbon dioxide from the atmosphere using bricks of calcium hydroxide*. *Cell Reports Physical Science*, 2023. **4**(4): p. 14.
128. Zhang, C., et al., *Direct air capture of CO₂ by KOH-activated bamboo biochar*. *Journal of the Energy Institute*, 2022. **105**: p. 399-405.
129. Lackner, K.S., *Capture of carbon dioxide from ambient air*. *The European Physical Journal Special Topics*, 2009. **176**(1): p. 93-106.
130. Wang, T., K.S. Lackner, and A. Wright, *Moisture Swing Sorbent for Carbon Dioxide Capture from Ambient Air*. *Environmental Science & Technology*, 2011. **45**(15): p. 6670-6675.
131. He, H.K., et al., *Reversible CO₂ capture with porous polymers using the humidity swing*. *Energy & Environmental Science*, 2013. **6**(2): p. 488-493.
132. Wang, T., et al., *Characterization of kinetic limitations to atmospheric CO₂ capture by solid sorbent*. *Greenhouse Gases-Science and Technology*, 2016. **6**(1): p. 138-149.
133. Armstrong, M., et al., *Rapid CO₂ capture from ambient air by sorbent-containing porous electrospun fibers made with the solvothermal polymer additive removal technique*. *Aiche Journal*, 2019. **65**(1): p. 214-220.
134. Hou, C.L., et al., *Porosity and hydrophilicity modulated quaternary ammonium-based sorbents for CO₂ capture*. *Chemical Engineering Journal*, 2021. **413**: p. 12.
135. Wang, X.R., et al., *CO₂ Absorption over Ion Exchange Resins: The Effect of Amine Functional Groups and Microporous Structures*. *Industrial & Engineering Chemistry Research*, 2020. **59**(38): p. 16507-16515.

136. Wang, T., et al., *Designing Moisture-Swing CO₂ Sorbents through Anion Screening of Polymeric Ionic Liquids*. *Energy & Fuels*, 2017. **31**(10): p. 11127-11133.
137. Song, J.Z., et al., *Moisture Swing Ion-Exchange Resin-PO₄ Sorbent for Reversible CO₂ Capture from Ambient Air*. *Energy & Fuels*, 2019. **33**(7): p. 6562-6567.
138. Hegarty, J., et al., *Expanding the Library of Ions for Moisture-Swing Carbon Capture*. *Environmental Science & Technology*, 2023: p. 12.
139. Dong, H., et al., *Humidity sensitivity reducing of moisture swing adsorbents by hydrophobic carrier doping for CO₂ direct air capture*. *Chemical Engineering Journal*, 2023. **466**: p. 9.
140. Sakwa-Novak, M.A., et al., *Poly(ethylenimine)-Functionalized Monolithic Alumina Honeycomb Adsorbents for CO₂ Capture from Air*. *Chemsuschem*, 2016. **9**(14): p. 1859-1868.
141. Wijesiri, R.P., et al., *CO₂ Capture from Air Using Pelletized Polyethylenimine Impregnated MCF Silica*. *Industrial & Engineering Chemistry Research*, 2019. **58**(8): p. 3293-3303.
142. Sujan, A.R., et al., *Direct CO₂ Capture from Air using Poly(ethylenimine)-Loaded Polymer/Silica Fiber Sorbents*. *Acs Sustainable Chemistry & Engineering*, 2019. **7**(5): p. 5264-5273.
143. Reneker, D.H. and A.L. Yarin, *Electrospinning jets and polymer nanofibers*. *Polymer*, 2008. **49**(10): p. 2387-2425.
144. Williams, G.R.R.-A., B.T.; Luo, C.J. , *2 Electrospinning Fundamentals*, in *Nanofibres in Drug Delivery*. 2018, UCL Press: London.
145. Zheng, Y., *3 Fabrication on bioinspired surfaces*, in *Bioinspired Design of Materials Surfaces*, Y. Zheng, Editor. 2019, Elsevier. p. 99-146.
146. Taylor, G.I., *Disintegration of water drops in an electric field*. *Proceedings of the Royal Society of London. Series A. Mathematical and Physical Sciences*, 1964. **280**(1382): p. 383-397.
147. Xue, J.J., et al., *Electrospinning and Electrospun Nanofibers: Methods, Materials, and Applications*. *Chemical Reviews*, 2019. **119**(8): p. 5298-5415.
148. Taylor, G.I., *Electrically driven jets*. *Proceedings of the Royal Society of London. A. Mathematical and Physical Sciences*, 1969. **313**(1515): p. 453-475.
149. Reneker, D.H.F., H.; editors, *Polymeric Nanofibres (ACS Symposium Series, No. 918)*. 2005, Washington, DC: American Chemical Society.
150. Reneker, D.H., et al., *Bending instability of electrically charged liquid jets of polymer solutions in electrospinning*. *Journal of Applied Physics*, 2000. **87**(9): p. 4531-4547.
151. Fong, H., I. Chun, and D.H. Reneker, *Beaded nanofibers formed during electrospinning*. *Polymer*, 1999. **40**(16): p. 4585-4592.
152. Gu, S.Y., J. Ren, and G.J. Vancso, *Process optimization and empirical modeling for electrospun polyacrylonitrile (PAN) nanofiber precursor of carbon nanofibers*. *European Polymer Journal*, 2005. **41**(11): p. 2559-2568.
153. Fridrikh, S.V., et al., *Controlling the fiber diameter during electrospinning*. *Physical Review Letters*, 2003. **90**(14): p. 4.
154. Haider, A., S. Haider, and I.-K. Kang, *A comprehensive review summarizing the effect of electrospinning parameters and potential applications of nanofibers in biomedical and biotechnology*. *Arabian Journal of Chemistry*, 2018. **11**(8): p. 1165-1188.
155. Lee, K.H., et al., *Characterization of nano-structured poly(ϵ -caprolactone) nonwoven mats via electrospinning*. *Polymer*, 2003. **44**(4): p. 1287-1294.
156. Luo, C.J., E. Stride, and M. Edirisinghe, *Mapping the Influence of Solubility and Dielectric Constant on Electrospinning Polycaprolactone Solutions*. *Macromolecules*, 2012. **45**(11): p. 4669-4680.
157. Bae, H.-S., et al., *Fabrication of highly porous PMMA electrospun fibers and their application in the removal of phenol and iodine*. *Journal of Polymer Research*, 2013. **20**(7): p. 158.
158. Fallahi, D., et al., *Effect of applied voltage on jet electric current and flow rate in electrospinning of polyacrylonitrile solutions*. *Polymer International*, 2008. **57**(12): p. 1363-1368.

159. Beachley, V. and X. Wen, *Effect of electrospinning parameters on the nanofiber diameter and length*. Materials Science and Engineering: C, 2009. **29**(3): p. 663-668.
160. Zargham, S., et al., *The Effect of Flow Rate on Morphology and Deposition Area of Electrospun Nylon 6 Nanofiber*. Journal of Engineered Fibers and Fabrics, 2012. **7**(4): p. 42-49.
161. De Vrieze, S., et al., *The effect of temperature and humidity on electrospinning*. Journal of Materials Science, 2009. **44**(5): p. 1357-1362.
162. Mailley, D., A. Hebraud, and G. Schlatter, *A Review on the Impact of Humidity during Electrospinning: From the Nanofiber Structure Engineering to the Applications*. Macromolecular Materials and Engineering, 2021. **306**(7): p. 25.
163. Beck, J.S., et al., *A new family of mesoporous molecular sieves prepared with liquid crystal templates*. Journal of the American Chemical Society, 1992. **114**(27): p. 10834-10843.
164. Zhao, D.Y., et al., *Triblock copolymer syntheses of mesoporous silica with periodic 50 to 300 angstrom pores*. Science, 1998. **279**(5350): p. 548-552.
165. Zholobenko, V.L., et al., *Initial stages of SBA-15 synthesis: An overview*. Advances in Colloid and Interface Science, 2008. **142**(1): p. 67-74.
166. Björk, E.M., *Synthesizing and Characterizing Mesoporous Silica SBA-15: A Hands-On Laboratory Experiment for Undergraduates Using Various Instrumental Techniques*. Journal of Chemical Education, 2017. **94**(1): p. 91-94.
167. Konegger, T., C. Drechsel, and H. Peterlik, *In-situ small angle X-ray scattering (SAXS) – A versatile tool for clarifying the evolution of microporosity in polymer-derived ceramics*. Microporous and Mesoporous Materials, 2021. **324**: p. 111268.
168. Davies, T.E., et al., *Experimental methods in chemical engineering: Scanning electron microscopy and X-ray ultra-microscopy—SEM and XuM*. The Canadian Journal of Chemical Engineering, 2022. **100**(11): p. 3145-3159.
169. Ardenne, V., *The scanning electron microscope: theoretical fundamentals (in German)*. Z Physk, 1938. **109**: p. 553.
170. Oatley, C.W., *The early history of the scanning electron microscope*. Journal of Applied Physics, 1982. **53**(2): p. R1-R13.
171. Dunlap, M. and J. Adaskaveg, *Introduction to the scanning electron microscope. Theory, practice, & procedures*. Facility for Advance Instrumentation. UC Davis, 1997. **52**.
172. Cheney, B., *Introduction to scanning electron microscopy*. Materials Engineering department San Jose State University, 2007.
173. Sutton, M.A., et al., *Scanning electron microscopy for quantitative small and large deformation measurements part I: SEM imaging at magnifications from 200 to 10,000*. Experimental mechanics, 2007. **47**: p. 775-787.
174. PerkinElmer, *Thermogravimetric Analysis: A Beginner's Guide*. 2015.
175. Xu, W., et al., *Fundamentals of TGA and SDT*. 2005.
176. Li, P., et al., *Oxidation Kinetics of AlN Under CO₂ Atmosphere*. Metallurgical and Materials Transactions B, 2012. **43**: p. 406-412.
177. Silverstein, R.M.W., F.X., *Infrared Spectroscopy*, in *Spectrometric Identification of Organic Compounds*, N. Rose, Editor. 1997, John Wiley & Sons, Inc.
178. Blum, M.M. and H. John, *Historical perspective and modern applications of attenuated total reflectance—Fourier transform infrared spectroscopy (ATR-FTIR)*. Drug testing and analysis, 2012. **4**(3-4): p. 298-302.
179. Mendes, E. and N. Duarte, *Mid-infrared spectroscopy as a valuable tool to tackle food analysis: A literature review on coffee, dairies, honey, olive oil and wine*. Foods, 2021. **10**(2): p. 477.
180. Subramanian, A. and L. Rodriguez-Saona, *Chapter 7 - Fourier Transform Infrared (FTIR) Spectroscopy*, in *Infrared Spectroscopy for Food Quality Analysis and Control*, D.-W. Sun, Editor. 2009, Academic Press: San Diego. p. 145-178.
181. Silverstein, R.M., et al., *Spectrometric Identification of Organic Compounds*. 2014: Wiley.
182. International Union of, P. and C. Applied, *adsorption*.

183. Thommes, M., et al., *Physisorption of gases, with special reference to the evaluation of surface area and pore size distribution (IUPAC Technical Report)*. Pure and applied chemistry, 2015. **87**(9-10): p. 1051-1069.
184. Brunauer, S., P.H. Emmett, and E. Teller, *Adsorption of Gases in Multimolecular Layers*. Journal of the American Chemical Society, 1938. **60**(2): p. 309-319.
185. Barrett, E.P., L.G. Joyner, and P.P. Halenda, *The Determination of Pore Volume and Area Distributions in Porous Substances. I. Computations from Nitrogen Isotherms*. Journal of the American Chemical Society, 1951. **73**(1): p. 373-380.
186. Thomson, W., 4. *On the equilibrium of vapour at a curved surface of liquid*. Proceedings of the Royal Society of Edinburgh, 1872. **7**: p. 63-68.
187. De Boer, J., et al., *Thet-curve of multimolecular N2-adsorption*. Journal of colloid and interface science, 1966. **21**(4): p. 405-414.
188. Derome, A.E., *Modern NMR Techniques for Chemistry Research*. 1987: Elsevier Science & Technology Books.
189. Atkins, P. and J. De Paula, *Physical chemistry*. 2006, Macmillan.
190. Carbajo, R.J. and J.L. Neira, *NMR for Chemists and Biologists*. Vol. 162. 2013: Springer.
191. Bhande, S.S. and S. Bhosale, *Biosensor: Tools and Techniques for Characterization and Analysis*, in *Nanomaterials for Sustainable Development: Opportunities and Future Perspectives*, R.S. Mane, R.P. Sharma, and A.P. Kanakdande, Editors. 2023, Springer Nature Singapore: Singapore. p. 25-63.
192. Duer, M.J., *Introduction to Solid-State NMR Spectroscopy*. 2005: Wiley.
193. Kaseman, D. *Chemical Shift (Shielding)*. [cited 2024 12th August]; Available from: [https://chem.libretexts.org/Bookshelves/Physical_and_Theoretical_Chemistry_Textbook_Maps/Supplemental_Modules_\(Physical_and_Theoretical_Chemistry\)/Spectroscopy/Magnetic_Resonance_Spectroscopies/Nuclear_Magnetic_Resonance/NMR_-_Theory/NMR_Interactions/Chemical_Shift_\(Shielding\)](https://chem.libretexts.org/Bookshelves/Physical_and_Theoretical_Chemistry_Textbook_Maps/Supplemental_Modules_(Physical_and_Theoretical_Chemistry)/Spectroscopy/Magnetic_Resonance_Spectroscopies/Nuclear_Magnetic_Resonance/NMR_-_Theory/NMR_Interactions/Chemical_Shift_(Shielding)).
194. Polenova, T., R. Gupta, and A. Goldbourt, *Magic Angle Spinning NMR Spectroscopy: A Versatile Technique for Structural and Dynamic Analysis of Solid-Phase Systems*. Analytical Chemistry, 2015. **87**(11): p. 5458-5469.
195. Hartmann, S. and E. Hahn, *Nuclear double resonance in the rotating frame*. Physical Review, 1962. **128**(5): p. 2042.
196. Lagergren, S., *Zur theorie der sogenanntnen adsorption geloster stoffe*. 1898.
197. Ho, Y.S. and G. McKay, *Pseudo-second order model for sorption processes*. Process Biochemistry, 1999. **34**(5): p. 451-465.
198. Avrami, M., *Kinetics of phase change. I General theory*. The Journal of chemical physics, 1939. **7**(12): p. 1103-1112.
199. Avrami, M., *Granulation, phase change, and microstructure kinetics of phase change. III*. The Journal of chemical physics, 1941. **9**(2): p. 177-184.
200. Fanfoni, M. and M. Tomellini, *The Johnson-Mehl-Avrami-Kohnogorov model: A brief review*. Il Nuovo Cimento D, 1998. **20**(7): p. 1171-1182.
201. Liu, Q., et al., *Kinetics Studies of CO2 Adsorption/Desorption on Amine-Functionalized Multiwalled Carbon Nanotubes*. Industrial & Engineering Chemistry Research, 2014. **53**(29): p. 11677-11683.
202. Martell, J.D., et al., *Kinetics of cooperative CO 2 adsorption in diamine-appended variants of the metal-organic framework Mg 2 (dobpdc)*. Chemical science, 2020. **11**(25): p. 6457-6471.
203. Li, C.L., et al., *Synthesis of highly ordered, extremely hydrothermal stable SBA-15/Al-SBA-15 under the assistance of sodium chloride*. Chemistry of Materials, 2007. **19**(2): p. 173-178.
204. Hiyoshi, N., K. Yogo, and T. Yashima, *Adsorption characteristics of carbon dioxide on organically functionalized SBA-15*. Microporous and Mesoporous Materials, 2005. **84**(1-3): p. 357-365.
205. Sayari, A., A. Heydari-Gorji, and Y. Yang, *CO2-induced degradation of amine-containing adsorbents: reaction products and pathways*. Journal of the American Chemical Society, 2012. **134**(33): p. 13834-13842.

206. Anyanwu, J.-T., Y. Wang, and R.T. Yang, *Tunable amine loading of amine grafted mesoporous silica grafted at room temperature: Applications for CO₂ capture*. *Chemical Engineering Science*, 2022. **254**: p. 117626.
207. Min, Y.J., et al., *Direct Air Capture of CO₂ Using Poly(ethyleneimine)-Functionalized Expanded Poly(tetrafluoroethylene)/Silica Composite Structured Sorbents*. *Acs Applied Materials & Interfaces*, 2022. **14**(36): p. 40992-41002.
208. Zhang, Y., et al., *Balsam-Pear-Skin-Like Porous Polyacrylonitrile Nanofibrous Membranes Grafted with Polyethyleneimine for Postcombustion CO₂ Capture*. *ACS Applied Materials & Interfaces*, 2017. **9**(46): p. 41087-41098.
209. Breunig, M., et al., *Electrospun, non-woven fiber membranes of porous polyimides with high carbon dioxide uptakes and selectivities*. *Microporous and Mesoporous Materials*, 2022. **329**: p. 8.
210. Zainab, G., et al., *Free-standing, spider-web-like polyamide/carbon nanotube composite nanofibrous membrane impregnated with polyethyleneimine for CO₂ capture*. *Composites Communications*, 2017. **6**: p. 41-47.
211. Zainab, G., et al., *Amine-impregnated porous nanofiber membranes for CO₂ capture*. *Composites Communications*, 2018. **10**: p. 45-51.
212. Kim, D.W., et al., *Evaluation of CO₂ adsorption capacity of electrospun carbon fibers with thermal and chemical activation*. *Journal of Applied Polymer Science*, 2017. **134**(47): p. 45534.
213. Zainab, G., et al., *Electrospun carbon nanofibers with multi-aperture/opening porous hierarchical structure for efficient CO₂ adsorption*. *Journal of Colloid and Interface Science*, 2020. **561**: p. 659-667.
214. Maruccia, E., et al., *Effect of Thermal Stabilization on PAN-Derived Electrospun Carbon Nanofibers for CO₂ Capture*. *Polymers*, 2021. **13**(23): p. 13.
215. Chiang, Y.C., W.T. Chin, and C.C. Huang, *The Application of Hollow Carbon Nanofibers Prepared by Electrospinning to Carbon Dioxide Capture*. *Polymers*, 2021. **13**(19): p. 17.
216. Nan, D., J. Liu, and W. Ma, *Electrospun phenolic resin-based carbon ultrafine fibers with abundant ultra-small micropores for CO₂ adsorption*. *Chemical Engineering Journal*, 2015. **276**: p. 44-50.
217. Heo, Y.-J., et al., *Synthesis of PAN/PVDF nanofiber composites-based carbon adsorbents for CO₂ capture*. *Composites Part B: Engineering*, 2019. **156**: p. 95-99.
218. Jeong, D., et al., *Electrospun melamine-blended activated carbon nanofibers for enhanced control of indoor CO₂*. *Journal of Applied Polymer Science*, 2019. **136**(28): p. 47747.
219. Othman, F.E.C., et al., *Polyethyleneimine-impregnated activated carbon nanofiber composited graphene-derived rice husk char for efficient post-combustion CO₂ capture*. *Nanotechnology Reviews*, 2022. **11**(1): p. 926-944.
220. Iqbal, N., et al., *Highly flexible NiCo₂O₄/CNTs doped carbon nanofibers for CO₂ adsorption and supercapacitor electrodes*. *Journal of Colloid and Interface Science*, 2016. **476**: p. 87-93.
221. Ali, N., et al., *Porous, flexible, and core-shell structured carbon nanofibers hybridized by tin oxide nanoparticles for efficient carbon dioxide capture*. *Journal of Colloid and Interface Science*, 2020. **560**: p. 379-387.
222. Meng, A.Y., et al., *Hierarchical TiO₂/Ni(OH)₂ composite fibers with enhanced photocatalytic CO₂ reduction performance*. *Journal of Materials Chemistry A*, 2018. **6**(11): p. 4729-4736.
223. Rodaev, V.V., et al., *The Nanofibrous CaO Sorbent for CO₂ Capture*. *Nanomaterials*, 2022. **12**(10): p. 9.
224. Senevirathna, H.L., et al., *Morphology Design and Fabrication of Bio-Inspired Nano-MgO-Mg(OH)₂ via Vapor Steaming to Enable Bulk CO₂ Diffusion and Capture*. *Materials*, 2022. **15**(2): p. 9.
225. Zhang, Y.G., et al., *Ultrahigh Metal-Organic Framework Loading and Flexible Nanofibrous Membranes for Efficient CO₂ Capture with Long-Term, Ultrastable Recyclability*. *Acs Applied Materials & Interfaces*, 2018. **10**(40): p. 34802-34810.

226. Li, Z.Y., et al., *A phase conversion method to anchor ZIF-8 onto a PAN nanofiber surface for CO₂ capture*. Rsc Advances, 2021. **12**(2): p. 664-670.
227. Chiang, Y.C. and W.T. Chin, *Preparation of Zeolitic Imidazolate Framework-8-Based Nanofiber Composites for Carbon Dioxide Adsorption*. Nanomaterials, 2022. **12**(9): p. 18.
228. Samanta, A., et al., *Post-Combustion CO₂ Capture Using Solid Sorbents: A Review*. Industrial & Engineering Chemistry Research, 2012. **51**(4): p. 1438-1463.
229. Korah, M.M., et al., *Electrospun Poly(vinyl alcohol)-L-Arginine Nanofiber Composites for Direct Air Capture of CO₂*. Acs Es&T Engineering, 2022: p. 14.
230. Shao, C.L., et al., *A novel method for making silica nanofibres by using electrospun fibres of polyvinylalcohol/silica composite as precursor*. Nanotechnology, 2002. **13**(5): p. 635-637.
231. Kanehata, M., B. Ding, and S. Shiratori, *Nanoporous ultra-high specific surface inorganic fibres*. Nanotechnology, 2007. **18**(31): p. 7.
232. Yu, Y.X., et al., *Silica ceramic nanofiber membrane with ultra-softness and high temperature insulation*. Journal of Materials Science, 2022. **57**(6): p. 4080-4091.
233. Chempoint. LUDOX® TMA. [cited 2024 25th July]; Available from: <https://www.chempoint.com/products/grace/ludox-monodispersed-colloidal-silica/ludox-colloidal-silica/ludox-tma>.
234. Yu, Y., et al., *Silica ceramic nanofiber membrane with ultra-softness and high temperature insulation*. Journal of Materials Science, 2022. **57**(6): p. 4080-4091.
235. Zhuravlev, L., *Concentration of hydroxyl groups on the surface of amorphous silicas*. Langmuir, 1987. **3**(3): p. 316-318.
236. Van Der Voort, P., et al., *Effect of porosity on the distribution and reactivity of hydroxyl groups on the surface of silica gel*. Journal of the Chemical Society, Faraday Transactions, 1991. **87**(24): p. 3899-3905.
237. Alghunaim, N.S., *Optimization and spectroscopic studies on carbon nanotubes/PVA nanocomposites*. Results in Physics, 2016. **6**: p. 456-460.
238. Acik, G., C.E. Cansoy, and M. Kamaci, *Effect of flow rate on wetting and optical properties of electrospun poly (vinyl acetate) micro-fibers*. Colloid and Polymer Science, 2019. **297**: p. 77-83.
239. Liu, Y.F., et al., *Flexible Stretchable, Dry-Resistant MXene Nanocomposite Conductive Hydrogel for Human Motion Monitoring*. Polymers, 2023. **15**(2): p. 12.
240. Capeletti, L.B. and J.H. Zimnoch, *Fourier transform infrared and Raman characterization of silica-based materials*. Applications of molecular spectroscopy to current research in the chemical and biological sciences, 2016. **32**: p. 137-144.
241. Fidalgo, A. and L.M. Ilharco, *Chemical tailoring of porous silica xerogels: local structure by vibrational spectroscopy*. Chemistry—A European Journal, 2004. **10**(2): p. 392-398.
242. Cruz-Quesada, G., et al., *Hybrid xerogels: Study of the sol-gel process and local structure by vibrational spectroscopy*. Polymers, 2021. **13**(13): p. 2082.
243. Al-Oweini, R. and H. El-Rassy, *Synthesis and characterization by FTIR spectroscopy of silica aerogels prepared using several Si (OR)₄ and R'' Si (OR')₃ precursors*. Journal of Molecular Structure, 2009. **919**(1-3): p. 140-145.
244. Restrepo, I., et al., *The effect of molecular weight and hydrolysis degree of poly (vinyl alcohol)(PVA) on the thermal and mechanical properties of poly (lactic acid)/PVA blends*. Polímeros, 2018. **28**: p. 169-177.
245. Geng, S., et al., *Plasticizing and crosslinking effects of borate additives on the structure and properties of poly (vinyl acetate)*. RSC advances, 2017. **7**(13): p. 7483-7491.
246. Masuda, K., H. Kaji, and F. Horii, *CP/MAS 13C NMR analyses of hydrogen bonding and the chain conformation in the crystalline and noncrystalline regions for poly (vinyl alcohol) films*. Journal of Polymer Science Part B: Polymer Physics, 2000. **38**(1): p. 1-9.
247. Masuda, K., H. Kaji, and F. Horii, *Solid-state 13C NMR and 1H CRAMPS investigations of the hydration process and hydrogen bonding for poly (vinyl alcohol) films*. Polymer journal, 2001. **33**(4): p. 356-363.

248. Luhmer, M., et al., *High-resolution ²⁹Si solid-state NMR study of silicon functionality distribution on the surface of silicas*. Magnetic resonance imaging, 1996. **14**(7-8): p. 911-913.
249. Ojeda-López, R., et al., *SBA-15 materials: calcination temperature influence on textural properties and total silanol ratio*. Adsorption-Journal of the International Adsorption Society, 2015. **21**(8): p. 659-669.
250. Fidalgo, A., et al., *Role of the alkyl-alkoxide precursor on the structure and catalytic properties of hybrid sol-gel catalysts*. Chemistry of Materials, 2005. **17**(26): p. 6686-6694.
251. Brambilla, R., et al., *Sol-gel preparation of aminopropyl-silica-magnesia hybrid materials*. Journal of Sol-Gel Science and Technology, 2011. **59**(1): p. 135-144.
252. Bacsik, Z., et al., *Temperature-Induced Uptake of CO₂ and Formation of Carbamates in Mesocaged Silica Modified with *n*-Propylamines*. Langmuir, 2010. **26**(12): p. 10013-10024.
253. Bacsik, Z., et al., *Mechanisms and Kinetics for Sorption of CO₂ on Bicontinuous Mesoporous Silica Modified with *n*-Propylamine*. Langmuir, 2011. **27**(17): p. 11118-11128.
254. Sánchez-Vicente, Y., et al., *A new sustainable route in supercritical CO₂ to functionalize silica SBA-15 with 3-aminopropyltrimethoxysilane as material for carbon capture*. Chemical Engineering Journal, 2015. **264**: p. 886-898.
255. Srikanth, C.S. and S.S.C. Chuang, *Infrared Study of Strongly and Weakly Adsorbed CO₂ on Fresh and Oxidatively Degraded Amine Sorbents*. Journal of Physical Chemistry C, 2013. **117**(18): p. 9196-9205.
256. Radi, S., et al., *Organically modified silica with pyrazole-3-carbaldehyde as a new sorbent for solid-liquid extraction of heavy metals*. Molecules, 2013. **19**(1): p. 247-262.
257. Hansen, M. and H.J. Jakobsen, *Complete analysis of the high-resolution proton coupled carbon-13 NMR spectra of toluene*. Journal of Magnetic Resonance (1969), 1975. **20**(3): p. 520-529.
258. Pinto, M.L., et al., *Adsorption and Activation of CO₂ by Amine-Modified Nanoporous Materials Studied by Solid-State NMR and ¹³CO₂ Adsorption*. Chemistry of Materials, 2011. **23**(6): p. 1387-1395.
259. Protsak, I.S., et al., *A ²⁹Si, ¹H, and ¹³C Solid-State NMR Study on the Surface Species of Various Depolymerized Organosiloxanes at Silica Surface*. Nanoscale Research Letters, 2019. **14**: p. 1-15.
260. Bauer, F., et al., *Water-based functionalization of mesoporous siliceous materials, Part 1: Morphology and stability of grafted 3-aminopropyltriethoxysilane*. Microporous and Mesoporous Materials, 2017. **250**: p. 221-231.
261. Teramoto, Y., et al., *The role of ozone in the reaction mechanism of a bare zeolite-plasma hybrid system*. Catalysts, 2015. **5**(2): p. 838-850.
262. Chiang, C.-H., N.-I. Liu, and J.L. Koenig, *Magic-angle cross-polarization carbon 13 NMR study of aminosilane coupling agents on silica surfaces*. Journal of Colloid and Interface Science, 1982. **86**(1): p. 26-34.
263. Brochier-Salon, M.-C., M. Bardet, and N. Belgacem, *Solvolytic-hydrolytic of *N*-bearing alkoxy silanes: Reactions studied with ²⁹Si NMR*. Silicon Chemistry, 2008. **3**: p. 335-350.
264. Zheng, F., et al., *Ethylenediamine-modified SBA-15 as regenerable CO₂ sorbent*. Industrial & Engineering Chemistry Research, 2005. **44**(9): p. 3099-3105.
265. Sudeep, P.K., Z. Page, and T. Emrick, *PEGylated silicon nanoparticles: synthesis and characterization*. Chemical Communications, 2008(46): p. 6126-6127.
266. Wilfong, W.C., C.S. Srikanth, and S.S.C. Chuang, *In Situ ATR and DRIFTS Studies of the Nature of Adsorbed CO₂ on Tetraethylenepentamine Films*. ACS Applied Materials & Interfaces, 2014. **6**(16): p. 13617-13626.
267. Foo, G.S., et al., *Elucidation of Surface Species through in Situ FTIR Spectroscopy of Carbon Dioxide Adsorption on Amine-Grafted SBA-15*. Chemsuschem, 2017. **10**(1): p. 266-276.

268. Lashaki, M.J., H. Ziaei-Azad, and A. Sayari, *Insights into the Hydrothermal Stability of Triamine-Functionalized SBA-15 Silica for CO₂ Adsorption*. *Chemsuschem*, 2017. **10**(20): p. 4037-4045.
269. Valdebenito, F., et al., *CO₂ Adsorption of Surface-Modified Cellulose Nanofibril Films Derived from Agricultural Wastes*. *ACS Sustainable Chemistry & Engineering*, 2018. **6**(10): p. 12603-12612.
270. Steinbeck, C., S. Krause, and S. Kuhn, *NMRShiftDB - Constructing a free chemical information system with open-source components*. *Journal of Chemical Information and Computer Sciences*, 2003. **43**(6): p. 1733-1739.
271. Banfi, D. and L. Patiny, www.nmrdb.org: Resurrecting and processing NMR spectra on-line. *Chimia*, 2008. **62**(4): p. 280-281.
272. Castillo, A.M., L. Patiny, and J. Wist, *Fast and accurate algorithm for the simulation of NMR spectra of large spin systems*. *Journal of Magnetic Resonance*, 2011. **209**(2): p. 123-130.
273. Gök, Y. and H.Z. Gök, *Synthesis, characterization and catalytic performance in enantioselective reactions by mesoporous silica materials functionalized with chiral thiourea-amine ligand*. *Research on Chemical Intermediates*, 2021. **47**(2): p. 853-874.
274. Nartowski, K.P., et al., *¹⁹F NMR spectroscopy as a highly sensitive method for the direct monitoring of confined crystallization within nanoporous materials*. *Angewandte Chemie*, 2016. **128**(31): p. 9050-9054.
275. Didas, S.A., et al., *Effect of Amine Surface Coverage on the Co-Adsorption of CO₂ and Water: Spectral Deconvolution of Adsorbed Species*. *The Journal of Physical Chemistry Letters*, 2014. **5**(23): p. 4194-4200.
276. Observatory, N.E. *Land Surface Temperature*. 2024 [cited 2024 22nd May]; Available from: https://earthobservatory.nasa.gov/global-maps/MOD_LSTD_M.
277. Bollini, P., et al., *Dynamics of CO₂ Adsorption on Amine Adsorbents. 2. Insights Into Adsorbent Design*. *Industrial & Engineering Chemistry Research*, 2012. **51**(46): p. 15153-15162.
278. Gabelman, A., *Adsorption Basics: Part 1*. 2017: American Institute of Chemical Engineers.
279. McCabe, W.L., J.C. Smith, and P. Harriott, *Unit operations of chemical engineering*. 1993: McGraw-hill.
280. Wadi, B., et al., *Evaluation of Moderately Grafted Primary, Diamine, and Triamine Sorbents for CO₂ Adsorption from Ambient Air: Balancing Kinetics and Capacity under Humid Conditions*. *Industrial & Engineering Chemistry Research*, 2021. **60**(36): p. 13309-13317.
281. Loganathan, S. and A.K. Ghoshal, *Amine tethered pore-expanded MCM-41: A promising adsorbent for CO₂ capture*. *Chemical Engineering Journal*, 2017. **308**: p. 827-839.
282. Pinto, M.L., et al., *Adsorption and Activation of CO₂ by Amine-Modified Nanoporous Materials Studied by Solid-State NMR and ¹³CO₂ Adsorption*. *Chemistry of Materials*, 2011. **23**(6): p. 1387-1395.
283. Chen, C.-H., et al., *Spectroscopic Characterization of Adsorbed ¹³CO₂ on 3-Aminopropylsilyl-Modified SBA15 Mesoporous Silica*. *Environmental Science & Technology*, 2017. **51**(11): p. 6553-6559.
284. Afonso, R., et al., *Unravelling the Structure of Chemisorbed CO₂ Species in Mesoporous Aminosilicas: A Critical Survey*. *Environmental Science & Technology*, 2019. **53**(5): p. 2758-2767.
285. Mafra, L., et al., *Structure of Chemisorbed CO₂ Species in Amine-Functionalized Mesoporous Silicas Studied by Solid-State NMR and Computer Modeling*. *Journal of the American Chemical Society*, 2017. **139**(1): p. 389-408.
286. Vieira, R., et al., *"Hidden" CO₂ in Amine-Modified Porous Silicas Enables Full Quantitative NMR Identification of Physi- and Chemisorbed CO₂ Species*. *Journal of Physical Chemistry C*, 2021. **125**(27): p. 14797-14806.
287. Bollini, P., S.A. Didas, and C.W. Jones, *Amine-oxide hybrid materials for acid gas separations*. *Journal of Materials Chemistry*, 2011. **21**(39): p. 15100-15120.

288. Sayari, A. and Y. Belmabkhout, *Stabilization of Amine-Containing CO₂ Adsorbents: Dramatic Effect of Water Vapor*. Journal of the American Chemical Society, 2010. **132**(18): p. 6312-+.
289. Goeppert, A., et al., *Easily Regenerable Solid Adsorbents Based on Polyamines for Carbon Dioxide Capture from the Air*. Chemsuschem, 2014. **7**(5): p. 1386-1397.
290. Sardo, M., et al., *Unravelling moisture-induced CO₂ chemisorption mechanisms in amine-modified sorbents at the molecular scale*. Journal of Materials Chemistry A, 2021. **9**(9): p. 5542-5555.
291. Serna-Guerrero, R. and A. Sayari, *Modeling adsorption of CO₂ on amine-functionalized mesoporous silica. 2: Kinetics and breakthrough curves*. Chemical Engineering Journal, 2010. **161**(1): p. 182-190.
292. Loganathan, S., et al., *CO₂ adsorption kinetics on mesoporous silica under wide range of pressure and temperature*. Chemical Engineering Journal, 2014. **256**: p. 1-8.
293. Álvarez-Gutiérrez, N., et al., *Kinetics of CO₂ adsorption on cherry stone-based carbons in CO₂/CH₄ separations*. Chemical Engineering Journal, 2017. **307**: p. 249-257.
294. Liu, F., et al., *CO₂ adsorption behavior and kinetics on polyethylenimine modified porous phenolic resin*. Journal of Porous Materials, 2017. **24**(5): p. 1335-1342.
295. Shirzad, K. and C. Viney, *A critical review on applications of the Avrami equation beyond materials science*. Journal of the Royal Society Interface, 2023. **20**(203): p. 20230242.
296. Zagorowsky, G., et al., *Investigation of kinetics of solid-phase synthesis of lithium orthosilicate*. Journal of thermal analysis and calorimetry, 1999. **55**(2): p. 699-705.
297. Azizian, S., *Kinetic models of sorption: a theoretical analysis*. Journal of Colloid and Interface Science, 2004. **276**(1): p. 47-52.
298. Anyanwu, J.T., Y.R. Wang, and R.T. Yang, *SBA-15 Functionalized with Amines in the Presence of Water: Applications to CO₂ Capture and Natural Gas Desulfurization*. Industrial & Engineering Chemistry Research, 2021. **60**(17): p. 6277-6286.
299. Anyanwu, J.-T., Y. Wang, and R.T. Yang, *Influence of water on amine loading for ordered mesoporous silica*. Chemical Engineering Science, 2021. **241**: p. 116717.
300. Mittal, N., et al., *Postcombustion CO₂ capture using N-(3-trimethoxysilylpropyl) diethylenetriamine-grafted solid adsorbent*. Energy Science & Engineering, 2015. **3**(3): p. 207-220.
301. Chang, F.-Y., et al., *Adsorption of CO₂ onto amine-grafted mesoporous silicas*. Separation and Purification Technology, 2009. **70**(1): p. 87-95.
302. Bacsik, Z. and N. Hedin, *Effects of carbon dioxide captured from ambient air on the infrared spectra of supported amines*. Vibrational Spectroscopy, 2016. **87**: p. 215-221.
303. Abhilash, K.A.S., et al., *Functionalized Polysilsesquioxane-Based Hybrid Silica Solid Amine Sorbents for the Regenerative Removal of CO₂ from Air*. Acs Applied Materials & Interfaces, 2015. **7**(32): p. 17969-17976.
304. McDonald, T.M., et al., *Cooperative insertion of CO₂ in diamine-appended metal-organic frameworks*. Nature, 2015. **519**(7543): p. 303-308.
305. Madhugiri, S., et al., *Electrospun MEH-PPV/SBA-15 Composite Nanofibers Using a Dual Syringe Method*. Journal of the American Chemical Society, 2003. **125**(47): p. 14531-14538.
306. Almuhammed, S., et al., *Electrospinning of PAN nanofibers incorporating SBA-15-type ordered mesoporous silica particles*. European Polymer Journal, 2014. **54**: p. 71-78.
307. Gámez, E., et al., *Antibacterial effect of thymol loaded SBA-15 nanorods incorporated in PCL electrospun fibers*. Nanomaterials, 2020. **10**(4): p. 616.
308. Bollini, P., et al., *Oxidative Degradation of Aminosilica Adsorbents Relevant to Postcombustion CO₂ Capture*. Energy & Fuels, 2011. **25**(5): p. 2416-2425.
309. Li, W., et al., *Steam-stripping for regeneration of supported amine-based CO₂ adsorbents*. ChemSusChem, 2010. **3**(8): p. 899-903.

310. Ilkaeva, M., et al., *Assessing CO₂ Capture in Porous Sorbents via Solid-State NMR-Assisted Adsorption Techniques*. *Journal of the American Chemical Society*, 2023. **145**(16): p. 8764-8769.

